Probing of Incomplete Fusion Dynamics at Energies ~ 4-7 MeV/nucleon

ABSTRACT

of the thesis submitted for the award of

DOCTOR OF PHILOSOPHY

in

PHYSICS

(Experimental Nuclear Physics)

by

Pushpendra P. Singh

Under the Supervision of

Dr. B. P. Singh

Department of Physics

Aligarh Muslim University, Aligarh, INDIA

2008

PROBING OF INCOMPLETE FUSION DYNAMICS AT ENERGIES $\approx$ 4-7 MeV/nucleon

ABSTRACT

of

the thesis submitted for the award of

DOCTOR OF PHILOSOPHY

in

PHYSICS

(Experimental Nuclear Physics)

by

PUSHPENDRA P. SINGH

under the supervision of

DR. B. P. SINGH

Department of Physics

Aligarh Muslim University, Aligarh (UP)-202 202, INDIA

2008

ABSTRACT

This thesis explains some of the aspects of heavy ion (HI) induced reactions at energies near and above the fusion barrier (B_{fus}), which has been a topic of considerable interest in the past decades. In recent years, the study of reaction dynamics in HI interactions has acquired central place in nuclear physics research [1, 2, 3, 4, 5, 6, 7]. It has been noticed that the HI-induced reactions are widely different from light ion induced reactions due to large B_{fus} and due to the availability of different ℓ-bins. The above difference is because of the fact that the charge and mass of HI's are larger than the light ions, and thus the energy and momentum carried in by the HI's are relatively large, which makes the HI-induced reactions more complex. In favorable conditions (only if the projectile energy is comparable to the B_{fus}), associated input angular momentum (ℓ) is supposed to be large enough to produce nuclei in extreme conditions (high excitation energy and spin). Since, the de-Broglie wavelength in HI-induced reactions is of the order of nuclear dimensions, therefore, the interaction may be explained by adopting semi-classical approach [8]. Classically, the interaction trajectories depending on different ℓ-bins and/or impact parameters lying within the target dimensions may lead prominently to the reaction processes like; (i) Complete fusion (CF), and (ii) Incomplete fusion (ICF). For CF to occur, the entrance channel angular momentum (ℓ) should be $\leq \ell_{crit}$, the upper limit of sustainable angular momentum. In such a case, the attractive nuclear potential overcomes the sum of repulsive Coulomb and centrifugal potentials during the projectile-target interaction. This implies large transmission probability, even for higher partial waves ($\ell \leq \ell_{crit}$). Consequently, the target nucleus hugs the projectile with the involvement of all nucleonic degrees of freedom essentially at projectile energy comparable to the B_{fus} or well above it. Absorption of projectile and target nucleus means that, after a while, nucleons from both the projectile and the target lose their previous collective and individual characteristics and take on a set of new characteristics in a single nuclear potential leading to the formation of the composite system. The CF reactions are said to occur probably at zero/small values of impact parameters and for the input angular momenta range $0 \leq \ell \leq \ell_{crit}$, where the probability of CF is supposed to be maximum. In case of CF, the total linear momentum of the projectile is given to the composite system and hence the nuclei recoil at angles very close to the beam direction. The mass of the composite system is nearly equal to the sum of the projectile and the target nucleus masses [8, 12]. It may, further, be pointed out that the kinetic energy of projectile in the center of mass frame is converted into the excitation energy of the compound nucleus (CN). All the kinetic energy which is allowed by momentum conservation is distributed statistically among all accessible internal degrees of freedom until the memory of its mode of formation is lost, except that required by the conservation of energy, total angular momentum, and parity.

Moreover, the CN is only formed if the life-time of the merged system (projectile plus target nucleus) is long enough to attain thermodynamic equilibrium. The CN thus formed, de-excites by the evaporation of light nuclear particle(s) alongwith characteristic γ-radiations. Each particle takes away a definite amount of excitation energy from the equilibrated system, but only a small amount of angular momentum. With the stipulation that fission is also an acceptable modes of de-excitation in favorable conditions. The CN in case of CF, is assumed to be formed via essentially a single route with pre-determined mass and charge, excitation energy, angular momentum, etc. The angular distribution of the emitted particle(s) from a CN may be obtained by simple classical considerations. In such a case, evaporation residues (target-like fragments) are expected to be concentrated in forward cone. Further, it has been experimentally observed that the total CF cross-section (σ_{CF}) is smaller than the total reaction cross-section (σ_R) at a given projectile energy [10]. As a matter of fact, large angular momenta inhibit CF, which is expressed as a ℓ cut-off for CF (ℓ_{crit}), above which the centrifugal potential is so large which prevents fusion between two colliding nuclei. The sharp-cut-off model calculates the cross-section for CF as a summation of contributing ℓ-values from ℓ=0 upto a limiting value ℓ=ℓ_{crit}, where the probability of CN formation is assumed to be maximum. Since, ℓ-values are related to the interaction trajectories, therefore, at higher ℓ-values beyond ℓ_{crit} or at relatively higher values of impact parameters, minimum mass overlap between projectile and target nuclei takes place. This is obvious when a grazing collision involves only the tails of nuclear matter, where fusion incompleteness may lead to the so called ICF.

Incomplete fusion (ICF) corresponds to the reaction dynamics where an incompletely fused composite system is formed as a result of partial linear momentum transfer (LMT) from projectile to the target nucleus. In case of ICF relatively less nucleonic degrees of freedom are expected to be involved as that in CF. As already mentioned, at relatively higher projectile energies and at finite values of impact-parameters, CF gradually gives way to the ICF, where the centrifugal potential (V_{cent}) increases. Under the influence of centrifugal force field, the driving angular momenta exceeds its critical limit (ℓ_{crit}) for CF, as such, the attractive nuclear potential (V_{nucl}) is no more strong enough to capture entire projectile by the target nucleus. At relatively small centrifugal potentials, a pocket remains in the potential energy curve in the vicinity of critical distance of approach. However, the pocket in the entrance channel potential almost vanishes at high input angular momentum (depends on projectile energy and the value of impact parameter). As such, no fusion can occur unless a part of projectile is emitted to release excess driving angular momenta. After the prompt emission of a part of projectile (predominantly α-cluster(s) in case of ^{16}O and ^{12}C beams) allows a loss of input angular momenta($\Delta\ell$), so that another curve is attained corresponding to a lower ℓ-value where

the pocket does exist. As such, the remnant is now supposed to have input angular momentum less than or equal to its own critical limit for fusion with the target nucleus. Eventually, an incompletely fused composite (IFC) system (a part of projectile plus target nucleus) appears with less charge and mass as that of CF population. Further, the ICF is associated with the ℓ-bins above the ℓ_{crit}. The statement about the ℓ-window in the entrance channel for ICF reaction dynamics, is based on the comparison of the population of 'yrast' states (spin distribution) in final nuclei populated via CF and/or ICF [12].

It may, however, be pointed out that in case of ICF, most of the time either α-particle or cluster of α-particles (i.e., ^{8}Be or ^{12}C) depending on the incident ion, escape as unfused spectator. Nonetheless, the viscous forces between interacting partners also play an important role in the occurrence of fusion and fusion-like (ICF) processes [11]. At relatively higher projectile energies (or at large relative velocities) the viscous force between interacting partners decreases, which may significantly reduces the sticking probability of projectile with target nucleus. However, it has experimentally been observed that there is no such boundary of input angular momentum for CF and ICF, both the processes are found to contribute significantly below and above their input angular momentum limits. Apart from the well estabilished CF reaction dynamics, ICF in HI-induced (A$\leq$20) reactions has been a topic of renewed interest after the observation of such processes even at energies near and/or just above the B_{fus} [13, 14, 18]. Large-scale efforts in the field of interest have been made to understand the multitude of ICF processes at energies $\approx$ 4-7 MeV/nucleon, where only complete fusion (CF) is expected to be dominant. As of now, several dynamical models viz; SUMRULE model[12], Break-Up Fusion (BUF) model[15], Promptly Emitted Particles (PEP's) model[16], Exciton model[17], HOT SPOT model[19], etc., have been proposed to explain some of the characteristics of ICF reaction dynamics. As a matter of fact, the above existing models qualitatively explain the experimental data particularly at E/A $\geq$ 10.5 MeV, however, none of the proposed models is able to reproduce the experimental data obtained at energies as low as $\approx$4-7 MeV/nucleon[20].

Further, in several HI-reactions, significant ICF contribution has been observed [21, 22, 23], even at energies just above the B_{fus}, which has become the motivation to study ICF dynamics at relatively low bombarding energies. Apart from that, Parker *et al.*[24], observed forward α-particles in low-Z heavy ion interactions on ^{51}V target at E/A $\approx$ 6 MeV. Morgenstern *et al.* [25], observed the velocity spectra of evaporation residues in the interaction of ^{40}Ar with Boron and Carbon targets. Morgenstern *et al.*[26, 27], have also shown that, ICF reactions significantly contribute to the total reaction cross-section for mass asymmetric systems as compared to mass symmetric systems at the same relative velocity. Further, it has also been observed that both the processes contribute significantly below and above their input angular momentum limits[28]. Since

then, the ICF reaction dynamics has been extensively studied, nevertheless, no clear picture regarding the multiplicity of linear momentum transfer, effect of mass asymmetry, role of different ℓ-values associated with different reaction processes could be drawn, and/or such studies are still limited for a few projectile-target combinations in medium mass region i.e., A $\approx$ 150. As such, in order to have better a understanding of reaction dynamics, it is required to further investigate the underlying processes for above mentioned aspects.

In the present work, in order to explore some of the important issues related to the ICF reaction dynamics at energies near and just above the B_{fus}, i.e., $\approx$ 4-7 MeV/nucleon, the information of considerable value have been obtained from the measurements of;

- Excitation functions (EFs): as an indication of ICF reaction dynamics in which the relative contributions of CF and ICF processes have been deduced,
- Forward recoil range distributions (RRDs): as a proof of fractional linear momentum transfer in which significant fusion incompleteness, associated with fractional degree of linear momentum transfer (LMT) has been observed, and
- Spin-distributions and feeding intensity profiles of evaporation residues (ERs): to probe the entirely different entry state populations in CF and ICF reaction processes.

The experiments for all the above measurements have been performed at the Inter-University Accelerator Center (IUAC), New Delhi, India. In the first set of experiments, the measurements have been carried out to understand the influence of incomplete fusion on complete fusion at energies near and above the Coulomb barrier. Excitation functions for ^{168m}Lu, ^{167}Lu, ^{167}Yb, ^{166}Tm, ^{179}Re, ^{177}Re, ^{177}W, ^{178}Ta and ^{177}Hf radionuclides populated via complete and/or incomplete fusion of ^{16}O with ^{159}Tb and ^{169}Tm have been measured and analyzed over a wide projectile energy range i.e., $E_{proj}\approx$75-95 MeV. Recoil-catcher technique followed by γ-spectrometry has been employed in the present measurements. The radio-nuclide ^{177}W is found to have contribution coming from its pre-cursor decay, which has been separated out from its cumulative cross-section. Experimental data have been compared with the predictions of statistical model code PACE2. Sizable enhancement in the experimentally measured production cross-sections has been observed in case of α-emitting channels over the theoretical predictions, which has been attributed to be coming from incomplete fusion of projectile at these energies. Analysis of experimental data indicates that incomplete fusion is in competition

with complete fusion, and is observed to be dominant at higher energies. As such, an attempt has been made to estimate the fraction of incomplete fusion for both the systems, and has been found to be sensitive to the projectile energy and mass asymmetry of interacting partners. The detailed discussion of these measurements are given in chapter-2 of this thesis [29]. Further, in order to confirm the findings of the measurement and analysis of EFs presented in Chapter-2, and also to investigate fusion incompleteness due to fractional linear momentum transfer from projectile to target nucleus, most probable forward recoil ranges of various radio-nuclides produced via CF and/or ICF in ^{16}O+^{159}Tb and ^{16}O+^{169}Tm systems have been measured at $\approx$ 90 MeV and $\approx$ 87 MeV, respectively. In this chapter, the measurement and analysis of forward mean recoil ranges for different radio-nuclides have been performed within the framework of degree of linear momentum transfer from projectile to the target nucleus by adopting break-up fusion model considerations. Different full and fractional linear momentum transfer components corresponding to the fusion of ^{16}O and/or ^{12}C and ^{8}Be transfer from ^{16}O projectile to the target nucleus have been observed. Further, the experimentally measured recoil range distributions can be used to deduce the relative strengths of full and fractional linear momentum transfer components. As such, an attempt has been made to separate out the relative percentage contributions of CF and ICF by the analysis of experimentally measured forward recoil ranges. The detailed discussion on experimental set-up, measurement and analysis, results obtained and their interpretations are given in the Chapter-3 [30]. While, in the second set of experiments, aiming to probe the incomplete fusion dynamics within the framework of input angular momenta, spin-distributions of various reaction products populated via xn,α/2αxn-channels have been measured for ^{16}O+^{169}Tm system at E$\approx$5.6 MeV/nucleon and ^{12}C+^{169}Tm at E$\approx$4-7 MeV/nucleon. Prompt γ-rays in coincidence with fast charged particles (Z=1,2) have been recorded to obtain the information about involved reaction processes on the basis of their experimentally observed spin-populations during de-excitation. The experimentally observed spin-distributions for direct-α-emitting channels (associated with incomplete fusion) have been found to be distinctly different than that observed for fusion-evaporation (complete fusion) channels. The mean value of driving input angular momenta associated with various direct-α/2αxn-channels have been found to be higher than that observed for fusion-evaporation xn/αxn-channels, and increases with direct-α-multiplicity in the forward cone. Experimentally measured production yields of fusion-evaporation xn/αxn-channels have been found to be in good agreement with the predictions of theoretical model code PACE4. Further, in order to understand the feeding probability in both complete and incomplete fusion reaction products, an attempt has been made to generate feeding intensity profiles from spin-distribution data for both the systems. It has been observed that the complete fusion products are strongly fed

over a broad spin range, however, incomplete fusion products are found to be less fed and/or the population of lower spin states are strongly hindered. In the present work, the mean value of input angular momenta ($J_\circ$) is found to be $\approx$ 10 $\hbar$ for xn-channels, while for direct-αxn and 2αxn-channels (ICF products) the value of $J_\circ$ approaches to $\approx$ 13 $\hbar$ and $\approx$ 16 $\hbar$, respectively. It is interesting to note that, the value of $J_\circ$ for α-emitting channels (^{177}Re isotope) identified from backward gated spectra is also found to be $\approx$ 9-10 $\hbar$, which indicates involvement of significantly less input angular momenta as compared to ^{177}Re isotope populated via direct-α-emitting channels ($\approx$13-14 $\hbar$). The smallness of $J_\circ$ indicates the involvement of less input angular momenta in CF reactions as compared to ICF reactions. As such, the approximate but quite useful essence which emerged from these measurements about how the driving input angular momenta (ℓ) increases with the direct-α multiplicity, can be represented as;

$$\ell_{(ICF-\alpha xn)} \approx 1.3\ell_{(CF-xn/\alpha xn)} \tag{1}$$

$$\ell_{(ICF-2\alpha xn)} \approx 1.23\ell_{(ICF-\alpha xn)} \approx 1.6\ell_{(CF-xn/\alpha xn)} \tag{2}$$

It may, further, be pointed out that the multiplicity of direct-α-particles in forward cone (ICF-α) increases with $J_\circ$, indicates the variation of ℓ-values (impact parameter dependent) even at energy as low as 5.6 MeV/nucleon. As such, on the basis of aforementioned description, it may be inferred that the ICF occurs in the peripheral interactions (at finite values of impact parameters). The detailed discussion of the experimental and electronic set-ups, the method of analysis, findings etc., are given in Chapter-4 of this thesis [31, 32]. The conclusions and future perspectives of the present work are given in the last Chapter of this thesis.

=*=*=*=

Bibliography

[1] M. Lunardona, *et al.*, Nucl. Phys. **A652**, 3-16 (1999).

[2] E. Z. Buthelezi, *et al.*, Nucl. Phys. **A734**, 553-556 (2004).

[3] P. R. S. Gomes, *et al.*, Phys. Rev. **C73**, 064606 (2006).

[4] P. Vergani, *et al.*, Phys. Rev. **C48**, 1815 (1993).

[5] A. Diaz-Torres and I. J. Thompson, Phys. Rev. **C65**, 024606 (2002).

[6] F. Amorini, *et al.*, Phys. Rev. **C58**, 987 (1998).

[7] M. Dasgupta, *et al.*, Phys. Rev. **C70**, 024606 (2004).

[8] P. E. Hodgson, E. Gadioli and E. Gadioli Erba, Introductory Nuclear Physics, Chapter **23**, Clarendon Press , Oxford (1997).

[9] R.-D. Herzberg, *et al.*, Nature, **V442**, 896 (2006).

[10] E. Gadioli, *et al.*, Nucl. Phys. **A641**, 271 (1998).

[11] A. C. Berriman, Nature **V413**, 144 (2001).

[12] J. Wilczynski, *et al.*, Nucl. Phys. **A373**, 109 (1982).

[13] D. J. Hinde, *et al.*, Phys. Rev. **C 39**, 2268 (1989).

[14] D. J. Hinde, *et al.*, Phys. Rev. **C 45**, 1229 (1992).

[15] T. Udagawa and T. Tamura, Phys. Rev. Lett. **45**, 1311 (1980).

[16] J. P. Bondrof, *et al.*, Nucl. Phys. **A333**, 285 (1980).

[17] M. Blann, Phys. Rev. Lett. **27**, 337 (1971).

[18] L. M. Pant, *et al.*, Eur. Phys. J. **A11**, 47 (2001).

[19] R. Weiner and Westrom, Nucl. Phys. **A386**, 282 (1977).

[20] S-Wilczynska K., *et al.*, Phys. Rev. Lett.**42**, 1599 (1979).

[21] Manoj Kumar Sharma, *et al.*, J. Phys. Soc. Japan **72**, 1917 (2003).

[22] Pushpendra P. Singh, M. Phil. Dissertation, A. M. University, Aligarh, India (2005), unpublished.

[23] Sunita Gupta, *et al.*, J. Phys. Soc. Japan **71**, 2434 (2002).

[24] D. J. Parker, *et al.*, Phys. Rev. C**39**, 2256 (1989).

[25] H. M. Morgenstern, *et al.*, Phys. Rev. Lett. **52**, 1104 (1984).

[26] H. Morgenstern, *et al.*, Z. Phys. A **313**, 39 (1983).

[27] H. Morgenstern, *et al.*, Phys. Lett. **113B**, 463 (1982).

[28] I. Tserruya, *et al.*, Phys. Rev. Lett. **60**, 14 (1988).

[29] Pushpendra P. Singh, *et al.*, Phys. Rev. **C77**, *014607 (2008)*.

[30] Pushpendra P. Singh, *et al.*, Euro. Phys. J. **A34**, 29-39 (2007).

[31] Pushpendra P. Singh, *et al.*, Phys. Rev. **C78**, 017602 (2008)

[32] Pushpendra P. Singh, *et al.*, Phys. Lett. B (2008) in press.

LIST OF PUBLICATIONS

submitted with the Ph.D. thesis entitled

Probing of Incomplete Fusion Dynamics at Energies ~ 4-7 MeV/nucleon

in

PHYSICS

(Experimental Nuclear Physics)

by

Pushpendra P. Singh

Under the Supervision of

Dr. B. P. Singh

Department of Physics
Aligarh Muslim University, Aligarh, INDIA

2008

List of Publications

(International Journals)

1. *Probing of incomplete fusion dynamics by spin distribution measurement*
Pushpendra P. Singh, B. P. Singh, Unnati, Manoj Kumar Sharma, R. Kumar, D. Singh, R. P. Singh, S. Muralithar, M. A. Ansari, R. Prasad and R. K. Bhowmik.
Phys. Lett. B (2008), doi:10.1016/j.physletb.2008.11.035 (in press).

2. *Spin distribution studies: A sensitive probe for incomplete fusion reaction dynamics*
Pushpendra P. Singh, B. P. Singh, Manoj Kumar Sharma, Unnati, R. Kumar, K. S. Golda, D. Singh, R. P. Singh, S. Muralithar, M. A. Ansari, R. Prasad and R. K. Bhowmik.
Phys. Rev. C 78, 017602 (2008).

3. *Influence of incomplete fusion on complete fusion: Observation of large incomplete fusion fraction at E/A ≈5-7 MeV*
Pushpendra P. Singh, B. P. Singh, Manoj K. Sharma, Unnati, Devendra P. Singh, Rakesh Kumar, K. S. Golda and R. Prasad.
Phys. Rev. C77, 014607 (2008).

4. *Observation of complete- and incomplete-fusion components in $^{159}Tb,^{169}Tm(^{16}O,x)$ reactions: Measurement and analysis of forward recoil ranges at E/A≈6 MeV.*
Pushpendra P. Singh, Manoj K. Sharma, Unnati, Devendra P. Singh, Rakesh Kumar, B. P. Singh, and R. Prasad.
Euro. Phys. J. A 34, 29-39 (2007).

5. *Production of fission like events after complete and/or in-complete fusion of ^{16}O with ^{159}Tb and ^{169}Tm at E/A≈6 MeV.*
Pushpendra P. Singh, B. P. Singh, Bhavna Sharma, Unnati, Manoj K. Sharma, H. D. Bhardwaj, Rakesh Kumar, K. S. Golda and R. Prasad.
Int. J. Modern Phys. E17, No.3, 549-566 (2008).

6. *Observation of a large incomplete fusion in $^{16}O+^{103}Rh$ system at ≈40-85 MeV*
Unnati, Pushpendra P. Singh, Devendra P. Singh, Manoj K. Sharma, B. P. Singh, and R. Prasad
Nucl. Phys. A 811, 77-92 (2008).

7. *Large pre-equilibrium emission in $\alpha+^{nat}Ni$ interaction at ≈ 8-45 MeV*
Abhishek Yadav, Pushpendra P. Singh, M. M. Musthafa, Devendra P. Singh, Unnati, Manoj K. Sharma, B. P. Singh, and R. Prasad
Phys. Rev. C 78, 044606 (2008).

8. *A study of reaction mechanism in $^{16}O+^{27}Al$ system: Measurement and analysis of excitation functions and angular distributions.*
Manoj K. Sharma, Unnati, Devendra P. Singh, Pushpendra P. Singh, B. P. Singh, and R. Prasad.
Phys. Rev. C75, 064608 (2007).

9. *A study of pre-equilibrium emission of neutrons in $^{93}Nb(\alpha, xn)$ reactions*
Manoj K. Sharma, H.D. Bhardwaj, Unnati, Pushpendra P Singh, Devendra P. Singh, B.P. Singh and R. Prasad.
Euro. Phys. J. A31, 43-51 (2006).

Physics Letters B ••• (••••) •••–•••

Contents lists available at ScienceDirect

Physics Letters B

www.elsevier.com/locate/physletb

Probing of incomplete fusion dynamics by spin-distribution measurement

Pushpendra P. Singh [a,b], B.P. Singh [a,*], M.K. Sharma [a], Unnati Gupta [a], Rakesh Kumar [b], D. Singh [a], R.P. Singh [b], S. Murlithar [b], M.A. Ansari [a], R. Prasad [a], R.K. Bhowmik [b]

[a] Accelerator Laboratory, Department of Physics, A.M. University, Aligarh (UP) 202002, India
[b] NP Group, Inter-University Accelerator Center, PO Box 10502, New Delhi 110067, India

ARTICLE INFO

Article history:
Received 22 May 2008
Received in revised form 5 October 2008
Accepted 12 November 2008

Editor: V. Metag

PACS:
25.70.-z
25.70.Gh
25.70.Jj
25.70.Mn

Keywords:
Particle-γ-coincidence technique
Heavy-ion induced complete and incomplete fusion processes
Spin distribution and feeding intensity measurement

ABSTRACT

Aiming to probe incomplete fusion dynamics in $^{16}O + ^{169}Tm$ system, spin-distributions of various reaction products populated via *xn*-, $\alpha/2\alpha xn$-channels have been measured at $E \approx 5.6$ MeV/nucleon. Prompt γ-rays in coincidence with fast charged particles ($Z = 1, 2$) have been recorded to achieve the information about involved reaction processes on the basis of their experimentally observed spin-populations during de-excitation. The experimentally observed spin-distributions for direct-α-emitting channels (associated with incomplete fusion) have been found to be distinctly different than that observed for fusion-evaporation (complete fusion) channels. The mean value of driving input angular momenta associated with various direct-$\alpha/2\alpha xn$-channels have been found to be higher than that observed for fusion-evaporation $xn/\alpha xn$-channels, and increases with direct-α-multiplicity in forward cone. Experimentally measured, normalized production yields of fusion-evaporation $xn/\alpha xn$-channels have been found to be in good agreement with the predictions of theoretical model code PACE4. Further, in order to understand the feeding probability in both complete and incomplete fusion reaction products, an attempt has been made to generate feeding intensity profiles from spin-distribution data. It has been observed that the complete fusion products are strongly fed over a broad spin range, while incomplete fusion products are found to be less fed and/or the population of lower spin states are strongly hindered.

Production of fast projectile-like fragments (PLFs) associated with incomplete fusion (ICF) dynamics is a topic of resurgent interest at energies near and/or above the fusion barrier (B_{fus}) [1–9], where only complete fusion (CF) is expected to be dominant [10–15]. The production of fast PLFs in ICF dynamics has been first investigated by Britt and Quinton in their pioneering measurements [16]. Later, the similar studies were carried out by Galin et al. [17]. Semi-classically, heavy ion (HI) induced CF and ICF processes can be disentangled on the basis of driving input angular momenta (ℓ) imparted in the system due to various interaction trajectories [18–23]. The probability of CF corresponds to the summation of all ℓ-values from $\ell = 0$ to a limiting value $\ell = \ell_{crit}$, which is expected to be maximum at $\ell = \ell_{crit}$ and assumed to be zero for $\ell > \ell_{crit}$ (as per the sharp cut-off approximation) [24–27]. In case of CF, the attractive nuclear potential overwhelms the sum of repulsive Coulomb and centrifugal potentials in central and/or near central (small values of impact parameters) collisions. Consequently, the target nucleus hugs the entire projectile involving all nucleonic degrees of freedom leading to the formation of fully equilibrated compound nucleus (CN). While, at relatively higher values of impact-parameters, under the influence of centrifugal potential the driving input angular momenta exceeds its critical limit (ℓ_{crit}) for CF, where the attractive nuclear potential is no more strong enough to capture entire projectile. As a result, no fusion can occur unless a part of projectile is emitted to release excess driving input angular momenta. As such, prompt emission of a part of projectile (predominantly α-cluster in case of ^{16}O and ^{12}C beams) takes place to provide sustainable input angular momenta to the system. After such an emission, the remnant now has resulting input angular momenta less than or equal to its own critical limit for fusion with the target nucleus [28,29]. Eventually, an incompletely fused composite system (a part of projectile plus target nucleus) appears with relatively less charge and mass than that of CF population. Further, ICF is assumed to be associated with the ℓ-values above the ℓ_{crit} for CF. However, Tserruya et al. [30], observed that there is no sharp limit of input angular momenta for CF and ICF, both the processes are found to contribute significantly below and above their input angular momenta limits. Moreover, Gerschel [31] suggested that the localization of ℓ-window also depends on target deformation at energies $\leqslant 10$ MeV/nucleon. In case of deformed targets peripheral collisions are observed with

* Corresponding author. Tel.: +91 941 2133929, fax: +91 571 2701001.
E-mail addresses: pushpendrapsingh@gmail.com (P.P. Singh), bpsinghamu@gmail.com (B.P. Singh), ranjan@iuac.ernet.in (R.K. Bhowmik).

0370-2693/$ – see front matter
doi:10.1016/j.physletb.2008.11.035

ℓ-values in the vicinity of ℓ_{crit} for CF, while for spherical targets, the ℓ-window is found to be centered around the ℓ-values $\leqslant 0.5\ell_{crit}$. However, the advances in the understanding of ICF dynamics took place after the particle–γ coincidence measurements by Inamura et al. [32] and Zolonowski et al. [33]. In addition, Geoffroy et al. [34], measured correlation of charged-particle(s) energies and angles alongwith the γ-multiplicities, where ICF processes have been observed to have originated from undamped peripheral collisions. Since then, ICF dynamics has been extensively studied, nevertheless, no clear picture of underlying process in the framework of driving input angular momenta has been drawn at projectile energies $\approx$ 4–7 MeV/nucleon. Some outstanding features of ICF dynamics that have emerged from literature are; (i) the CN via ICF is expected to form with relatively less mass and charge as compared to the total mass and charge of interacting partners [35,36]; (ii) the recoil velocity of heavy reaction products is expected to be less than those populated via CF process [37,38]; (iii) the angular distribution of ejectiles show maxima at forward angles, where α-particle(s) are emitted with a velocity centered around the projectile velocity, termed as direct-α-particle(s) [7,16]; (iv) the spin-distribution and side-feeding pattern of evaporation residues (ERs) have been found to be distinctly different for ICF than that observed for CF [32,33]; and, (v) ICF has been observed to be prominent for more mass asymmetric systems as compared to mass symmetric systems [39–42].

With a view to describe the production of fast PLFs associated with ICF dynamics, a variety of dynamical models, viz. Break-Up Fusion (BUF) [43,44], SUMRULE [45], Promptly Emitted Particles (PEPs) [46], Fermi-jet [47,48], Hot Spot [49], Moving-Source [50], Exciton [51,52] models have been proposed. Apart from these, Overlap model [2,53,54] and Multistep Direct Reaction theory [55] have also been proposed, and Morgenstern et al. [39,56], correlated the probability of ICF reactions to the entrance channel mass asymmetry. It may, further, be pointed out that the aforementioned models/theories, generally, have been used to fit the experimental data obtained at energies $E/A \geqslant 10.5$ MeV or so. However, none of the proposed models is able to fit the experimental data obtained at relatively low bombarding energies i.e., $\approx$ 4–7 MeV/nucleon. As such, due to the unavailability of any reliable theoretical model to explain the emission of fast PLFs associated with ICF at energies $\approx$ 4–7 MeV/nucleon, the study of ICF is still an active area of investigations. Recently, significant ICF contribution has been observed even at energies just above the B_{fus} [30,57–59], which has become the motivation to study ICF dynamics at low bombarding energies. Apart from that, Dracoulis et al. [61], Lane et al. [62], and Mullins et al. [63] reported ICF as a promising route to produce high spin states in final reaction products using light HI beams even at low bombarding energies, although a perfect modeling of ICF processes is apart [60,62,63].

In order to figure out which bunch of driving input angular momenta is associated with a particular reaction channel, a particle–γ coincidence experiment has been performed for ^{16}O + ^{169}Tm system at 5.6 MeV/nucleon at the Inter-University Accelerator Center (IUAC), New Delhi, India. Spin-distributions of different reaction products have been measured to probe entirely different spin-populations corresponding to the CF and ICF dynamics [32]. The same projectile-target combination has been chosen for the present measurement as in Ref. [57,65], where the information about ICF contribution has been obtained by the analysis of excitation functions and forward recoil ranges measurements. The present work not only strengthens our earlier findings but also provide additional qualitative information on the driving input angular momenta in various reaction channels. In order to record particle–γ coincidences, Gamma Detector Array (GDA) alongwith Charged Particle Detector Array (CPDA) set-up has been used. The GDA is an assembly of 12 Compton suppressed, high resolution HPGe γ-spectrometers at angles 45°, 99°, 153° with respect to the beam axis and there are 4 detectors at each of these angles. However, the CPDA is a set of 14-phoswich detectors housed in a 14-cm diameter scattering chamber, covering nearly 90% of the total solid angle. All 14 detectors of CPDA have been divided into the angular rings; (i) Forward angle (F) 10°–60°, (ii) Sideways (S) 60°–120°and (iii) Backward angle (B) 120°–170°. Depending on the fast and slow components of the CPDA, proton and α-particles in each angular ring can be identified. Spectroscopically pure, self-supporting ^{169}Tm (100%) target of thickness $\approx$ 0.93 mg/cm^2 (prepared by rolling technique) has been bombarded with $^{16}O^{+7}$ ($E \approx 90$ MeV) beam delivered from 15UD–Pelletron Accelerator. In order to remove the scattered beam, CPDs have been covered by Al-absorbers of appropriate thicknesses. At forward angles (F) 10°–60°, the detectors are supposed to detect both; (i) fusion–evaporation (CF) α-particles of average energy, i.e., E_α (evaporation) $\approx$ 18 MeV, and (ii) ICF 'fast' α-particles belonging to the same velocity as that of incident projectile, i.e., 22.5 MeV. In order to cut-off fusion–evaporation α-particles emitted in the forward cone, an additional Al-absorber of appropriate thickness has been kept on forward angle (F) 10°–60° CPDs so that only ICF 'fast' α-particles ($E \geqslant$ 18 MeV) may be detected in forward cone. In-beam prompt γ-ray spectra have been recorded in multi parameter mode, which includes different coincidences like; α and 2α detected in backward, forward and 90° angles. Further, in order to identify the xn-channels (produced predominantly via CF), singles data has also been collected. Data analysis has been performed in two steps. In first step, the efficiency determination and gain matching of HPGe detectors have been carried out by counting the radio-activity (before and/after the experiment) of standard γ-sources (^{152}Eu and ^{133}Ba) kept at target position. After proper gain-matching, different coincidence conditions have been projected onto γ-spectra to generate particle ($Z = 1, 2$) gated spectra. In order to improve the data statistics, assuming the angular distribution of the observed γ-rays to be isotropic, all gated spectra for a particular gating condition have been summed up. However, in the second step, different reaction products expected to be populated via CF and/or ICF have been identified from their characteristic γ-lines from the gated and/or singles spectra. Several xn-channels (predominantly populated via CF) such as; $^{185-xn}Ir$, have been identified by looking into singles spectra. For the identification of pxn-channels, backward(B)-α-gated spectra has been subtracted from backward(B)-particles($Z = 1, 2$)-gated spectra to achieve proton-gated spectra. However, $\alpha xn/2\alpha xn$ (CN-α)-channels produced via CF have been identified from the backward(B)-α-gated spectra. Further, as per the definition of ICF, the fast-α-particles (particles of the order or projectile velocity) are expected to be emitted only in forward cone (F). As such, $\alpha xn/2\alpha xn$(Direct-α)-channels produced via ICF have been identified from forward(F)-α-gated spectra. The intensity and area under the photo-peak (efficiency corrected) of the characteristic prompt γ-transitions assigned to the particular reaction products were used to determine the relative production yield. The γ-ray energies and their intensities used in the present work have been taken from RADWARE level scheme directory [64]. In order to generate experimental spin-distributions of various CF and ICF reaction products, relative production yields have been plotted as a function of experimentally observed spin (J_{obs}^{exp}) corresponding to prompt γ-transitions. For better comparison of different reaction channels (xn, αxn and $2\alpha xn$) in a panel, relative production yields have been normalized with their own highest experimentally measured values (Y_{obs}^{max}) at lowest J_{obs}^{min}. Further, as an analytical representation of data, the experimentally measured spin-distributions obtained as mentioned above have been fitted by a function of following type [32]:

$$Y = Y_\circ / [1 + \exp(J - J_\circ)/\Delta], \quad (1)$$

Please cite this article in press as: P.P. Singh et al., Probing of incomplete fusion dynamics by spin-distribution measurement, Physics Letters B (2008), doi:10.1016/j.physletb.2008.11.035

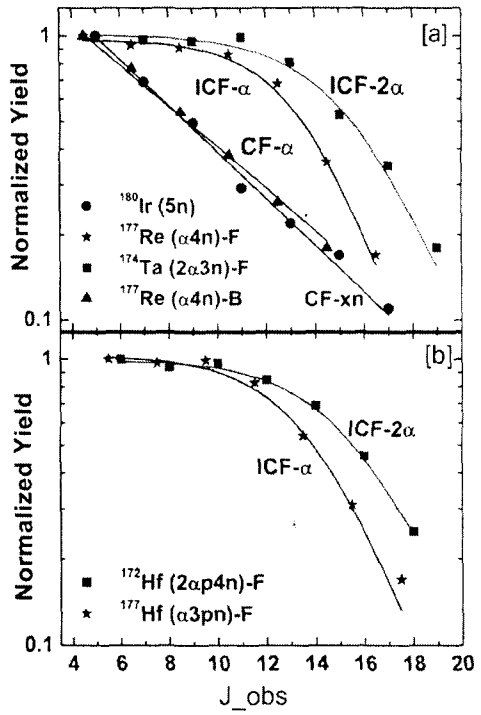

Fig. 1. Experimentally measured spin-distributions for different residues populated via *xn* (CF product) and $\alpha xn/2\alpha xn$ (both CF and/or ICF products) in ^{16}O + ^{169}Tm system at ≈ 5.6 MeV/nucleon. The nomenclature used in the plots indicate the involved reaction dynamics i.e., ICF-α and ICF-2α means, involved reaction dynamics is ICF with one α and 2α-multiplicity, respectively. While, CF-α indicates CF with one α-multiplicity identified from backward α-gated spectra. The nomenclature also shows that the exist channels are composed by the one given residual nucleus, α-particle(s) (M_{alpha} = 1–2), neutron(s) and/or proton(s). 'F' and 'B' represent the reaction products identified respectively from 'Forward' and 'Backward' α-gated spectra. The lines and curves through data points are the result of best fit procedure explained in the text.

where; Δ is related to the width of mean input angular momenta (J_o) and Y_o is the normalization constant. Here, J_o is a sensitive parameter, which provides the qualitative information about the driving input angular momenta associated with various reaction channels.

Experimentally measured spin-distributions for *xn*, αxn and $2\alpha xn$ channels populated via CF and/or ICF are plotted in Figs. 1(a), (b). The errors have not been shown in these figures and are estimated to be ⩽ 10%. Since the normalized yield (Y_{nor}) at different J_{obs} for a particular reaction product have been obtained as a ratio of Y_{obs}^{max} at J_{obs}^{min} to Y_{obs} at different J_{obs} values. As such, the fractional errors significantly reduced in the value of Y_{nor}, it has been checked that the inclusion of these reduced errors does not alter the fitting of spin-distribution, and hence the present analysis. Different reaction channels have been labeled by self-explanatory notations of corresponding emission cascade. It can be observed from the Figs. 1(a), (b), there is a striking difference in the spin-distributions for different reaction products expected to be populated via CF and ICF, which indicates the involvement of entirely different reaction dynamics in the production of these reaction products. As shown in these figures, the intensity of *xn*-channels (predominantly populated via CF) falls off rather quickly with J_{obs} or the intensity is increasing steeply towards the band head, indicating strong feeding during the deexcitation of CN. However, for αxn- and $2\alpha xn$-channels identified from forward(F)-α-gated spectra (associated with ICF), the intensity appears to be almost constant up to a certain value of observed spin, i.e., $J_{obs} \approx 10\hbar$ for direct-α-emitting channels, and $J_{obs} \approx 12\hbar$ for direct-2α-emitting channels. As such, on the basis of observed trends, it can be inferred that the intensity is not increasing towards band head after ≈ 10 and 12$\hbar$ for direct-α/2α-emitting channels. These observations indicate the absence of feeding to the lowest members of the 'yrast' band and/or the population of low spin states are strongly hindered in αxn and $2\alpha xn$ channels (associated with ICF dynamics). Moreover, for αxn and/or $2\alpha xn$-channels, it may be pointed out that the intensity increases with J_{obs} upto $J \approx 10$–$12\hbar$, respectively, indicating significant feeding upto $J \approx 10$–$12\hbar$ from the entry point. Further, in order to show entirely different observed trends of spin-distributions for CF and ICF products, same ERs populated via forward-α (ICF) and backward-α (CF) emitting channels (Re-isotopes) have been compared and plotted in Fig. 1(a). As can be seen from this figure, the spin-distribution for ^{177}Re isotope identified from backward-α-gated spectra has been found to be distinctly different than that observed from forward-α-gated spectra, which again indicates the involvement of entirely different reaction dynamics. The spin-distribution of ^{177}Re (α4*n*) isotope identified from backward-α-gated spectra shows the same trend as has been observed for *xn*-channel (CF). Further, Fig. 1(b) shows the spin-distributions of ^{172,177}Hf isotopes identified from forward-α-gated spectra, which are likely to reflect the similar characteristics as that observed for direct-α-emitting channels. Although, the dispute on this point has been discussed by Gerschel [31]. Further, in general, the spin at half yield i.e., the mean value of input angular momenta (J_o) is found to be ≈ 10$\hbar$ for *xn*-channels, while for direct-αxn and $2\alpha xn$-channels (ICF products) the value of J_o approaches to ≈ 13$\hbar$ and ≈ 16$\hbar$, respectively. It is interesting to note that, the value of J_o for α-emitting channels (^{177}Re isotope) identified from backward gated spectra is also found to be ≈ 9–10$\hbar$, which indicates involvement of significantly less input angular momenta as compared to ^{177}Re isotope populated via direct-α-emitting channels (≈ 13–14$\hbar$). The smallness of J_o indicates the involvement of less input angular momenta in CF reactions as compared to ICF reactions. As such, the approximate but quite useful essence which emerged from these measurements about how the driving input angular momenta (ℓ) increases with the direct-α multiplicity, can be represented as:

$$\ell_{(ICF-\alpha xn)} \approx 1.3\ell_{(CF-xn/\alpha xn)}, \quad (2)$$

$$\ell_{(ICF-2\alpha xn)} \approx 1.23\ell_{(ICF-\alpha xn)} \approx 1.6\ell_{(CF-xn/\alpha xn)}. \quad (3)$$

It may, further, be pointed out that the multiplicity of direct-α-particles in forward cone (ICF-α) increases with J_o, indicates the variation of ℓ-values (impact parameter dependent) even at energy as low as 5.6 MeV/nucleon. As such, on the basis of aforementioned description, it may be inferred that the ICF occurs in the peripheral interactions (at finite values of impact parameters).

In order to check the accuracy and self-consistency of presently measured spin-distributions, an attempt has been made to estimate relative production yield of each reaction product from spin-distribution data. The experimentally measured relative yield of individual reaction product has been extrapolated up to $J = 0\hbar$, and the yield value at $J = 0\hbar$ ($Y^{J=0}$) has been normalized with the total yield (sum of all fusion–evaporation channels) to estimate relative yield value of each reaction product. In the same way the relative production yield of individual reaction products, calculated using theoretical model code PACE4, have also been normalized with the total yield of fusion–evaporation channels. The ratio of experimentally measured and theoretically calculated relative yields (Y_{EXP}/Y_{PACE4}) for all fusion–evaporation channels has been plotted in Fig. 2. As shown in this figure, both the experimentally and theoretically calculated values agree reasonably well within the experimental uncertainties, strengthening the measured spin-distributions.

Further, as indicated in Figs. 1(a), (b), the intensity of 'yrast'-line transitions decreases gradually with high spin for CF, while,

Please cite this article in press as: P.P. Singh et al., Probing of incomplete fusion dynamics by spin-distribution measurement, Physics Letters B (2008), doi:10.1016/j.physletb.2008.11.035

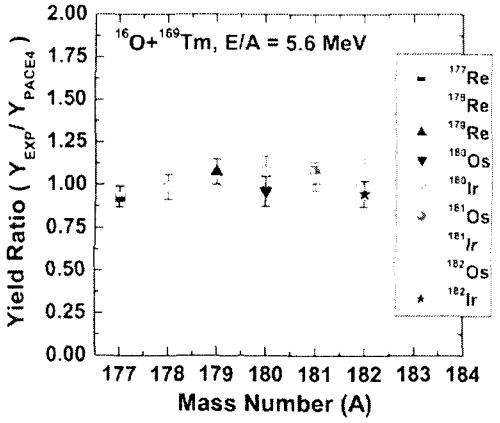

Fig. 2. The ratio of experimentally measured and theoretically estimated relative production yield of residues populated only via CF in ^{16}O + ^{169}Tm system at ≈ 5.6 MeV/nucleon.

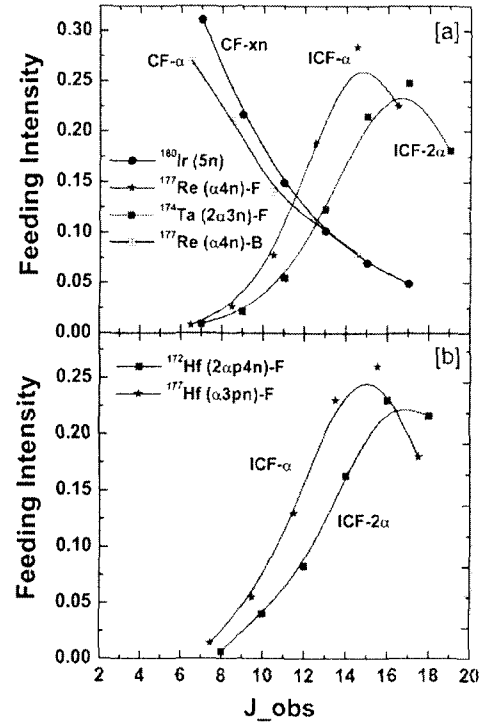

Fig. 3. Deduced feeding intensities of gamma cascades of different ER's expected to be produced via; *xn*, *αxn* and/or *2αxn* channels in ^{16}O + ^{169}Tm system at ≈ 5.6 MeV/nucleon. The lines and curves through data points are drawn to just guide the eye.

in case of ICF the intensity remains almost constant up to a certain limiting spin value and decreases rapidly for transitions of higher spin, indicating entirely different de-excitation patterns for CF and ICF from entry states to the 'yrast' line. This implies a rather smooth and broad feeding distribution for the 'yrast'-states in case of CF. However, for ICF channels this distribution must have a 'narrow window' meaning thereby a well localized angular momentum region where a given projectile-like fragment is emitted in contrast to the large window for the fusion reactions. As such, in order to understand the feeding pattern in different reaction channels associated with CF and/or ICF, the feeding intensity of γ-population have been deduced from the experimentally measured spin-distributions of reaction products. The feeding intensity for studied reaction channels have been plotted as a function of J_{obs} and are given in Figs. 3(a), (b). As shown in these figures, the feeding intensity for forward gated *αxn* and *2αxn*-channels is found to be increasing upto $J \approx 14\hbar$ and $J \approx 17\hbar$, respectively from the higher spin states (entry side), indicating that the high spin states are strongly fed even in case of ICF channels. However, as the residual nucleus de-excites, the feeding intensity decreases gradually with available excitation energy and/or angular momentum, which indicates the absence of feeding to the lowest members of the 'yrast' band or the low spin states are less populated in *αxn* and *2αxn*-channels identified from forward-*α*-gated spectra. Such feeding intensity pattern is expected to arise from narrow ℓ-window, localized near and/or above to the critical angular momentum for CF, that is associated with ICF. Furthermore, as shown in Figs. 3(a), (b), the feeding intensity is showing sharp exponential rise towards low spin states for all *xn*-channels (CF), indicating strong feeding. Apart from that, for better comparison of forward and backward *α*-channels populated via ICF and CF, respectively, the feeding intensity pattern for backward(B)-*α*-channels alongwith forward(F)-*α*-channels have also been plotted in Figs. 3(a), (b). As can be seen from this figure, feeding intensity of *αxn*-channel identified from backward(B)-*α*-gated spectra shows exponential rise towards lower spin states, as expected for CF dynamics, where the band is fed over a broad spin range. Further, the feeding intensity is found to be less in the production of ^{177}Re isotopes identified from backward(B)-*α*-gated spectra, as compared to *xn*-channels. This difference may be because of the fact that the neutron emission carry almost negligible angular momentum from CN, while, emission of an *α*-particle from CN takes away significant amount of angular momentum and excitation energy, which may not provide broad feeding range towards the band head.

In conclusion of the present work, it may be inferred that the experimentally measured spin-distributions of direct-*α*/*2α*-emitting channels (ICF reaction products) identified from forward(F)-*α*-gated spectra have been found to be distinctly different than that observed for CF reaction products. The population of low spin states are observed to be strongly hindered and/or less fed in ICF reaction products, while significant feeding has been observed over the broad spin range in case of CF. It may, further, be pointed out that, the value of mean input angular momentum increases with direct-*α* multiplicity in forward cone, which indicates the competition from successively opened ICF channels for each ℓ-value above ℓ_{crit} for normal fusion (CF) even at projectile energy 5.6 MeV/nucleon. This confirms the fact that ICF reactions predominantly occur due to influence of centrifugal potential at higher values of impact parameters, where only CF is expected to be dominant. As such, it may not be out of place to mention that the ICF is a natural extension of the fusion processes for those interaction trajectories for which the limit of input angular momenta do not allow CF. The extension of the present work at different energies would be interesting, and helpful for the refinement of the present findings. As such, it has been proposed to extend the above measurements at different projectile energies to generate some systematics and to compare the entry/exit state spin-populations, which will be presented in the forthcoming paper(s).

Acknowledgements

It is our pleasure to thank Prof. Amit Roy, Director of the Inter-University Accelerator Center, New Delhi, India for extending all the experimental facilities, and Prof. Zoran Basrak, Ruder Boskovic Institute (RBI), Zagreb, Croatia, for several scientific discussions to improve this manuscript. One of the authors (P.P.S.) thanks to the IUAC for financial support and hospitality, M.K.S. thanks the DST, and R.P. thanks the UGC and the DST for financial assistance.

References

[1] M. Dasgupta, et al., Nucl. Phys. A 787 (1) (2007) 144.
[2] A. Diaz-Torres, et al., Phys. Rev. Lett. 98 (2007) 152701.
[3] L.R. Gasques, et al., Phys. Rev. C 74 (2006) 064615.
[4] P.R.S. Gomes, et al., Phys. Lett. B 601 (2004) 20.
[5] M. Dasgupta, et al., Phys. Rev. C 70 (2004) 024606.
[6] L.F. Canto, et al., Phys. Rev. C 58 (1998) 1107.
[7] N. Arena, et al., Phys. Rev. C 50 (1994) 880.
[8] E. Gadioli, et al., Nucl. Phys. A 641 (1998) 271.
[9] P. Vergani, et al., Phys. Rev. C 48 (1993) 1815.
[10] W. Trautmann, et al., Phys. Rev. Lett. B 53 (1984) 1630.
[11] L. Corradi, et al., Phys. Rev. C 71 (2005) 014609.
[12] D.J. Parker, et al., Phys. Rev. C 30 (1984) 143.
[13] M. Cavinato, et al., Phys. Rev. C 52 (1995) 2577.
[14] B.S. Tomar, et al., Phys. Rev. C 49 (1994) 941.
[15] M. Crippa, et al., Z. Phys. A 350 (1994) 121.
[16] H.C. Britt, A.R. Quinton, Phys. Rev. 124 (1961) 877.
[17] J. Galin, et al., Phys. Rev. C 9 (1974) 1126.
[18] J. Pochodzalla, et al., Phys. Lett. B 181 (1) (1986) 33.
[19] H.W. Wilschut, et al., Phys. Lett. B 138 (1) (1984) 43.
[20] M.B. Tsang, et al., Phys. Lett. B 134 (3) (1984) 169.
[21] H. Oeschler, et al., Phys. Lett. B 127 (3) (1983) 177.
[22] P. Piattelli, et al., Phys. Lett. B 442 (1) (1998) 48.
[23] S.E. Arnell, et al., Phys. Lett. B 129 (1) (1983) 23.
[24] J.H. Barker, et al., Phys. Rev. Lett. 45 (1980) 424.
[25] D.J. Parker, et al., Phys. Rev. C 39 (1989) 2256.
[26] J.R. Wu, I.Y. Lee, Phys. Rev. Lett. 45 (1980) 8.
[27] D. Hojman, et al., Phys. Rev. C 74 (2006) 044604.
[28] T. Inamura, et al., Phys. Lett. B 84 (1982) 71;
T. Inamura, et al., Phys. Rev. C 32 (1985) 1539.
[29] W. Trautmann, et al., Phys. Rev. Lett. 53 (1984) 1630.
[30] I. Tserruya, et al., Phys. Rev. Lett. 60 (1988) 14.
[31] C. Gerschel, Nucl. Phys. A 387 (1982) 297.
[32] T. Inamura, et al., Phys. Lett. B 68 (1977) 51.
[33] D.R. Zolnowski, et al., Phys. Lett. 41 (1978) 92.
[34] K.A. Geoffory, et al., Phys. Rev. Lett. 43 (1979) 1303.
[35] D.J. Parker, et al., Phys. Rev. C 44 (1991) 1528;
D.J. Parker, et al., Phys. Rev. C 35 (1987) 161.
[36] M.N. Namboodiri, et al., Phys. Rev. C 35 (1987) 149.
[37] E. Gadioli, et al., Nucl. Phys. A 641 (3) (1998) 271.
[38] R.A. Zingarelli, et al., Phys. Rev. C 48 (1993) 651.
[39] H.M. Morgenstern, et al., Phys. Rev. Lett. 52 (1984) 1104;
H.M. Morgenstern, et al., Z. Phys. A 313 (1983) 39.
[40] J.B. Natowitz, et al., Z. Phys. A 325 (1986) 467.
[41] H. Morgenstern, et al., Phys. Lett. B 113 (1982) 463.
[42] K.H. Hanold, et al., Phys. Rev. C 48 (1993) 723.
[43] T. Udagawa, T. Tamura, Phys. Rev. Lett. 45 (1980) 1311.
[44] J.R. Wu, I.Y. Lee, Phys. Rev. Lett. 45 (1980) 8.
[45] J. Wilczynski, et al., Nucl. Phys. A 373 (1982) 109;
J. Wilczynski, et al., Phys. Rev. Lett. 45 (1980) 606.
[46] J.P. Bondrof, et al., Nucl. Phys. A 333 (1980) 285.
[47] D.H.E. Gross, J. Wilczynski, Phys. Lett. B 67 (1977) 1.
[48] H. Tricoire, Z. Phys. A 312 (1983) 221.
[49] R. Weiner, M. Westrom, Nucl. Phys. A 386 (1977) 282.
[50] T.C. Awes, et al., Phys. Rev. C 24 (1981) 89.
[51] M. Blann, Phys. Rev. C 23 (1981) 205.
[52] T. Otsuka, K. Harada, Phys. Lett. B 121 (1983) 106.
[53] B.G. Harvey, Nucl. Phys. A 444 (1985) 498.
[54] M.H. Simbel, A.Y. Abdul Magd, Z. Phys. A 294 (1980) 277.
[55] V.I. Zagrebaev, Ann. Phys. (N.Y.) 197 (1990) 33.
[56] H. Morgenstern, W. Bohne, W. Galster, K. Grabisch, Z. Phys. A 324 (1986) 443.
[57] P.P. Singh, et al., Phys. Rev. C 77 (2008) 014607;
P.P. Singh, et al., Eur. Phys. J. A 34 (2007) 29, and the references therein.
[58] S. Chakrabarty, et al., Nucl. Phys. A 678 (2000) 355.
[59] U. Gupta, et al., Nucl. Phys. A 811 (2008) 77.
[60] A. Jungclaus, et al., Phys. Rev. C 67 (2003) 034302;
A. Jungclaus, et al., Phys. Rev. C 66 (2002) 014312.
[61] G.D. Dracoulis, et al., J. Phys. G: Nucl. Part. Phys. 23 (1997) 1191, and references therein.
[62] G.J. Lane, et al., Phys. Rev. C 60 (1999) 067301.
[63] S.M. Mullins, et al., Phys. Rev. C 58 (1998) 831;
S.M. Mullins, et al., Phys. Rev. C 61 (2000) 044315.
[64] RADWARE, the level scheme directory on http://radware.phy.ornl.gov/agsdir1.html.
[65] M.K. Sharma, et al., Phys. Rev. C 70 (2004) 044606.

Please cite this article in press as: P.P. Singh et al., Probing of incomplete fusion dynamics by spin-distribution measurement, Physics Letters B (2008), doi:10.1016/j.physletb.2008.11.035

Spin-distribution measurement: A sensitive probe for incomplete fusion dynamics

Pushpendra P. Singh,[1,*] B. P. Singh,[1,†] Manoj Kumar Sharma,[1] Unnati,[1] R. Kumar,[2] K. S. Golda,[2] D. Singh,[1] R. P. Singh,[2] S. Muralithar,[2] M. A. Ansari,[1] R. Prasad,[1] and R. K. Bhowmik[2,‡]

[1]*Department of Physics, A. M. University, Aligarh (UP) 202002, India*

[2]*NP-Group, Inter-University Accelerator Center, P.O. Box No. 10502, New Delhi 110067, India*

(Received 26 May 2008; published 30 July 2008)

Spin distributions of various reaction products populated via complete and/or incomplete fusion of ^{16}O with ^{169}Tm have been measured at projectile energy ≈5.6 MeV/nucleon. Particle ($Z = 1, 2$) γ-coincidences have been employed to achieve the information about involved reaction modes on the basis of their entry state spin populations. The experimentally measured spin distributions for incomplete fusion products have been found to be distinctly different than those observed for complete fusion products. The driving input angular momenta associated with incomplete fusion products have been found to be relatively higher than complete fusion products, and increases with direct α-multiplicity. It has also been observed that incomplete fusion products are less fed and/or the population of lower spin states are strongly hindered, while complete fusion products indicating strong feeding over a broad spin range.

DOI: 10.1103/PhysRevC.78.017602 PACS number(s): 25.70.Gh, 25.70.Jj, 25.70.Mn

Incomplete fusion (ICF) in heavy ion (HI) induced reactions has been a topic of renewed interest at energies near and/or above the fusion barrier (B_{fus}) [1–6]. Large-scale efforts have been in progress to understand the multitude of ICF processes at energies ≈5–7 MeV/nucleon, where only complete fusion (CF) is expected to be dominant [7–9]. Firstly, the ICF dynamics has been investigated by Britt and Quinton in their pioneering measurements on the production of energetic forward-peaked α-particles [10]. Similar studies were carried out by Galin *et al.* [11]. However, the advances in the understanding of ICF dynamics took place after the particle-γ-coincidence measurements by Inamura *et al.* [12] and Zolonowski *et al.* [22]. In addition, Geoffroy *et al.* [13], measured correlation of charged-particle energies and angles with γ-multiplicities, where ICF processes have been shown to originate from undamped peripheral collisions. It is now known that the CF occurs for the driving input angular momentum ℓ up to a limiting value, i.e., ℓ equal to ℓ_{crit} [14]. The probability of CF is assumed to be unity for ℓ equal to ℓ_{crit} and expected to be zero for $\ell > \ell_{crit}$ (as per sharp cut-off approximation) [15–17]. In case of CF, the attractive nuclear potential overcomes the sum of repulsive Coulomb and centrifugal potentials. Consequently, the target nucleus hugs the projectile with the involvement of all nucleonic degrees of freedom leading to the formation of fully equilibrated compound nucleus (CN). While, at relatively higher projectile energies and at finite values of impact parameters, CF gradually gives way to ICF, where the centrifugal potential increases for the higher values of impact parameters. Under the influence of the centrifugal force field, the attractive nuclear potential is not strong enough to capture the entire projectile. Therefore, an incompletely fused composite system (a part of projectile plus target nucleus) appears in the exit channel. In addition, if the input angular momentum exceeds the critical limit (ℓ_{crit}) for CF, no fusion can occur unless a part of the projectile is emitted to release excess driving input angular momenta. After emission of a part of the projectile, the remnant is now supposed to have resulting input angular momenta less than or equal to its own critical limit for fusion to occur [13,18,19]. Further, it has also been observed that both the processes contribute significantly below and above their input angular momentum limits [20]. Moreover, Gerschel [21] suggested that the localization of ℓ-window depends on the target deformation at energies $\leqslant$10 MeV/nucleon. Where, in case of deformed targets peripheral collisions are observed with ℓ-values in the vicinity of ℓ_{crit} for CF, while for spherical targets, the ℓ-window is found to be centered around values $\leqslant 0.5\ell_{crit}$. The ICF dynamics has been extensively studied, nevertheless, no clear picture about the multiplicity of input angular momenta associated with different reaction channels has been drawn. A variety of dynamical models viz.; Break-Up Fusion (BUF) [23,24], SUMRULE [25], Promptly Emitted Particles (PEP's) [26], Fermi-jet [27,28], Hot Spot [29], Moving-Source [30], Exciton [31,32] models have been proposed to explain the characteristics of ICF dynamics. These models generally have been used to fit the experimental data obtained at energies $\geqslant$10 MeV/nucleon. However, none of the proposed models is able to reproduce the experimental data obtained at energies as low as ≈4–7 MeV/nucleon. Recently, significant ICF contributions have been observed even at energies just above the B_{fus} [33–35], which has become the motivation to investigate ICF at relatively low bombarding energies. Apart from that, Dracoulis *et al.* [36], Lane *et al.* [37], and Mullins *et al.* [38] reported that ICF can selectively populate high spin states in final reaction products even at low bombarding energies, and can be used as a spectroscopic tool. However, a perfect modeling of the ICF processes is still lacking.

In view of the above motivations, an experiment has been performed at the Inter-University Accelerator Center (IUAC), New Delhi, INDIA, employing the particle-γ-coincidence

*Also at: NP-Group, Inter-University Accelerator Center, P.O. Box No. 10502, New Delhi 110 067, India.

†bpsinghamu@gmail.com

‡ranjan@iuac.ernet.in

technique. A spectroscopically pure, self-supporting natural ^{169}Tm (100%) target of thickness ≈0.93 mg/cm^2 prepared by the rolling technique has been bombarded with a 90 MeV $^{16}O^{+7}$ beam delivered from the 15UD-Pelletron Accelerator. The above projectile-target combination has been chosen because of the well-known prompt γ-transitions in the possible reaction products and also to supplement our earlier studies [33,39], where the information about ICF contribution has been obtained by the measurement and analysis of excitation functions and forward recoil ranges. The present work not only strengthens our earlier findings but also provides additional qualitative information on the driving input angular momenta associated with various CF and ICF channels. In this experiment, particle-γ-coincidence events have been recorded using the Gamma Detector Array (GDA) along with Charged Particle Detector Array (CPDA) setup. The GDA is an assembly of 12 Compton suppressed, high resolution HPGe γ-spectrometers at angles 45°, 99°, 153° with respect to the beam axis and there are four detectors at each of these angles. However, the CPDA is a set of 14-phoswich detectors housed in a 14 cm diameter scattering chamber, covering nearly 90% of total solid angle so that the angular distribution of charged particles ($Z = 1, 2$) in ≈4π-solid angle may be recorded. All 14 detectors of CPDA have been divided into the three angular rings: (i) forward angle (F) 10°–60°, (ii) sideways (S) 60°–120°, and (iii) backward angle (B) 120°–170°. In order to remove the scattered beam, CPDs have been covered by Al absorbers of appropriate thicknesses. In the present experiment, at ≈90 MeV projectile energy, the forward angles (F) CPD's 10°–60°, are expected to detect two α-components; i.e., (i) the fusion-evaporation (CF) α-particles of average energy $E_\alpha \approx 18$ MeV, and (ii) the ICF 'fast' α-particles of $E_{\text{direct-}\alpha} \approx 22.5$ MeV. As such, in order to record only 'fast' α-particles in forward cone (F), an Al absorber of appropriate thickness has been kept at forward angle (F) 10°–60° CPD's to cutoff low energy alpha component (i.e., $E_\alpha \approx 18$ MeV). All HPGe γ-detectors of GDA setup have been calibrated using various standard γ-sources of known strength. The efficiency of high-resolution HPGe γ-spectrometers have been determined by putting ^{152}Eu and ^{133}Ba γ-sources at the target position. The ^{241}Am-source has been used for CPDA gain matching. In-beam prompt γ-ray spectra have been recorded in multiparameter mode employing different gating conditions. Off-line data analysis has been performed by projecting α-backward (for CF products) and α-forward gates (for ICF products) on γ-spectra. Specific exit channels have been identified by looking into various α-gated spectra. The main reaction channels that were identified in the forward cone in coincidence with fast α-particle(s) have been ^{169}Tm(^{16}O,αxn)$^{181-x}$Re, ^{169}Tm(^{16}O,αpxn)$^{180-x}$W, ^{169}Tm(^{16}O,$2\alpha xn$)$^{177-x}$Ta, and ^{169}Tm(^{16}O,$2\alpha pxn$)$^{176-x}$Hf. However, the residues which have been identified in backward cone are ^{169}Tm(^{16}O,αxn)$^{181-x}$Re and ^{169}Tm(^{16}O,pxn)$^{184-x}$Os. The normal xn-channels ^{169}Tm(^{16}O,xn)$^{185-x}$Ir (CF products) have been identified from singles spectra and confirmed from decay γ-lines. Areas under the peaks of relevant γ-transitions have been used to obtain the relative production yield of different reaction products.

In the present work, different reaction modes have been identified on the basis of entry state spin population in a residual nucleus prior to its deexcitation [12], which are expected to be entirely different in CF and ICF reactions. The spin distributions [i.e., the yield (intensity) profile as a function of observed spin (J_{obs})] of residual nuclei have been measured for the given projectile-target combination at ≈5.6 MeV/nucleon. Experimentally measured spin distributions of evaporation residues have been fitted to a function of the following type adopted as the simplest analytical representation of data:

$$Y = Y_\circ/[1 + \exp(J - J_\circ)/\Delta], \quad (1)$$

where Δ is related to the width of input angular momentum ($J_\circ$) and $Y_\circ$ is the normalization constant. Here, $J_\circ$ is a sensitive parameter and provides the qualitative information about the mean driving input angular momenta associated with different reaction channels.

Experimentally measured spin distributions for xn, αxn and $2\alpha xn$-channels are presented in Figs. 1 and 2. For a

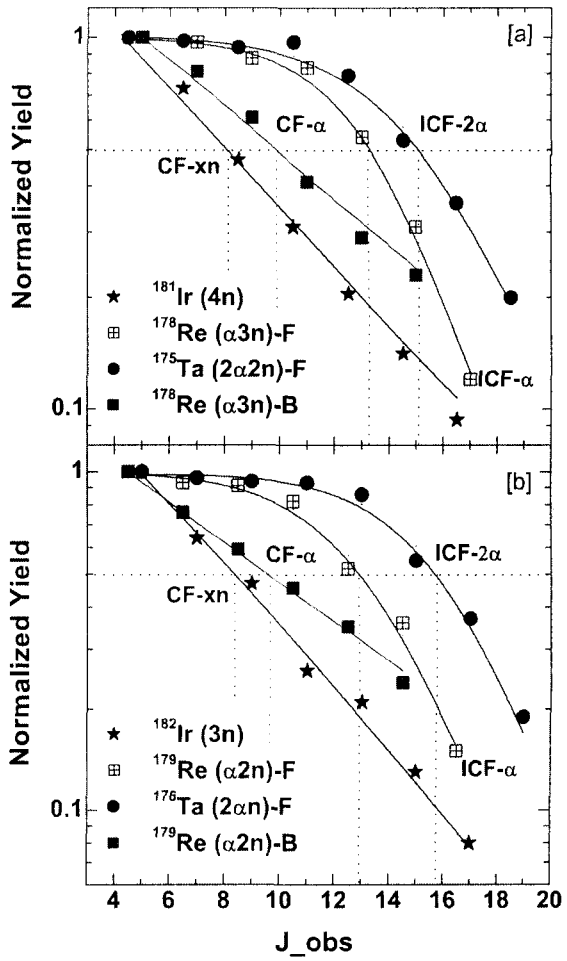

FIG. 1. (Color online) Experimentally measured spin distributions for different residues populated via xn (predominantly via CF) and $\alpha xn/2\alpha xn$ (both CF and/or ICF) channels in ^{16}O+^{169}Tm system at ≈5.6 MeV/nucleon. Notations 'F' and 'B' represent the reaction products identified respectively from 'Forward' and 'Backward' α-gated spectra. The lines and curves through data points are the result of best fit procedure explained in the text.

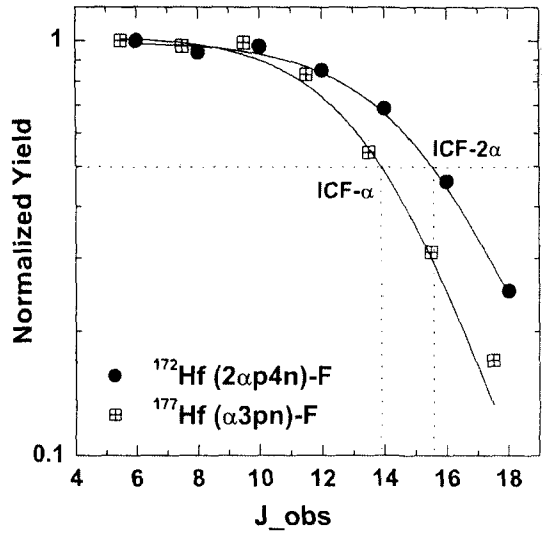

FIG. 2. (Color online) Explanation of the figure is same as Fig. 1.

better comparison of xn, αxn, and $2\alpha xn$ channels in a panel, relative yields of different CF and ICF products have been normalized to their own maximum observed yield values at lowest J_{obs}. The errors have not been shown in these figures as they have been estimated to be $\leqslant 10\%$, and the inclusion of these errors is not likely to modify the present analysis. Reaction channels are labeled by self-explanatory notation of corresponding emission cascade. It can be observed from Figs. 1 and 2 that the experimentally measured spin distributions for ICF products are found to be distinctly different than that observed for CF products. The intensity of the xn-channels (predominantly populated via CF and identified from singles spectra) falls off rather quickly toward high spin states in the 'yrast' band, indicating strong feeding during the deexcitation of CN. This gradual monotonic increase in the intensity toward the band head is due to the fact that CF reactions lead to a CN of definite excitation energy (E^*), but with a broad spin distribution. In this case, the yrast states will be fed over a broad spin range. However, for αxn and/or $2\alpha xn$ channels identified from forward α-gated spectra (associated with ICF), the yield appears to be almost constant up to $J \approx 10\hbar$ for α-emitting channels, and $J \approx 12\hbar$ for 2α-emitting channels. Further, by comparison, CF and ICF spin distributions for ^{178,179}Re isotopes identified from backward-α-gated spectra (CF products) are found to be distinctly different than those observed from forward-α-gated (ICF products) spectra, Figs. 1(a, b). The yield of ^{178,179}Re isotopes identified from the backward cone is found to fall steeply with increasing spin, indicating strong feeding as expected for CF. The same characteristics of the spin distribution have also been observed in the case of ^{172,177}Hf isotopes populated via $2\alpha pxn$ and αxpn channels, Fig. 2. These results imply the absence of feeding to the lowest members of the 'yrast' band, or the population of low spin states are strongly hindered in direct α-emitting channels (ICF products). Moreover, the yield decreases above $J \approx 10$–$12\hbar$, indicating significant feeding at entry-state spin populations in the ICF processes. The observed trends likely reflect the fact that the entry-spin distribution for ICF reaction products is narrow and peaked at large ℓ-values. However, the dispute on this point has been discussed by Gerschel [21].

Moreover, in general, the value of $J_\circ$ is found to be $\approx 8\hbar$ for xn-channels, while for forward-αxn and $2\alpha xn$-channels $J_\circ$ is found to be $\approx 13\hbar$ and $\approx 16\hbar$, respectively. Again, it is interesting to note that, the $J_\circ$ value for α-emitting channels (^{178,179}Re isotopes) identified from backward α-gated spectra is found to be $\approx 10\hbar$, which indicates the involvement of significantly less input angular momenta as compared to ^{178,179}Re isotopes populated via direct-α-emitting channels. It may also be seen from the deduced values of $J_\circ$ that the multiplicity of direct α-particles increases with the driving input angular momenta, which shows the variation of ℓ-bins with different values of impact parameters at a given projectile energy. As such, it may be inferred that the lower ℓ-values do not contribute to the ICF, significantly.

In order to check the accuracy and self-consistency of the presently measured spin distributions, an attempt has been made to estimate the relative production yield of each reaction product from spin-distribution data. The experimentally measured relative yield of the individual reaction product has been extrapolated up to $J = 0\hbar$, and the yield value at $J = 0\hbar$ ($Y^{J=0}$) has been normalized with the total yield (sum of all fusion-evaporation channels) to estimate the relative yield value of each reaction product. In the same way the relative production yield of individual reaction products, calculated using theoretical model code PACE4, have been normalized with the total yield of fusion-evaporation channels.The ratio of experimentally measured and theoretically calculated relative yields (Y_{EXP}/Y_{PACE4}) for all fusion-evaporation channels has been plotted in Fig. 3. As shown in this figure, both the experimental and theoretical data agree reasonably well within the experimental uncertainties, strengthens/gives confidence in the measured spin distributions.

On the basis of results presented in this paper, it may be concluded that the low ℓ-values are strongly hindered and/or

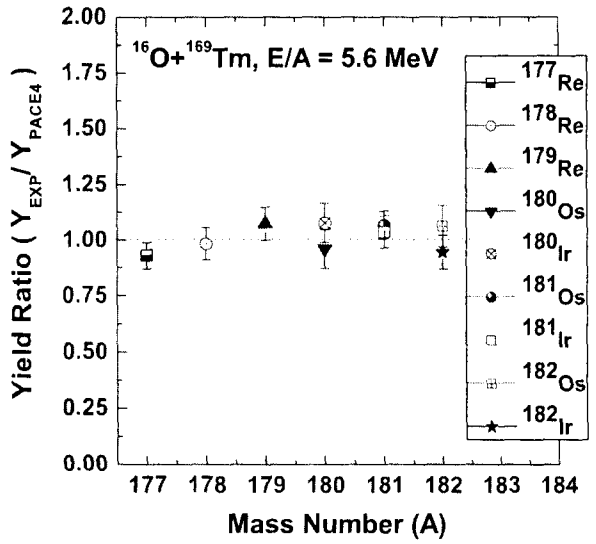

FIG. 3. (Color online) The yield ratio Y_{EXP}/Y_{PACE4} of different residues produced only via CF of ^{16}O with ^{169}Tm at projectile energy $\approx$5.6 MeV/nucleon.

less fed in ICF. This confirms the fact that ICF reactions predominantly occur due to large input angular momenta coming from higher values of impact parameters. It may further be pointed out that the competition from successively opened ICF-channels (direct-α multiplicity) increases with driving input angular momenta. Each ℓ-value above ℓ_{crit} for normal fusion (CF) is expected to contribute to the direct-α emitting channels. As such, ICF seems to be a natural extension of the fusion processes for those interaction trajectories for which the driving input angular momentum does not allow CF. The extension of the present work at different energies would be interesting, and helpful for the refinement of the present findings. As such, it has been proposed to extend the above measurement for different projectile energies to generate some systematics.

The authors are thankful to Prof. Amit Roy, Inter-University Accelerator Center (IUAC), New Delhi, INDIA, for extending all the facilities, and Prof. Zoran Basrak for several scientific discussions to improve this manuscript. One of the authors (P.P.S.) thanks the IUAC for financial support and hospitality, M.K.S. thanks the DST, and R.P. thanks the UGC and the DST for financial assistance.

[1] L. F. Canto, R. Donangelo, L. M. deMatos, M. S. Hussein, and P. Lotti, Phys. Rev. C **58**, 1107 (1998).
[2] E. Gadioli *et al.*, Nucl. Phys. **A641**, 271 (1998).
[3] P. R. S. Gomes *et al.*, Phys. Lett. **B601**, 20 (2004).
[4] P. Vergani *et al.*, Phys. Rev. C **48**, 1815 (1993).
[5] W. Trautmann *et al.*, Phys. Rev. Lett. **B53**, 1630 (1984).
[6] L. Corradi *et al.*, Phys. Rev. C **71**, 014609 (2005).
[7] D. J. Parker, J. Asher, T. W. Conlon, and I. Naqib, Phys. Rev. C **30**, 143 (1984).
[8] M. Cavinato *et al.*, Phys. Rev. C **52**, 2577 (1995).
[9] M. Crippa *et al.*, Z. Phys. A **350**, 121 (1994).
[10] H. C. Britt and A. R. Quinton, Phys. Rev. **124**, 877 (1961).
[11] J. Galin *et al.*, Phys. Rev. C **9**, 1126 (1974).
[12] T. Inamura *et al.*, Phys. Lett. **B68**, 51 (1977).
[13] K. A. Geoffroy *et al.*, Phys. Rev. Lett. **43**, 1303 (1979).
[14] E. A. Bakkum, P. Decowski, K. A. Griffioen, R. J. Meijer, and R. Kamermans, Phys. Rev. C **39**, 2094 (1989).
[15] J. H. Barker *et al.*, Phys. Rev. Lett. **45**, 424 (1980).
[16] J. R. Wu and I. Y. Lee, Phys. Rev. Lett. **45**, 8 (1980).
[17] D. Hojman, N. Wang, X. Wu, Z. Li, M. Liu, and W. Scheid, Phys. Rev. C **74**, 044604 (2006).
[18] T. Inamura *et al.*, Phys. Lett. **B84**, 71 (1982); Phys. Rev. C **32**, 1539 (1985).
[19] W. Trautmann *et al.*, Phys. Rev. Lett. **53**, 1630 (1984).
[20] I. Tserruya *et al.*, Phys. Rev. Lett. **60**, 14 (1988).
[21] C. Gerschel, Nucl. Phys. **A387**, 297 (1982).
[22] D. R. Zolnowski *et al.*, Phys. Rev. Lett. **41**, 92 (1978).
[23] T. Udagawa and T. Tamura, Phys. Rev. Lett. **45**, 1311 (1980).
[24] J. R. Wu and I. Y. Lee, Phys. Rev. Lett. **45**, 8 (1980).
[25] J. Wilczynski *et al.*, Nucl. Phys. A **373**, 109 (1982); Phys. Rev. Lett. **45**, 606 (1980).
[26] J. P. Bondrof *et al.*, Nucl. Phys. **A333**, 285 (1980).
[27] D. H. E. Gross and Wilczynski, Phys. Lett. **B67**, 1 (1977).
[28] H. Tricoire, Z. Phys. A **312**, 221 (1983).
[29] R. Weiner and Westrom, Nucl. Phys. **A386**, 282 (1977).
[30] T. C. Awes *et al.*, Phys. Rev. C **24**, 89 (1981).
[31] M. Blann, Phys. Rev. C **23**, 205 (1981).
[32] T. Otsuka and K. Harada, Phys. Lett. **B121**, 106 (1983).
[33] Pushpendra P. Singh *et al.*, Phys. Rev. C **77**, 014607 (2008); Eur. Phys. J. A **34**, 29 (2007), and references therein.
[34] I. Tserruya *et al.*, Phys. Rev. Lett. **60**, 14 (1988).
[35] D. J. Parker, J. J. Hogan, and J. Asher, Phys. Rev. C **35**, 161 (1987).
[36] G. D. Dracoulis *et al.*, J. Phys. G: Nucl. Part. Phys. **23**, 1191 (1997).
[37] G. J. Lane, G. D. Dracoulis, A. P. Byrne, A. R. Poletti, and T. R. McGoram, Phys. Rev. C **60**, 067301 (1999).
[38] S. M. Mullins *et al.*, Phys. Lett. **B393**, 279 (1997); Phys. Rev. C **61**, 044315 (2000).
[39] Manoj K. Sharma *et al.*, Phys. Rev. C **70**, 044606 (2004).

Influence of incomplete fusion on complete fusion: Observation of a large incomplete fusion fraction at $E \approx 5$–7 MeV/nucleon

Pushpendra P. Singh,* B. P. Singh,† Manoj Kumar Sharma, Unnati, Devendra P. Singh, and R. Prasad
Accelerator Laboratory, Department of Physics, A. M. University, Aligarh (UP) 202 002, India

Rakesh Kumar and K. S. Golda
NP-Group, Inter University Accelerator Center, Aruna Asaf Ali Road, P. O. Box 10502, New Delhi 110 067, India
(Received 16 April 2007; revised manuscript received 9 August 2007; published 15 January 2008)

Experiments have been carried out to explore the reaction dynamics leading to incomplete fusion of heavy ions at moderate excitation energies. Excitation functions for ^{168}Lu^{m}, ^{167}Lu, ^{167}Yb, ^{166}Tm, ^{179}Re, ^{177}Re, ^{177}W, ^{178}Ta, and ^{177}Hf radio-nuclides populated via complete and/or incomplete fusion of ^{16}O with ^{159}Tb and ^{169}Tm have been studied over the wide projectile energy range $E_{\rm proj} \approx 75$–95 MeV. Recoil-catcher technique followed by off-line γ-spectrometry has been employed in the present measurements. Experimental data have been compared with the predictions of theoretical model code PACE2. The experimentally measured production cross sections of α-emitting channels were found to be larger as compared to the theoretical model predictions and may be attributed to incomplete fusion at these energies. During the analysis of experimental data, incomplete fusion has been found to be competing with complete fusion. As such, an attempt has been made to estimate the incomplete fusion fraction for both the systems, and has been found to be sensitive for projectile energy and mass asymmetry of interacting partners.

DOI: 10.1103/PhysRevC.77.014607 PACS number(s): 25.70.Gh, 25.70.Jj, 25.70.Mn

I. INTRODUCTION

The reaction dynamics studies at energies near and above the Coulomb barrier (CB) with light heavy ions ($Z \leqslant 10$) and high-Z targets have been a topic of considerable interest [1–3]. Recent experimental data [4–8] at these energies indicate that the most dominating fusion processes are (a) complete fusion (CF) and (b) in-complete fusion (ICF). For incident energies up to a little above the Coulomb barrier, with the collision trajectories of input angular momentum $\ell \leqslant \ell_{\rm crit}$, heavy ion interaction is dominated by entire linear momentum transfer from projectile to target nucleus leading to complete fusion process. As a consequence, a fully equilibrated excited compound nucleus of pre-determined charge, mass, and angular momenta is supposed to be formed via essentially a single route, after which the light nuclear particle(s) and characteristic γ-radiations are emitted as a means of deexcitation. However, at relatively high bombarding energies and for input angular momentum $\ell \geqslant \ell_{\rm crit}$, complete fusion gradually gives way to incomplete fusion, where fractional mass and charge as well as the linear momentum of projectile are transferred to the target nucleus, due to the prompt emission of α-clusters in forward cone with almost projectile velocity. As a result of such process, projectile-like and target-like partners may come into picture in the exit channel. Such kind of reactions were first observed by Britt and Quinton [9] in the bombardment of heavy targets by ^{12}C, ^{14}N, and ^{16}O projectiles at energies well above the Coulomb barrier. Further, particle-γ coincidence studies by Inamura *et al.* [10] contributed a great deal to the understanding of underlying dynamics. Some of the important features of incomplete fusion process are (i) ICF contributes a significant fraction to the reaction cross section in case of low-Z projectiles and high-Z targets; (ii) the forward mean-ranges of recoils show relatively smaller depth in the stopping medium than that of complete fusion residues, strengthening the concept of fractional momentum transfer; (iii) the outgoing projectile-like fragments are mainly concentrated in forward cone and their energy spectrum essentially peak at the projectile velocity [9]; and (iv) the spin distribution of evaporation residues populated via incomplete fusion are found to be distinctly different as observed for complete fusion process [10,11].

In order to explain some of these features several dynamical models viz. SUMRULE model [12], Break-Up Fusion (BUF) model [13], Promptly Emitted Particles (PEP's) model [14], etc., have been proposed. The SUMRULE model of Wilczynski *et al.* [12] considers that ICF processes mainly occur in peripheral interactions and are localized in the angular momentum space above the critical angular momentum for the complete fusion. The peripheral nature of ICF has also been emphasized by Trautmann *et al.* [15] and Inamura *et al.* [16,17]. The BUF-model of Udagawa and Tamura [13] is based on the distorted wave Born approximation (DWBA) formalism for elastic breakup, where the projectile is supposed to breakup into α-clusters as it approaches the nuclear field of target nucleus. One of the fragments of projectile is assumed to fuse with target nucleus to form an incompletely fused composite system (ICF) and unfused fragment continues to move nearly undeflected or less deflected in the forward cone with almost projectile velocity. However, in PEP's model [14], the particles transferred from the projectile to target nucleus are assumed to get accelerated in the nuclear field of target nucleus and hence, acquire extra velocity to escape. Moreover, the leading-particle model of Natowitz *et al.* [18], hybrid model of Blann *et al.* [19],

*pushpendrapsingh@gmail.com; also at: NP-Group, Inter-University Accelerator Center, Aruna Asaf Ali Road, P. O. Box 10502, New Delhi 110 067, India.
†bpsinghamu@gmail.com

and Fermi-jet model [20–22] have also been proposed and seem to explain some of the experimental data related to incomplete fusion. As a matter of fact, the above existing models qualitatively explain the experimental data particularly at $E/A \geqslant 10.5$ MeV, but are not consistent at relatively low bombarding energies [10,23,24]. Moreover, during the past decade, several reports indicated the onset of incomplete fusion even at low bombarding energies, i.e., $E/A \approx 5$–7 MeV [25–29]. Parker *et al.* [30] observed forward α-particles in low-Z heavy ion interactions on ^{51}V target at $E/A \approx 6$ MeV. Morgenstern *et al.* [31] observed the velocity spectra of evaporation residues in the interaction of ^{40}Ar with boron and carbon targets. Morgenstern *et al.* [32] have also showed that, incomplete fusion reactions significantly contribute to the total reaction cross section for mass asymmetric systems as compared to mass symmetric systems at the same relative velocity. Later studies by Vineyard *et al.* [33] and Beck *et al.* [34] also supported the systematics presented by Morgenstern *et al.* [32]. However, the detailed conclusions regarding the multiplicity of linear momentum transfer, effect of mass asymmetry, role of different ℓ-bins associated with incomplete fusion processes, could not be drawn and such studies are still limited for few projectile-target combinations in medium mass region, i.e., $A \approx 150$. Moreover, the ICF reactions are considered to be a promising route to produce high spin states in heavy residues using light heavy ion beams ($A \leqslant 16$) even at low bombarding energies [35–37]. As such, in order to have better understanding of incomplete fusion dynamics, precise experimental data covering a wide range of periodic table and energies are required. The study of ICF dynamics in the framework of all these aspects may provide key parameters to determine optimum irradiation conditions for the production of radioactive ion beams (RIBs) [38,39].

In view of the availability of limited data covering only few projectile-target combinations at $E/A \approx 5$–7 MeV, our group has undertaken a program of precise measurement and analysis of excitation functions (EF's), recoil range distributions (RRD's), and spin distributions of residues populated via complete and/or incomplete fusion using particle-γ coincidence technique for various projectile-target combinations over a wide projectile energy range. As a part of ongoing programme to explore the dynamics of light heavy ion induced reactions (mainly complete and incomplete fusion), excitation functions for a large number of residues produced in several projectile-target combinations have been measured [27,40,41]. The present work deals with the extension of our earlier observations and a part of the analysis of these systems have already been published [40–42]. In this work, the influence of incomplete fusion on complete fusion has been studied and cross sections for nine radio-nuclides populated in ^{16}O+^{159}Tb and ^{16}O+^{169}Tm systems have been presented. The present paper is organized as follows. The experimental details and the evaporation residues identification are given in Sec. II. The experimentally measured EFs for both the systems have been compared with the predictions of statistical model code PACE2 and detailed analysis is given in Sec. III. The influence of incomplete fusion on complete fusion has been studied by the deduction of incomplete fusion fraction calculated on the lines of Gomes *et al.* [54] and the detailed discussion is given in Sec. IV. Section V deals with the summary and conclusions of the present work.

II. EXPERIMENTAL DETAILS

The experiments were carried out at the Inter-University Accelerator Center (IUAC), New Delhi, India using 15-UD Pelletron Accelerator facilities. A brief description of experimental details, such as target preparation and irradiations, post irradiation analysis, identification of evaporation residues, etc., are presented in the following subsections.

A. Target preparation

The self-supporting ^{159}Tb (abundance = 99.99%) targets of thickness $\approx$0.83 mg/cm^2 were prepared by rolling method and the ^{169}Tm (abundance = 100%) targets of $\approx$0.65 mg/cm^2 thickness were deposited on Al-backing of $\approx$1.5 mg/cm^2 thickness, using vacuum-evaporation technique. The Al-backing of ^{169}Tm targets served as energy degrader as well as catcher foil during the irradiations. The ^{159}Tb targets were backed by thick Al-catchers of $\approx$2 mg/cm^2 thickness to trap the recoiling nuclei. Since, a precise knowledge of the target thickness is an essential part of the absolute cross-section measurement of different reaction products, therefore, the thickness of each target was determined by α-transmission method. This technique is based on the measurement of the energy loss per unit path length by 5.487 MeV α-particles obtained from standard ^{241}Am source, while passing through the material of target. The targets were cut into the size of 1.2 $\times$ 1.2 cm^2 and were pasted on Al-holders having concentric hole of 1.0 cm diameter. The Al-holders were used for rapid dissipation of heat produced during the irradiations.

B. Irradiations

The irradiations have been carried out in the general purpose scattering chamber (GPSC) having an invacuum transfer facility (ITF) using conventional recoil-catcher technique. The ITF has been used to minimise the time lapse between the stop of irradiations and beginning of the counting. Two stacks each containing four and five samples of ^{159}Tb were irradiated at beam energies $\approx$87 and 95 MeV, while, two stacks of ^{169}Tm targets having four and three samples each were irradiated at energies $\approx$92 and $\approx$95 MeV by an $^{16}O^{7+}$ beam. The beam current was monitored $\approx$30–50 nA for both the systems in all irradiations. The targets along with Al-catcher foils were placed normal to the beam direction so that the recoiling nuclei, which have been populated during the interaction of projectile and target nuclei may be trapped in the catcher foil thickness. Keeping in view the half-lives of interest, irradiations have been carried out for $\approx$8–10 h. The beam flux was calculated by the total charge collected in the Faraday cup, placed behind the target-catcher foil assembly, using a current integrator device.

C. Post irradiation analysis

After the irradiation the stack of targets along with catcher foils was taken out from the GPSC with the help of an ITF. The evaporation residues populated in each target-catcher foil assembly via complete and/or incomplete fusion of ^{16}O

were identified by counting the induced activities using high resolution HPGe γ-ray spectrometer of 100 c.c. active volume coupled to PC through CAMAC based FREEDOM software. The energy and efficiency calibration of γ-spectrometer has been done using various standard γ-radiation sources of known strength. Further, the spectrometer resolution was $\approx$2 keV for 1.33 MeV γ-ray of ^{60}Co source. In the present work, the standard γ-sources and the irradiated samples were counted in the same geometry to keep the geometry dependent detector efficiency same for both. The geometry dependent efficiency ($G\varepsilon$) of HPGe γ-ray spectrometer for different source-detector separation was estimated using following relation:

$$G\varepsilon = \frac{N_o}{N_{ao}\,\theta\, e^{(-\lambda t)}}, \tag{1}$$

where N_o is the observed disintegration rate of the standard γ-source at the time of measurement, N_{ao} is the disintegration rate at the time of manufacture, λ is the decay constant, t is the lapse time between the manufacture of the source and start of counting, θ is the branching ratio of the characteristic γ-rays. Attention was paid to keep the dead time of the detector $\leqslant 10\%$ by suitably adjusting the source-detector separations. Keeping in view the half-lives of interest, the counting of activities induced in the samples were performed for a considerably long period.

D. Identification of evaporation residues

As already discussed, the evaporation residues populated via different reaction processes are likely to decay to the ground state by emitting characteristic γ-radiations, whose detection is an unique way for their identification. Thus, the observed intensity of the induced activities is a measure of production probability of evaporation residues. The γ-ray spectra of individual target-catcher foil assembly were recorded at the increasing times. The typical γ-ray spectra of ^{159}Tb and ^{169}Tm samples irradiated by $^{16}O^{7+}$ at $\approx$95 MeV are shown in Figs. 1 and 2. The various peaks in observed γ-ray

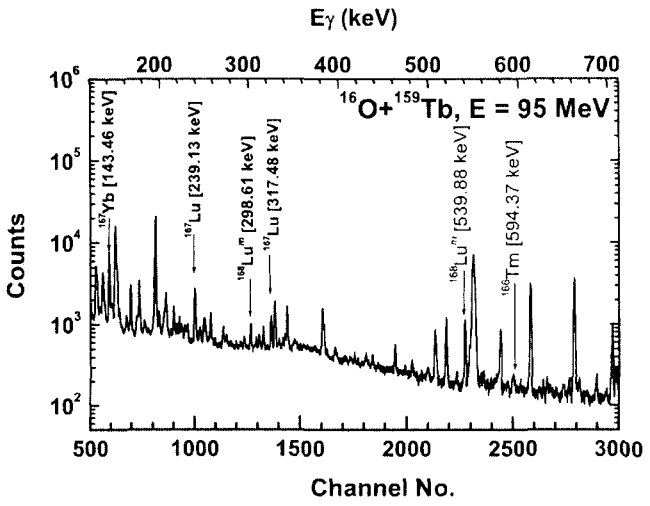

FIG. 1. Typical γ-ray spectra showing γ-lines of different radionuclides populated via CF and/or ICF in ^{16}O+^{159}Tb system at projectile energy $\approx$95 MeV.

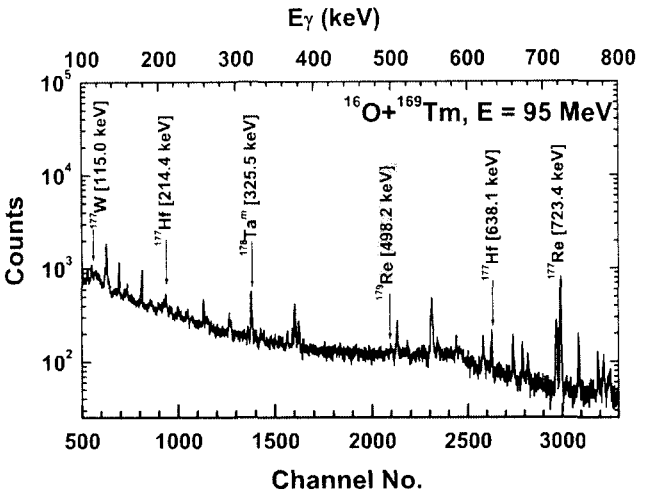

FIG. 2. Typical γ-ray spectra showing γ-lines of different radionuclides populated via CF and/or ICF in ^{16}O+^{169}Tb system at projectile energy $\approx$95 MeV.

spectra were assigned to the different evaporation residues. The reaction products were identified not only by the energy of the characteristic γ-radiations but also by the measured half-lives of residues. The measured half-lives of evaporation residues were found to be in good agreement with the literature values. Data analysis have been performed using FREEDOM software for nuclear data analysis. Area under the peaks of identified γ-lines of evaporation residues were used to estimate the count rate followed by production probability measurement. Nuclear data like half-lives, γ-ray energies, etc., have been taken from the Table of Isotopes [45] and Nuclear Wallet Card [43]. Identified evaporation residues along with their spectroscopic properties are given in Tables I and II.

E. Determination of production cross sections

A change in the composition of the target nucleus takes place, as a result of different reaction processes forming the evaporation residues, which may be identified on the basis their half-lives and characteristics γ-radiations. The intensities of the characteristic γ-radiations were used to estimate the reaction cross sections. A FORTRAN program EXP-SIGMA based on the following formulation has been used for the

TABLE I. List of identified evaporation residues produced in ^{16}O+^{159}Tb system via complete and/or in-complete fusion.

Reactions	Residues	E_γ (keV)	half-life	J_π	a_γ (%)
^{159}Tb(^{16}O,$\alpha 3n$)	$^{168}_{71}$Lu^{m}	298.61	6.7 min	3+	17
		539.88			47
^{159}Tb(^{16}O,$\alpha 4n$)	$^{167}_{71}$Lu	239.13	57.5 min	7/2+	8.2
		317.48			1.5
^{159}Tb(^{16}O,$\alpha p 3n$)	$^{167}_{70}$Yb	143.46	17.5 min	5/2−	2.10
^{159}Tb(^{16}O,$2\alpha n$)	$^{166}_{69}$Tm	594.37	7.7 h	2+	3.08
		1176.68			8.4

TABLE II. List of identified evaporation residues produced in $^{16}O+^{169}Tm$ system via complete and/or in-complete fusion.

Reactions	Residues	E_γ (keV)	Half-life	J_π	a_γ (%)
$^{169}Tm(^{16}O,\alpha p3n)$	$^{177}_{74}W$	115.0	2.21 h	1/2−	59
		426.94			13.1
$^{169}Tm(^{16}O,\alpha 2pn)$	$^{178}_{73}Ta$	325.5	2.36 h	7−	94.1
		331.6			32
$^{169}Tm(^{16}O,\alpha 3pn)$	$^{177}_{72}Hf$	214.4	51.4 min	7/2−	8.3
		638.1			20.0
$^{169}Tm(^{16}O,\alpha 4n)$	$^{177}_{75}Re$	1118.4	14.0 min	5/2−	25
		723.4			15
$^{169}Tm(^{16}O,\alpha 2n)$	$^{179}_{75}Re$	221.9	19.5 min	5/2+	3.6
		401			7.3
		498.2			5.7

determination of the production cross sections of evaporation residues [44],

$$\sigma_r = \frac{C_{t=0}}{N_0\theta\phi G_\ell K[1-\exp(-\lambda t_1)]}, \quad (2)$$

where $C_{t=0}$ is the total number of observed counts at the time of stop the irradiation, N_0 is the initial number of target nuclei, θ is the branching ratio of the characteristic γ-ray, ϕ is the flux of incident beam, G_ℓ is the geometry dependent efficiency of the spectrometer for a particular γ-ray energy, and $K = [1-\exp(-\mu d)]/\mu d$ is the self-absorption correction factor for the material of the sample of thickness d (gm/cm^2) and of absorption coefficient μ (cm^2/gm). The factor $[1-\exp(-\lambda t_1)]$ is a saturation correction factor. In the present work, excitation functions for nine evaporation residues $^{168}Lu^m(\alpha 3n)$, $^{167}Lu(\alpha 4n)$, $^{167}Yb(\alpha p3n)$, and $^{166}Tm(2\alpha n)$ produced in $^{16}O+^{159}Tb$ system, and $^{179}Re(\alpha 2n)$, $^{177}Re(\alpha 4n)$, $^{177}W(\alpha p3n)$, $^{178}Ta(\alpha 2pn)$, and $^{177}Hf(\alpha 3pn)$ produced in $^{16}O+^{169}Tm$ system have been measured. The measured cross sections of identified evaporation residues are presented in Tables III and IV.

The errors in the measured production cross-sections may arise mainly because of (i) the nonuniform thickness of samples that may lead to the uncertainty in the determination of the number of target nuclei. To check the uniformity of the sample, thickness of the each sample was measured at different positions by α-transmission method. It is estimated that the error in the thickness of the sample material is less than 1%. (ii) Fluctuations in the beam current may result in the variation of incident flux, proper care has been taken to keep the beam current constant as far as possible and, correction in flux determination from the fluctuation in beam current has been applied. (iii) Uncertainity in the determination of geometry dependent spectrometer efficiency. The error in the efficiency determination due to the statistical fluctuations in counts is estimated to be less than 2%. (iv) The losses of the product nuclei recoiling out of the sample may introduce large errors in the measured cross sections. The thickness of the catcher foils was sufficient to stop even the most energetic residues, moreover, in the present measurements both the sample and the catcher foils were counted together and hence, the losses due to the recoiling of nuclei is avoided. (v) The dead time of the spectrometer was kept $\leqslant 10\%$ by suitably adjusting sample-detector distance. These errors exclude the uncertainty of the nuclear data such as branching ratio, decay constant, etc., which have been taken from the Table of Isotopes [45]. The overall errors from these factors including statistical error are estimated to be $\leqslant 15\%$.

TABLE III. Experimentally measured production cross sections for evaporation residues populated via ICF and/or CF in $^{16}O+^{159}Tb$ system along with the projectile energies.

Lab energy (MeV)	$\sigma(^{168}Lu^m)$ (mb)	σ (^{167}Lu) (mb)	σ (^{167}Yb) (mb)	σ (^{166}Tm) (mb)
75.2 ± 0.9	3 ± 0.59	–	–	–
78.7 ± 0.9	12 ± 1.86	–	–	1.93 ± 0.36
83.2 ± 0.9	57 ± 6.81	5 ± 1.12	9 ± 1.23	7 ± 1.24
87.2 ± 0.8	69 ± 9.8	46 ± 6.54	28 ± 4.22	28 ± 3.11
89.6 ± 1.0	87 ± 11.67	59 ± 9.61	49 ± 5.94	31 ± 5.69
94.6 ± 0.4	145 ± 16.93	118 ± 17.52	21 ± 3.63	49 ± 7.56

III. DATA ANALYSIS: STATISTICAL MODEL CALCULATIONS WITH PACE2

In order to examine the extent to which the observed quantities are described in terms of the equilibrated decay of $^{175}Ta^*$ and $^{185}Ir^*$ populated in the interaction of ^{16}O with ^{159}Tb and ^{169}Tm within the energy range $E \approx 75$–95 MeV, the presently measured excitations functions have been compared with those calculated using statistical model code PACE2 (based on Hauser-Feshbach theory) [46]. The code PACE2 is based on statistical approach of CN deexcitation by Monte Carlo procedure. The angular momentum projections are calculated at each stage of deexcitation. The angular momentum conservation is explicitly taken into account at each step, and the CF cross sections are calculated using BASS formula [47].

The partial cross section (σ_ℓ) for the formation of compound nucleus at a particular angular momentum ℓ and specific bombarding energy, E is given by

$$\sigma_\ell = \frac{\lambda^2}{4\pi}(2\ell+1)T_\ell, \quad (3)$$

where λ is reduced wavelength and the transmission coefficients T_ℓ may be given by the expression

$$T_\ell = \left[1+\exp\left(\frac{\ell-\ell_{max}}{\Delta}\right)\right]^{-1}, \quad (4)$$

where Δ is the diffuseness parameter and ℓ_{max} the maximum amount of ℓ detained by total fusion cross section,

$$\sigma_F = \sum_{\ell=0}^{\infty}\sigma_\ell. \quad (5)$$

The optical model potentials of Becchetti and Greenlees [48] are used for calculating the transmission coefficients for

TABLE IV. Experimentally measured production cross sections for evaporation residues populated via ICF and/or CF in $^{16}O+^{169}Tm$ system along with the projectile energies.

E_{beam} (MeV)	σ_{cum} (^{177}W) (mb)	σ_{ind} (^{177}W) (mb)	σ (^{178}Ta) (mb)	σ (^{177}Hf) (mb)	σ (^{177}Re) (mb)	σ (^{179}Re) (mb)
74.9 ± 0.9	–	–	–	–	–	3 ± 0.89
78.7 ± 0.9	17 ± 2.49	–	36 ± 4.58	8 ± 0.89	–	14 ± 1.24
82.0 ± 0.8	41 ± 4.3	35 ± 3.17	87 ± 8.91	11 ± 1.27	5 ± 1.09	19 ± 3.02
85.8 ± 0.8	36 ± 5.9	28 ± 4.63	106 ± 7.61	28 ± 2.32	7 ± 1.04	39 ± 4.64
88.9 ± 1.0	73 ± 6.2	58 ± 5.31	143 ± 13.57	37 ± 2.59	13 ± 1.96	46 ± 5.36
91.6 ± 0.4	79 ± 8.3	62 ± 6.48	149 ± 12.81	40 ± 3.71	15 ± 2.97	37 ± 6.98
94.6 ± 0.4	96 ± 9.5	61 ± 7.19	194 ± 18.41	63 ± 6.51	31 ± 3.17	32 ± 3.71

neutron and proton, and optical model potential of Satchler [49] is used for α-particle emissions. In the description of γ-ray competitions, emission of $E1$, $E2$, $M1$, and $M2$ γ-ray are included and the γ-rays strength for different transitions, are taken from tables of Endt [50]. In this code, the level density parameter $a(=A/K)$, is one of the important parameters, where, A is the mass number of the nucleus and K is a free parameter. The value of K may be varied to match the experimental data. In the present work, we tested the experimental data using different values of level density parameters from $A/11$ to $A/8$ MeV^{-1}. As a representative case, the effect of the variation of above parameter 'K' on calculated EF's for the population of Lu isotopes via CF and/or ICF in $^{16}O+^{159}Tb$ system is shown in Figs. 3(a) and 3(b). As can be observed from this figure, the theoretical predictions with different input parameters are almost similar or a very small change comes into picture for higher value of level density parameter at relatively higher projectile energies. It may, however be pointed out that a value of $K \geqslant 10$, may give rise to the anomalous effect in particle multiplicity, and compound nucleus temperature [51]. Though, it is possible to explain all the excitation functions with different values of parameters of the code for individual channels, however, from the physics point of view, it is quite unreasonable. As such, in the present work all the calculations have been performed consistently using same set of parameters for all the channels. The value of level density parameter (a) was taken as $A/8$ MeV^{-1}, i.e., $K = 8$, as suggested by Gilbert and Cameron [52]. This set of parameters reproduced the excitation functions for complete fusion channels satisfactorily, as mentioned in our earlier publications [40,41]. This further shows that the optical model parameters used in these calculations are satisfactory. It may, however, be pointed out that the ICF process is not taken into account in code PACE2. Hence, the enhancement of experimentally measured production cross sections as compared to the theoretical predictions may be attributed to the incomplete fusion process.

A. Excitation functions: $^{16}O+^{159}Tb$ system

In Figs. 3 and 4, the experimentally measured and theoretically calculated excitation functions for four radio-nuclides $^{167,168}Lu^m$, ^{167}Yb, and ^{166}Tm produced in $^{16}O+^{159}Tb$ system in the energy range ≈70–95 MeV are shown. The reaction products $^{167,168}Lu^m$ have ground and metastable states of half-lives 51.5 min and 6.7 min, respectively. The reaction products $^{167,168}Lu^m$ may be formed both via complete and/or incomplete fusion of ^{16}O with ^{159}Tb. In case of complete fusion, composite system $^{175}Ta^*$ is formed, which may decay via the emission of an α-particle and three or four neutrons leaving behind the above residues. The same residues may also be populated via ICF, it can be explained by assuming the breakup of ^{16}O-nucleus into its fragments viz. ^{12}C and ^4He (α-particle) in the nuclear force field of target nucleus. One of the fragments ^{12}C fuses with ^{159}Tb, forming an incompletely fused composite system $^{171}Lu^*$, which may decay by the emission of three neutrons forming $^{168}Lu^m$ and four neutrons forming ^{167}Lu. Similarly, the reaction product ^{167}Yb, which has ground state of half-life 17.5 min, is expected to be populated via

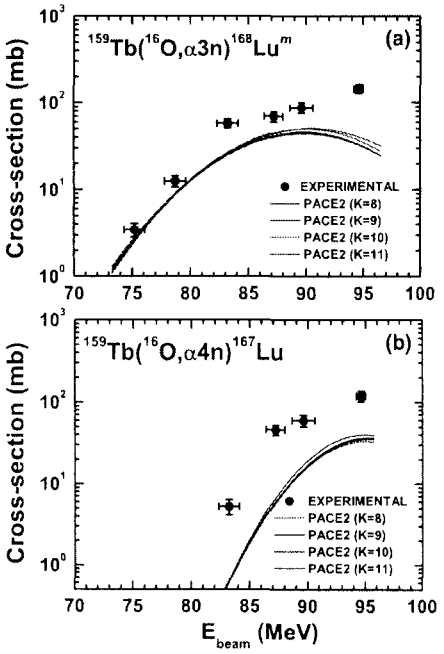

FIG. 3. (Color online) Experimentally measured and theoretically calculated excitation functions for $^{167,168}Lu^m$ isotopes, expected to be populated via $\alpha4n$ and $\alpha3n$ channels in $^{16}O+^{159}Tb$ system. The dark circles indicates the experimental data points and the solid lines represents the polynomial fit to the PACE2 predictions at different input parameters.

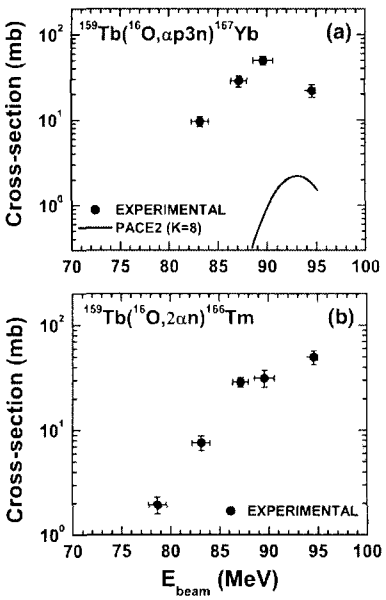

FIG. 4. Experimentally measured and theoretically calculated excitation functions for (a) ^{167}Yb populated via $\alpha p3n$ channel, and (b) ^{166}Tm populated via $2\alpha n$ channel in interaction ^{16}O+^{159}Tb system. Sold lines represents the PACE2 predictions. For ^{166}Tm residue, the theoretical predictions found to negligible and hence, not plotted in the figure.

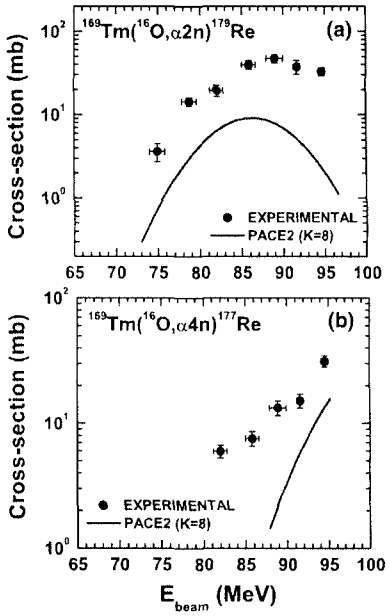

FIG. 5. Experimentally measured and theoretically calculated EF's for ^{177,179}Re isotopes expected to be populated via $\alpha 4n$ and $\alpha 2n$ in ^{16}O+^{169}Tm system. Explanation of symbols is the same as in Figs. 3 and 4.

complete fusion ($\alpha p3n$) channel and/or incomplete fusion (i.e., the fusion of ^{12}C with ^{159}Tb) followed by subsequent emission of one proton and three neutrons from ^{171}Lu*. The remaining α-fragment (^{4}He) of the incident ion is assumed to go on moving with beam velocity in forward direction without any significant interaction with target nucleus. Similarly, the evaporation residue ^{166}Tm ($t_{1/2} = 7.7$ h), is expected to be populated via fusion of ^{8}Be and subsequent emission of one neutron from ^{167}Tm*. However, the remaining part ^{8}Be (two α-particles) behaves like a spectator. It may be observed from Fig. 3(a), the experimentally measured cross sections are almost matching with PACE2 calculations in the energy range ≈75–80 MeV. However, in the higher energy region the measured cross sections are some what under predicted by PACE2 calculations. This may be explained by assuming that only complete fusion contributes to the formation of ^{168}Lu^m in the energy range ≈75–80 MeV, while, as the energy increases both complete and incomplete fusion contribute to the production probability. In the similar way, the theoretical values of cross-sections for most of the α-emitting channels are found to be some what underpredicted than that of experimental data, as indicated in Figs. 3(a), 3(b), and 4(a). Since, ICF is not taken into consideration in code PACE2, therefore, substantially large cross sections (in case of ^{167,168}Lu^m and ^{167}Yb evaporation residues) as compared to the theoretical ones cannot be the uncertainty in measurement and hence may be attributed to the contribution coming from incomplete fusion process of the type

$$^{16}\mathrm{O}(^{12}\mathrm{C} + {}^4\mathrm{He}) \Rightarrow {}^{12}\mathrm{C} + {}^{159}\mathrm{Tb} \Rightarrow {}^{171}\mathrm{Lu}^* + {}^4\mathrm{He}$$

(α as spectator).

Further, in case of reaction product ^{166}Tm($2\alpha n$), the theoretical predictions of PACE2 give an almost negligible cross section and hence are not shown in Fig. 4(b). This indicates that the major contribution for the population of ^{166}Tm comes from incomplete fusion process of the type

$$^{16}\mathrm{O}(^8\mathrm{Be} + {}^8\mathrm{Be}) \Rightarrow {}^8\mathrm{Be} + {}^{159}\mathrm{Tb} \Rightarrow {}^{167}\mathrm{Tm}^* + {}^8\mathrm{Be}$$

(beryllium as spectator).

B. Excitation functions: ^{16}O+^{169}Tm system

The excitation functions for five radio-nuclides ^{177,179}Re, ^{177}W, ^{178}Ta, and ^{177}Hf populated in the interaction of ^{16}O with ^{169}Tm within the energy range ≈75–95 MeV are shown in Figs. 5 and 6. As already indicated in the earlier section, the above residues may be populated via complete and/or incomplete fusion of ^{16}O with ^{169}Tm. The production of these residues leading to α-emission channels may also be explained in terms of the breakup of ^{16}O into ^{12}C and ^{4}He followed by fusion of ^{12}C with ^{169}Tm forming an incompletely fused composite system ^{181}Re*. The reaction products ^{177,179}Re, having half-lives of 14 min and 19.7 min, are expected to be populated via the emission of four and two neutrons from ^{181}Re*. Thus, the evaporation residues ^{177}Re and ^{179}Re may not only be populated via incomplete fusion but may have significant probability of being formed via complete fusion of the projectile leading to the formation of ^{185}Ir*, which may decay by the emission of two and four neutrons along with an α particle. The complete fusion component calculated by PACE2 code is shown in Fig. 5 by solid lines. As can be seen from these figures, the calculated cross-section values by PACE2 have lower magnitudes than the experimental data, which indicates the contribution from incomplete fusion at these

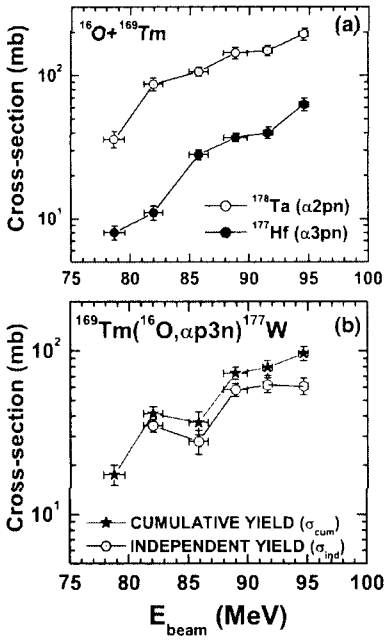

FIG. 6. Experimentally measured excitation functions for (a) ^{178}Ta and ^{177}Hf, (b) ^{177}W, evaporation residues expected to be populated via, respectively, $\alpha 2pn, \alpha 3pn$, and $\alpha p3n$ channels in ^{16}O+^{169}Tm system. The theoretical predictions are found to be negligible for these residues and hence are not shown in this figure. The different lines are drawn to guide the eye to the experimental data points. In (b) open circles indicate the independent yield of ^{177}W and cumulative yield is represented by solid stars.

energies. Similarly, the reaction products ^{178}Ta and ^{175}Hf have half-lives 2.45 h and 51.4 min, respectively and are expected to be populated via $\alpha 2pn$ and $\alpha 3pn$ channels, respectively, in which α-particle behaves as spectator. Since, the theoretical predictions of code PACE2 are negligible in case of ^{177}W, ^{178}Ta, and ^{177}Hf residues, and are therefore not shown in the Fig. 6(a) and 6(b). As such, it may be inferred that the major contribution to these reaction channels come from incomplete fusion processes of the type

$$^{16}\mathrm{O}(^{12}\mathrm{C} + {}^{4}\mathrm{He}) \Rightarrow {}^{12}\mathrm{C} + {}^{169}\mathrm{Tm} \Rightarrow {}^{181}\mathrm{Re}^{*} + {}^{4}\mathrm{He}$$

(α as spectator).

The evaporation residue ^{177}W (half-life of 2.21 h) may be populated via three different reaction channels; (a) complete fusion of ^{16}O, i.e.,

$$^{16}\mathrm{O} + {}^{169}\mathrm{Tm} \Rightarrow {}^{185}\mathrm{Ir}^{*} \Rightarrow {}^{177}\mathrm{W} + \alpha + p + 3n;$$

(b) incomplete fusion of ^{16}O, i.e.,

$$^{16}\mathrm{O}(^{12}\mathrm{C} + {}^{4}\mathrm{He}) + {}^{169}\mathrm{Tm} \Rightarrow {}^{181}\mathrm{Re}^{*} + {}^{4}\mathrm{He(spectator)}{}^{181}\mathrm{Re}^{*} \Rightarrow {}^{177}\mathrm{W} + p + 3n;$$

and, (c) β^+ emission and/or EC decay of higher charge precursor, i.e.,

$$^{16}\mathrm{O} + {}^{169}\mathrm{Tm} \Rightarrow {}^{177}\mathrm{Re}^{*} + {}^{4}\mathrm{He} + 4n$$
$$^{177}\mathrm{Re}^{*} \Rightarrow {}^{177}\mathrm{W} + \beta^{+}/\mathrm{EC}.$$

Since, the theoretical calculations (PACE2) for the CF channel '(a)' give negligible cross sections [and hence are not shown in Fig. 6(b)], it may be assumed that the residue ^{177}W is populated predominantly via ICF [channel '(b)'] and the precursor decay [channel '(c)']. Since, ^{177}W is populated via ICF and precursor decay, hence, an attempt has been made to separate out the contribution due to the precursor decay from the cumulative activity of ^{177}W. Brief details of the method used for separating precursor contribution are given here [8]

$$\sigma_{\mathrm{cum}} = \sigma_{\mathrm{ind}} + F_{\mathrm{pre}}\sigma_{\mathrm{pre}}, \tag{6}$$

where; σ_{cum} and σ_{ind} represent, respectively, the cumulative and independent yield of the residue, σ_{pre} stands for the independent contribution of the precursor. The value of precursor fraction (F_{pre}) depends on the branching ratio P_p for precursor decay to the residue and is given by

$$F_{\mathrm{pre}} = P_p \frac{T_{\mathrm{ind}}^{1/2}}{T_{\mathrm{ind}}^{1/2} - T_{\mathrm{pre}}^{1/2}}, \tag{7}$$

here, $T_{\mathrm{ind}}^{1/2}$ and $T_{\mathrm{pre}}^{1/2}$ are the half-lives of the precursor and the daughter residues, respectively. This cumulative cross section is given by

$$\sigma_{\mathrm{cum}} = \sigma_{\mathrm{ind}} + P_p \frac{T_{\mathrm{ind}}^{1/2}}{T_{\mathrm{ind}}^{1/2} - T_{\mathrm{pre}}^{1/2}}\sigma_{\mathrm{pre}}. \tag{8}$$

The values of branching ratios and the half-lives required for obtaining the coefficient F_{pre} are taken from Refs. [42,44]. Using the above formulation, in the present case, the cumulative yield (σ_{cum}) and independent yield (σ_{ind}) for ^{177}W are related as follows:

$$\sigma_{\mathrm{cum}}(^{177}\mathrm{W}) = \sigma_{\mathrm{ind}}(^{177}\mathrm{W}) + 1.118\sigma_{\mathrm{pre}}(^{177}\mathrm{Re}), \tag{9}$$

where, $\sigma_{\mathrm{pre}}(^{177}\mathrm{Re})$ is the independent yield of the precursor. As such, the precursor contribution of ^{177}W at different energies has been subtracted from cumulative yield for the determination of independent yield. The measured cumulative cross sections (σ_{cum}) as well as independent cross sections (σ_{ind}) for ^{177}W residue deduced in such a way are given in Table IV and are also plotted in Fig. 6(b). As can be seen from this figure, the precursor (^{177}Re) of ^{177}W contributes a finite value of yield to the production of ^{177}W. Moreover, the precursor (^{177}Re) starts contributing to the production probability at $\approx$82 MeV, which is found to increase with projectile energy. It may, however, be pointed out that the cumulative and independent yields of ^{177}W reaction product are almost same up to $\approx$87 MeV (within the error bars), which indicates a small contribution from the precursor for the energies up to $\approx$87 MeV, while as the energy increases the precursor contribution increases as inferred from the data points at $\approx$95 MeV. As shown in the figure, the solid stars represent the cumulative cross section of the residue ^{177}W, while the open circles represent the independent yield of this residue. A closer look at Fig. 6(b) indicates that σ_{cum} for ^{177}W and σ_{ind} for the independent production of ^{177}W have cross sections with a very small difference at lower energies. However, as one moves toward the relatively higher energy the difference also increases to a sizable value, indicating the influence of precursor contribution in this case.

Although, it may not be possible to directly obtain the relative contribution of complete and incomplete fusion from

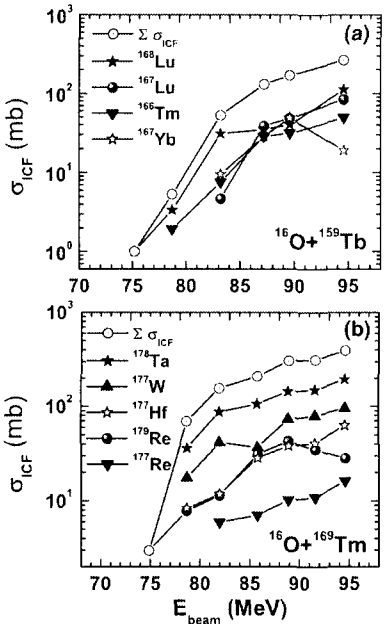

FIG. 7. Deduced incomplete fusion contribution as a function of projectile energy for (a) ^{16}O+^{159}Tb and (b) ^{16}O+^{169}Tm systems. Open circles represent the sum of all incomplete fusion channels ($\Sigma\sigma_{ICF}$). Data points are connected using lines just to guide the eye.

the measurement of excitation functions, however, an attempt has been made to obtain the incomplete fusion contribution. The production cross sections which have been measured experimentally may be attributed to the both complete and/or incomplete fusion. As already mentioned, the enhancement in the experimentally measured production cross sections than that of PACE2 predictions may be attributed to incomplete fusion processes. As such, the incomplete fusion contribution for individual channels has been deduced by subtracting complete fusion cross sections (σ_{CF}) (obtained by PACE2) from the experimentally measured cross sections (σ_{EXP}) at respective projectile energies, as suggested by Gomes *et al.* [54]. The incomplete fusion contributions (σ_{ICF}) deduced as mentioned in Ref. [54] for presently measured evaporation residues are plotted in Figs. 7(a) and 7(b) along with the sum of all incomplete fusion channels ($\Sigma\sigma_{ICF}$) as a function of projectile energy. The lines drawn in these figures are just to guide the eyes. As can be seen from these curves, in general, the incomplete fusion contribution increases with projectile energy, which is expected as the break-up probability of the incident ion significantly increases with projectile energy.

In the present work, the cross sections for CF and/or ICF channels have also been calculated using the SUMRULE model [12], which is based on the generalized concept of critical angular momentum as already discussed in Sec. I. In these calculations, it is assumed that ICF channels open only for those partial waves which have ℓ-values $\geqslant \ell_{crit}$. On the other hand partial waves with $\ell \leqslant \ell_{crit}$, contributes to CF process. In these calculations, the input parameters such as temperature (T) of the contact zone of interacting partners, the diffuseness parameter (Δ) of transmission probability distribution (T_ℓ), and the Coulomb interaction radius (R_c) are taken as 3.5 MeV, 1.7 unit of angular momentum, and 12 fm, respectively, as suggested by Wilczynski *et al.* [12]. In the present work, it has been observed that the experimental cross section for fusion-evaporation channels agree reasonably well with the predictions of the SUMRULE model. However, there is a large discrepancy between measured and calculated cross-section values for ICF channels. As a typical example for ICF channels producing Lu isotopes in ^{16}O+^{159}Tb system, and Re isotopes in ^{16}O+^{169}Tm system, the SUMRULE calculations are lower by a factor of more than 100 in general. Similar discrepancy has also been observed in case of ^{13}C+^{181}Ta system studied by Babu *et al.* [53] in their experiment at projectile energy $\approx$6 MeV/nucleon. As a matter of fact, Wilczynski *et al.* [12] tested the SUMRULE model for the reactions at 8–10 MeV or higher energies and found satisfactory agreement in calculated and experimental cross sections. One of the possible reasons for the above disagreement in case of ICF channels in case of present measurements may be the non-validity of the generalized concept of critical angular momentum at energies with in the range of $\approx$5–7 MeV/nucleon. Further, the cluster structure of incident ion may also play an important role in ICF reactions.

IV. INCOMPLETE FUSION FRACTION (F_{ICF})

As already mentioned in the earlier section, the sum of all incomplete fusion components is taken as the total incomplete fusion contribution ($\Sigma\sigma_{ICF}$). The contribution coming from all incomplete fusion channels ($\Sigma\sigma_{ICF}$) and the sum of all complete fusion channels ($\Sigma\sigma_{CF}$) obtained from PACE2 calculations are plotted along with the total fusion cross section ($\sigma_{TF} = \Sigma\sigma_{CF} + \Sigma\sigma_{ICF}$) for presently studied systems ^{16}O+^{159}Tb and ^{16}O+^{169}Tm in Figs. 8(a) and 8(b). As can be observed from these figures, the CF component has measurable contribution even at $\approx$70 MeV, while ICF contribution seems to start from $\approx$75 MeV, in the case of presently studied systems. Further, as can be observed from Figs. 8(a) and 8(b), the separation between the plots for $\Sigma\sigma_{TF}$ (solid stars) and σ_{CF} (solid circles) increases with projectile energy, which indicates that the ICF contributes larger production yield at relatively high projectile energies. This may be on account of the increasing probability of the break-up of incident ion into α-clusters (^{12}C+α and/or ^{8}Be+^{8}Be) as the projectile energy increases. It may, however, be pointed out that the difference between the plots for $\Sigma\sigma_{CF}$ (solid stars) and σ_{TF} (solid circles) is more for ^{16}O+^{169}Tm system as compared to ^{16}O+^{159}Tb system at different energies. It may be because of the fact that, ^{16}O+^{169}Tm system is more mass asymmetric as that of ^{16}O+^{159}Tb system, indicating the dependence of underlying process on mass asymmetry of interacting partners. Further, the data seems to support the sensitiveness of incomplete fusion on projectile energy and mass asymmetry of interacting partners, as inferred by Morgenstern *et al.* [56]. An attempt has been made to investigate the affect of above variables on the relative contributions of complete and incomplete fusion fraction. The percentage incomplete fusion fraction (F_{ICF}) for both the systems has been estimated from the experimentally

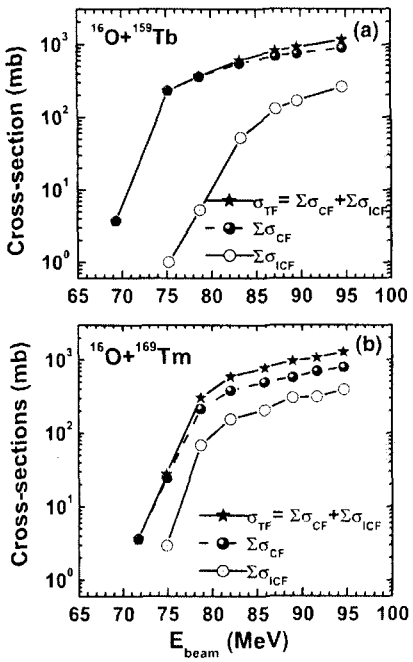

FIG. 8. Total fusion probability (σ_{TF}) along with the sum of complete ($\Sigma\sigma$CF) and incomplete fusion contributions ($\Sigma\sigma_{ICF}$) at different energies for (a) ^{16}O+^{159}Tb and (b) ^{16}O+^{169}Tm systems.

measured production cross sections as given below:

$$F_{ICF} = \frac{\Sigma\sigma_{ICF}}{\sigma_{TF}} \times 100. \quad (10)$$

The F_{ICF} for both the systems has been deduced at different energies and is plotted as a function of reduced projectile energy (E_{beam}/V_b, where V_b is Coulomb barrier of respective systems) in Figs. 9(a) and 9(b). The reduced projectile energy (E_{beam}/V_b) has been used to incorporate the effect of Coulomb barrier while comparing different projectile-target combinations in a plot. As can be seen from Fig. 9(a), at the threshold of ICF (i.e., ≈75 MeV in case of ^{16}O+^{169}Tm system) the relative percentage F_{ICF} is found to ≈10% of the total fusion cross section (σ_{TF}), which increases with projectile energy. At the highest studied energy (i.e., ≈95 MeV) the relative percentage of ICF fraction approaches to ≈30% of σ_{TF}. Similar energy dependence of ICF fraction for ^{16}O+^{159}Tb system has also been observed, where ICF fraction at ≈75 MeV is found to be ≤1% of σ_{TF}, but at ≈95 MeV, it approaches to ≈20% of the total fusion cross section. Further, the percentage ICF contribution is an order of magnitude higher for ^{16}O+^{169}Tm system as compared to ^{16}O+^{159}Tb system at ≈75 MeV. However, it almost approaches to nearly the same value at higher energies. This may be because of the fact that as the beam energy increases, the effect of Coulomb barrier goes on diminishing. An attempt has also been made to estimate the similar energy dependent of F_{ICF} for ^{12}C+^{128}Te and ^{12}C+^{165}Ho systems studied earlier [3,27] and is shown in Fig. 9(b). The percent F_{ICF} for ^{12}C+^{165}Ho system is shown in the inset of Fig. 9(b) in order to see the variation more clearly. As can be seen from this figure, the incomplete fusion fraction for these systems also increases with the projectile energy. It may, however, be pointed out on the basis of Figs. 9(a) and 9(b) that the ICF fraction for ^{12}C and ^{16}O induced reactions increases with the charge and mass of target nucleus. Further, the difference between two systems at different projectile energies can be seen quite clearly, where the ICF fraction is found to be more for ^{16}O+^{169}Tm system than that for ^{16}O+^{159}Tb system, which shows the sensitiveness of ICF fraction to the mass asymmetry of interacting partners.

Mogenstern *et al.* [55], suggested that the onset of incomplete fusion is governed by the relative velocity ($v_{relative}$) of projectile (i.e., $\sqrt{2}(E_{c.m.} - V_b)/\mu$, here; V_b is the CB between the interacting partners, $E_{c.m.}$ is the projectile energy in center of mass system and μ is the reduced mass of the system) and mass asymmetry of the interacting partners. With this in view, the percentage F_{ICF} for ^{16}O+^{159}Tb, ^{16}O+^{169}Tm, ^{12}C+^{128}Te, and ^{12}C+^{165}Ho systems has been deduced at a constant value of $v_{relative}$. The mass asymmetry dependent percentage ICF fraction is shown in Fig. 10. As can be seen from this figure, in general, the data points suggest more ICF probability for more mass asymmetric systems than relatively mass symmetric system, which support the systematics presented by Morgenstern *et al.* [56]. However, the percentage ICF fraction for ^{16}O+^{169}Tm system is not following the general trend as inferred from the plot (Fig. 10). The above conflict in the measurements can be explained by considering projectile structure effect along with the mass asymmetry of interaction partners. As such, it can be pointed out that, for ^{16}O-induced reactions with ^{159}Tb and ^{169}Tm, percentage ICF fraction is more for mass asymmetric system. However, for ^{12}C-induced reactions with ^{128}Te and ^{165}Ho, the percentage F_{ICF} is also indicate the similar trends as that of ^{16}O-induced reactions. As such, it may not be out of order to state that, mass asymmetry is also a function of

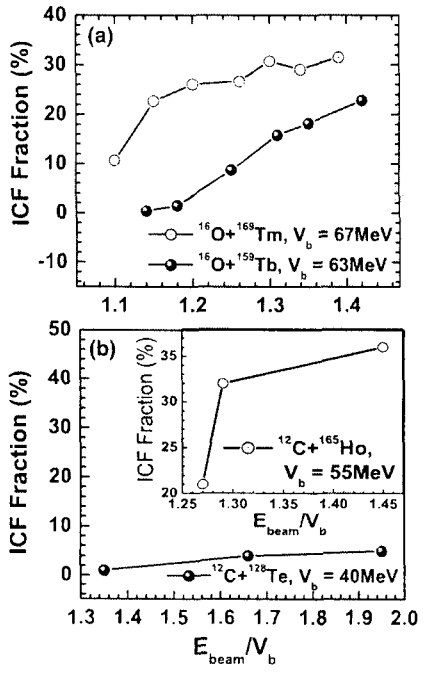

FIG. 9. Percentage incomplete fusion fraction (F_{ICF}) as a function of reduced projectile energy (E_{beam}/V_b) for (a) ^{16}O+^{159}Tb, ^{16}O+^{169}Tm and (b) ^{12}C+^{128}Te and ^{12}C+^{165}Ho (inset) systems.

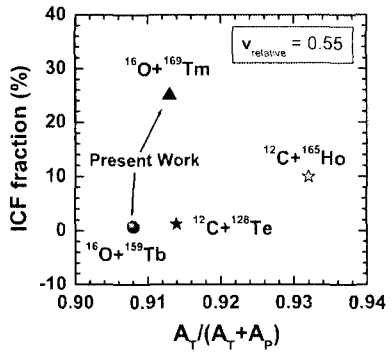

FIG. 10. Variation of percentage ICF fraction as a function of mass asymmetry of interacting partners at constant relative velocity ($v_{\text{relative}} = 0.55$) for different systems.

projectile structure. However, for better understanding of underlying processes, detailed measurements for various projectile-target combinations are required.

V. SUMMARY AND CONCLUSIONS

In this paper, some of the results of the experiments performed in order to study the influence of incomplete fusion on complete fusion process have been presented. Excitation functions for four radio-nuclides; ^{168m,167}Lu, ^{167}Yb, and ^{166}Tm produced in $^{16}O+^{159}Tb$ system, and five radio-nuclides; ^{179,177}Re, ^{177}W, ^{178}Ta, and ^{177}Hf produced in $^{16}O+^{169}Tm$ via complete and/or incomplete fusion in the energy range $\approx$75–95 MeV have been measured. The experimental data have been compared with the predictions of theoretical model code PACE2. The enhancement in the production cross sections, in case of α-emission channels (after correcting the precursor contribution, if any), as compared to PACE2 calculations has been attributed to the incomplete fusion reaction. The incomplete fusion fraction (F_{ICF}) is found to be $\leqslant$1% at $\approx$75 MeV, while, it is approaching $\approx$20% of the total fusion cross section (σ_{TF}) at $\approx$95 MeV for $^{16}O+^{159}Tb$ system. However, F_{ICF} is found to be $\approx$10% at $\approx$75 MeV and observed to be $\approx$30% of σ_{TF} at $\approx$95 MeV for $^{16}O+^{169}Tm$ system. It may however be pointed out that F_{ICF} is also found to be more in mass asymmetric systems than that of mass symmetric systems, though, the projectile structure effect appears to play a significant role in the systematics but this conjecture needs to be confirmed by further experimental data. The observation of large percentage F_{ICF} may be attributed to the prompt breakup of projectile into α-clusters ($^{16}O \Rightarrow {}^{12}C+{}^{4}He$ and/or $^{8}Be{}^{8}Be$), the probability of breakup increasing with the incident projectile energy. Hence, it may be inferred that, in general, the percentage F_{ICF} is sensitive for projectile energy, mass asymmetry of interacting partners (projectile structure effect apart). The percentage F_{ICF} have been found to increase with projectile energy. The present observations are thus in agreement with the Morgenstern systematics [56]. As such, it may be concluded that apart from complete fusion, the ICF is also a process of greater importance at these energies, and hence, while predicting the total reaction cross section, the contribution coming from incomplete fusion may also be taken into consideration. Moreover, in order to have better understanding of complete and incomplete fusion and perfect modeling of incomplete fusion processes, it would be quite interesting to perform more detailed experiments for different projectile-target combinations. The additional information can be obtained regarding the ICF processes by the measurement of spin distribution of residues populated by CF as well as ICF, using particle-γ coincidence technique both at relatively low and higher bombarding energies.

ACKNOWLEDGMENTS

The authors are thankful to Prof. Amit Roy, Inter-University Accelerator Center (IUAC), New Delhi, India for extending all the facilities for carrying out the experiments. Dr. R. K. Bhowmik and Prof. P. R. S. Gomes for several scientific discussions to improve this manuscript. Thanks are also due to Dr. S. Murlithar and Dr. R. P. Singh for their support and encouragement during the experiments. One of the authors (P.P.S.) thanks the IUAC for support and hospitality.

[1] F. Schussler, H. Nifenecker, B. Jakobsson, V. Kopljar, K. Soderstrom, S. Leray, C. Ngo, S. Souza, J. P. Bondorf, and K. Sneppen, Nucl. Phys. **A584**, 704 (1995).

[2] E. Gadioli, C. Brattari, M. Cavinato, E. Fabrici, E. Gadioli Erba, V. Allori, A. Di. Filippo, S. Vailati, T. G. Stevens, S. H. Connell, J. P. F. Sellschop, F. M. Nortier, G. F. Steyn, and C. Marchetta, Nucl. Phys. **A641**, 271 (1998).

[3] S. Gupta, B. P. Singh, M. M. Musthafa, H. D. Bhardwaj, and R. Prasad, Phys. Rev. C **61**, 064613 (2000).

[4] L. Corradi *et al.*, Phys. Rev. C **71**, 014609 (2005).

[5] M. Dasgupta, P. R. S. Gomes, D. J. Hinde, S. B. Moraes, R. M. Anjos, A. C. Berriman, R. D. Butt, N. Carlin, J. Lubian, C. R. Morton, J. O. Newton, and A. Szanto de Toledo, Phys. Rev. C **70**, 024606 (2004).

[6] S. Chakrabarty, B. S. Tomar, A. Goswami, G. K. Gubbi, S. B. Manohar, A. Sharma, B. B. Kumar, and S. Mukherjee, Nucl. Phys. **A678**, 355 (2000).

[7] D. J. Parker, J. Asher, T. W. Conlon, and I. Naqib, Phys. Rev. C **30**, 143 (1984).

[8] M. Cavinato, E. Fabrici, E. Gadioli, P. Vergani, M. Crippa, G. Colombo, I. Redaeli, and M. Ripamonti, Phys. Rev. C **52**, 2577 (1995).

[9] H. C. Britt and A. R. Quinton, Phys. Rev. **124**, 877 (1961).

[10] T. Inamura, M. Ishihara, T. Fukuda, T. Shimoda, and H. Hiruta, Phys. Lett. **B68**, 51 (1977).

[11] P. P. Singh, B. P. Singh, Unnati, B. Sharma, M. K. Sharma, R. Kumar, K. S. Golda, D. Singh, S. Muralithar, R. P. Singh, H. D. Bhardwaj, M. A. Ansari, R. Prasad, and R. K. Bhowmik, DAE-BRNS, Nucl. Phys. Sym. V **51**, 361 (2006).

[12] J. Wilczynski, K. Siwek-Wilczynaski, J. Van Driel, S. Gonggrijp, D. C. J. M. Hageman, R. V. F. Janssens, J. Lukasiak, R. H. Siemssen, and S. Y. Van der Werf, Nucl. Phys. **A373**, 109 (1982).

[13] T. Udagawa and T. Tamura, Phys. Rev. Lett. **45**, 1311 (1980).

[14] J. P. Bondrof, J. N. De, G. Fai, A. O. T. Karvinen, and J. Randrup, Nucl. Phys. **A333**, 285 (1980).
[15] W. Trautmann, O. Hansen, H. Tricoire, W. Hering, R. Ritzka, and W. Trombik, Phys. Rev. Lett. **53**, 1630 (1984).
[16] T. Inamura, T. Kjima, T. Nomura, T. Sugitate, and H. Utsunomiya, Phys. Lett. **B84**, 71 (1982).
[17] T. Inamura, A. C. Kahler, D. R. Zolnowski, U. Garg, T. T. Sugihara, and M. Wakai, Phys. Rev. C **32**, 1539 (1985).
[18] J. B. Natowitz, S. Leray, R. Lukas, C. Ngo, E. Tomasi, and C. Volant, Z. Phys. A **325**, 467 (1986).
[19] M. Blann *et al.*, Phys. Rev. C **31**, 295 (1985).
[20] J. P. Bondrof *et al.*, Nucl. Phys. **A333**, 285 (1980).
[21] D. H. E. Gross and J. Wilczynski, Phys. Lett. **B67**, 1 (1977).
[22] H. Tricoire *et al.*, Z. Phys. A **312**, 221 (1983).
[23] H. C. Britt and A. R. Quinton, Phys. Rev. **124**, 877 (1961).
[24] K. Siwek-Wilczynska *et al.*, Phys. Rev. Lett. **42**, 1599 (1979).
[25] S. Chakrabarty, B. S. Tomar, A. Goswami, G. K. Gubbi, S. B. Manohar, A. Sharma, B. B. Kumar, and S. Mukharjee, Nucl. Phys. **A678**, 355 (2000).
[26] P. Vergani, E. Gadioli, E. Vaciago, E. Fabrici, E. Gadioli Erba, M. Galmarini, G. Ciavola, and C. Marchetta, Phys. Rev. C **48**, 1815 (1993).
[27] M. K. Sharma, B. P. Singh, S. Gupta, M. M. Musthafa, H. D. Bhardwaj, and R. Prasad, J. Phys. Soc. Jpn. **72**, 1917 (2003).
[28] P. P. Singh, M. Phil. dissertation, A. M. University, Aligarh, India (2005), unpublished.
[29] S. Gupta, B. P. Singh, M. M. Musthafa, H. D. Bhardwaj, M. K. Sharma, R. Prasad, and A. K. Sinha, J. Phys. Soc. Jpn. **71**, 2434 (2002).
[30] D. J. Parker, J. J. Hogan, and J. Asher, Phys. Rev. C **39**, 2256 (1989).
[31] H. Morgenstern, W. Bohne, W. Galster, and K. Grabisch, Z. Phys. A **324**, 443 (1986).
[32] H. Morgenstern, W. Bohne, W. Galster, and K. Grabisch, Phys. Rev. Lett. **52**, 1104 (1984).
[33] M. F. Vineyard, J. S. Bauer, J. F. Crum, C. H. Gosdin, R. S. Trotter, D. G. Kovar, C. Beck, D. J. Henderson, R. V. F. Janssens, B. D. Wilkins, C. F. Maguire, J. F. Mateja, F. W. Prosser, and G. S. F. Stephens, Phys. Rev. C **45**, 1784 (1992).
[34] C. Beck, D. G. Kovar, S. J. Sanders, B. D. Wilkins, D. J. Henderson, R. V. F. Janssens, W. C. Ma, M. F. Vineyard, T. F. Wang, C. F. Maguire, F. W. Prosser, and G. Rosner, Phys. Rev. C **39**, 2202 (1989).
[35] P. Walker and G. Dracoulis, Nature (London) **399**, 35 (1999).
[36] S. M. Mullins *et al.*, Phys. Lett. **B393**, 279 (1997).
[37] M. Kaci *et al.*, Phys. Rev. C **56**, R600 (1997).
[38] C. Rubbia *et al.*, Report CERN/AT/95-94(ET).
[39] M. M. Musthafa, M. K. Sharma, B. P. Singh, and R. Prasad, App. Rad. Isot. **62**, 419 (2005).
[40] M. K. Sharma, Unnati, B. K. Sharma, B. P. Singh, H. D. Bhardwaj, R. Kumar, K. S. Golda, and R. Prasad, Phys. Rev. C **70**, 044606 (2004).
[41] M. K. Sharma, Unnati, B. P. Singh, H. D. Bhardwaj, R. Kumar, K. S. Golda, and R. Prasad, Nucl. Phys. **A776**, 83 (2006).
[42] P. P. Singh, M. K. Sharma, Unnati, D. P. Singh, R. Kumar, K. S. Golda, B. P. Singh, and R. Prasad, Eur. Phys. J. A **34**, 29 (2007).
[43] J. K. Tuli, Nuclear Wallet Card, National Nuclear Data Center, Brookhaven National Laboratory, Upton, New York, USA (2000).
[44] B. P. Singh, Ph.D. thesis, A. M. University, Aligarh, India (1991), unpublished.
[45] E. Brown and R. B. Firestone, *Table of Isotopes* (Wiley, New York, 1986).
[46] A. Gavron, Phys. Rev. C **21**, 230 (1980).
[47] R. Bass, Nucl. Phys. **A231**, 45 (1985).
[48] F. D. Becchetti and G. W. Greenlees, Phys. Rev. **182**, 1190 (1969).
[49] G. R. Satcher, Nucl. Phys. **70**, 177 (1965).
[50] P. M. Endt *et al.*, At. Data Nucl. Data Tables **26**, 47 (1981).
[51] J. P. Lestone, Phys. Rev. C **53**, 2014 (1996).
[52] A. Gilbert and A. G. N. Cameron, Can. J. Phys. **43**, 1446 (1965).
[53] K. S. Babu, R. Tripathi, K. Sudarshan, B. D. Srivastva, A. Gowswami, and B. S. Tomar, J. Phys. G **29**, 1011 (2003)
[54] P. R. S. Gomes, I. Padron, M. D. Rodriguez, G. V. Marti, R. M. Anjos, J. Lubian, R. Vegia, R. Liguori Neto, E. Crema, N. Added, L. C. Chamon, J. O. Fernadez Niello, O. A. Capurro, A. J. Pacheco, J. E. Testoni, D. Abriola, A. Arazi, M. Ramirez, and M. S. Hussein, Phys. Lett. **B601**, 20 (2004).
[55] H. Morgenstern, W. Bohne, K. Grabisch, H. Lehr, and W. Stoffler, Z. Phys. A **313**, 39 (1983).
[56] H. Morgenstern, W. Bohne, W. Galster, K. Grabisch, and A. Kyanowski, Phys. Rev. Lett. **52**, 1104 (1984).

Eur. Phys. J. A **34**, 29–39 (2007)
DOI 10.1140/epja/i2007-10487-1

THE EUROPEAN PHYSICAL JOURNAL A

Regular Article – Experimental Physics

Observation of complete- and incomplete-fusion components in ^{159}Tb,^{169}Tm(^{16}O, x) reactions: Measurement and analysis of forward recoil ranges at E/A $\approx$ 5–6 MeV

Pushpendra P. Singh[1,a], Manoj Kumar Sharma[1], Unnati[1], Devendra P. Singh[1], Rakesh Kumar[2], K.S. Golda[2], B.P. Singh[1,b], and R. Prasad[1]

[1] Accelerator Laboratory, Department of Physics, A. M. University, Aligarh (UP)-202 002, India
[2] NP Group, Inter-University Accelerator Center, P. O. Box No. 10502, New Delhi-110 067, India

Received: 18 April 2007 / Revised: 18 September 2007
Published online: 30 October 2007 – © Società Italiana di Fisica / Springer-Verlag 2007
Communicated by R. Krücken

Abstract. With a view to study complete- and incomplete-fusion components in ^{159}Tb,^{169}Tm(^{16}O, x) reactions, experiments have been carried out at the Inter-University Accelerator Center, New Delhi, India using the 15UD Pelletron accelerator facilities. The forward mean recoil ranges for some radio-nuclides; ^{168m}Lu, ^{167}Lu, ^{167}Yb, ^{166}Tm produced in the ^{16}O + ^{159}Tb system at $\approx$ 90 MeV, and ^{179}Re, ^{177}Re, ^{177}W, ^{178}Ta and ^{177}Hf produced in the ^{16}O + ^{169}Tm system at $\approx$ 87 MeV have been measured. The recoil-catcher activation technique followed by off-line γ-spectrometry has been employed in the present work. The analysis of forward mean ranges for different radio-nuclides has been done in the framework of the degree of linear momentum transfer from projectile to target nucleus by adopting break-up fusion model considerations. Different complete- and incomplete-fusion components, which may be attributed to the fusion of ^{16}O and/or ^{12}C and ^{8}Be transfer from the ^{16}O projectile to the target nucleus have been observed. An attempt has also been made to separate out the relative percentage contributions of complete- and incomplete-fusion components using experimentally measured forward recoil ranges. The complete-fusion contributions deduced from recoil range distribution are found to be consistent with the prediction of the theoretical model code PACE. The analysis of data indicates the complete- and incomplete-fusion competition for both the systems at the given energies.

PACS. 25.70.Mn Projectile and target fragmentation – 25.70.Gh Compound nucleus

1 Introduction

The understanding of light–heavy-ion ($4 \leq A \leq 20$) induced reactions has been a topic of great interest in recent years. It is now a well-established fact that at energies near and/or above the Coulomb barrier, the most dominating reaction process is the formation and decay of an equilibrated compound nucleus (CN) followed by the entire projectile fusion with the target nucleus [1–3], which is termed as complete fusion (CF). Nonetheless, incomplete fusion (ICF) has been found as a competing fusion-like process at energies even a little above the Coulomb barrier [4–9]. ICF is mainly characterized by the fractional fusion of the projectile with the target nucleus, due to the prompt emission of forward-peaked projectile-like fragments (PLFs) at the initial stage of interaction. The possibilities of ICF were first pointed out by Britt and Quintan [10]. However, the additional information regarding ICF processes has been found by Inamura *et al.* [11]. In order to illustrate the CF and ICF in heavy-ion interactions, it is instructive to use the terminology of impact parameter. In central collisions or mainly at zero impact parameter ($0 \leq \ell \leq \ell_{crit}$), the interacting partners may merge together with the strong involvement of all nucleonic degrees of freedom. In such a case, the interaction time is long enough ($\approx 10^{-16}$ s) to allow the complete thermalization leading to the CN formation. Thus, the CN formed by essentially a single route may de-excite via the emission of light nuclear particles and characteristic γ-radiations. Apart from that, at relatively high projectile energies and non-zero impact parameters ($\ell_{crit} \leq \ell \leq \ell_{max}$), CF gradually gives way to ICF. In the case of ICF, it is assumed that the projectile may lose α-clusters as it approaches the nuclear field of the target nucleus, which may move at forward angles with almost projectile velocity. Again statistical equilibrium of merging nucleons (a part of projectile plus target nucleus) is achieved. As a result of such a partial fusion of

[a] e-mail: pushpendrapsingh@gmail.com
[b] e-mail: bpsinghamu@gmail.com

projectile: i) the CN is supposed to form with less mass and charge as compared to the total mass and charge of the interacting partners; ii) the recoil velocity of the reaction products should be less than the complete-fusion population and iii) the angular distribution of ejectiles is expected to show maxima at forward angles. In the case of ICF processes, the mass transfer occurs mostly from the lighter to the heavier partner, the feature observed more prominently for mass asymmetric systems as compared to mass symmetric systems [12–14]. Another way to characterize the CF and/or ICF processes is the measurement of forward recoil ranges, even when a single reaction product is produced via several mechanisms. The linear momentum transfer (LMT) is the signature of the interaction of the projectile and the target nucleus and hence can be used to probe the reaction dynamics associated with the different reaction products. The dependence of ICF on the projectile energy is well established, but it is less clear to what extent the LMT depends on the projectile energy and interacting trajectories for different projectile-target combinations. However, in addition, to understand ICF, time-of-flight measurements have also been performed by Morgenstern *et al.* [15], but only the information about the mass of the residues could have been obtained, and not about their atomic numbers.

In order to get a better understanding of incomplete-fusion processes, several dynamical models, have been proposed, like the break-up fusion (BUF) model [16], the sum rule model [17], the promptly emitted particles (PEPs) model [18], the exciton model [19], etc. In the sum rule model, Wilczynski *et al.* [17] inferred that incomplete fusion is mainly confined to the angular-momentum space above the critical momentum (ℓ_{crit}) for complete fusion, and originated from peripheral interactions. The peripheral nature of ICF has also been emphasized by Trautmann *et al.* [20], and Inamura *et al.* [21,22]. The BUF model of Udagawa and Tamura is based on the distorted-wave Born approximation (DWBA) in which the projectile is assumed to break-up into its fragments (*e.g.*, ^{16}O may break-up into ^{12}C + α and/or ^{8}Be + ^{8}Be) as it approaches the nuclear field of the target nucleus, either of the fragment may fuse with the target nucleus [16], while, the remnant moves forward as a spectator and gives rise to projectile-like fragments (PLFs). According to the PEP model, the nucleons transferred from the projectile to the target nucleus may get accelerated in the nuclear force field of the target nucleus and consequently acquire extra velocity to escape [18]. The exciton model assumes that the projectile nucleons undergo a series of collisions with the target nucleus creating particle-hole excitations which de-excite by emitting fast nuclear particles [19]. On the other hand, Mermaz *et al.* [23], could explain the energy and angular distribution of the projectile-like fragments using DWBA formalism for the surface transfer reactions. The existing models, generally, have been used to fit the experimental data obtained at projectile energies $E/A \geq 10.5$ MeV, but there are somewhat conflicting observations for the experimental data at relatively low bombarding energies, *i.e.*, 5–7 MeV/nucleon. As such, there is no theoretical model available so far for ICF, which can provide satisfactory fitting to the experimental data obtained at energies 5–7 MeV/nucleon. Some studies, however, showed the onset of ICF process at $\approx$ 5–7 MeV/nucleon. Parker *et al.* [24] observed ICF even at $E/A \approx 6$ MeV using low-Z heavy ions. Recently, there is a renewed interest in the study of ICF dynamics after the observation of these reactions at relatively low bombarding energies [25–28]. Moreover, the ICF reactions are considered to be the promising route to produce high-spin states in heavy residues using light–heavy-ion beams ($A \leq 16$) even at low bombarding energies [29–31].

Further, some of the important issues associated with ICF dynamics at the given energy range are: i) the degree of fusion incompleteness, *i.e.*, the degree of LMT associated with ICF at different energies, ii) the relative contributions of CF and ICF processes have not yet been fully explored or limited to a few projectile-target combinations. As such, in order to have a better understanding of the underlying processes, a comprehensive study of excitation functions, forward ranges and angular distributions of recoils in HI-induced reactions has been undertaken by our group [26,25,32–35]. In the present work, which is the extension of our earlier observations presented in ref. [36], the forward recoil ranges of several radio-nuclides ^{168m}Lu, ^{167}Lu, ^{167}Yb, ^{166}Tm, ^{179}Re, ^{177}Re, ^{177}W, ^{178}Ta and ^{177}Hf populated via complete and/or incomplete fusion of ^{16}O with ^{159}Tb and with ^{169}Tm have been studied at, respectively, $\approx$ 90 MeV and $\approx$ 87 MeV. An attempt has also been made to separate out the relative percentage contributions of CF and ICF components using experimentally measured forward recoil ranges. The CF contributions deduced from recoil range distribution are found to be in good agreement with the predictions of PACE. The recoil-catcher technique followed by off-line gamma-spectroscopy has been used in the present work; related experimental details are given in sect. 2. How the forward ranges of recoils have been deduced is given in sect. 3. While, sect. 4, deals with the results and discussion, the summary and conclusions of the present work are given in sect. 5.

2 Experimental details

The experiments have been performed using $\approx$ 90 MeV and $\approx$ 87 MeV ^{16}O ion beam delivered from the 15UD-Pelletron accelerator of the Inter-University Accelerator Center (IUAC), New Delhi, India. Irradiations have been carried out in the General Purpose Scattering Chamber (GPSC) along with an In-vacuum Transfer Facility (ITF). Although the methodological details are somewhat similar to those already given in ref. [36], however, for quick reference, a brief description of sample preparation and irradiations, post-irradiation analysis etc., is given in the following subsections.

2.1 Sample preparation and irradiations

In the present work, a self-supporting sample of ^{159}Tb (abundance = 99.99%) of thickness $t \approx 0.80$ mg/cm^2 has

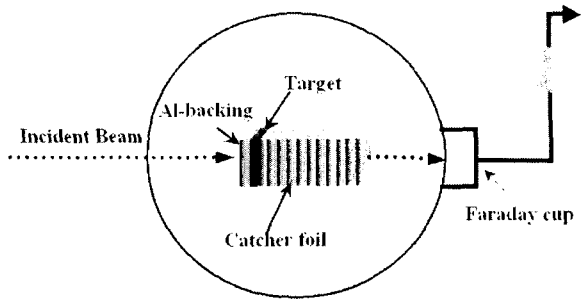

Fig. 1. A typical target-catcher foil set-up used for the measurement of forward recoil ranges of reaction products.

been prepared by the rolling method, while a sample of ^{169}Tm (abundance = 100%) of thickness $t \approx 0.60\,\mathrm{mg/cm^2}$ has been deposited by the electro-deposition technique on an Al foil (prepared by the rolling method) of thickness $t \approx 1.5\,\mathrm{mg/cm^2}$. The thickness of the samples has been estimated by the α-transmission method, which is based on the measurement of the energy lost by α-particles while passing through the sample material. α-particles of 5.486 MeV energy were obtained from the ^{241}Am standard α-source. The samples have been pasted on rectangular Al holders (size $1.2 \times 1.2\,\mathrm{cm^2}$) having concentric holes of 1.0 cm diameter. Al holders have been used for rapid heat dissipation during the irradiations. The irradiations have been performed using an $^{16}O^{7+}$-beam in GPSC-ITF. Stacks of Al catcher foils (sufficient to stop the CN formed via full linear momentum transfer) have been placed just after the target, so that the heavy slow residues populated via CF and/or ICF could be trapped at various Al catcher foil thicknesses. A typical target-catcher foil set-up used for the measurement of forward recoil ranges is shown in fig. 1. In the case of the ^{169}Tm target deposited on the Al foil, the target has been mounted in such a way that the Al-backing first faces the beam so that the recoiling nuclei (if any of very short range) does not stop in the target backing itself. The irradiations have been carried out for the duration of ≈ 12 h, with a beam current ≈ 30–40 nA. The delay time between the end of irradiation and the beginning of counting was minimized using in-vacuum transfer of samples. The total charge collected in the Faraday cup has been used to calculate the beam flux during the irradiations.

2.2 Post-irradiation details and ERs identification

The stacks of the samples backed by Al catchers were taken out from the scattering chamber after irradiations using an ITF. The activities produced in each catcher foil of the stack were counted separately using a pre-calibrated high-resolution HPGe spectrometer of 100 c.c. active volume coupled with the CAMAC-based FREEDOM software. The HPGe spectrometer was pre-calibrated both for energy and efficiency using various standard γ-sources like ^{22}Na, ^{54}Mn, ^{57,60}Co, ^{133}Ba, ^{137}Cs and ^{152}Eu. The resolution of the γ-spectrometer was found to be ≈ 2 keV, for 1.33 MeV γ-ray of ^{60}Co source, during the counting of the samples. The efficiency (geometry dependent) of the HPGe detector for various source-detector separations was determined using different standard sources. The formulation used for the efficiency determination is given elsewhere in ref. [36]. Typical γ-ray spectra of irradiated ^{159}Tb and ^{169}Tm samples, respectively, at ≈ 90 and ≈ 87 MeV are shown in fig. 2 and fig. 3. The various peaks which have been used for the recoil range analysis are assigned to the different reaction products on the basis of their characteristic γ-ray energies and measured half-lives, and are clearly indicated in the given figures. The list of the radio-nuclides populated in ^{16}O + ^{159}Tb and ^{16}O + ^{169}Tm, the energy of identified γ-rays used for the decay-curve analysis and the recoil range measurement along with their branching ratios are given in tables 1 and 2. The evaporation residues (ERs) populated via the process of CF and/or ICF are supposed to be trapped at different catcher foil thicknesses, depending on the ERs recoil velocity and/or the degree of linear momentum transfer associated with the mode of formation. The residues are likely to decay to the ground state by emitting characteristic γ-radiations, whose detection can be used as a probe for their identification. Thus, the induced activities can be used to measure

Table 1. List of identified evaporation residues produced in the ^{16}O+^{159}Tb system via complete and/or incomplete fusion.

Residues	E_γ (keV)	Half-life	J_π	a_γ (%)
$^{168m}_{71}$Lu(α3n)	298.61	6.7 min	3+	17
	539.88[a]			47
$^{167}_{71}$Lu(α4n)	239.13[a]	57.5 min	7/2+	8.2
	317.48			1.5
$^{167}_{70}$Yb(αp3n)	143.46[a]	17.5 min	5/2−	2.10
$^{166}_{69}$Tm(2αn)	594.37	7.7 h	2+	3.08
	1176.68[a]			8.4

[a] γ-transitions used for data analysis.

Table 2. List of identified evaporation residues produced in the ^{16}O+^{169}Tm system via complete and/or incomplete fusion.

Residues	E_γ (keV)	Half-life	J_π	a_γ (%)
$^{177}_{71}$W(αp3n)	115.0[a]	2.21 h	1/2−	59
	426.9			13.1
$^{178}_{73}$Ta(α2pn)	325.5[a]	2.36 h	7−	94.1
	331.6			32
$^{177}_{72}$Hf(α3pn)	214.4	51.4 min	7/2−	8.3
	638.1[a]			20
$^{177}_{75}$Re(α4n)	1118.4[a]	14.0 min	5/2−	25
	723.4			15
$^{179}_{75}$Re(α2n)	221.9	19.5 min	5/2+	3.6
	401[a]			7.3
	498.2			5.7

[a] γ-transitions used for data analysis.

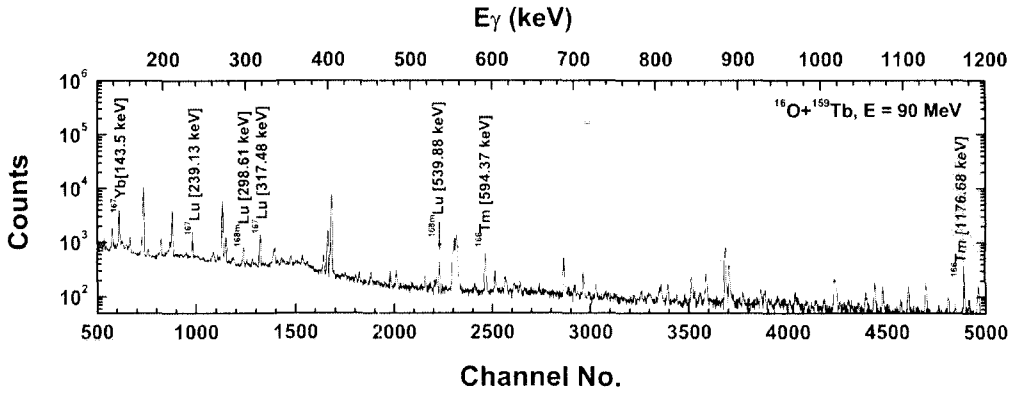

Fig. 2. The observed γ-ray spectrum of the ^{159}Tb sample irradiated by an $^{16}O^{7+}$ beam at energy ≈ 90 MeV. The γ-lines have been assigned to different ERs expected to be populated via CF and/or ICF reaction dynamics.

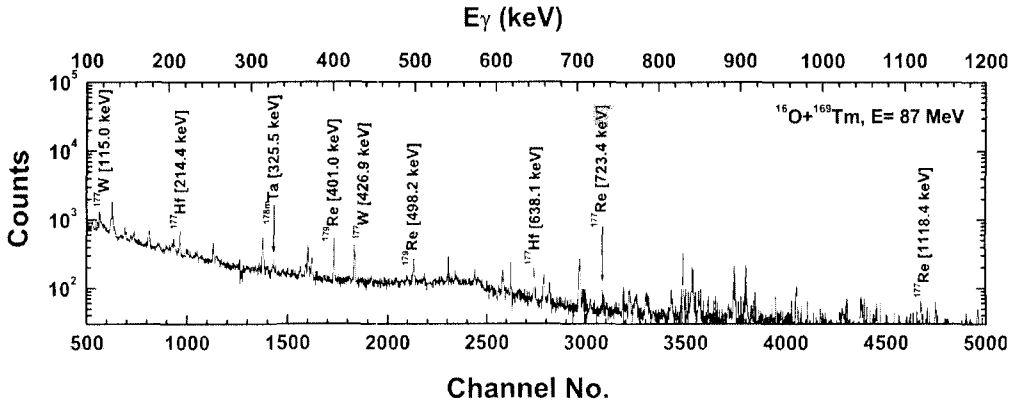

Fig. 3. The observed γ-ray spectrum of the ^{169}Tm sample irradiated by an $^{16}O^{7+}$ beam at energy ≈ 87 MeV. The γ-lines have been assigned to different ERs expected to be populated via CF and/or ICF reaction dynamics.

the production probability of evaporation residues. Therefore, the γ-ray spectra of each foil have been recorded at increasing times so that the decay curve analysis can be done to measure the half-lives of the residues. The observed peaks in the γ-ray spectra (figs. 2 and 3) have been assigned to the different reaction products. The experimental data points of decay curves have been fitted using the least-square fitting option of the ORIGIN graphics software. The measured half-lives of the evaporation residues were found to be in good agreement with the literature values. Data analysis has been performed using the FREEDOM software for nuclear-data analysis. Nuclear data like half-lives, gamma-ray energies, etc., have been taken from the table of isotopes [37].

2.3 Production yield measurement of ERs

The measured intensities of the characteristic γ-radiations were used to estimate the production yield of evaporation residues. A FORTRAN program EXP-SIGMA based on the following formulation has been used for the determination of the production yield of evaporation residues [38]:

$$\sigma_{prod} = \frac{C_{t=0}}{N_0 \theta \phi G_\varepsilon K[1 - \exp(-\lambda t_1)]}, \quad (1)$$

where $C_{t=0}$ is the total number of counts at the end of the irradiation. N_0 is the initial number of target nuclei. θ is the branching ratio of the characteristic γ-ray. ϕ is the flux of the incident beam. G_ε is the geometry-dependent efficiency of the spectrometer for a particular γ-ray energy and $K = [1 - \exp(-\mu d)]/\mu d$ is the self-absorption correction factor for the material of the sample of thickness d (gm/cm^2) and of absorption coefficient μ (cm^2/gm). The factor $[1 - \exp(-\lambda t_1)]$ is the saturation correction factor. In the present work, the production probability of ERs ^{168m}Lu(α3n), ^{167}Lu(α4n), ^{167}Yb(αp3n) and ^{166}Tm(2αn) produced in the $^{16}O + ^{159}$Tb system, and ^{179}Re(α2n), ^{177}Re(α4n), ^{177}W(αp3n), ^{178}Ta(α2pn), and ^{177}Hf(α3pn) produced in the $^{16}O + ^{169}$Tm system has been measured at different catcher foil thicknesses to estimate the recoil range distributions.

2.3.1 Uncertainties in measurements

Errors in the measured production yield of ERs may arise because of several reasons *viz*: i) non-uniform deposition of the target material and inaccurate estimate of the foil thickness may lead to uncertainties in the determination

of the number of target nuclei in the sample. Although it is hard to know the uncertainity in the target thickness, however, to check the uniformity of the sample, the thicknesses of the samples were measured at different locations of the same sample by the α-transmission method as well as by the weighing method. It is estimated that the error in the target thickness is $\approx 1\%$. ii) Fluctuations in the beam current during the irradiations may result in the variation of the incident flux. Proper care has been taken to keep the beam current constant within 10%. It is estimated that the beam fluctuations may introduce an error of $\approx 3\%$. iii) Uncertainty in the determination of the geometry-dependent efficiency of the spectrometer may give rise to error in the production cross-sections. Statistical errors in counting of the standard sources may give rise to an error in the efficiency, which was minimised by accumulating a large number of counts for comparatively larger times (≈ 5000 s). Experimental data on the geometry-dependent efficiencies with γ-ray energy at a fixed source-detector seperation has been fitted with a power law curve. The uncertainity due to the fitting of the efficiency curve is estimated to be less than 3%. The uncertainity in determining the efficiency may also appear due to the solid-angle effect, because the irradiated samples were not point sources like the standard source, but they had a diameter of ≈ 4 mm. It is estimated that the error in the efficiency due to the solid-angle effect is less than 6%. iv) During the stack irradiation, the beam traverses the thickness of the material, thus the initial beam intesity is reduced. It is estimated that the error due to the decrease in beam intensity be around 2%. v) In all the measurements, the dead time of the spectrometer was kept $\leq 10\%$ by suitably adjusting the sample-detector distance and the corrections for it were applied to the counting rate. Further, the uncertainties of the nuclear data like branching ratio, decay constant etc., which have been taken from the table of isotopes [37] have not been taken into consideration. The overall errors from these factors including the statistical error are estimated to be $\leq 15\%$.

3 Recoil range distributions

The CF and ICF processes are based on the recoil velocity of the reaction products, which depends on the degree of the linear momentum transfer (ρ_{LMT}) from the projectile to the target nucleus. For incomplete fusion, ρ_{LMT} may be given as

$$\rho_{LMT} = \frac{P_{frac}}{P_{proj}} , \tag{2}$$

where P_{frac} is the linear momentum of the fused fraction of the projectile and P_{proj} is the entire linear momentum of the projectile. As already mentioned, ρ_{LMT} is proportional to the fused mass of the projectile, *i.e.*, maximum LMT may give maximum recoil velocity to the reaction products. This is supposed to be a promising way of investigating the full momentum transfer in the case of the complete-fusion process, and a relatively small recoil momentum in a partial momentum transfer reaction (ICF). Since, in the CF process, the maximum ρ_{LMT} gets transferred from the projectile to the target nucleus, therefore, for a given entrance channel the CN has predetermined mass, energy and momenta. While, in the case of ICF, a partial ρ_{LMT} leads to the formation of an incompletely fused composite system in excited state. For an incompletely fused composite system, the above-mentioned quantities (mass, energy and momenta of CN) may not have unique values. This may be because of the fluctuations in the fused mass from the projectile to target nucleus and interaction trajectories. The experimentally measured forward recoil ranges of final reaction products in the stopping medium may be an indication of the ρ_{LMT} involved. As such, the radio-nuclides populated via a lower degree of LMT, show relatively smaller depth (momentum transfer component) in the stopping medium as compared to the entire LMT populations. For a different ρ_{LMT}, the residues may have different recoil ranges in the stopping medium. Therefore, the forward recoil range distributions may be used as a probe to investigate the partial fusion of the projectile in ICF processes.

As already mentioned, the measurement of the projected ranges of the reaction products may be an indication for the degree of linear momentum transfer (ρ_{LMT}) from the projectile to the target nucleus. For a given reaction product formed via particle evaporation from a recoiling intermediate with a well-defined velocity v_0, the velocity distribution will be symmetric about v_0 with a width which depends upon the evaporation process and, in particular, upon the number of alpha-particles evaporated in case of incomplete fusion processes. For the CN formed via complete fusion the velocity v_0 may be written as

$$v_0 = v_{CN} = \frac{\sqrt{2mE}}{M} , \tag{3}$$

where, m is the projectile mass, M is the total mass of the system (projectile + target), and E is the projectile energy. Further, as already mentioned, for any intermediate complex which is supposed to be formed via a partial fusion of the projectile, the recoil velocity will be less than that achieved by the complete momentum transfer population. Therefore, the reaction products populated via incomplete fusion will show relatively smaller depth in the stopping medium as compared to complete-fusion reaction products. The measured RRD of a detected evaporation residue can thus, in principle, be used as a probe to identify the fusion mode, and to separate out the relative contributions of various partial-fusion components to the formation of a particular evaporation residue in case of incomplete-fusion reactions.

3.1 Estimation and analysis of RRDs

As already mentioned, the trapped recoiling reaction products in the catcher foils were identified by their characteristic γ-radiations as well as their decay-curve analysis. The production cross-sections (σ_{prod}) for identified reaction products were computed using the standard formulation given in sect. 3. In order to obtain the normal-

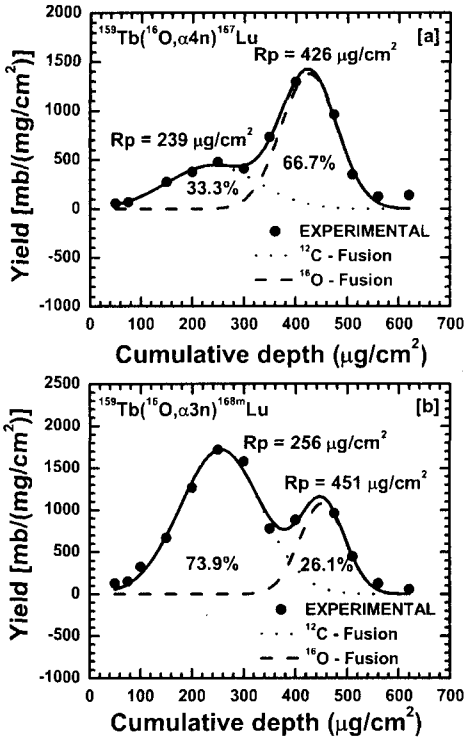

Fig. 4. The experimentally measured recoil range distributions for (a) ^{167}Lu(α4n), and (b) ^{168m}Lu(α3n) produced in the ^{16}O+ ^{159}Tb system at ≈ 90 MeV. The percentage fractions of ^{12}C and ^{16}O fusion are found to be (a) ≈ 33.3% and ≈ 66.7% for the production of ^{167}Lu, and (b) ≈ 73.9% and ≈ 26.1% for the production of ^{168m}Lu.

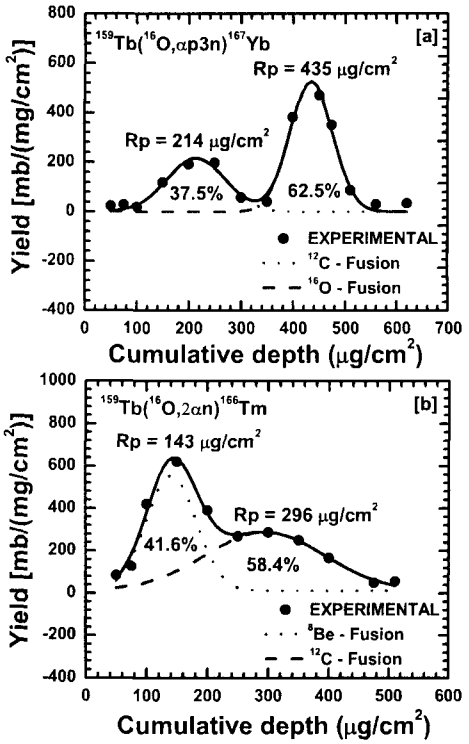

Fig. 5. The experimentally measured recoil range distributions for (a) ^{167}Yb(αp3n), and (b) ^{166}Tm(2αn) produced in the ^{16}O + ^{159}Tb system at ≈ 90 MeV. The percentage fractions of ^{12}C and ^{16}O fusion are found to be ≈ 37.5% and ≈ 62.5% as indicated in (a). The percentage fractions of ^{8}Be and ^{12}C fusion are found to be ≈ 41.6% and ≈ 58.4% as indicated in (b).

ized yield as a function of cumulative depth in the catcher stack, the cross-section of the reaction products in each catcher foil was divided by its measured thickness. The resulting normalized yields of different reaction products have been plotted against cumulative catcher foil thicknesses to obtain the differential recoil range distributions and are plotted in figs. 4-8. The size of the circles in figs. 4-8 includes the uncertainty in the yield values. As can be seen from these figures, the measured RRDs clearly indicate the different momentum transfer components, depending on the fused mass of the projectile with the target nucleus.

Further, the relative contributions of complete and incomplete fusion in the production of a particular reaction product may be computed by fitting the experimentally measured RRDs with Gaussian peaks using the ORIGIN software. The yield curves of evaporation residues obtained from RRD are assumed to be Gaussian in nature and may be given as [39]

$$Y = Y_0 + \frac{A}{\sqrt{2\pi w_A^2}} e^{-(R-R_p)^2/2w_A^2}, \quad (4)$$

where R_p is the most probable mean range, w_A is the width parameter (FWHM) of the recoil range distribution, and A is the area under the peak. Further, the normalized yield Y may be estimated by the chi square fit (χ^2) from the experimentally determined production yield at different catcher foil thicknesses and may be represented as follows:

$$\chi^2 = \frac{1}{m-p-1}\{Y(A) - Y_0(A)\}^2. \quad (5)$$

The value of the chi square fit (χ^2) was minimized in this analysis using a non-linear least-square fit routine, keeping the width parameter (w_A) and most probable mean range (R_p) of the evaporation residues as a free parameter.

Moreover, as indicated in figs. 4-8, most of the residues show more than one RRD component. In such cases, the experimentally measured normalized yields have been fitted using the multi-peak option in a similar way as mentioned above. The contribution of different fusion components (^{16}O, ^{12}C and ^{8}Be fusion) have been obtained by dividing the area under the peak of the corresponding fusion component by the total area associated with the experimental data. The percentage contributions coming from different complete- and/or incomplete-fusion components deduced in such a way for the residues populated in both the systems are indicated in figs. 4-8, along with their corresponding channels.

Table 3. Experimentally measured most probable ranges $R_{p(exp)}$ deduced from RRD curves, and theoretically estimated forward mean ranges $R_{p(the)}$ for CF and ICF components using the range-energy relation along with the reaction products produced in the $^{16}O + ^{159}Tb$ system at ≈ 90 MeV.

Residues	$R_{p(exp)}$ $\mu g/cm^2$ CF of ^{16}O	$R_{p(the)}$ $\mu g/cm^2$ CF of ^{16}O	$R_{p(exp)}$ $\mu g/cm^2$ ICF of ^{12}C	$R_{p(the)}$ $\mu g/cm^2$ ICF of ^{12}C	$R_{p(exp)}$ $\mu g/cm^2$ ICF of ^{8}Be	$R_{p(the)}$ $\mu g/cm^2$ ICF of ^{8}Be
$^{167}Lu(\alpha 4n)$	426 ± 18	432	239 ± 15	245	-	-
$^{168m}Lu(\alpha 3n)$	451 ± 25	432	256 ± 13	245	-	-
$^{167}Yb(\alpha p3n)$	435 ± 14	432	214 ± 21	245	-	-
$^{166}Tm(2\alpha n)$	-	-	296 ± 27	245	143 ± 19	126

4 Interpretation of the experimental results

4.1 $^{16}O + ^{159}Tb$ System

In figs. 4-5, the experimentally measured recoil range distributions for four reaction products $^{167,168m}Lu$, ^{167}Yb and ^{166}Tm, populated via complete and/or incomplete fusion in the $^{16}O + ^{159}Tb$ system at ≈ 90 MeV are shown. The reaction products $^{167,168m}Lu$ have ground and metastable state of half-lives 51.5 min and 6.7 min, respectively. As can be seen from fig. 4(a)-(b), these reaction products ($^{167,168m}Lu$) may be formed both via complete and/or incomplete fusion of ^{16}O with ^{159}Tb. In case of CF, the composite system $^{175}Ta^*$ is formed, which may decay via the statistical emission of an alpha-particle and 3 or 4 neutrons leaving behind the above residues. The above residues may also be populated, if it is assumed that, as soon as the incident ^{16}O nucleus approaches the nuclear range of target nucleus, it may break up into α-clusters *viz* ^{12}C and ^{4}He(alpha). One of the fragments ^{12}C fuses with ^{159}Tb, forming an incompletely fused composite system, $^{171}Lu^*$, which may decay by the emission of, respectively, three neutrons forming ^{168m}Lu and four neutrons forming ^{167}Lu. As can be observed from fig. 4(a), and as already mentioned the RRD for the residue ^{167}Lu show both complete- and incomplete-fusion components having two peaks at the cumulative catcher thickness at $\approx 239\,\mu g/cm^2$ (due to ^{12}C fusion) and $\approx 426\,\mu g/cm^2$ (due to ^{16}O fusion). The observed mean recoil range of ^{16}O fusion with ^{159}Tb corresponds to the expected recoil range of the compound system ^{175}Ta in aluminum, calculated using the classical approach and the stopping-power tables of Northcliffe and Schilling. It may, however, be pointed out that, the relative contribution of ^{12}C fusion for the reaction $^{159}Tb(^{16}O,\alpha 4n)^{167}Lu$ (fig. 4(a), indicated by the dotted curve) is found to be $\approx 33\%$, while the contribution from ^{16}O fusion (indicated by the dashed curve) is $\approx 67\%$. The observation of a peak at relatively smaller cumulative depth clearly indicates the lower degrees of LMT involved in the process. The reaction product ^{168m}Lu also shows two components, respectively, at $\approx 256\,\mu g/cm^2$ (due to ^{12}C fusion) and at $\approx 451\,\mu g/cm^2$ (due to ^{16}O fusion). Similarly, for the reaction $^{159}Tb(^{16}O,\alpha 3n)^{168m}Lu$, the contributions of the ^{12}C (ICF) and ^{16}O (CF) fusion (fig. 4(b), indicated by the dotted and the dashed curve) are found to be $\approx 74\%$ and $\approx 26\%$, respectively. The above description clearly indicates that the linear momentum transfer for the peaks at different cumulative depths in the stopping medium involves different degree of linear momentum transfer (p_{LMT}).

Further, the reaction product ^{167}Yb, which has a ground state of half-life 17.5 min, is expected to be populated via the complete-fusion ($\alpha p3n$) channel and/or incomplete fusion (*i.e.*, the fusion of ^{12}C with ^{159}Tb) followed by subsequent emission of one proton and three neutrons from $^{171}Lu^*$. The remaining alpha-fragment (^{4}He) of the incident ion is assumed to go on moving with the beam velocity in the forward direction without any significant interaction with the target nucleus. As indicated in fig. 5(a), there are two LMT components, respectively at $\approx 214\,\mu g/cm^2$ (that belongs to ^{12}C fusion) and $\approx 435\,\mu g/cm^2$ (due to ^{16}O fusion). The relative contributions of ICF (due to ^{12}C fusion) and CF (due to ^{16}O fusion) for the reaction $^{159}Tb(^{16}O,\alpha p3n)^{167}Yb$ are found to be $\approx 37.5\%$ and $\approx 62.5\%$ respectively, as indicated in fig. 5(a) by the dotted and the dashed curve. While, the evaporation residue $^{166}Tm(2\alpha n)$ of half-life $t_{1/2} = 7.7$ h, is expected to be populated via the fusion of ^{8}Be and subsequent emission of one neutron from $^{167}Tm^*$. However, the remaining part ^{8}Be (two α-particles) behaves like spectator. It may be observed from fig. 5(b), that there are two LMT components, at $\approx 143\,\mu g/cm^2$ and $\approx 296\,\mu g/cm^2$, due to ^{8}Be and ^{12}C fusion, respectively, indicating the major contribution for the population of the above residue only from the two incomplete-fusion channels. It may, however, be pointed out that the relative contribution coming from ^{8}Be and ^{12}C fusion (fig. 5(b), indicated by dotted and dashed curves) is found to be $\approx 42\%$ and $\approx 58\%$, respectively. In table 3, the experimentally measured most probable ranges $R_{p(exp)}$, and theoretically estimated forward mean ranges $R_{p(the)}$ for CF and/or ICF components using the range-energy relation for the reaction products produced at ≈ 90 MeV are given. As can be seen from this table, the experimentally measured most probable ranges for both CF and/or ICF components agree well with the theoretical ones within the experimental uncertainty. The error shown in $R_{p(exp)}$ indicates the fitting errors of the Gaussian distribution to the experimental data.

4.2 $^{16}O + ^{169}Tm$ system

The recoil range distributions for $^{177,179}Re$, ^{177}W, ^{178}Ta and ^{177}Hf reaction residues populated in the interaction of

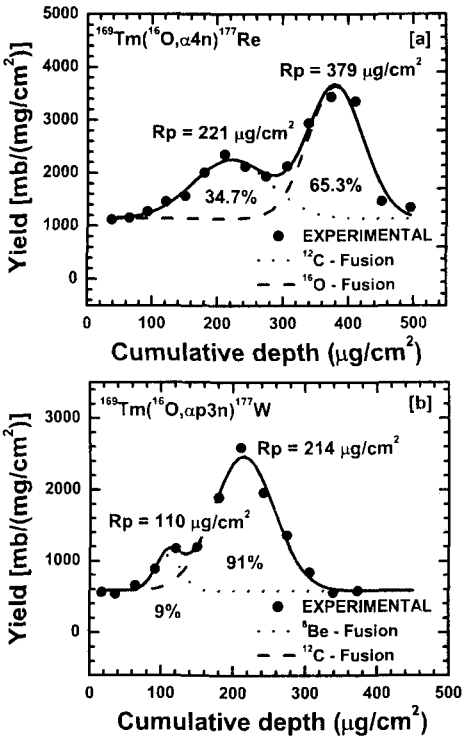

Fig. 6. The experimentally measured recoil range distributions for (a) ^{177}Re(α4n), and (b) ^{177}W(αp3n) produced in the ^{16}O+ ^{169}Tm system at $\approx$ 87 MeV. The percentage fractions of ^{12}C and ^{16}O fusion are found to be $\approx$ 34.7% and $\approx$ 65.3% for the production of ^{177}Re, as indicated in (a), while the percentage fractions of ^{8}Be and ^{12}C fusion are found to be $\approx$ 9% and $\approx$ 91% for the production of ^{177}W, as indicated in (b).

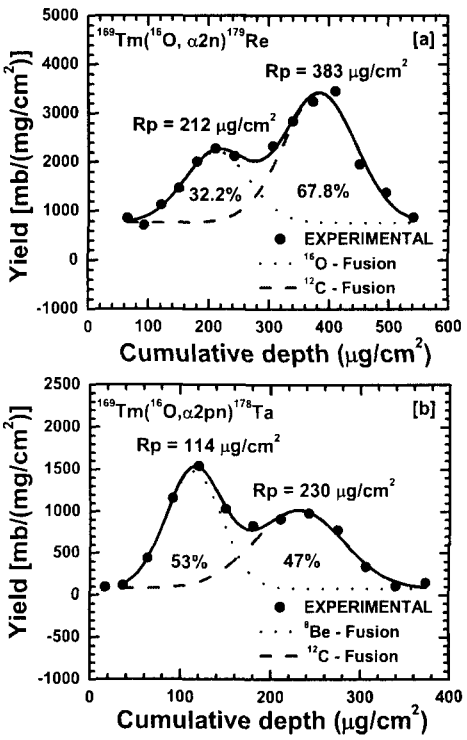

Fig. 7. The experimentally measured recoil range distributions for (a) ^{179}Re(α2n), and (b) ^{178}Ta(α2pn) produced in the ^{16}O+ ^{169}Tm system at $\approx$ 87 MeV. The percentage fractions of ^{12}C and ^{16}O fusion are found to be $\approx$ 32.2% and $\approx$ 67.8% for the production of ^{179}Re, as indicated in (a), while the percentage fractions of ^{8}Be and ^{12}C fusion are found to be $\approx$ 53% and $\approx$ 47% for the production of ^{178}Ta, as indicated in (b).

^{16}O with ^{169}Tm at $\approx$ 87 MeV are shown in figs. 6-8. As already indicated in the previous section, the above residues may be populated both via complete and/or incomplete fusion of ^{16}O with ^{169}Tm. The population of these residues in α-emission channels may also be explained in terms of the break-up of ^{16}O into ^{12}C and ^{4}He(α-particle) followed by fusion of ^{12}C with ^{169}Tm forming an incompletely fused composite system, ^{181}Re*. As shown in fig. 6(a), the reaction product ^{177}Re of half-life 14 min is expected to be populated via the emission of four neutrons from ^{181}Re* and show two peaks, respectively at $\approx$ 221 μg/cm^2 (that belongs to ^{12}C fusion) and $\approx$ 379 μg/cm^2 (that belongs to ^{16}O fusion). Thus, the evaporation residues ^{177}Re may not only be populated via incomplete fusion but may have significant probability of being formed by the CF of the projectile leading to the formation of ^{185}Ir*, which may decay by the emission of two and four neutrons along with an alpha particle. Similarly, the reaction product ^{177}W(αp3n) having half-life 2.21 h is also expected to be populated dominantly via ICF of ^{12}C with ^{169}Tm, leading to the formation of ^{181}Re*. The reaction product ^{177}W may come into play after the emission of a proton and three neutrons from ^{181}Re*. As can be seen from fig. 6(b), there are two LMT components, respectively at $\approx$ 110 μg/cm^2 (that belongs to ^{8}Be fusion) and $\approx$ 214 μg/cm^2 (that belongs to ^{12}C fusion) associated with an incomplete fusion of the following type:

$$^{16}\mathrm{O}(^{12}\mathrm{C} + {}^{4}\mathrm{He}) \Rightarrow {}^{12}\mathrm{C} + {}^{169}\mathrm{Tm} \Rightarrow {}^{181}\mathrm{Re}^* + {}^{4}\mathrm{He}$$

(alpha as spectator).

It may, however, be pointed out that the LMT component at a relatively smaller depth, *i.e.*, $\approx$ 110 μg/cm^2 may be associated with the ICF of ^{8}Be with the target nucleus, which may lead to the formation of ^{177}Ta*. The final reaction product ^{177}W may also be populated via β^+-emission and/or EC decay of the higher charge precursor isobar ^{177}Ta* via incomplete fusion of ^{8}Be of following type:

$$^{16}\mathrm{O}(^{8}\mathrm{Be} + {}^{8}\mathrm{Be}) \Rightarrow {}^{8}\mathrm{Be} + {}^{169}\mathrm{Tm} \Rightarrow {}^{177}\mathrm{Ta}^* + {}^{8}\mathrm{Be}$$

(beryllium as spectator).

Similarly, the reaction products ^{178}Ta and ^{179}Re have half-lives 2.45 h and 19.5 min, respectively, and are expected to be populated via α2pn and α2n channels, respectively, in which the α-particle may be assumed to behave as spectator. As indicated in fig. 7(a), ^{179}Re is expected

Table 4. Experimentally measured most probable ranges $R_{p(exp)}$ deduced from RRD curves, and theoretically estimated forward mean ranges $R_{p(the)}$ for CF and ICF components using the range-energy relation along with the reaction products produced in the $^{16}O + ^{169}Tm$ system at ≈ 87 MeV.

Residues	$R_{p(exp)}$ μg/cm^2 CF of ^{16}O	$R_{p(the)}$ μg/cm^2 CF of ^{16}O	$R_{p(exp)}$ μg/cm^2 ICF of ^{12}C	$R_{p(the)}$ μg/cm^2 ICF of ^{12}C	$R_{p(exp)}$ μg/cm^2 ICF of ^{8}Be	$R_{p(the)}$ μg/cm^2 ICF of ^{8}Be
^{177}Re(α4n)	379±22	402	221±13	228	–	–
^{177}W(αp3n)	–	–	214 ± 17	228	110 ± 11	117
^{179}Re(α2n)	383 ± 21	402	212 ± 18	228	–	–
^{178}Ta(α2pn)	–	–	230 ± 15	228	114 ± 17	117
^{177}Hf(α3pn)	–	–	216 ± 17	228	–	–

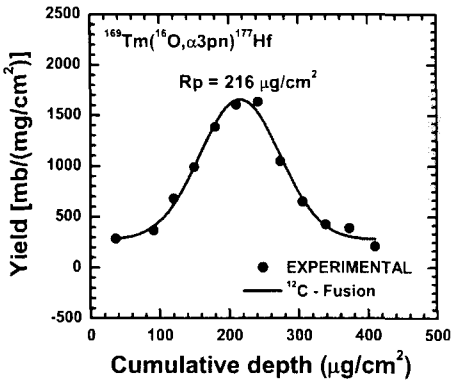

Fig. 8. The experimentally measured recoil range distribution for ^{177}Hf(α3pn) produced in the $^{16}O + ^{169}Tm$ system at $\approx$ 87 MeV. As discussed in the text, this product is expected to be populated only via incomplete fusion of ^{12}C.

to be populated via both complete and/or incomplete fusion and hence shows two LMT components, respectively at $\approx 212\,\mu g/cm^2$ (due to ^{12}C fusion) and $\approx 383\,\mu g/cm^2$ (due to ^{16}O fusion). While, ^{178}Ta is populated only via incomplete fusion and shows two LMT components, respectively, at $\approx 114\,\mu g/cm^2$ (that belongs to ^{8}Be fusion) and $\approx 383\,\mu g/cm^2$ (that belongs to ^{12}C fusion), which are shown in fig. 7(b). Further, the RRD for reaction product ^{177}Hf(α3pn), having half-life of 51.4 min is found to have only one peak corresponding to a cumulative depth $\approx 216\,\mu g/cm^2$, indicating the population of this residue by incomplete fusion of ^{12}C only, as indicated in fig. 8. A comparison of $R_{p(exp)}$ and $R_{p(the)}$ for various channels produced in the $^{16}O + ^{169}Tm$ system is given in table 4, and they agree reasonably well.

Further, an attempt has been made to compare the experimental range integrated cross-sections with that of theoretical predictions based on the PACE code. The CF contributions deduced from forward recoil range data σ_{exp}(CF) have been compared with the CF contributions deduced using the fusion-evaporation model code PACE based on Monte Carlo simulation. A comparison of the CF contributions is given in tables 5 and 6 for various residues. It may be pointed out that the code does not take the ICF process into account. As can be seen from these tables, the experimentally deduced contributions of

Table 5. Experimentally measured cumulative (CF+ICF) production cross-sections, deduced (using RRDs) cross-section for ICF and CF components and the theoretically calculated (PACE) cross-sections for the residues produced in the $^{16}O + ^{159}Tb$ system at ≈ 90 MeV.

Residues	σ_{exp} (mb) CF+ICF	σ_{exp} (mb) ICF	σ_{exp} (mb) CF	σ_{the} (mb) CF
^{167}Lu	46 ± 6.6	15 ± 2.2	30 ± 4.4	26.50
^{168m}Lu	146 ± 18.5	108 ± 13.7	37 ± 4.8	42.46
^{167}Yb	49 ± 7.6	18 ± 3.2	30 ± 4.4	27.18
^{166}Tm	31 ± 5.7	31 ± 5.7	–	–

Table 6. Experimentally measured cumulative (CF+ICF) production cross-sections, deduced (using RRDs) cross-section for ICF and CF components and the theoretically calculated (PACE) cross-sections for the residues produced in the $^{16}O + ^{169}Tm$ system at ≈ 87 MeV.

Residues	σ_{exp} (mb) CF+ICF	σ_{exp} (mb) ICF	σ_{exp} (mb) CF	σ_{the} (mb) CF
^{177}Re	26 ± 4.1	9 ± 1.5	17 ± 2.6	19.8
^{177}W	39 ± 5.9	39 ± 5.9	–	–
^{179}Re	23 ± 3.7	8 ± 1.2	15 ± 2.5	13.4
^{178}Ta	106 ± 12.6	106 ± 12.6	–	–
^{177}Hf	48 ± 7.3	48 ± 7.3	–	–

CF agree well with the theoretical values within the experimental uncertainties. Moreover, as already indicated in sects. 4.1 and 4.2, the RRDs for the residues ^{166}Tm, ^{177}W, ^{178}Ta and ^{177}Hf show peaks corresponding to the ICF of ^{8}Be and/or ^{12}C only and hence experimental CF contributions for these residues are not shown in these tables. It may be pointed out that the PACE predictions do not give any contribution for these residues as well. As such, it may again be inferred that these residues are dominantly produced in an ICF process. In the above description, it is assumed that the residues produced by CF of ^{16}O, ICF of ^{12}C and ICF of ^{8}Be would produce residues with the observed average recoil ranges. It has been pointed out by Parker *et al.* [40] that detailed theoretical calculations indicate that even accounting for pre-equilibrium emission of particles ($z = 1, 2$) and evaporation of either "n" or

"p" or an α-particle, it is not possible to explain the recoil range distribution of several reaction products by considering only occurrences of CF or pre-equilibrium processes. The enhancement in cross-sections for the production of Re, W, Ta and Hf isotopes, that one observes, may be attributed to the ICF processes. It may, further, be mentioned that the observation of clear recoil range distributions obtained in the present work may be considered as a direct proof of ICF processes at the studied energies.

5 Summary and conclusions

The recoil range distributions of nine evaporation residues; ^{168m}Lu, ^{167}Lu, ^{167}Yb, ^{166}Tm, ^{179}Re, ^{177}Re, ^{177}W, ^{178}Ta and ^{177}Hf produced in ^{16}O + ^{159}Tb and ^{16}O + ^{169}Tm systems, respectively, at ≈ 90 MeV and ≈ 87 MeV have been studied. The results presented in this paper on the measurement and analysis of the mean forward recoil ranges of reaction products strongly revealed a significant contribution from the partial linear momentum transfer of the projectile associated with incomplete fusion. Different momentum transfer components are attributed to the ^{12}C and/or ^{8}Be transfer from the ^{16}O projectile to the target nucleus. An attempt has also been made to obtain the relative contribution of complete- and/or incomplete-fusion components. It has been found that, in general, the residues are not only populated via complete fusion but incomplete fusion is also found to play an important role in the production of different reaction products involving direct α-cluster emission at these energies. However, in the case of ^{166}Tm, ^{177}W, ^{178}Ta and ^{177}Hf residues, the RRD data clearly indicate that the ICF reaction mechanism is dominant at the energies of interest in the present work. The above measurements are also consistent with the theoretical predictions based on the model code PACE. A detailed study on the angular distribution of target-like and projectile-like fragments may provide important additional information on incomplete-fusion reaction dynamics. However, particle-gamma coincidence studies can further provide deeper insight into the underlying mechanism.

The authors are thankful to the Director of IUAC, New Delhi for extending experimental facilities. They are also thankful to Dr. R.K. Bhaumik, Dr. S. Muralithar and Dr. R.P. Singh for their support during the experiments and several scientific discussions. One of the authors (PPS) thanks IUAC New Delhi, for support and hospitality. The authors are also thankful to the Chairman of the Department of Physics, AMU, for providing all the necessary facilities.

References

1. F. Schussler, H. Nifenecker, B. Jakobsson, V. Kopljar, K. Soderstrom, S. Leray, C. Ngo, S. Souza, J.P. Bondorf, K. Sneppen, Nucl. Phys. A **584**, 704 (1995).
2. E. Gadioli, C. Brattari, M. Cavinato, E. Fabrici, E. Gadioli Erba, V. Allori, A. Di. Filippo, S. Vailati, T.G. Stevens, S.H. Connell, J.P.F. Sellschop, F.M. Nortier, G.F. Steyn, C. Marchetta, Nucl. Phys. A **641**, 271 (1998).
3. P. Vergani, E. Gadioli, E. Vaciago, E. Fabrici, E. Gadioli Erba, M. Galmarini, G. Ciavola, C. Marchetta, Phys. Rev. C **48**, 1815 (1993).
4. Ch. Ngo, Prog. Part. Nucl. Phys. **16**, 139 (1985).
5. R.H. Siemssen, Nucl. Phys. A **400**, 245 (1983).
6. D.J. Parker, J. Asher, T.W. Conlon, I. Naqib, Phys. Rev. C **30**, 143 (1984).
7. W.J. Kox, A.R. Quinton, C.E. Anderson, Phys. Rev. **120**, 2120 (1960).
8. D.R. Zolnowski, H. Yamada, S.E. Cala, A.C. Kahler, T.T. Sugihara, Phys. Rev. Lett. **41**, 92 (1978).
9. H. Freiesleben, H.C. Britt, J. Birkelund, J.R. Huizenga, Phys. Rev. C **10**, 245 (1974).
10. H.C. Britt, A.R. Quinton, Phys. Rev. **124**, 877 (1961).
11. T. Inamura, M. Ishihara, T. Fukuda, T. Shimoda, H. Hiruta, Phys. Lett. B **68**, 51 (1977).
12. H.M. Morgenstern, W. Bohne, W. Galster, K. Grabisch, Phys. Rev. Lett. **52**, 1104 (1984).
13. H. Morgenstern, W. Bohne, K. Grabisch, H. Lehr, W. Stoffler, Z. Phys. A **313**, 39 (1983).
14. H. Morgenstern, W. Bohne, W. Galster, K. Grabisch, Phys. Rev. Lett. **52**, 1104 (1984).
15. H. Morgenstern, W. Bohne, K. Grabisch, D.G. Kovar, H. Lehr, Phys. Lett. B **113**, 463 (1982).
16. T. Udagawa, T. Tamura, Phys. Rev. Lett. **45**, 1311 (1980).
17. J. Wilczynski, K. Siwek-Wilczynaski, J. Van Driel, S. Gonggrijp, D.C.J.M. Hageman, R.V.F. Janssens, J. Lukasiak, R.H. Siemssen, S.Y. Van der Werf, Nucl. Phys. A **373**, 109 (1982).
18. J.P. Bondrof *et al.*, Nucl. Phys. A **333**, 285 (1980).
19. M. Blann *et al.*, Phys. Rev. C **31**, 1285 (1985).
20. W. Trautmann, Ole Hansen, H. Tricire, W. Hering, R. Ritzka, W. Trombik, Phys. Rev. Lett. **53**, 1630 (1984).
21. T. Inamura, T. Kjima, T. Nomura, T. Sugitate, H. Utsunomiya, Phys. Lett. B **84**, 71 (1982).
22. T. Inamura, A.C. Kahler, D.R. Zolnowski, U. Garg, T.T. Sugihara, M. Wakai, Phys. Rev. C **32**, 1539 (1985).
23. M.C. Mermaz, R. Dayras, J. Barette, B. Berthier, D.M. De Castro Rizzo, O. Cisse, R. Legrain, A. Pagano, E. Plollaco, H. Delgrage, W. Mitting, B. Hausch, G. Langano, A. Palmeri, Nucl. Phys. A **441**, 129 (1985).
24. D.J. Parker, J.J. Hogan, J. Asher, Phys. Rev. C **35**, 161 (1987).
25. Manoj K. Sharma *et al.*, Nucl. Phys. A **776**, 83 (2006).
26. Sunita Gupta *et al.*, Phys. Rev. C **61**, 64613 (2000).
27. D. Hojman, M.A. Cardona, A. Arazi, O.A. Capurro, J.O. Fernandez-Niello, G.V. Marti, A.J. Pacheco, J.E. Testoni, D. Bazzacco, A. Burlon, J. Davidson, M. Davidson, G. de Angelis, M. De Poli, M.E. Debray, A. Dadea, A.J. Kreiner, S.M. Lenzi, S. Lunardi, N.H. Medina, D.R. Napoli, C. Rossi Alvarez, C. Ur, Phys. C **74**, 044604 (2006).
28. M. Crippa, E. Gadioli, P. Vergani, G. Ciavola, C. Marchetta, M. Bonardi, Z. Phys. A **350**, 121 (1994).
29. P. Walker, G. Dracoulis, Nature (London) **399**, 35 (1999).
30. S.M. Mullins *et al.*, Phys. Lett. B **393**, 279 (1997).
31. M. Kaci *et al.*, Phys. Rev. C **56**, R600 (1997).
32. Sunita Gupta, B.P. Singh, M.M. Musthafa, H.D. Bhardwaj, R. Prasad, Phys. Rev. C **62**, 006743 (2000).
33. Sunita Gupta, B.P. Singh, M.M. Musthafa, H.D. Bhardwaj, Manoj Kumar Sharma, R. Prasad, A.K. Sinha, J. Phys. Soc. Jpn. **62**, 2434 (2002).

34. Manoj Kumar Sharma, B.P. Singh, Sunita Gupta, M.M. Musthafa, H.D. Bhardwaj, R. Prasad, A.K. Sinha, J. Phys. Soc. Jpn. **72**, 1917 (2003).
35. Manoj Kumar Sharma, Unnati, B.K. Sharma, B.P. Singh, H.D. Bhardwaj, Rakesh Kumar, K.S. Golda, R. Prasad, Phys. Rev. C **70**, 044606 (2004).
36. Pushpendra P. Singh, B.P. Singh, Manoj Kumar Sharma, Unnati, Devendra P. Singh, Rakesh Kumar, K.S. Golda, R. Prasad, submitted to Phys. Rev. C (2007).
37. E. Browne, R.B. Firestone, *Table of Radioactive Isotopes* (Wiley, New York, 1986).
38. Pushpendra P. Singh, M. Phil. Dissertation, A.M. University, Aligarh, India (2005) unpublished.
39. G.N. Simonoff, J.M. Alexander, Phys. Rev. B **133**, 104 (1964).
40. D.J. Parker, P. Vergani, E. Gadioli, J.J. Hogan, F. Verttore, E. Gadioli-Erba, E. Fabrici, M. Galmarini, Phys. Rev. C **44**, 1528 (1991).

International Journal of Modern Physics E
Vol. 17, No. 3 (2008) 549–566

World Scientific
www.worldscientific.com

PRODUCTION OF FISSION-LIKE EVENTS AFTER COMPLETE AND/OR INCOMPLETE FUSION OF ^{16}O WITH ^{159}Tb AND ^{169}Tm AT E/A $\approx$ 6 MeV

PUSHPENDRA P. SINGH*, B. P. SINGH†, BHAVNA SHARMA, UNNATI, MANOJ K. SHARMA and R. PRASAD

Department of Physics, A. M. University, Aligarh(UP)-202 002, India
**pushpendrapsingh@gmail.com*
†bpsinghamu@gmail.com

RAKESH KUMAR

Inter-University Accelerator Center, P. O. Box No. 10502, New Delhi-110 067, India

H. D. BHARDWAJ

Department of Physics, D. S. N. College, Unnao(UP)-209 801, India

Received 26 January 2007

With a view to study heavy-ion induced fission after complete and/or incomplete fusion reactions, experiments have been performed at the Inter-University Accelerator Center (IUAC), New Delhi, India. The production cross-sections for more than 40 fission-like events ($25 \leq Z \leq 45$) produced in $^{16}O + ^{159}Tb$ and $^{16}O + ^{169}Tm$ systems, respectively, at $E/A = 5.6$ and 5.9 MeV have been measured using the recoil-catcher technique followed by off-line γ-spectroscopy. The analysis of the data indicates that fission is one of the competing modes of de-excitation of excited composite system formed via complete and/or incomplete fusion processes, where the evaporation of light nuclear particle(s) are more likely to be expected. Attempts have also been made to study isotopic yield distributions of Yttrium (^{83,84m,85,87m}Y) and Strontium (^{80,81,83,85m}Sr) isotopes in $^{16}O + ^{159}Tb$ system, and Indium (^{105,107,108,110}In) and Technetium (^{99m,101,104,105}Tc) isotopes in $^{16}O + ^{169}Tm$ system. The statistical analysis of the isotopic yield distribution has also been carried out to determine the most probable values of mass and charge of fission-like events in two systems.

Keywords: Activation technique; off-line γ-spectrometry; complete and/or incomplete fusion; fission-like events; $^{16}O + ^{159}Tb$ and $^{16}O + ^{169}Tm$ systems; isotopic yield distribution; $E/A = 5.6$ and 5.9 MeV.

1. Introduction

The dynamics of heavy ion interaction leading to the production of fission-like events at intermediate energies has been a topic of current interest during the last few years. The heavy ion (HI) induced reactions are widely different from light ion induced reactions because of the fact that both projectile and target are

many nucleon systems, consequently they have large natural electrostatic repulsion (Coulomb barrier) between interacting partners. The input angular momentum (ℓ) of HIs with respect to the center of mass is very large and therefore it is possible to produce nuclei with high excitation energy and high spins. Since the de-Broglie wavelength of incident HI's is very small i.e. of the order of nuclear dimensions, therefore, the interaction shows the semi-classical features and hence, the motion of the incident ions may be treated semi-classically. The classical trajectories of a projectile leading to the different reaction processes may be classified on the basis of impact parameter. At low energies, the projectile interacts only through the Coulomb field at very large impact parameter and leads to the *distant collision*. If the impact parameter is comparable to the sum of radii of interacting partners, *grazing collision* takes place and the projectile can be elastically or inelastically scattered.[1] Moreover, when the projectile interacts with the target nucleus at relatively high bombarding energy, just enough to enter in the nuclear range of target nucleus, then *deep inelastic collision* (*DIC*) dominates.[2,3] In such a case, the nuclear densities rise very rapidly in the surface region, and a few nucleons may get transferred from projectile to target nucleus. If the projectile interacts with the target nucleus very strongly at still smaller values of impact parameter, it may give rise to phenomena like (a) Fusion: complete fusion (CF) and/or incomplete fusion (ICF). The CF and ICF processes may be classified on the basis of input angular momentum multiplicity. In case of CF, with the collision trajectories $\ell \leq \ell_{\text{crit}}$, the interacting partners may be trapped in the pocket of entrance channel potential, and hence entire mass of the projectile fuses with the target nucleus leading to the formation of excited composite system.[4] The total kinetic energy and linear momentum of the projectile are shared among all the constituents of the composite system leading to the fully equilibrated compound nucleus. For collision trajectories with $\ell \geq \ell_{\text{crit}}$, the pocket in the entrance channel potential vanishes, and therefore such trajectories leads to the fusion incompleteness, i.e. the nuclear field is no longer strong enough to trap all the nucleons with target nucleus, as a consequence, fractional momentum transfer takes place. In such a case, the incident projectile is assumed to break-up into fragments in the presence of nuclear field of target nucleus. One of the fragments may fuse with target nucleus leading to the formation of excited incompletely fused composite system and the remnant may be assumed to traverse along the beam direction with almost the same velocity as that of incident projectile without any significant interaction[5–9] with the target nucleus, and (b) Fusion-Fission: The main assumption of this process is that with CF and/or ICF of projectile, the resultant composite system attains thermodynamical equilibrium and proceeds towards fission, depending on the available excitation energy and entrance channel mass asymmetry.[10,11] This may be explained as a result of gradual decrease of shell effects with increasing excitation energy of the composite system. The final reaction products may come into picture after emission of few nucleons and characteristic γ-radiations from fission-like events.[12–15]

The production cross-sections measurement of such reaction residues in heavy ion HI interactions have been extensively carried out during the last few years and a large amount of experimental data for various fissioning systems has been generated, leading to the development of various nuclear models.[16–19] Even after considerable progress, the comprehensive understanding of reaction dynamics of HI interaction in general, and below the actinide region in particular, is still lacking. HI's have been used as projectile to study the spliting of excited composite system leading to the production of fission-like events over a wide range of fissility (Z^2/A), excitation energy and entrance channel angular momentum.[20–23] Studies on the effect of excitation energy and angular momentum on various fission observables have provided deeper insight into the nuclear reaction dynamics. Most of the investigators have concentrated on few nuclei e.g. on ^{235}U and ^{239}Pu, to produce a tremendous amount of high precision data necessary for the technical application in nuclear reactors and/or in nuclear weapons.[24] The development of future nuclear power energetics with applications of hybrid technologies using accelerator based incineration system requires a knowledge of cross-sections of such nuclear reaction products in a wide range of projectile-target combinations. However, more experimental data is also required to determine optimum irradiation conditions for producing radioactive isotopes of interest. The cross-section data of such products are also in demand for the production of specific radioactive ion beams (RIBs) and is a key parameter for the development of recently proposed Accelerator Driven Sub-critical (ADS) reactor system, popularly known as energy amplifiers.[25]

Nishio *et al.*[26] have also shown that fission of incompletely fused composite nucleus is one of the dominant processes other than fission of compound nucleus at intermediate energies. This study showed that several reaction channels open-up at medium bombarding energies $E/A \geq 8$ MeV. In the present work, it is exciting to observe fission-like events in CF and ICF of a projectile at $E/A \approx 6$ MeV. The experimental data for such fusion-fission reactions in HI interaction is still limited and a comprehensive understanding of HI induced fission at medium energies is still lacking. As such, in order to measure the production cross-sections of radio-nuclides produced in HI interaction, a program of precise measurements and analysis of Excitation Functions (EFs), Recoil Range Distributions (RRDs), Angular Distribution (ADs) and charge and mass-distribution of fission-like events in HI induced reactions have been undertaken by our group.[27–30] In the present work, the production cross-sections for 46 fission-like events, which are expected to be formed via the process of fission in ^{16}O + ^{159}Tb and ^{16}O + ^{169}Tm systems at energies, respectively, $E/A \approx 5.6$ and 5.9 MeV have been measured. In our earlier reports, the cross-sections for a large number of residues populated via CF and/or ICF in these systems have already been presented over a wide energy range.[31,32] Present work has indicated that the radionuclides expected to be populated via the process of fission may be the admixture of fission after CF and/or fission after ICF processes. As such, an attempt has also been made to study the isotopic yield distribution of Yttrium (Y) and Strontium (Sr) isotopes populated in ^{16}O + ^{159}Tb

system and Technetium (Tc) and Indium (In) isotopes populated in $^{16}O + ^{169}Tm$. To the best of our knowledge these measurements have been performed for the first time. The out line of the present paper can be summerised as follows. In Sec. 2 the experimental procedure is briefly discussed, while Sec. 3 and 4 deals with the reaction product identification and measurements, respectively. The results and discussion, summary and conclusions are given in Sec. 5 and 6 of the paper respectively.

2. Experimental Procedure

The present work has been carried out using a $^{16}O^{7+}$ beam from 15-UD Pelletron accelerator of the Inter-University Accelerator Center (IUAC), New Delhi, India. The details like target preparation, irradiation of samples, post-irradiation analysis etc. are given in the following subsections.

2.1. *Sample preparation and irradiation*

The sample of ^{159}Tb (99.99%) used in the present measurements was a self supporting foil, prepared by rolling method. The ^{169}Tm (100%) sample was prepared on Al-backing by vacuum-evaporation technique. The thickness of each sample was measured by α-transmission method, in which 5.487 MeV α-particles obtained from ^{241}Am source were allowed to pass through the samples to estimate the energy loss per unit path length while traversing the sample material. The thicknesses of Tb and Tm samples were, respectively, ≈ 1.8 mg/cm^2 and ≈ 0.6 mg/cm^2. The thicknesses of Al-backing used for Tb sample was ≈ 2 mg/cm^2, and for Tm samples it was ≈ 1.5 mg/cm^2, which served as energy degrader as well as catcher foils during the irradiation. The samples were cut into the size of 1.2×1.2 cm^2 and were pasted on Al-holder having concentric hole of 1.0 cm diameter. The Al-holder was used for rapid dissipation of heat produced during the irradiation.

The irradiations were carried out in the General Purpose Scattering Chamber (GPSC) of 1.5 m diameter having In-vacuum Transfer Facility (ITF). The main advantage of ITF is that, one can replace the sample without disturbing the vacuum of the chamber, so that the delay-time between the stop of irradiation and beginning of the counting may be minimized. The samples of ^{159}Tb and ^{169}Tm along with appropriate catcher foils were irradiated by $^{16}O^{7+}$ beam at $E/A \approx 5.6$ and 5.9 MeV, respectively, with beam current $\approx$30 and 50 nA. The samples along with Al-catcher foils were placed normal to the beam direction with sample material facing the beam so that the recoiling reaction products may be trapped in the catcher foil thickness. Keeping in view the half-lives of the interest, the irradiations were carried out for $\approx$8 h duration for each projectile-target combination. The beam flux was monitored using an ORTEC current integrator device by taking into account the charge collected in the Faraday cup placed behind the target-catcher foil assembly.

2.2. *Post irradiation analysis*

After irradiation, the targets along with catcher foils were taken out from the GPSC employing ITF assembly. The activities induced in the target-catcher foil assembly were followed by off-line γ-spectrometry. A pre-calibrated High Purity Germanium (HPGe) γ-ray spectrometer of 100 c.c. active volume coupled to a PC through CAMAC based FREEDOM software[34] has been used for off-line counting. The calibration of spectrometer has been done using standard γ-radiation sources of known strengths like ^{60}Co, ^{137}Cs, ^{152}Eu etc., which emit γ-rays over a wide range of energies. The geometry dependent efficiency (G_ε) of HPGe detector at a given energy was estimated for efficiency correction in the observed spectra. Furthermore, the spectrometer resolution was $\approx$2 keV for 1.33 MeV γ-ray of ^{60}Co source. In the present work, the standard γ-sources and irradiated target-catcher foil assemblies were counted in the same geometry in order to avoid the solid angle effect during the counting. Attention was paid to keep the dead time of the detector less then 10% by suitably adjusting the source-detector separations.

3. Reaction Product Identification

As already mentioned the induced activities in the target-catcher foil assemblies have been followed by off-line γ-spectroscopy and the γ-ray spectra were recorded at increasing times, keeping in view the decay curve analysis for reaction products identification. A typical γ-ray spectra along with some of the assigned residues populated in $^{16}O^{7+}$ induced reactions on ^{159}Tb and ^{169}Tm at, respectively, $E/A = 5.6$ and 5.9 MeV are shown in Figs. 1 and 2. The radio-nuclides populated via CF and

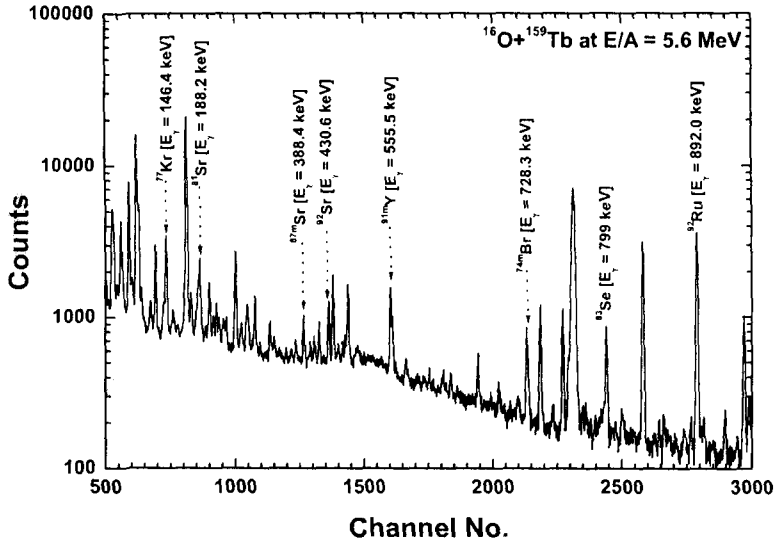

Fig. 1. Typical γ-ray spectrum in $^{16}O + ^{159}$Tb system at $E/A = 5.6$ MeV, indicating the different reaction products.

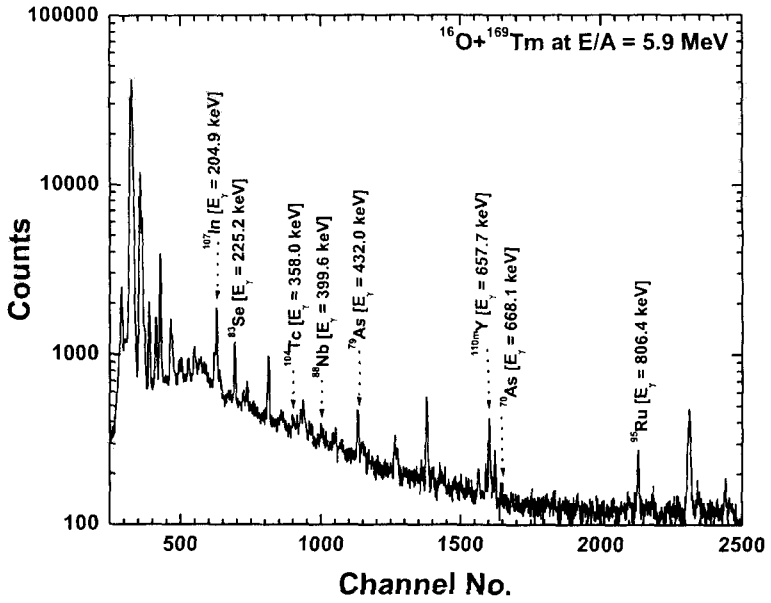

Fig. 2. Typical γ-ray spectrum in $^{16}O + ^{169}Tm$ system at E/A = 5.9 MeV, indicating the different reaction products.

Table 1 List of the residues populated via CF and/or ICF of ^{16}O with ^{159}Tb (taken from the Ref. 28).

S. No.	Nuclide (channel)	σ_{EXP}
1.	^{172}Ta $(3n)$	11 ± 2.4
2.	^{171}Ta $(4n)$	228 ± 39.2
3.	^{170}Ta $(5n)$	263 ± 38.74
4.	^{171}Hf $(p3n)$	340 ± 73.5
5.	^{170g}Hf $(p4n)$	574 ± 68.8
6.	^{171}Lu $(2p2n)^a$	611 ± 64.0
7.	^{170}Lu $(\alpha n)^a$	31 ± 5.44
8.	^{169}Lu $(\alpha 2n)^a$	80 ± 9.45
9.	^{165}Tm $(2\alpha 2n)^a$	10 ± 1.3

[a]Populated via CF and/or ICF.

ICF may de-excite by the evaporation of nuclear particles and/or characteristic γ-radiations, and also by the process of fission. As can be seen from the spectra given in Figs. 2 and 3, different peaks in the spectrum have been assigned to the several radionuclides populated via fusion(CF and/or ICF)-fission reactions. In order to determine the production cross-sections of these residues, first of all it is desirable to identify them. In order to identify the various residues, the preliminary analysis was performed by identifying their characteristic γ-rays in the spectra which have been recorded with increasing time. This is a very specific way for the identification

T-6308

Table 2. List of the residues populated via CF and/or ICF of ^{16}O with ^{169}Tm (taken from the Ref. 29).

S. No.	Nuclide (channel)	σ_{EXP}
1.	^{182}Ir $(3n)$	8 ± 1.4
2.	^{181}Ir $(4n)$	183 ± 27.2
3.	^{182}Os $(p2n)$	18 ± 3.7
4.	^{181g}Os $(p3n)$	173 ± 22.8
5.	^{181}Re $(2p2n)^a$	441 ± 66.9
6.	^{178}Re $(\alpha 3n)^a$	34 ± 5.5
7.	^{175}Hf $(2\alpha pn)^a$	4 ± 0.6
8.	^{172}Lu $(3\alpha n)^a$	28 ± 3.3

[a]Populated via CF and/or ICF.

Table 3. List of identified fission-like events produced in $^{16}O + ^{159}Tb$ system along with their spectroscopic properties.

S. No.	Nuclide	J_π	half-life	E_γ(keV)	$a_\gamma(\%)$*
1.	^{77}Kr	5/2+	1.24 h	146.4	37.6
2.	^{84m}Y	1−	40 m	1039.8	45.2
3.	^{85m}Sr	1/2−	67.6 m	151.1	12.4
4.	^{75}Br	3/2−	1.61 h	427	4.5
5.	^{104}Tc	3+	18.3 m	535.0	13.1
6.	^{83}Y	7+	3.19 h	479.4	91.0
7.	^{85}Y	9/2+	49.7 m	555.5	94.90
8.	^{87m}Y	1/2−	10.3 m	432.3	2.0
9.	^{81}Sr	1/2−	22.15 m	188.2	16.0
10.	^{80}Sr	1/2−	2.79 h	388.4	82.3
11.	^{83}Sr	0+	2.71 h	430.6	3.33
12.	^{74m}Br	4+	46 m	728.3	35
13.	^{83}Se	9/2+	22.3 m	799	31.9
14.	^{88}Kr	0+	2.84 h	834.8	13
15.	^{94}Ru	0+	51.8 m	892.0	25
16.	^{102}Ag	5+	12.9 m	964.2	1.4
17.	^{95}Ru	5/2+	1.64 h	1178	5.2
18.	^{79}Rb	5/2+	22.9 m	1184	0.249
19.	^{87}Zr	9/2+	1.68 h	1227	100
20.	^{110}In	7+	4.9 h	1305.2	0.34
21.	^{78}As	2−	90.7 m	1308.7	12.4
22.	^{112}Ag	2−	3.13 h	1312	1.20

of reaction products, because each radio-active isotope has a unique decay mode. Thus, the observed intensity of the γ-ray of induced activity is a measure of the production cross-section of that particular reaction channel. Since there were several residues which may emit γ-rays of nearly same energy, the simple γ-ray energy identification may not be enough and hence, the intensity of the photo-peaks were plotted as a function of time to get the half-lives of the residues. The residues were identified not only by their characteristic γ-rays energies but also by the analysis of decay curves. From the analysis of spectra and decay-curves, the identified reaction

Table 4. List of identified fission-like events produced in $^{16}O + ^{169}Tm$ system along with their spectroscopic properties.

S. No.	Nuclide	J_π	half-life	E_γ(keV)	a_γ(%)*
1.	^{107}In	9/2+	32.4 m	204.9	48
2.	^{66}Ge	0+	2.26 h	108.8	10.5
3.	^{88}Nb	8+	14.3 m	399.6	31
4.	^{95}Y	1/2−	10.3 m	954.1	19
5.	^{83}Se	9/2+	22.3 m	225.2	31.9
6.	^{99m}Tc	7/2+	7.2 m	319.2	0.9
7.	^{109}Sn	5/2+	18.0 m	331.0	9.7
8.	^{105}Tc	9/2+	11.1 m	667.3	9.7
9.	^{79}As	3/2−	9.0 m	432.0	1.50
10.	^{105}In	9/2+	5.0 m	131.4	100
11.	^{108m}Rh	5+	6.0 m	433.9	43
12.	^{95}Ru	5/2+	1.64 h	806.4	4.09
13.	^{92}Y	2−	3.54 h	448.5	2.34
14.	^{98m}Nb	5+	51.3 m	787.3	93
15.	^{87}Kr	5/2+	1.27 h	402.6	49.6
16.	^{92}Sr	0+	2.71 h	953.4	3.6
17.	^{101}Tc	9/2+	14.0 m	127.2	2.86
18.	^{78}Ge	0+	1.4 h	293.9	4
19.	^{110m}In	2+	69.1 m	657.7	98
20.	^{104}Tc	3+	18.0 m	358.0	79
21.	^{115}Ag	1/2−	20.0 m	131.4	2.9
22.	^{70}As	4+	52.6 m	668.1	21.2
23.	^{112}Ag	2−	3.13 h	617.4	43.4
24.	^{108m}In	7+	58.0 m	242.7	38

products have been found to have almost half the charge and mass as compared to the composite system populated via CF and/or ICF of the projectile. As such, the reaction products cannot be considered as target and/or projectile-like fragments. It is more convenient to explain them as fission-like events expected to be produced as a consequence of fusion (CF and/or ICF)-fission reaction channel. Furthermore, the radionuclides populated via CF and/or ICF of ^{16}O with ^{159}Tb and ^{169}Tm at the given energies are tabulated in Tables 1 and 2 with their production cross-sections.[31,32] These nuclides are assumed to split up leading to the formation of fission-like events. The list of identified fission-like events along with their spectroscopic properties are given in the Tables 3 and 4. The nuclear data of radionuclides which have been used in the analysis are taken from the Table of Isotopes.[36]

4. Measurements

The intensities of characteristic γ-lines have been used to determine the production cross-sections of different fission-like events, using a FORTRAN programme EXP-SIGMA based on the following formulation,[35]

$$\sigma_r = \frac{C_{t=0}}{N_0 \theta \phi G_\varepsilon K[1 - \exp(-\lambda t_1)]} \tag{1}$$

where
$C_{t=0}$ = The count rate just after the irradiation, i.e. at zero time,
N_0 = Initial number of nuclei in the target,
θ = Branching ratio of the characteristic γ-rays,
ϕ = Flux of the incident beam,
G_ϵ = Geometry dependent efficiency of the spectrometer,
$K=[1-\exp(-\mu d)]/\mu d$ = The self absorption correction factor for the γ-ray in the material of the sample of thickness $d\,(\mathrm{gm/cm^2})$ and the absorption coefficient $\mu\,(\mathrm{cm^2/gm})$
λ = Decay constant of the radionuclides, and
t_1 = Time of irradiation.

As has already been mentioned, the CF and ICF reaction products may undergo fission. The production cross-sections for a large number of fission-like events ($25 \leq$

Table 5. Cumulative (C) and independent (I) production cross-sections of fission like events produced in E/A = 5.6 MeV ^{16}O induced fusion-fission reaction with ^{159}Tb.

S. No.	Nuclide	σ(mb)	S. No.	Nuclide	σ(mb)
1.	^{77}Kr	16 ± 1.8(I)	12.	^{74m}Br	67 ± 3.46(I)
2.	^{84m}Y	25 ± 3.13(I)	13.	^{83}Se	2 ± 0.4(I)
3.	^{80}Sr	0.89 ± 0.14(I)	14.	^{88}Kr	24 ± 2.13(I)
4.	^{75}Br	15 ± 2.56(I)	15.	^{94}Ru	1.6 ± 0.1(I)
5.	^{104}Tc	24.4 ± 3.27(I)	16.	^{102}Ag	46 ± 6.24(I)
6.	^{83}Y	2 ± 0.29(I)	17.	^{95}Ru	19 ± 2.1(I)
7.	^{85}Y	45 ± 4.71(I)	18.	^{79}Rb	6 ± 0.64(I)
8.	^{87m}Y	3 ± 0.4(C)	19.	^{87}Zr	3.9 ± 0.69(I)
9.	^{81}Sr	7 ± 0.9(I)	20.	^{110}In	4.6 ± 0.28(C)
10.	^{83}Sr	25 ± 2.77(I)	21.	^{78}As	3.8 ± 0.4(C)
11.	^{85m}Sr	1.5 ± 0.17(C)	22.	^{112}Ag	11.4 ± 1.4(I)

Table 6. Cumulative (C) and independent (I) production cross-sections of fission like events produced in E/A = 5.9 MeV ^{16}O induced fusion-fission reaction with ^{169}Tm.

S. No.	Nuclide	σ(mb)	S. No.	Nuclide	σ(mb)
1.	^{107}In	19 ± 1.96(I)	13.	^{92}Y	30 ± 3.46(I)
2.	^{66}Ge	4 ± 0.69(I)	14.	^{98m}Nb	13 ± 1.46(I)
3.	^{88}Nb	26 ± 3.78(I)	15.	^{87}Kr	2 ± 0.13(I)
4.	^{95}Y	58 ± 3.46(C)	16.	^{92}Sr	28 ± 2.62(C)
5.	^{83}Se	11 ± 2.19(I)	17.	^{105}Tc	7 ± 1.01(I)
6.	^{99m}Tc	4 ± 0.41(I)	18.	^{78}Ge	33 ± 4.19(I)
7.	^{109}Sn	29 ± 2.58(I)	19.	^{110}In	5 ± 0.81
8.	^{101}Tc	28 ± 2.67(C)	20.	^{104}Tc	14 ± 1.79(I)
9.	^{79}As	75 ± 4.99(C)	21.	^{115}Ag	48 ± 2.49(C)
10.	^{105}In	2 ± 0.36(C)	22.	^{70}As	33 ± 2.34(C)
11.	^{108m}Rh	20 ± 1.57(C)	23.	^{112}Ag	69 ± 3.39
12.	^{95}Ru	83 ± 4.61(I)	24.	^{108}In	26 ± 2.52(I)

$Z \leq 45$) have been measured at given energies in $^{16}O + ^{159}Tb$ and $^{16}O + ^{159}Tm$ systems and are listed in the Tables 5 and 6, respectively. Furthermore, the errors mentioned in the cross-sections are the statistical errors of γ-ray counting. The errors in the cross-sections may come up mainly due to:

(i) Non-uniform thickness of the sample and inaccurate estimate of foil thickness may lead to uncertainty in the determination of the number of target nuclei in the sample. To check the uniformity of the sample, thickness of the sample was measured at different positions by α-transmission method. It is estimated that the error in the thickness of the sample material is expected to be less than 1%.
(ii) Fluctuations in the beam current may result in the variation of incident flux.
(iii) Uncertainty in the determination of geometry dependent spectrometer efficiency. The error in the efficiency determination due to the statistical fluctuations in counts is estimated to be less than 2%.
(iv) The beam intensity loss as the beam traverses the target catcher foil assembly.
(v) The losses of product nuclei recoiling out of the target may introduce large errors in the measured cross-sections. The thickness of the catcher foil was sufficient to stop even the most energetic residues, however, in the present measurements, both the sample and the catcher foils were counted together and hence the losses due to the recoiling of nuclei is avoided.
(vi) Dead time of the spectrometer was kept at less than 10% by suitably adjusting sample-detector distance. These errors exclude the uncertainty of the nuclear data like branching ratio, decay constant etc., which have been taken from the Table of Isotopes.[36]

5. Results and Discussion

5.1. $^{16}O + ^{159}Tb$ *system*

As reported in our earlier publication,[31] the most dominant CF and/or ICF reaction products are $^{170,171,172}Ta$, $^{170g,171}Hf$, $^{169,170,171}Lu$ and ^{165}Tm populated in the interaction of ^{16}O with ^{159}Tb at the given energy. As a typical example, the reaction products $^{170,171,172}Ta$ expected to be formed via CF of ^{16}O with ^{159}Tb leading to the formation of excited composite system $^{175}Ta^*$ which may decay by xn-channels ($x = 5, 4, 3$), leaving behind the above residues. While, the residues $^{170g,171}Hf$ expected to be populated via pxn-channels (4, 3). Furthermore, the residues $^{169,170,171}Lu$ and ^{165}Tm are expected to be populated via both CF and/or ICF ^{16}O, in which one of the fragments (say) ^{12}C fuses with ^{159}Tb nucleus, forming an incompletely fused composite system $^{171}Lu^*$ (or, the residues ^{171}Lu may be populated via emission of $2p2n$ from ^{159}Tb), which may decay by the emission of one neutron forming ^{170}Lu and two neutrons forming ^{169}Lu. Similarly, the reaction product ^{165}Tm is expected to be populated via $2\alpha 2n$ channel and/or ICF (fusion of ^{12}C with ^{159}Tb and/or ^{8}Be) followed by subsequent emission of light nuclear

particles from ^{171}Lu* and ^{167}Tm* composite systems. The remnant (^{4}He or ^{8}Be) of the incident ion is assumed to go on moving with beam velocity in a forward direction without any significant interaction with target nucleus. Furthermore, in the present work, the residues which are expected to be populated via CF and/or ICF, are assumed to undergo fission and give rise to fission-like events after emission of few nucleons and characterisitic γ-radiations. Therefore, attention has been paid to identify the fission-like events after CF and/or ICF processes. A list of fission-like events formed as a consequence of fission after CF and/or ICF, along with their spectroscopic properties, which have been assinged to be produced in ^{16}O + ^{159}Tb interactions at E/A = 5.6 MeV, as is already given in Table 3. The measured production cross-sections for these residues are given in Table 5.

5.2. ^{16}O + ^{169}Tm *system*

In ^{16}O + ^{169}Tm system at E/A = 5.9 MeV,[32] the main reaction residues are ^{181,182}Ir, ^{181g,182}Os ^{178,181}Re, ^{175}Hf and ^{172}Lu, expected to be populated via CF and/or ICF of ^{16}O with ^{169}Tm. The residues ^{181,182}Ir are populated via emission four and three neutrons, ^{181g,182}Os formed after subsequent emission of three and two neutrons along with one proton from excited completely fused composite system ^{185}Ir*. However, ^{178,181}Re, ^{175}Hf and ^{172}Lu are expected to be populated both via CF and/or ICF. As already indicated in the earlier section, the population of these ERs can be explained in terms of the break-up of ^{16}O into ^{12}C + ^{4}He and/or ^{8}Be + ^{8}Be and/or ^{4}He + ^{12}C followed by fusion of either fragment with ^{169}Tm nucleus forming an incompletely fused composite system ^{181}Re* or or^{173}Lu* in excited state. More than 20 fission-like events formed as a results of fusion (CF and/or ICF)-fission in this system have been identified and are given in Table 4 along with their spectroscopic properties. The production cross-sections of fission-like events have also been determined and are given in Table 6.

Furthermore, production cross-section for some of the fragments are substantially higher than expected at this energy. One of the possible reasons for the higher production cross-section values for fission-like events may be due to the fact that the fragments which are observed in these cases are populated from various decay chains and hence, they may have cumulative sum of cross-sections of these fragments. It should however be pointed out that in the present work the fission fragments which recoil in the backward direction are lost and no correction for this could be applied. However, if catcher foils are put at both sides of the target, then both the fragments of a particular fission event in forward as well as in backward directions may be trapped and identified. It is observed that, if activities of backward and forward catcher foils are measured then symmetric mass distribution is expected. As can be seen from Tables 5 and 6, the total production cross-section of fission-like events in ^{16}O + ^{159}Tb and ^{16}O + ^{169}Tb are found to be 353.69 mb and 667 mb respectively, which may be the indication of more fission-like events production possibility for mass assymmetric system.

Table 7. Comparison of isotopic yield distributions (σ_A^2) for different fissioning systems.

S. No.	System	E^*(MeV)	Element	σ_A^2
1.	$^{16}O + ^{159}Tb$[a]	57.1	Sr	3.31
2.	$^{16}O + ^{159}Tb$[a]	57.1	Y	4.41
3.	$^{16}O + ^{169}Tm$[a]	61.06	In	4.24
4.	$^{16}O + ^{169}Tm$[a]	61.06	Tc	4.62
5.	$^{7}Li + ^{232}Th^{43}$	41.7	Sb	4.08
6.	$^{7}Li + ^{232}Th^{43}$	41.7	I	3.96
7.	$^{11}B + ^{232}Th^{44}$	55.7	Sb	4.0
8.	$^{11}B + ^{232}Th^{44}$	55.7	I	5.43
9.	$^{11}B + ^{232}Th^{44}$	55.7	Cs	3.72
10.	$^{11}B + ^{238}U^{45}$	67.4	Rb	3.84 ± 0.16
11.	$^{11}B + ^{238}U^{45}$	67.4	Cs	3.95 ± 0.14
12.	$^{20}Ne + ^{238}U^{45}$	64.5	Rb	4.23 ± 0.40
13.	$^{20}Ne + ^{238}U^{45}$	64.5	Cs	4.26 ± 0.90

[a]Present work.

5.3. *Mass distribution of fission-like events*

Mass distribution is one of the important experimental observables directly related to the collective dynamics of fission.[37,38] Figures 3 and 4 show the plot of experimentally determined production cross-sections of various fission-like events as a function of their mass numbers in $^{16}O + ^{159}Tb$ and $^{16}O + ^{169}Tm$ systems at $E/A = 5.6$ and 5.9 MeV, respectively. It is evident from these figures that the mass

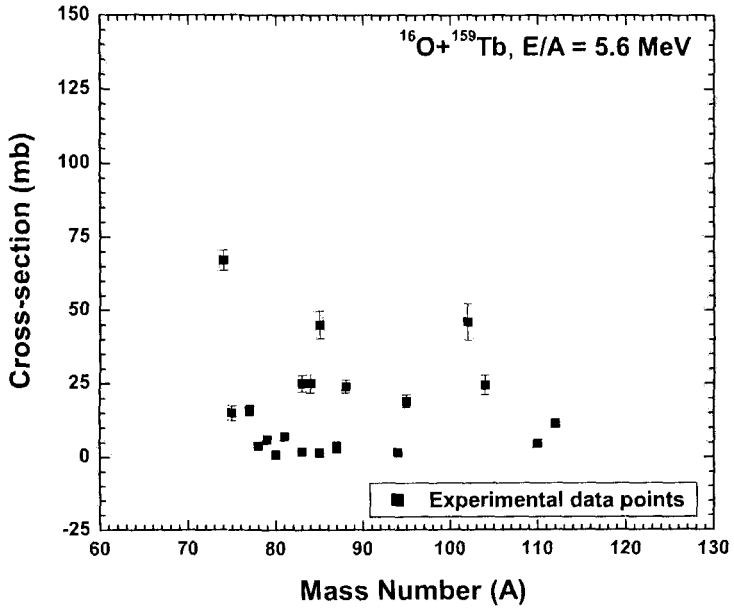

Fig. 3. Typical plot of production cross-sections as a function of mass numbers of fission-like events in $^{16}O + ^{159}Tb$ system at $E/A = 5.6$ MeV.

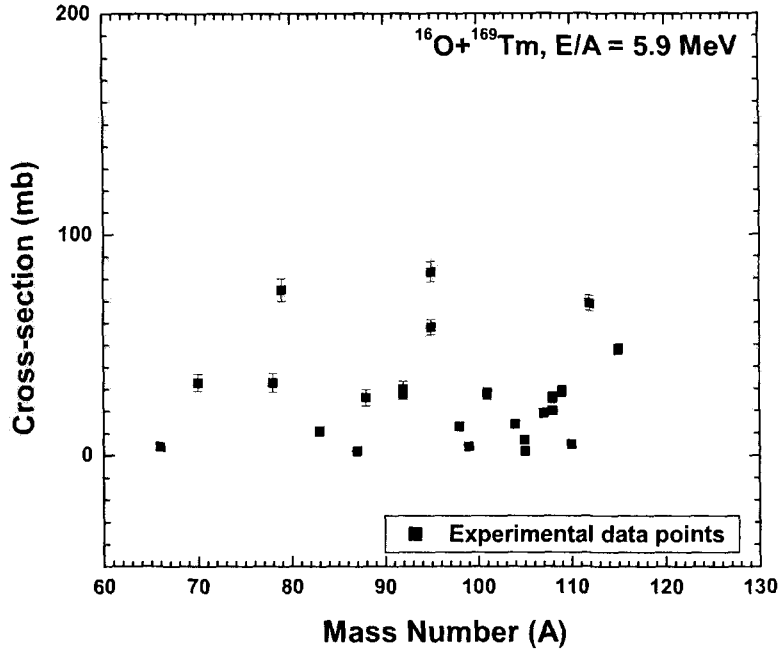

Fig. 4. Typical plot of production cross-sections as a function of mass numbers of fission-like events in $^{16}O + ^{169}Tm$ system at $E/A = 5.9$ MeV.

distribution have been found to be symmetric as expected at presently studied energies. The activities measured in the forward catcher foil were used for the mass distribution plots. As such, in order to obtain the mass distribution of fission-like events, the experimentally measured cross-sections have to be corrected for the charge distribution. In the present work, the compound nucleus populated via both channels (CF and/or ICF) for a given system is expected to be far away from the β-stability line, and therefore, the final fission-like events comes from the different decay chains. The yield of a particular mass chain $Y(A)$ is calculated from experimentally measured independent yield (Y_{IND}) or cumulative yield (Y_{CUM}) of the fission like event of mass A and atomic number Z using the following equations;[39]

$$Y(A) = Y_{IND}(A, Z)/Y_{FI}(A, Z) \tag{2}$$

$$Y(A) = Y_{CUM}(A, Z)/Y_{FC}(A, Z)\,. \tag{3}$$

Here $Y_{FI}(A, Z)$ and $Y_{FC}(A, Z)$ are, respectively, the fractional independent and cumulative yields, which are given by following Gaussian distribution equations;

$$Y_{FI}(A, Z) = \frac{1}{\sqrt{2\pi\sigma_Z^2}} \int_{Z-0.5}^{Z+0.5} e^{-(Z-Z_p)^2/2\sigma_Z^2} dZ \tag{4}$$

$$Y_{FC}(A, Z) = \frac{1}{\sqrt{2\pi\sigma_Z^2}} \int_{-\infty}^{Z+0.5} e^{-(Z-Z_p)^2/2\sigma_Z^2} dZ\,. \tag{5}$$

Here Z_p and σ_Z are, respectively, most probable charge and width parameter of isobaric yield distribution. Thus the calculation of mass yield for particular mass chain with mass number "A", from the experimentally measured yield of fission-like events require the value of Z_p and σ_Z. For independent measurements of yield at least three members in an isobaric chain are required to obtained the value of Z_p and σ_Z. Since it is difficult to measure three independent yields in an isobaric chain, an alternative approch may be used. In the present work, the isotopic yield distribution of fission-like events have been studied to estimate the charge distribution parameters.

The Z_p value for a perticular mass chain with mass number A may be calculated using unchanged charge distribution (UCD) hypothesis, as shown in the following formulation;[40,41]

$$Z_p(A) = \frac{A_p Z_{CN}}{A_{CN} - n_{\text{average}}} \tag{6}$$

where A_p is the most probable mass number for a given Z, A_{CN} and Z_{CN} is the mass and charge of CN and n_{average} is average number of fission neutrons. If A_p is the most probable mass of the isotopic yield distribution for a given Z then the the value of σ_A may be converted into σ_Z using following equation;[42]

$$\sigma_Z = \frac{\sigma_A \cdot Z}{A_p}. \tag{7}$$

The values of σ_Z are found to be 0.83 and 0.96, respectively for Y and Sr, while for In and Tc they are 0.96 and 0.90, respctively, calculated from the distribution parameters obtained from the experimental data. The details of how the width parameters σ_A and most probable mass A_p have been deduced is given in the Sec. 5.6.

5.4. *Isotopic yield distribution for Y, Sr, In and Tc isotopes*

In order to estimate width parameter for primary isotopic yield distribution, attempts have been made to study this distribution for different fission-like events in both systems. Some systematics have been used to find out the distribution parameters. The fission-like event of mass number A for fixed Z may be the result of the neutron evaporation from several reaction products of a decay chain. Thus, the total yield of decay chain $Y_T(A)$ may be expressed in terms of the corresponding evaporation residue yields $Y(A')$ using following equation;

$$Y_T(A) = \sum_{1}^{n} P_n Y(A') \tag{8}$$

where A' $(= A + n_{avr})$ is the mass number of evaporation residue emitting n number of neutrons leading to the final reaction product (fission-like event) with mass A, P_n is the probability of neutron emission by the evaporation residue with mass A'.

Assuming the Gaussian distribution for the evaporation residues, their production yield may be given as

$$Y(A') = \frac{Y_Z}{\sqrt{2\pi\sigma^2_{A'}}} e^{-(A'-A'_p)^2/2\sigma^2_{A'}} . \tag{9}$$

Here A'_p is the most probable mass, $\sigma^2_{A'}$ is the width parameter of the isotopic yield distribution and Y_Z is the elemental yield i.e. unchanged the neutron emission from evaporation residues. The total yield $Y_T(A)$ of corresponding decay chain may be obtained from the yield of evaporation residues $Y(A')$ using following equation;

$$Y^C(A) = \sum_{\nu=1}^{n} f_\nu \frac{Y_Z}{\sqrt{2\pi\sigma^2_{A'}}} e^{-(A'-A'_p)^2/2\sigma^2_{A'}} . \tag{10}$$

As already mentioned, the mean square deviation of the calculated isotopic yields $Y^C(A)$ from the experimentally determined production yields $Y^E(A)$ may be estimated by chi square fit and may be represented as follows;

$$\chi^2 = \frac{1}{m-p-1}\{Y^C_j(A) - Y^E_j(A)\}^2 . \tag{11}$$

The value of chi squire fit (χ^2) was minimized using a nonlinear least square fit routine, keeping the width parameter (σ'_A) and most probable mass (A'_p) of the evaporation residue as free parameters using ORIGIN software.

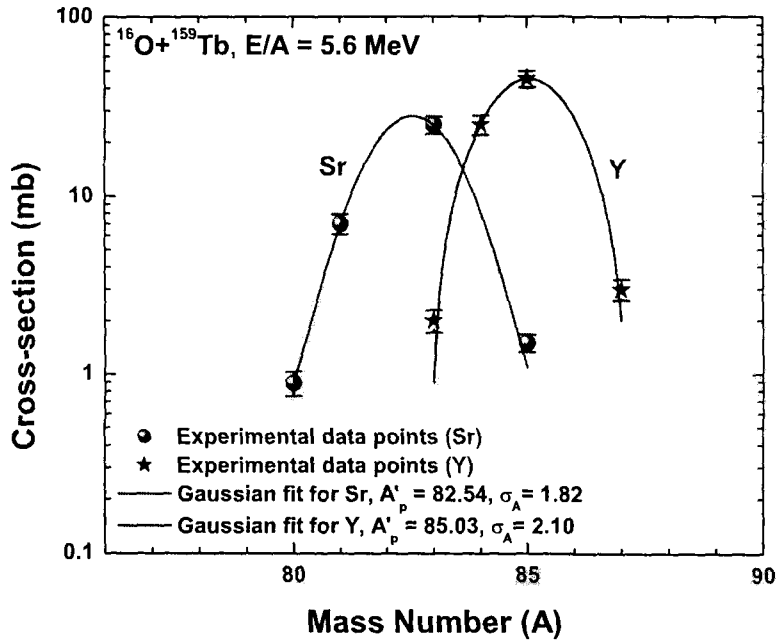

Fig. 5. Isotopic yield distributions for Yttrium (^{83,84m,85,87m}Y) and Strontium (^{80,81,83,85m}Sr) isotopes in ^{16}O + ^{159}Tb system.

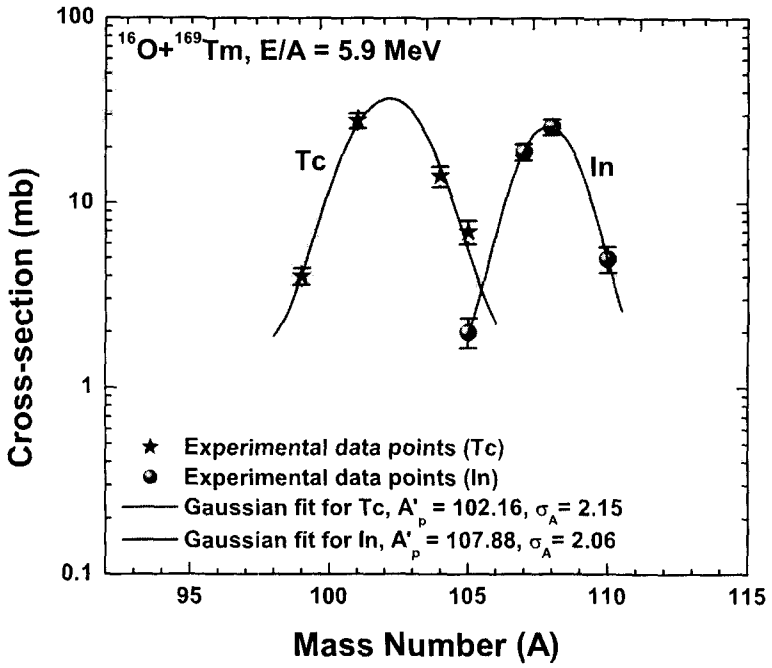

Fig. 6. Isotopic yield distributions for Indium (^{105,107,108,110}In) and Technetium (^{99m,101,104,105}Tc) isotopes in $^{16}O + ^{169}Tm$ system.

The experimental data have been analyzed as given above. Experimentally determined isotopic yield distributions of Yttrium (^{83,84m,85,87m}Y) and Strontium (^{80,81,83,85m}Sr) isotopes in $^{16}O + ^{159}Tb$ system, and Indium (^{105,107,108,110}In) and Technetium (^{99m,101,104,105}Tc) isotopes in $^{16}O + ^{169}Tm$ system are plotted in Figs. 5 and 6. As already discussed, the parameters for isotopic yield distributions were obtained by fitting the respective production cross-sections to a Gaussian distribution. As shown in these figures, the values of the most probable mass A_p is found to be, respectively, 85.03 and 82.54 for Y and Sr, and 107.88 and 102.16 for In and Tc. The width parameters σ_A of isotopic yield distributions for Y, Sr, In and Tc are found to be 2.10, 1.82, 2.06 and 2.15 respectively. Furthermore, the σ_A values reported in the literature for a large number of other fissioning systems are also given in Table 5 along with the presently determined values of these parameters. As can be seen from this table, the σ_A values determined in the present work are close to the literature values.

6. Summary and Conclusions

In the present work, production cross-sections for several fission-like events after CF and/or ICF in $^{16}O + ^{159}Tb$ and $^{16}O + ^{159}Tb$ system at ≈6 MeV/nucleon have been measured to study mass and charge distributions. Moreover, isotopic yield distributions have also been studied using experimentally measured production cross-

sections of Yttrium (Y) and Strontium (Sr) isotopes in $^{16}O + ^{159}Tb$ and Indium (In) and Technetium (Tc) isotopes in $^{16}O + ^{169}Tm$, which have been found to be symmetric as expected. Analysis of the data indicates that the nuclear fission is one of the dominating decay modes of heavy nuclei expected to be populated via complete and/or incomplete fusion at excitation energy ≈ 63 MeV. As such, while predicting the total reaction cross-sections at medium energies, fission contribution should also be taken into consideration. Additional information on various observables of fusion-fission reaction dynamics may be obtained by measuring angular distribution.

Acknowledgments

The authors wish to thank Dr. Amit Roy (Director) and technical staff of Inter-University Accelerator Center (IUAC), New Delhi-67, INDIA for extending all the facilities to carry out these experiments. We are also thankful to Dr. R. K. Bhowmik and Dr. S. K. Dutta for their support during the experiments and several scientific discussions. One of the authors (PPS) thanks the IUAC for providing financial support and hospitality. M. K. Sharma thanks the DST and Unnati the CSIR for financial support.

References

1. P. E. Hodgson, E. Gadioli and E. Gadioli Erba, *Introductory Nuclear Physics* (Clarendon Press, Oxford, 1997), Chapter 23.
2. J. Toke *et al.*, *Nucl. Phys. A* **440** (1985) 327.
3. K. Siwek-Wilczynaska, E. H. du marchie van Voothuysen, J. van Popta, R. H. Siemssen and J. Wilczynski, *Phys. Rev. Lett.* **42** (1979) 1599.
4. J. Blocki, J. Randrup, W. J. Swiatecki and C. F. Tsang, *Ann. Phys. (NY)* **105** (1977) 427.
5. M. Blann, *Phys. Lett.* **27** (1971) 337.
6. P. Vergani, *et al.*, *Phys. Rev. C* **48** (1993) 1815.
7. M. Chipra, *et al.*, *Z. Phys. A* **350** (1994) 121.
8. P. Vergani, *et al.*, *Phys. Rev. C* **48** (1993) 1815.
9. T. Inamura, M. Ishihara, T. Fakuda, T. Shimoda and H. Hiruta, *Phys. Lett. B* **68** (1977) 51.
10. W. J. Swiatecki, *Phys. Scr.* **24** (1981) 113.
11. C. Gregoire, C. Ngo and B. Remaud, *Phys. Lett. B* **99** (1981) 17.
12. D. J. Hinde *et al.*, *Phys. Rev. C* **45** (1992) 1229.
13. L. M. Pant *et al.*, *Eur. Phys. J. A* **11** (2001) 47.
14. T. Sikkeland, *et al.*, *Phys. Lett. B* **42** (1972) 201.
15. V. S. Ramamurthy and S. S. Kapoor, *Phys. Rev. Lett.* **54** (1985) 178.
16. V. M. Strutinsky, *Nucl. Phys. A* **95** (1967) 420.
17. K. H. Schimidt, J. Benlliure and A. R. Junghans, *Nucl. Phys. A* **693** (2001) 169.
18. C. Waggemans, *The Nuclear Physics Process* (CRC, London, 1991).
19. D. J. Hinde, J. R. Leigh, J. J. M. Bokhorst and J. O. Newton, *Nucl. Phys. A* **472** (1987) 318.
20. J. V. Kratz, J. O. Liljenzin, A. E. Norris and G. T. Seaborg, *Phys. Rev. C* **13** (1976) 2347.

21. Ch. Ngo, *Prog. Part. Nucl. Phys.* **16** (1985) 139.
22. J. R. D. Todd, A. R. Wolf, J. J. Hogan and D. J. Parker, *J. Phys. G* **19** (1993) 187.
23. V. S. Ramamurthy *et al.*, *Phys. Rev. Lett.* **65** (1990) 25.
24. E. P. Gavathus, *et al.*, *Phys. Rev. C* **51** (1995) 1991.
25. C. Rubbia *et al.*, Conceptual Design of a Fast Neutron Operated High Power Energy Amplifier, Report CERN/AT/95-94 (ET) 1995.
26. K. Nishio, H. Ikezoe, Y. Nagame, M. Asai, K. Tsukada, S. Mitsuoka, K. Tsuruts, K. Satou, C. J. Lin and T. Ohsawa, *Phys. Rev. Lett.* **93** (2004) 162701.
27. S. Gupta *et al.*, *Phys. Rev. C* **61** (2000) 064613.
28. S. Gupta *et al.*, *Int. J. of Modern Phys. E* **10** (2001) 1–9.
29. M. K. Sharma *et al.*, *J. Phys. Soc. of Japan* **72** (2003) 1917.
30. Unnati *et al.*, *Int. J. Mod. Phys. E* **14** (2005) 775.
31. M. K. Sharma *et al.*, *Phys. Rev. C* **70** (2002).
32. M. K. Sharma *et al.*, *Nucl. Phys. A* **776-4** (2006) 84.
33. R. Tripathi *et al.*, *Phys. Rev. C* **69** (2004) 024613.
34. FREEDOM: Data Acquisition and Analysis System designed to support the accelerator based experiments at the Nuclear Science Centre, New Delhi, India.
35. P. P. Singh and M. Phil. dissertation, A. M. University, Aligarh, India (2005), unpublished.
36. E. Brown and R. B. Firestone, *Table of Isotopes* (Wiley, New York, 1986).
37. A. C. Berriman, D. J. Hinde, M. Dasgupta, C. R. Morton, R. D. Butt and J. O. Newton, *Nature (London)* **413** (2001) 144.
38. D. J. Hinde, A. C. Berriman, R. D. Butt, M. Dasgupta, I. I. Gontcher, C. R. Morton, A. Mukherjee and J. O. Newton, *J. Nucl. Radiochem. Sci.* **3** (2002) 31.
39. R. Tripathi and A. Goswami, *Euro. Phys. J. A* **26** (2005) 271.
40. E. M. Kozuline, A. Ya. Rusanov and G. N. Smirenkin, *Phys. At. Nucl.* **56** (1993) 166.
41. A. Ramaswami, G. K. Gubbi, A. Goswami, B. S. Tomar and S. B. Manohar, *J. Rad. Nucl. Chem.* **246** (2000) 225.
42. H. Freiesleben and J. V. Kratz, *Phys. Rep.* **106** (1984) 1.
43. R. Tripathi, K. Sudarshan, S. Sodaye, B. S. Tomar, G. K. Gubbi, A. Goswami, A. V. R. Reddy and S. B. Manohar, *Radiochim. Acta* **90** (2002) 185.
44. G. K. Gubbi, A. Goswami, B. S. Tomar, A. Ramaswami, A. V. R. Reddy, P. P. Brute, S. B. Manohar and B. John, *Phys. Rev. C* **59** (1999) 3224.
45. M. de Saint-Simon, L. Lessard, W. Reisdrof, L. Remsberg, C. Thibault, E. Roeckl, R. Klpaisch, I. V. Kuznetsov, Yu. Ts. Oganessian and Yu. E. Penionshkevitch, *Phys. Rev. C* **14** (1976) 2185.

Available online at www.sciencedirect.com
ScienceDirect
Nuclear Physics A 811 (2008) 77–92
NUCLEAR PHYSICS A
www.elsevier.com/locate/nuclphysa

Observation of large incomplete fusion in $^{16}O + ^{103}Rh$ system at $\approx$ 3–5 MeV/nucleon

Unnati Gupta [a], Pushpendra P. Singh [a], Devendra P. Singh [a], Manoj Kumar Sharma [a], Abhishek Yadav [a], Rakesh Kumar [b], B.P. Singh [a,*], R. Prasad [a]

[a] *Accelerator Laboratory, Department of Physics, A.M. University, Aligarh-202002, India*
[b] *NP-Group, Inter-University Accelerator Center, PO Box No. 10502, Aruna Asaf Ali Marg, New Delhi-110067, India*

Received 26 April 2008; received in revised form 4 July 2008; accepted 7 July 2008

Available online 24 July 2008

Abstract

Incomplete fusion of $^{16}O(\approx 3–5$ MeV/nucleon) with ^{103}Rh has been investigated using measurement and analysis of excitation functions. Some $pxn/\alpha pxn$-channels are found to have contribution from pre-cursor decay, which has been separated out from cumulative cross-section of evaporation residues. The xn/pxn-channels are found to be satisfactorily reproduced with the predictions of PACE4 after subtraction of pre-cursor decay contribution, in general. Sizable enhancement in the experimental cross-sections has been observed for α-emitting channels over the theoretical once, which may be attributed to the incomplete fusion. The percentage fraction of incomplete fusion has also been deduced, which seems to be sensitive for projectile energy, entrance channel mass-asymmetry and/or projectile structure. The present work deals with the competition of incomplete fusion with complete fusion even at $\approx$ 3–5 MeV/nucleon for $^{16}O + ^{103}Rh$ system.

PACS: 25.70.Jj; 27.70.Gh

Keywords: Heavy ion induced reactions; Activation technique; Measurement of excitation functions; Comparisons with PACE4; Influence of incomplete fusion on complete fusion; Fraction of incomplete fusion as a function of projectile energy; Fraction of incomplete fusion as a function of mass-asymmetry

* Corresponding author. Tel.: +91 941 2133929; fax: +91 571 2701001.
E-mail address: bpsinghamu@gmail.com (B.P. Singh).

0375-9474/$ – see front matter
doi:10.1016/j.nuclphysa.2008.07.013

1. Introduction

In recent years, the study of reaction dynamics in heavy ion (HI) interactions has acquired central place in nuclear physics research [1–7]. The HI-induced reactions are widely different from light ion induced reactions due to large fusion barrier ($B_{\rm fus}$) and availability of different ℓ-bins. In favorable conditions (only if the projectile energy is comparable to the $B_{\rm fus}$), associated input angular momentum (ℓ) is supposed to be large enough to produce nuclei in extreme conditions (high excitation energy and spin). Since, the de-Broglie wavelength in HI-induced reactions is of the order of nuclear dimensions, therefore, the interaction may be explained by adopting semi-classical approach [8]. Classically, the interaction trajectories depending on different ℓ-bins and/or impact parameters lying within the target dimensions may lead prominently to reaction processes like (i) complete fusion (CF), and (ii) incomplete fusion (ICF). In case of CF, with the collision trajectories $0 \leqslant \ell \leqslant \ell_{\rm crit}$, the interacting partners may be trapped in the pocket of entrance channel potential involving all nucleonic degrees of freedom [9–11]. Consequently, the entire kinetic energy and linear momentum of the projectile are ultimately equally shared among all the constituents of the composite system leading to the fully equilibrated compound nucleus (CN). However, at relatively higher values of impact parameters for the collision trajectories (input angular momentum range) with $\ell \geqslant \ell_{\rm crit}$, the pocket in the entrance channel potential vanishes [12–14]. Therefore, the nuclear field of target nucleus is no longer strong enough to trap all the nucleons, consequently, the fractional momentum transfer takes place leading to the ICF process. As a result of ICF of projectile, (i) the CN is formed with less mass and charge as compared to the total mass and charge of interacting partners; (ii) the recoil velocity of the reaction products should be less than the complete fusion population and (iii) the angular distribution of ejectiles is expected to show maxima at forward angles. In case of ICF processes, the mass transfer occurs mostly from lighter to heavier partner, the feature observed more prominently for mass asymmetric systems as compared to mass symmetric systems [15–18].

With a view to explain various ICF processes, several dynamical models like; Break-Up Fusion (BUF) model [19], SUMRULE model [20], Promptly Emitted Particles (PEPs) model [21], EXCITON model [22], etc., have been proposed. In SUMRULE model, Wilczyński et al. [20] suggested that ICF is mainly confined to the ℓ-space above ($\ell_{\rm crit}$) for CF, and originate from peripheral interactions or non-central collisions. The non-central nature of ICF dynamics has also been emphasized by Trautmann et al. [14], and Inamura et al. [23,24]. The BUF-model [19] of Udagawa and Tamura is based on the Distorted Wave Born Approximation (*DWBA*), in which the projectile is assumed to break-up into constituent *alpha*-clusters (e.g., ^{16}O may break-up into $^{12}\mathrm{C} + \alpha$ and/or $^{8}\mathrm{Be} + {}^{8}\mathrm{Be}$) within the nuclear field range of target nucleus. One of the fragments may get fused with target nucleus (depending on the available ℓ-value) [19], while the remnant behaves like a spectator dominantly ejected in the forward cone. According to PEP model [21], the nucleons transferred from projectile to the target nucleus may get accelerated in the nuclear field of target nucleus and consequently acquire extra velocity to escape before equilibration. The EXCITON model assumes that the projectile nucleons undergo a series of collisions with the target nucleus creating particle-hole excitations, which de-excite by emitting fast nuclear particles [22]. Apart from these, Overlap model [25–27] and Multistep Direct Reaction theory [28] have also been proposed, and Morgenstern et al. [17,29], correlated the probability of ICF reactions to the entrance channel mass asymmetry. It may, further, be pointed out that the aforementioned models/theories, generally, have been used to fit the experimental data obtained at energies $E/A \geqslant 10.5$ MeV or so, but no satisfactory comparison has been made at relatively low bombarding energies (i.e., 5–7 MeV/nucleon). As such, due to the unavailability of any re-

liable theoretical model to fit the experimental data obtained at energies $\approx$ 5–7 MeV/nucleon, the study of ICF is still an active area of investigations. Furthermore, there is a renewed interest in the study of ICF dynamics after observation of these reactions at relatively low bombarding energies [30–33]. Moreover, the ICF reactions are considered to be a promising route to produce high spin states even at low bombarding energies [34,35]. Furthermore, some important issues associated with ICF dynamics at energies $\leqslant$ 7 MeV/nucleon are (i) the onset of ICF at energies slightly above the B_{fus}, and (ii) the relative contributions of CF and ICF processes, which have not yet been fully explored or limited up to a few projectile–target combinations only. Therefore, in order to have better understanding of ICF processes, a comprehensive study of excitation functions (EFs), forward recoil range distributions (RRDs) and angular distributions (ADs) of recoils in HI induced reactions have been undertaken by our group [30,36–38]. In the present work, the measurement of EFs for several radio-active isotopes produced in $^{16}\mathrm{O} + {}^{103}\mathrm{Rh}$ system have been performed in the energy range $\approx$ 50–85 MeV. Similar measurements for the same system have also been performed by Z. Buthelezi et al. [39], at energies $\approx$ 40–400 MeV. However, in the present work, precursor decay contributions (if any) in the production of several reaction products have also been estimated from cumulative cross-sections of residues, which has not been considered in Ref. [39]. As such, the present work may serve as the complement and/or as, at some places, supplement to the above measurements at energies $\approx$ 50–85 MeV. The present paper is organized as follows: the experimental details and methodology are given in Section 2. However, the production cross-section measurement and estimation of independent cross-section from cumulative cross-section are described in Section 3. The analysis of experimentally measured EFs with the predictions of statistical model code PACE4 are given in Section 4. The influence of ICF on CF and its dependence on projectile energy and mass-asymmetry of interacting partners are presented in Section 4.1, while, Section 5 deals with the summary and conclusions of the present work.

2. Experimental details and methodology

Experiments have been performed at the Inter-University Accelerator Centre (IUAC), New Delhi, India. The targets of ^{103}Rh of thickness $\approx$ 2.0 mg/cm^2 were prepared from the spectroscopically pure foils of natural Rhodium (^{103}Rh) employing rolling technique. The thickness of each target was determined by α-transmission method. The targets were fixed on Al-holders of 1.2 $\times$ 1.2 cm^2 size and concentric hole of $\approx$ 10 mm diameter. In order to cover a wide energy region in a single irradiation, energy degradation technique has been used. Two stacks, each containing three ^{103}Rh-target foils were irradiated by $^{16}\mathrm{O}^{7+}$ beam at energies $\approx$ 80 and 85 MeV, separately. Typical stacked foil arrangement used for EF measurements is shown in Fig. 1. The successive targets in the stack are backed by Al-catchers of appropriate thicknesses, so that the recoiling nuclei may be trapped in the catcher foil thickness itself. The incident energy on each target-catcher foil assembly in a stack has been estimated using code SRIM, based on stopping power formulation. The errors in the incident energies on each foil have been calculated as the energy loss at half thickness of the target/catcher foils. The first foil of the first stack at highest beam energy (i.e. $\approx$ 85 MeV) has an energy uncertainty of $\pm$2.06 MeV, however, the last foil of the second stack has the uncertainty of $\pm$2.77 MeV, calculated as discussed above. Irradiations have been carried out in the General Purpose Scattering Chamber (GPSC), with a beam current $\approx$ 10 pnA. Keeping in view, the half-lives of interest irradiations have been carried out for $\approx$ 8 hours. After the irradiation, the target-catcher foil assembly has been taken out from the scattering chamber with the help of invacuum transfer system. The activities produced in the

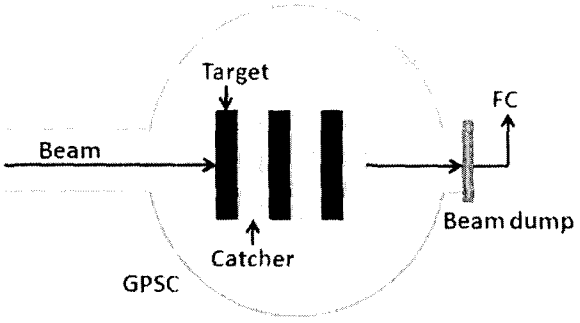

Fig. 1. Typical experimental setup for EF measurement using energy degradation technique.

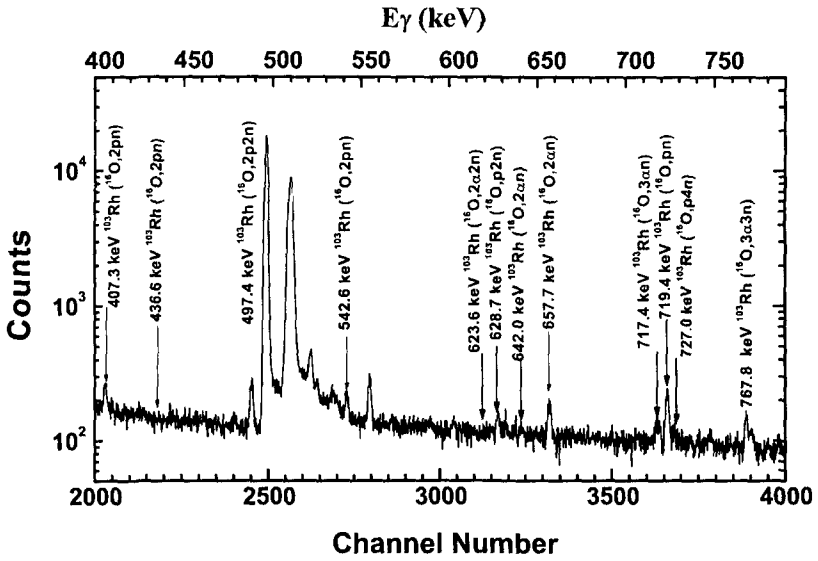

Fig. 2. Typical γ-ray spectrum of $^{16}O + {}^{103}Rh$ at ≈ 85 MeV, peaks are assigned to the different reaction products expected to be populated via complete and/or incomplete fusion.

samples were recorded by a pre-calibrated HPGe detector of 100 c.c. active volume coupled to a CAMAC based software FREEDOM.[1] The detector used in this experiment was pre-calibrated for energy and efficiency using various standard γ-sources, viz., ^{60}Co, ^{133}Ba and ^{152}Eu at different source-detector separations. The target-detector separation was suitably adjusted so as to keep the dead time $< 10\%$. In order to detect and follow the longer lived residues, the counting of irradiated samples has been done for a week or so. A relevant portion of a typical γ-ray spectra of the $^{16}O + {}^{103}Rh$ system at $\approx 82.94 \pm 2.06$ MeV is shown in Fig. 2. The residues were identified by their characteristic γ-rays as well as by decay curve analysis. A list of residues, γ-ray energies, abundances, etc., used in the present work are tabulated in Table 1. The spectroscopic data has been taken from the "Table of Radioactive Isotopes" by Browne and Firestone [40].

[1] FREEDOM, Data acquisition and analysis system designed to support the accelerator based experiments at the Nuclear Science Centre, New Delhi, India (2000).

Table 1
Spectroscopic properties of identified residues

Channel	Residue	Half-life	J^{π}	E_{γ} (keV)	γ (%)
(pn)	^{117g}Te	62 m	$(1/2)^+$	719.7	64.7
				1090.7	6.9
(p2n)	^{116}Te	2.49 h	0^+	628.7	1.0
(p3n)	^{115g}Te	5.8 m	$(7/2)^+$	1326.8	22.7
				1380.5	23.0
(p3n)	^{115m}Te	6.7 m	$(1/2)^+$	770.3	34.2
(p4n)	^{114}Te	15.2 m	0^+	244.6	33
				726.5	43
(2p)	^{117}Sb	2.8 h	$(5/2)^+$	158.6	85.9
(2p2n)	^{115}Sb	32.1 m	$(5/2)^+$	497.4	98
				489.1	1.3
(2α)	^{111g}In	2.8 d	$(9/2)^+$	171.3	90.2
				245.4	94.0
(2αn)	^{110g}In	4.9 h	7^+	641.6	25.9
				884.6	92.9
				937.4	68.4
(2αn)	^{110m}In	1.152 h	2^+	657.7	98.0
				1235.6	0.26
(2α2n)	^{109g}In	4.2 h	$(9/2)^+$	203.2	73.5
				623.6	6.0
(2α3n)	^{108g}In	58 m	7^+	242.7	38.0
(2α3n)	^{108m}In	39.6 m	2^+	311.9	1.01
				968.0	4.38
(3αn)	^{106m}Ag	8.28 d	6^+	451.0	27.6
				717.4	29.0
(3α3n)	^{104g}Ag	69.2 m	5^+	767.8	65.9
				555.8	92.8
(3α4n)	^{103g}Ag	65.7 m	$(7/2)^+$	146.0	28.3

3. Measurement of production cross-sections

The projectile energy dependent reaction cross-sections $\sigma_r(E)$, for different radio-nuclides have been determined using the following expression [48]:

$$\sigma_r = \frac{C_{t=0}}{N_0\theta\phi G_{\varepsilon} K[1-\exp(-\lambda t_1)]} \tag{1}$$

where

$C_{t=0}$ = The count rate just after the irradiation, i.e., at zero time,
N_0 = Initial number of nuclei in the target sample,
θ = Branching ratio of the characteristic γ-rays assigned to different reaction products,
ϕ = The incident beam flux,
G_{ε} = Geometry dependent efficiency of the HPGe detector,
$K = [1-\exp(-\mu d)]/\mu d$ = The self absorption correction factor for the γ-rays in the material of the sample of thickness d(gm/cm^2) and the absorption coefficient μ(cm^2/gm),
λ = Decay constant of the radio-nuclides, and
t_1 = Time of irradiation.

Further, the errors in the measured production cross-sections of different radio-nuclides may arise due to various factors like: (i) Non-uniform thickness of the samples, i.e., the inaccurate estimate of foil thickness may lead to the uncertainty in the determination of the number of target nuclei in the sample. However, in order to check the uniformity of the sample, thickness of each sample was measured at different positions by α-transmission method. The error in the thickness of the sample is estimated to be $\approx 1\%$. (ii) Fluctuations in the beam current may result in the variation of incident flux, as such proper care has been taken to maintain the beam current constant so that the error due to beam current fluctuations may be minimized. (iii) Uncertainty in the determination of geometry dependent spectrometer efficiency. The error in the efficiency determination due to the statistical fluctuations in counts is estimated to be less than 2%. (iv) The loss of product nuclei recoiling out of the target may introduce large errors in the measured cross-sections. The thickness of the catcher foils used in the present work were sufficient to stop even the most energetic residues. However, in the present measurements both the sample and the catcher foils were counted together and hence, the losses due to the recoiling of nuclei is avoided. (v) Dead time of the spectrometer was kept less than 10% by suitably adjusting sample-detector distance. The overall errors including statistical errors are estimated to be $\leqslant 15\%$, excluding the uncertainty in branching ratio, decay constant, etc., which have been taken from the "Table of Radioactive Isotopes" [40].

3.1. Estimation of independent cross-section from cumulative cross-sections

In the present work, the EFs for several radio-nuclides ^{117g}Te(pn), ^{116}Te(p2n), ^{115g,m}Te(p3n), ^{114}Te(p4n), ^{117}Sb(2p), ^{116g,m}Sb(2pn), ^{115}Sb(2p2n), ^{110}Sn(αp4n), ^{111g}In(2α), ^{110g,m}In(2αn), ^{109g}In(2α2n), ^{108g,m}In(2α3n), ^{106m}Ag(3αn), ^{104g}Ag(3α3n) and ^{103g}Ag(3α4n) expected to be populated via CF and/or ICF have been measured. Some of the pxn/αpxn-channels are found to have contribution from higher charge isobar pre-cursor through β^+-emission and/or electron capture (EC), where the cumulative cross-sections have been measured. For such cases, if the half-life of the pre-cursor is considerably smaller than that of the daughter residue, the independent production cross-sections (σ_{ind}) have been estimated from the cumulative production cross-sections (σ_{cum}). The σ_{cum} of a given residue is the sum of σ_{ind} and the cross-section for the independent production of its pre-cursor σ_{pre} multiplied by a numerical coefficient F_p, i.e.,

$$\sigma_{\text{cum}} = \sigma_{\text{ind}} + F_p \sigma_{\text{pre}}. \tag{2}$$

The value of F_p depends on the branching ratio P_p for pre-cursor decay to the residue and is given by

$$F_p = P_p \frac{T_{\text{ind}}^{1/2}}{T_{\text{ind}}^{1/2} - T_{\text{pre}}^{1/2}}, \tag{3}$$

here T_{pre} and T_{ind} are the half-lives of the pre-cursor and the residue. In this way the cumulative cross-section is given by

$$\sigma_{\text{cum}} = \sigma_{\text{ind}} + P_p \frac{T_{\text{ind}}^{1/2}}{T_{\text{ind}}^{1/2} - T_{\text{pre}}^{1/2}} \sigma_{\text{pre}}. \tag{4}$$

As a representative case, the evaporation residue ^{117g}Te (Fig. 3(a)) is likely to be populated via CF of ^{16}O with the ^{103}Rh nucleus forming the composite system ^{119}I* followed by the evap-

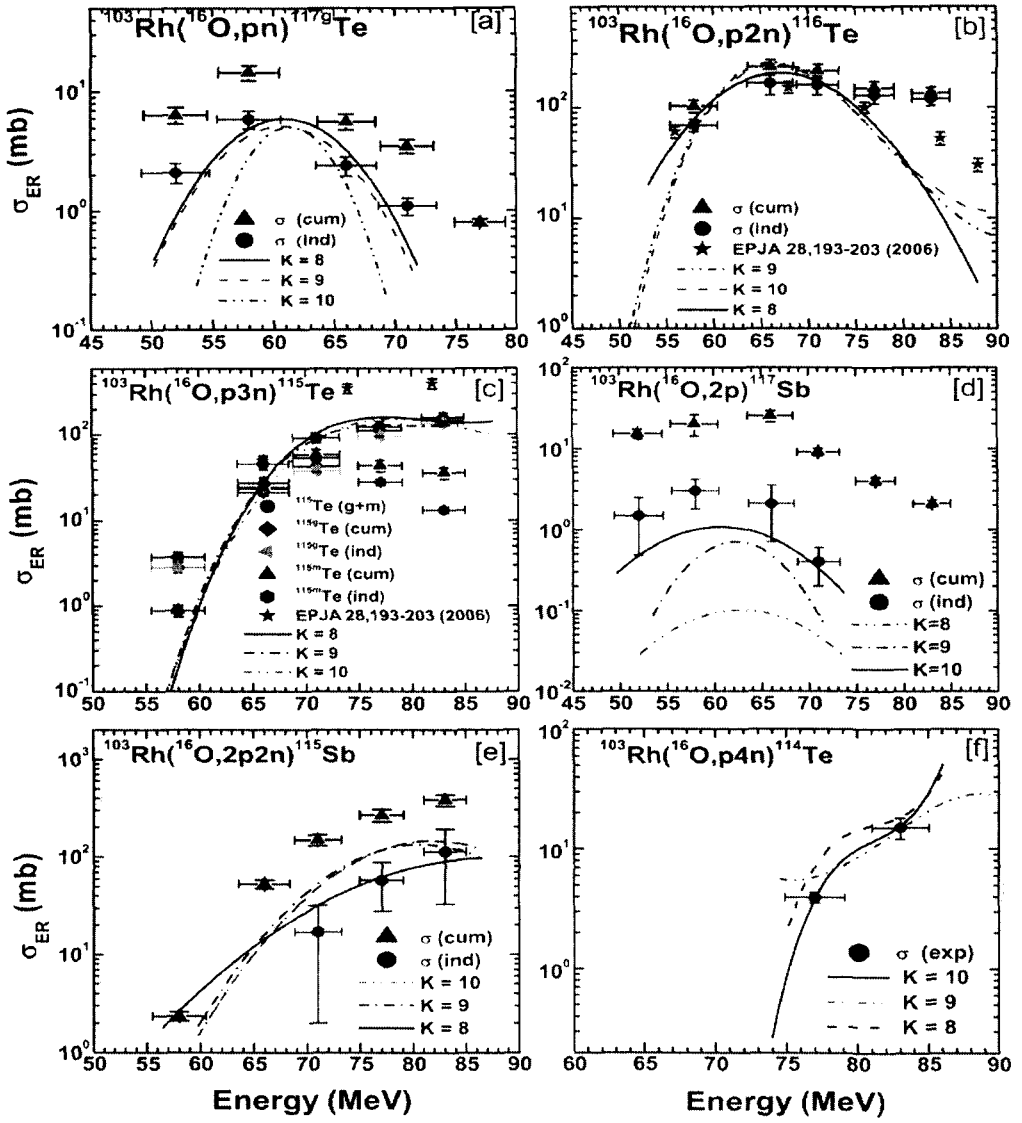

Fig. 3. Experimentally measured and theoretically calculated EFs for different residues populated via CF (xn/pxn-channels) in ^{16}O + ^{103}Rh system at ≈ 46–85 MeV. The lines represent the theoretical calculations done using code PACE4 for different values of K, where a value of $K = 8$ is found to be the best choice for the studied system. The solid (black) triangle and solid (red) circles, respectively, represent cumulative (σ_{cum}) and independent (σ_{ind}) production cross-section of residues. Measured EFs have been compared with Ref. [39], the experimental data points taken from Ref. [39], are given by solid star. Ground and metastable states (if any) are given in self explanatory manner in the figures. (For interpretation of the references to colour in this figure legend, the reader is referred to the web version of this paper.)

oration of a proton and a neutron. The same residue ^{117g}Te may also be populated by the β^+ emission and/or electron capture (EC) of higher charge pre-cursor isobar ^{117}I. As such, the measured activity of residues ^{117g}Te may have contribution from the decay of its pre-cursor isobar also. The values of branching ratios required for obtaining the coefficient F_p are taken from

Ref. [41]. Using the above formulation, the cumulative yield ($\sigma_{\rm cum}$) and independent yield ($\sigma_{\rm ind}$) for ^{117g}Te are related by the equation

$$\sigma_{\rm cum}(^{117g}{\rm Te}) = \sigma_{\rm ind}(^{117g}{\rm Te}) + 1.03\sigma_{\rm pre}(^{117g}{\rm I}). \tag{5}$$

Here $\sigma_{\rm pre}(^{117g}{\rm I})$ is the independent yield of the pre-cursor.

In the similar way, the independent production cross-sections for other residues have also been deduced from the $\sigma_{\rm cum}$ and $\sigma_{\rm pre}$ contributions. The independent production cross-sections have been compared with statistical model code PACE4 [43], and are found to agree reasonably well with the theoretical calculations. The optimization of input parameters has been done by achieving best fitting for CF products (xn/pxn-channels), details of the code PACE4 (which is the modified version of PACE2) and data analysis are discussed in the following section.

4. Analysis of EFs with PACE4

The calculation of theoretical production cross-sections for the evaporation residues populated via CF channels have been obtained using code PACE4. The code PACE4 (which is a revised version of PACE2) is based on Hauser–Feshbach approach. It may be pointed out that the ICF and PE-emission are not taken into consideration in this code. The cross-sections for evaporation residues are calculated using Bass formula [42]. The de-excitation of the compound nucleus is followed by Monte Carlo procedure. The projections of angular momentum are calculated at each stage of de-excitation, which enables the determination of angular distribution of the emitted particles. The optical model parameters for neutrons, protons and α-particles are used as default in the code [43]. The γ-ray strength functions for E_1, E_2 and M_1 transition were taken from tables of Endt [44]. This code has been modified to take into account the excitation energy dependence of level density parameter using the prescription of Kataria et al. [45].

The partial cross-section (σ_ℓ) for the formation of CN at angular momentum ℓ and specific bombarding energy E, is given by

$$\sigma_\ell = \frac{\lambda^2}{4\pi}(2\ell+1)T_\ell. \tag{6}$$

Here λ is the reduced wavelength. The transmission coefficients T_ℓ may be given by the expression

$$T_\ell = \left[1 + \exp\left(\frac{\ell - \ell_{\rm max}}{\Delta}\right)\right]^{-1} \tag{7}$$

where Δ is the diffuseness parameter and $\ell_{\rm max}$ the maximum value of ℓ detained by total fusion cross-section,

$$\sigma_F = \sum_{\ell=0}^{\infty}\sigma_\ell. \tag{8}$$

The transmission coefficients for the evaporation of light particles (n, p and α) during the de-excitation are obtained by optical model calculations [46,47]. The fission decay mode may be considered using a rotating liquid fission barrier routine [43]. As a typical example, at 85 MeV incident beam energy the values of $\ell_{\rm max}$ and Δ are $\approx 63\hbar$ and $\approx 2\hbar$. The level density in this code is calculated using the expression $a = A/K$, where A is the atomic mass number and K is a parameter called level density parameter. In these calculations K is an important parameter and affects the equilibrium component. As such, in order to show the effect of variation of K on

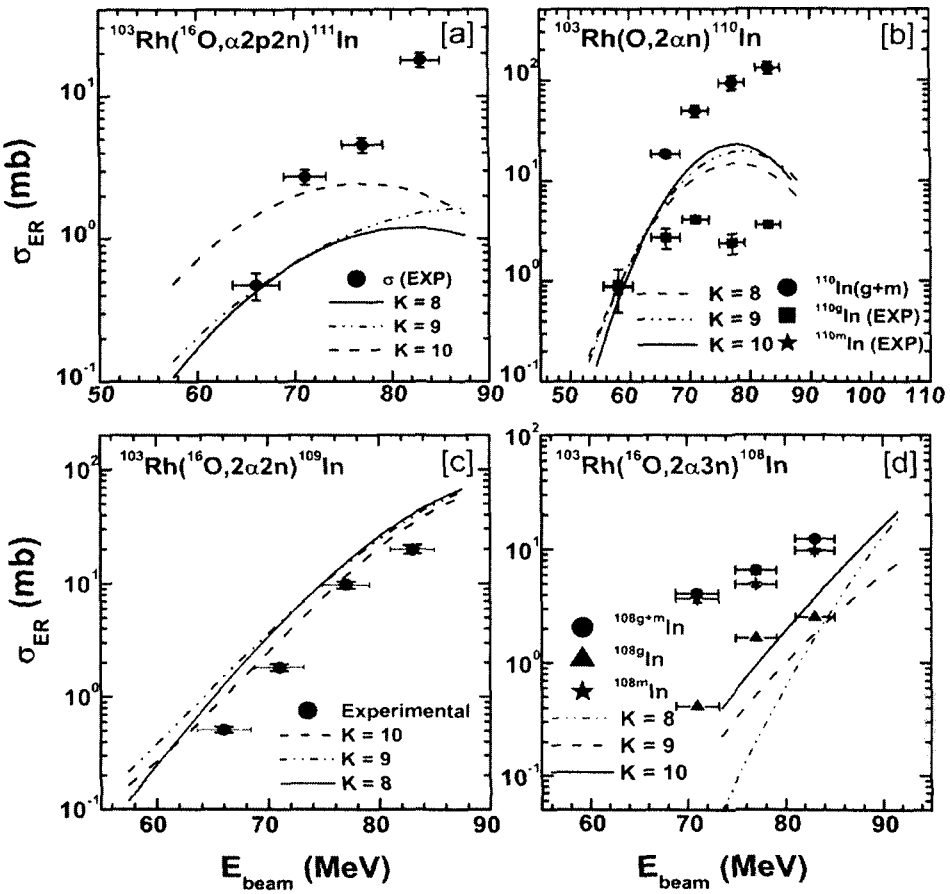

Fig. 4. Experimentally measured and theoretically calculated EFs for different residues populated via CF and/or ICF ($\alpha xn/2\alpha xn$-channels) in ^{16}O + ^{103}Rh system at ≈ 46–85 MeV. Dark circles represent the experimental cross-sections. The enhancement over the theoretical model predictions may be attributed to ICF processes.

calculated EFs, different values of K (8, 9 and 10) have been tested, and are shown in Figs. 3(a)–(f) and 4(a)–(d). It may be pointed out that, it might be possible to predict all the EFs with different values of parameters of the code for individual channels. However, it is not reasonable from the physics point of view. Further, a value of $K \geqslant 10$ may give rise to the anomalous effect in the particle multiplicity. In the present work, a value of $K = 8$ is found to give a satisfactory reproduction of experimental data for CF-channels within the experimental uncertainties.

The metastable state of ^{117}Te could not be observed due to its very short half-life (≈ 103 ms). As can be seen from the Figs. 3(a)–(f), the experimentally measured EFs for radio-nuclides ^{117g}Te(pn), ^{116}Te(p2n), ^{115g,m}Te(p3n), ^{115}Sb(2p2n), ^{117}Sb(2p) and ^{114}Te(p4n) are satisfactorily reproduced by theoretical model predictions within the experimental uncertainties, and may be assumed to be populated via CF (as there is no alpha-particle in exit-channels). Further, in some cases (Fig. 3) experimental data is somewhat enhanced as compared to the theoretical model predictions. In such cases the same residues may be populated via two different modes of decay, viz., (i) directly from the decay of CN (independent production), and (ii) through the β^+/EC decay of higher charge isobar pre-cursors. As such, the experimentally measured production cross-section

is expected to be the admixture of two different decay modes as mentioned above. The independent cross-section ($\sigma_{\rm ind}$) has been separated out from cumulative cross-section ($\sigma_{\rm cum}$) using prescription of Cavinato et al. [31], discussed in Section 3.1 of this paper. As can be seen from the figures, there is a reasonable agreement between theoretical and experimental EFs after subtracting the contribution coming from pre-cursor decay. However, in Fig. 3(b) the higher values of cross-sections in the tail portion of the EFs may be an indication of pre-equilibrium-emission at higher energies [49–52], which is not taken into account in these calculations.

4.1. Interpretation of experimental results

The fact that the measured EFs for almost all predominantly populated CF-channels could be reproduced by PACE4 predictions, gives confidence to the choice of input parameters of theoretical model code. Therefore, same set of input parameters has also been used to fit the EFs of all α-emitting channels. As can be observed from Figs. 4(a)–(d), the experimentally measured EFs are relatively higher as compared to the theoretical predictions. Since the theoretical model code PACE4 does not take ICF into account, therefore the enhancement in the experimentally measured production cross-sections may be attributed to the contribution coming from ICF of ^{16}O with target nucleus. As such, these residues are expected to be populated both via CF and/or ICF of projectile. The production of these residues is assumed to be originated from the successive decay of CN followed by entire projectile fusion in CF process, and/or via fusion of ^{12}C/^{8}Be from ^{16}O-projectile in ICF processes leading to ^{115}Sb*/^{111}In*, respectively. The final reaction products appear after emission of a few nucleons from ^{115}Sb*/^{111}In* (incompletely fused composites). In this case it has been assumed that ^{16}O projectile breaks-up into its α-clusters, viz., ^{12}C + α and/or ^{8}Be + ^{8}Be, a part of projectile fuses with ^{103}Rh, while remnant moves in forward cone with almost projectile velocity. As can be seen from Fig. 4(c), the theoretically calculated EFs for ^{103}Rh(^{16}O, 2α2n)^{109g}In reaction is almost matching/slightly higher than the experimental data for all values of K, revealing very less/negligible contribution from ICF. It may, however, be pointed out that recoil range distribution measurement for this channel may give some clue about its population via CF only. Further, experimentally measured EFs for 3αxn-channels ($x = 1, 3, 4$) are shown in Fig. 5. The theoretical calculations give negligible cross-sections for these residues and hence are not shown in Fig. 5, meaning thereby, these residues are likely to be populated only via ICF. It may also be pointed out that no choice of physically reasonable parameters in theoretical calculations could reproduce the population of these residues.

Moreover, the reaction ^{103}Rh(^{16}O, 3αn)^{106m}Ag may be explained assuming that only α-particle fuses with the target-nucleus leading to ^{107}Ag*, which emits a neutron leaving behind the residue ^{106m}Ag. Similarly, the reactions ^{103}Rh(^{16}O, 3α3n)^{104g}Ag and ^{103}Rh(^{16}O, 3α4n)^{103g}Ag, may be explained, if 3 and 4 neutrons are emitted, respectively from ^{107}Ag*. In these cases, ^{12}C may be assumed to be a spectator. Further, in order to understand the ICF contributions in all α-emitting channels, an attempt has also been made to estimate ICF fraction from the comparison of experimentally measured EFs and theoretically calculated ones [48]. In the present work, the contribution of ICF has been separated out for ^{111}In(α2p2n), ^{110}In(2αn), ^{108}In(2α3n), ^{106m}Ag(3αn), ^{104g}Ag(3α3n) and ^{103g}Ag(3α4n) reaction products which are expected to have contribution from both CF and/or ICF processes. The deduced ICF cross-sections for the residues ^{111,110,108}In and ^{103g,104g,106m}Ag have been plotted in Fig. 6(a). From these figure, it may be observed that the ICF contribution in all α-emitting channels increases with projectile energy, as expected.

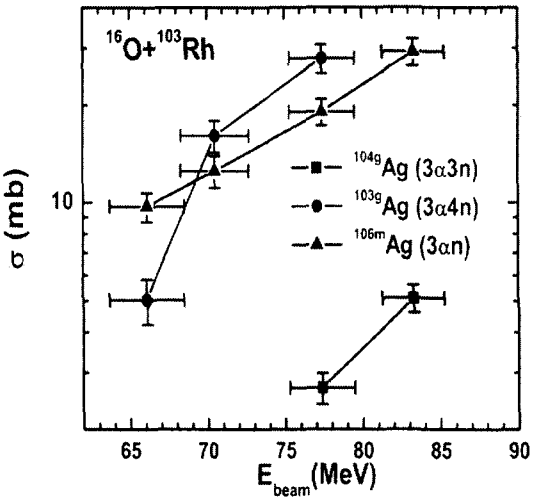

Fig. 5. Experimentally measured and theoretically calculated EFs for different residues expected to be populated via only incomplete fusion ($\alpha xn/2\alpha xn$-channels) of ^{16}O with ^{103}Rh.

Further, as indicated in Figs. 4(a), (b) and (d), ICF is expected to contribute significant amount to the evaporation residue cross-sections. As such, an attempt has been made to deduce the ICF contribution from experimentally measured and theoretically predicted EFs. Although, it is not possible to directly obtain the relative contribution of CF and ICF from the measurement of EFs, therefore some systematics has been followed. As already mentioned, the enhancement in the experimentally measured production cross-sections over theoretical model predictions based on CF calculations may be attributed to the contribution from ICF. As such, the ICF contribution for individual channels has been deduced by subtracting CF cross-sections (σ_{CF}) (predicted by theoretical model code) from the experimentally measured cross-sections (σ_{EXP}) at respective projectile energies, as suggested by Gomes et al. [3]. The ICF contributions (σ_{ICF}) deduced as mentioned in Ref. [3], for presently measured evaporation residues are plotted in Fig. 6(a) along with the sum of cross-section for all ICF channels ($\sum \sigma_{ICF}$) as a function of projectile energy. The lines drawn in these figures are just to guide the eyes. As can be seen from these curves, in general, the ICF contribution increases with projectile energy. It may be because of the fact that the projectile break-up probability of incident ion in the field of the target nucleus significantly increases with incident energy.

As mentioned, the sum of cross-sections for all measured ICF-channels ($\sum \sigma_{ICF}$) and the sum of cross-sections for all CF-channels ($\sum \sigma_{CF}$) obtained from theoretical model predictions are plotted along with the total fusion cross-section ($\sigma_{TF} = \sum \sigma_{CF} + \sum \sigma_{ICF}$) in Fig. 6(b). It can be observed from this figure that the CF component has measurable contribution even at ≈ 58 MeV, while ICF contribution seems to start from ≈ 66 MeV, in the present work. Further, it may be noted from Fig. 6(b), that the separation between the plots for $\sum \sigma_{TF}$ and σ_{CF} increases with projectile energy, which indicates larger contribution from ICF at relatively high projectile energies. This may be because of the fact that the break-up of projectile may be favored as the projectile energy increases. As such, in order to have better representation of projectile energy dependence on ICF contribution, the percentage ICF-fraction (F_{ICF}) has been estimated from the experimentally measured and theoretically calculated EFs similar to as in Ref. [48]. The

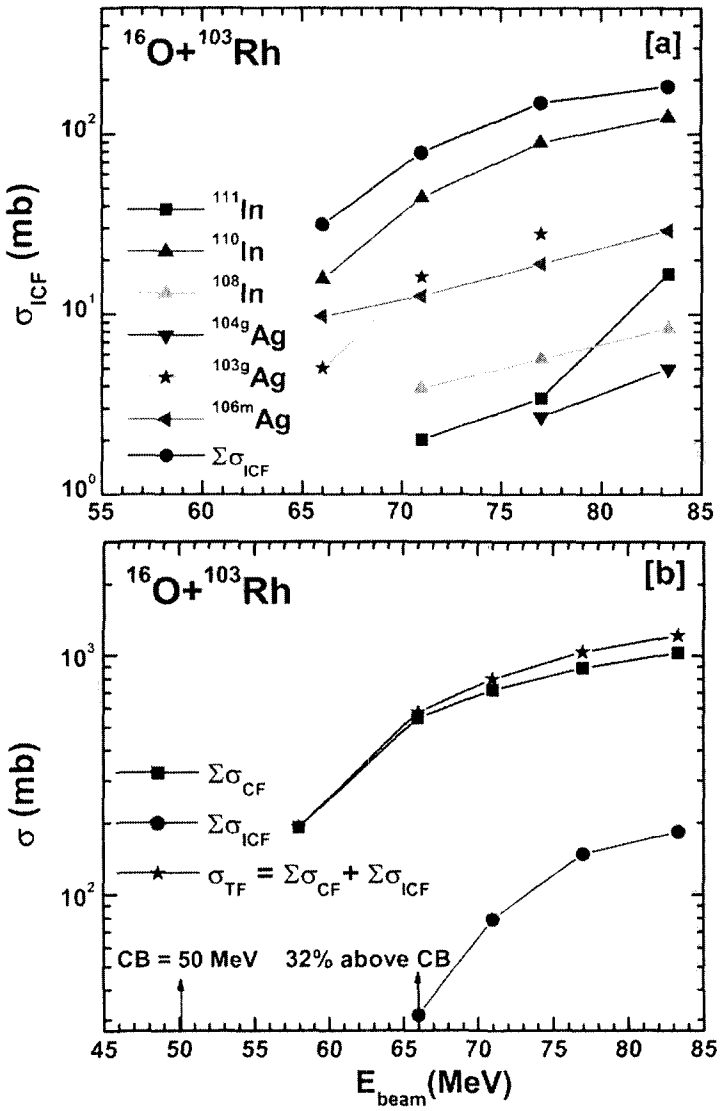

Fig. 6. (a) Deduced EFs for different ICF ($\alpha xn/2\alpha xn$-channels) residues, and (b) total fusion probability (σ_{TF}) along with the sum of complete fusion (σ_{CF}) and incomplete fusion (σ_{ICF}).

F_{ICF} for $^{16}O + ^{103}Rh$ system has been deduced at different energies and is plotted as a function of projectile energy normalized with Coulomb barrier (E_{beam}/V_b) in Fig. 7. The normalized projectile energy (E_{beam}/V_b) has been used to incorporate the effect of Coulomb barrier while comparing different projectile-target combinations in a plot, which is reported as best data reduction procedure for different systems [53]. As can be seen from Fig. 7, the relative percentage F_{ICF} is found to be $\approx 5.5\%$ of the total fusion cross-section (σ_{TF}) at $E_{beam}/V_b = 1.4$, which increases with normalized projectile energy. However, at ≈ 83 MeV (i.e. $E_{beam}/V_b = 1.77$) the relative percentage of F_{ICF} approaches to $\approx 16\%$ of σ_{TF}. Further, in order to support these measurements, similar energy dependence of F_{ICF} for $^{16}O + ^{159}Tb$ and $^{16}O + ^{169}Tm$ systems taken

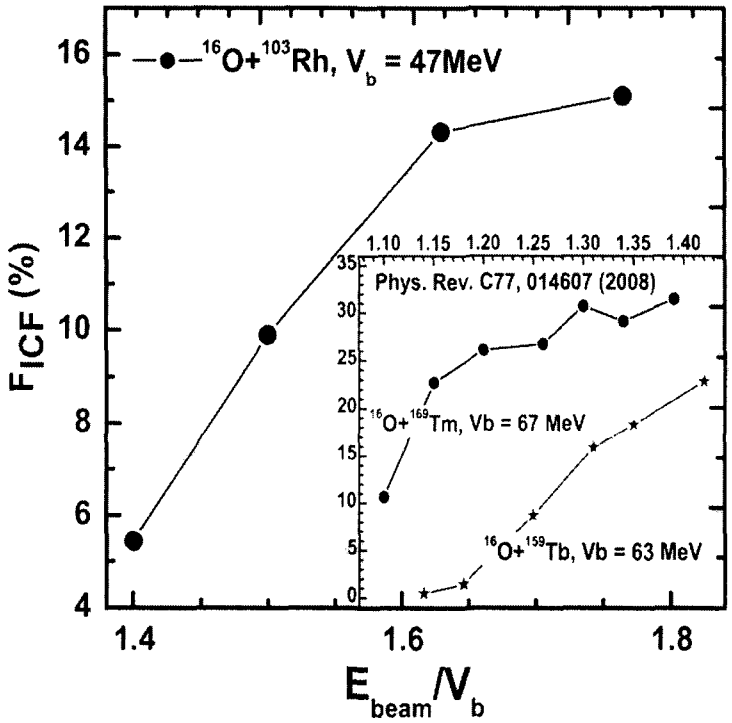

Fig. 7. The percentage ICF fraction (F_{ICF}) as a function of normalized projectile energy (E_{beam}/V_b) for $^{16}O + ^{103}Rh$ system, and also two different systems, viz., $^{16}O + ^{159}Tb$ and $^{16}O + ^{169}Tm$ shown from literature [48].

from our recent publications are also shown in the inset of this figure [48]. As can be noticed from the comparison of F_{ICF} for different projectile target combinations, the F_{ICF} is found to be $\approx 5.5\%$, $\approx 20\%$ and $\approx 30\%$ at the same $E_{beam}/V_b(= 1.4)$ value for $^{16}O + ^{103}Rh$, $^{16}O + ^{159}Tb$ and $^{16}O + ^{169}Tm$ systems, respectively. This striking observation clearly reveals the sensitiveness of F_{ICF} to the mass-asymmetry of interacting partners, which supports the systematics presented by Morgenstern et al. [15–18].

Moreover, similar mass-asymmetry dependence for ICF has been reported in one of our recent publications [48], wherein, it was emphasized that the F_{ICF} depends not only on the mass-asymmetry of interacting partners but also on projectile structure, which plays an important role in the underlying reaction mechanism. In the present work for $^{16}O + ^{103}Rh$ system, the similar systematics for ICF processes has been studied at given energies and presented in Fig. 8, at a constant value of $E_{beam}/V_b = 1.4$, as a representative case. As can be seen from this figure, the F_{ICF} is found to increase with mass-asymmetry, individually for both ^{16}O and ^{12}C as a projectile. It may, further, be pointed out that if one considers only the mass-asymmetry of interacting partners as presented by Morgenstern et al. [15–18], the F_{ICF} do not explain the observed systematics. As such, on the basis of systematics presented in this work and in our earlier publication [48], it may be inferred that not only mass-asymmetry of interacting partners but also the projectile structure effects should also be taken into account, while predicting the F_{ICF}. Further, the systematics can be supported and strengthened by some more experimental data for various projectile–target combinations.

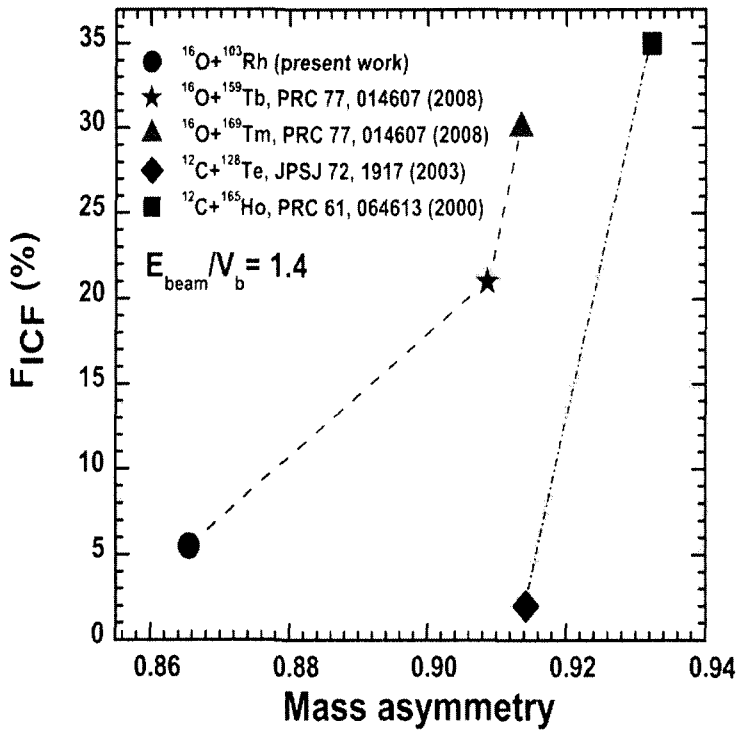

Fig. 8. The percentage ICF fraction (F_{ICF}) as a function of mass asymmetry at a constant normalized projectile energy.

5. Summary and conclusions

Measurement and analysis of EFs for several radio-nuclides produced via CF and/or ICF in $^{16}O + {}^{103}Rh$ system at energies $\approx$ 3–5 MeV/nucleon have been presented in this paper. Some pxn and αxn-channels are found to have contribution from both direct and pre-cursor decay of higher charge isobar. As such, an attempt has been made to deduce the independent production cross-section from cumulative and pre-cursor decay contribution of different radio-nuclides. The experimentally measured EFs have been compared with PACE4 predictions after correcting the pre-cursor decay contribution (if any), which have been found to agree reasonably well for xn/pxn-channels (CF-products). However, in case of α-emitting channels, significant enhancement in the production cross-sections has been observed as compared to theoretical model predictions. The observed enhancement in experimentally measured cross-sections may be assumed to come from the prompt break-up of projectile into α-clusters ($^{16}O \Rightarrow {}^{12}C + {}^{4}He$ and/or $^{8}Be + {}^{8}Be$) leading to the various ICF processes. It has also been observed that the probability of break-up increases with the projectile energy, which reveals the dependence of ICF processes sensitively on projectile energy. Moreover, in order to further confirm the findings of Morgenstern et al. [15–18], and of our recent publication [48], the dependence of F_{ICF} on mass-asymmetry and/or the projectile structure effect, experimental data for five experiments have been compared, wherein, the F_{ICF} is found to increase with mass-asymmetry, individually for both ^{16}O and ^{12}C as a projectile. Therefore, it can be inferred that mass-asymmetry of interacting partners along with projectile structure effects should also be taken into consideration to explain the F_{ICF} for different projectile–target combinations. As such, it may be concluded that apart from CF, the ICF is

also found to contribute significantly to the total reaction cross-section even at projectile energies as low as $\approx$ 3–5 MeV/nucleon. Therefore, while predicting the total reaction cross-section for a projectile–target combination, the contribution coming from ICF should also be taken into consideration. Further, the additional information of underlying processes can also be obtained by comparing a rich set of experimental data for various projectile–target combinations. However, the measurement of recoil range distribution and spin-distribution of residues populated by CF as well as ICF using particle-γ coincidence technique both at relatively low and higher bombarding energies may provide a more clear understanding of the incomplete fusion processes.

Acknowledgements

Authors are thankful to the Director, Inter-University Accelerator Center (IUAC), New Delhi, INDIA for extending all the facilities for carrying out the experiments. We are also thankful to Ms. K.S. Golda for her help during target preparation. One of the authors (Unnati) thanks to the CSIR, M.K.S. to the DST, and R.P. thanks to the DST and the UGC for financial support.

References

[1] M. Lunardona, C. Meriglianoa, G. Viestia, D. Fabrisa, G. Nebbiaa, M. Cinauserob, G. de Angelisb, E. Farneab, E. Fiorettob, G. Preteb, A. Brondic, G. La Ranac, R. Moroc, A. Principec, E. Vardacic, N. Gellid, F. Lucarellid, P. Pavana, D.R. Napolib, G. Vedovatob, Nucl. Phys. A 652 (1999) 3–16.
[2] E.Z. Buthelezi, E. Gadioli, G.F. Steyn, F. Albertini, C. Birattari, M. Cavinato, F. Cerutti, E. Fabrici, Nucl. Phys. A 734 (2004) 553–556.
[3] P.R.S. Gomes, I. Padron, E. Crema, O.A. Capurro, J.O. Fernandez Niello, A. Arazi, G.V. Mart, J. Lubian, M. Trotta, A.J. Pacheco, J.E. Testoni, M.D. Rodriguez, M.E. Ortega, L.C. Chamon, R.M. Anjos, R. Veiga, M. Dasgupta, D.J. Hinde, K. Hagino, Phys. Rev. C 73 (2006) 064606.
[4] P. Vergani, E. Gadioli, E. Vaciago, E. Fabrici, E. Gadioli Erba, M. Galmarini, G. Ciavola, C. Marchetta, Phys. Rev. C 48 (1993) 1815.
[5] A. Diaz-Torres, I.J. Thompson, Phys. Rev. C 65 (2002) 024606.
[6] F. Amorini, M. Cabibbo, G. Cardella, A. Di Pietro, P. Figuera, A. Musumarra, M. Papa, G. Pappalardo, F. Rizzo, S. Tudisco, Phys. Rev. C 58 (1998) 987.
[7] M. Dasgupta, P.R.S. Gomes, D.J. Hinde, S.B. Moraes, R.M. Anjos, A.C. Berriman, R.D. Butt, N. Carlin, J. Lubian, C.R. Morton, J.O. Newton, A. Szanto de Toledo, Phys. Rev. C 70 (2004) 024606.
[8] P.E. Hodgson, E. Gadioli, E. Gadioli Erba, Introductory Nuclear Physics, Clarendon Press, Oxford, 1997, Chapter 23.
[9] J. Pochodzallab, R. Butscha, B. Hecka, G. Rosnera, Phys. Lett. B 181 (1986) 33–37.
[10] H. Oeschler, M. Kollatz, W. Bohne, K. Grabisch, H. Lehr, H. Freiesleben, K.D. Hildenbrand, Phys. Lett. B (1983) 177–180.
[11] H.W. Wilschut, G.J. Balster, P.B. Goldhoorn, R.H. Siemssen, Z. Sujkowski, Phys. Lett. B 138 (1984) 43–46.
[12] J.B. Natowitz, E.T. Chulick, M.N. Namboodiri, Phys. Rev. C 6 (1972) 2133.
[13] K. Siwek-Wilczyńska, E.H. du Marchi van Voorthuysen, J. van Popta, R.H. Siemssen, J. Wilczyński, Phys. Rev. Lett. 42 (1979) 1599.
[14] W. Trautmann, O. Hansen, H. Tricoire, W. Hering, R. Ritzka, W. Trombik, Phys. Rev. Lett. 53 (1984) 1630.
[15] H.M. Morgenstern, W. Bohne, W. Galster, K. Grabisch, Phys. Rev. Lett. 52 (1984) 1104.
[16] H. Morgenstern, W. Bohne, K. Grabisch, H. Lehr, W. Stoffler, Z. Phys. A 313 (1983) 39.
[17] H. Morgenstern, W. Bohne, W. Galster, K. Grabisch, Phys. Rev. Lett. 52 (1984) 1104.
[18] H. Morgenstern, W. Bohne, K. Grabisch, D.G. Kovar, H. Lehr, Phys. Lett. 113B (1982) 463.
[19] T. Udagawa, T. Tamura, Phys. Rev. Lett. 45 (1980) 1311.
[20] J. Wilczyński, K. Siwek-Wilczyńska, J. van Driel, S. Gonggrijp, D.C.J.M. Hageman, R.V.F. Janssens, J. Lukasiak, R.H. Siemssen, S.Y. van der Werf, Phys. Rev. Lett. 45 (1980) 606.
[21] J.P. Bondrof, J.N. De, G. Fai, A.O.T. Karvinen, J. Randrup, Nucl. Phys. A 333 (1980) 285.
[22] M. Blann, Phys. Rev. Lett. 27 (1971) 337.
[23] T. Inamura, T. Kjima, T. Nomura, T. Sugitate, H. Utsunomiya, Phys. Lett. 84B (1982) 71.

[24] T. Inamura, A.C. Kahler, D.R. Zolnowski, U. Garg, T.T. Sugihara, M. Wakai, Phys. Rev. C 32 (1985) 1539.
[25] B.G. Harvey, Nucl. Phys. A 444 (1985) 498.
[26] M.H. Simbel, A.Y. Abdul Magd, Z. Phys. A 294 (1980) 277.
[27] A.Y. Abdul Magd, Z. Phys. A 298 (1980) 143.
[28] V.I. Zagrebaev, Ann. Phys. (N.Y.) 197 (1990) 33.
[29] H. Morgenstern, W. Bohne, W. Galster, K. Grabisch, Z. Phys. A 324 (1986) 443.
[30] M.K. Sharma, Unnati, B.K. Sharma, B.P. Singh, H.D. Bhardwaj, R. Kumar, K.S. Golda, R. Prasad, Phys. Rev. C 70 (2004) 044606.
[31] M. Cavinato, E. Fabrici, E. Gadioli Erba, P. Vergani, M. Crippa, G. Colombo, I. Redaeli, M. Ripamonti, Phys. Rev. C 52 (1995) 2577.
[32] M. Crippa, E. Gadioli, P. Vergani, G. Ciavola, C. Marchetta, M. Bonardi, Z. Phys. A 350 (1994) 121.
[33] D.J. Parker, J. Asher, T.W. Conlon, I. Naqib, Phys. Rev. C 30 (1984) 143;
D.J. Parker, J. Asher, T.W. Conlon, I. Naqib, Phys. Rev. C 35 (1987) 161.
[34] P. Walker, G.D. Dracoulis, Nature (London) 399 (1999) 35.
[35] G.D. Dracoulis, A.P. Byrne, T. Kibedi, T.R. McGoram, S.M. Mullins, J. Phys. G: Nucl. Part. Phys. 23 (1997) 1191, and references therein.
[36] M.K. Sharma, Unnati, B.P. Singh, R. Kumar, K.S. Golda, H.D. Bhardwaj, R. Prasad, Nucl. Phys. A 776 (2006) 83.
[37] S. Gupta, B.P. Singh, M.M. Muthafa, H.D. Bhardwaj, R. Prasad, Phys. Rev. C 61 (2000) 0064613.
[38] P.P. Singh, M.K. Sharma, Unnati, D.P. Singh, R. Kumar, K.S. Golda, B.P. Singh, R. Prasad, Eur. Phys. J. A 34 (2007) 29–39.
[39] E.Z. Buthelezi, F. Ceutti, E. Gadioli, G.F. Steyn, A. Pepe, S.H. Connell, A.A. Cowley, Eur. Phys. J. A 28 (2006) 193–203.
[40] E. Browne, R.B. Firestone, Table of Radioactive Isotopes, Wiley, New York, 1986.
[41] U. Reus, W. Westmeirer, At. Data Nucl. Data Tables 29 (1983) 338.
[42] R. Bass, Nucl. Phys. A 231 (1974) 45.
[43] A. Gavron, Phys. Rev. C 21 (1980) 230.
[44] P.M. Endt, At. Data Nucl. Data Tables 26 (1981) 47.
[45] S.K. Kataria, V.S. Ramamurthy, S.K. Kapoor, Phys. Rev. C 18 (1978) 549.
[46] F.D. Becchetti, G.W. Greenlees, Phys. Rev. 182 (1969) 1190.
[47] G.R. Satchler, Nucl. Phys. 70 (1965) 177.
[48] P.P. Singh, B.P. Singh, M.K. Sharma, Unnati, D.P. Singh, R. Prasad, R. Kumar, K.S. Golda, Phys. Rev. C 77 (2008) 014607, and the references therein.
[49] N. Patronis, C.T. Papadopoulos, S. Galanopoulos, M. Kokkoris, G. Perdikakis, R. Vlastou, A. Lagoyannis, S. Harissopulos, Phys. Rev. C 75 (2007) 034607.
[50] T.E. Rodrigues, M.N. Martins, C. Garcia, J.D.T. Arruda-Neto, J. Mesa, K. Shtejer, F. Garcia, Phys. Rev. C 75 (2007) 014605.
[51] J. Pal, S. Saha, C.C. Dey, P. Banerjee, S. Bose, B.K. Sinha, M.B. Chatterjee, S.K. Basu, Phys. Rev. C 71 (2005) 034605.
[52] W. Bauer, A. Botvina, Phys. Rev. C 52 (1995) R1760.
[53] P.R.S. Gomes, J. Lubian, I. Padron, R.M. Anjos, Phys. Rev. C 71 (2005) 017601.

Large pre-equilibrium contribution in α + ^{nat}Ni interactions at ≈8–40 MeV

Abhishek Yadav, Pushpendra P. Singh,* Manoj K. Sharma, Devendra P. Singh, Unnati, B. P. Singh,† and R. Prasad
Department of Physics, Aligarh Muslim University, Aligarh (UP) 202002, India

M. M. Musthafa
Department of Physics, Calicut University, Kerala, India
(Received 5 April 2008; published 8 October 2008)

To investigate pre-equilibrium emission of light nuclear particle(s), an experiment has been performed using α beams at the Variable Energy Cyclotron Center (VECC), Kolkata, India. In the present work, excitation functions for ^{58}Ni(α, p)^{61}Cu, ^{58}Ni(α, pn)^{60}Cu, ^{60}Ni(α, $p2n$)^{61}Cu, ^{60}Ni(α, n)^{63}Zn, ^{60}Ni(α, $2n$)^{62}Zn, ^{61}Ni(α, $3n$)^{62}Zn, and ^{61}Ni(α, $2n$)^{63}Zn reactions have been measured by using the stacked foil activation technique followed by off-line γ-ray spectroscopy. Experimentally measured excitation functions have been compared with the prediction of the theoretical model code ALICE-91 with and/or without the inclusion of pre-equilibrium emission. Analysis of the data suggests that an admixture of both equilibrium and pre-equilibrium emission is needed to reproduce experimental data at energies ≈8–40 MeV and reveals significant contribution from pre-equilibrium emission. An attempt has also been made to estimate the pre-equilibrium contribution, which has been found to depend on projectile energy and on number of emitted particle(s).

DOI: 10.1103/PhysRevC.78.044606 PACS number(s): 25.55.−e, 25.60.Dz, 25.70.Gh

Pre-equilibrium (PE) emission in light-ion-induced (LI-induced) reactions has been a topic of considerable interest during the past decade or so from both theoretical and experimental aspects, owing to the strong competition between equilibrium and the pre-equilibrium emission of light nuclear particles [1–4]. In PE emission, energetic light nuclear particles (neutrons and protons) are emitted predominantly at the initial stages of the nuclear interactions. The emission of light nuclear particles in the PE emission process followed by nonstatistical γ rays are assumed to arise from the interaction of the projectile with the target nucleons at the early stage of reaction. However, at later stages, a fully equilibrated compound nucleus (CN) may be formed and this nucleus further decays by statistical evaporation of light nuclear particles and/or characteristic γ radiations. Recent experiments have established that, at moderate excitation energies, the equilibrium decay is influenced by the emission of light nuclear particles before the equilibration of the composite system. Some of the important experimental signatures of PE emission that have emerged from the literature are (i) the presence of a larger number of high-energy light nuclear particles in the exit channel as compared to the number emitted in equilibrium decay, (ii) a forward-peaked angular distribution of light nuclear particles, and (iii) slowly decreasing tails of the excitation functions (EFs) [5–8]. A better understanding of these aforementioned characteristics of PE emission may provide important information about the involved reaction mechanism. The measurement and analysis of the EFs can be used as an informative probe of the PE emission process. In fact, the features of the EFs at low, medium, and high energies may reveal the characteristics of the involved reaction mechanism. The low-energy portion of EFs is dominated by the equilibrium decay; however, as the projectile energy increases the PE emission process becomes important and a slowly decreasing tail in the EFs becomes apparent [9–12]. Thus, the cross sections for emission of a given number of nucleons in a reaction may be measurable at energies where pure evaporative processes are greatly favored. To explain the PE emission of the highly excited composite system, several dynamical models have been proposed, including the internuclear cascade model (INC) [13,14], the quasifree scattering model (QFS) [15], and the pre-equilibrium EXCITON model [16–19]. The EXCITON model is considered to provide the most suitable description, particularly for α-induced reactions, in which the excitons—the excited particle (p) and hole (h)—are assumed to be produced through the interaction between projectile nucleons and target nucleus. These models have been used to describe various experimental data; however, the behavior of LI-induced reactions associated with the energy regime, entrance channel, mass asymmetry, etc. is still not well understood. Further, the LI-induced reactions are also important in basic research for the fundamental understanding of reaction dynamics and to test the validity of various available statistical model codes. Moreover, a rich set of experimental data on equilibrium and PE emission for various projectile-target combinations may be applicable in applied research on nuclear energy generation and/or waste management [20]. The experimental data on different reaction processes may also be useful in the production of medically important radionuclides and in reactor technology as well, particularly in the recently proposed Accelerator Driven Subcritical-reactor System (ADSS) [21,22]. This has led to a renewed interest in the study of nuclear reactions. With the motivation to study the interplay of equilibrium and pre-equilibrium emission processes, the EFs for seven α-induced reactions on natural nickel (^{nat}Ni) isotopes have been measured by using the stacked foil activation technique followed by off-line γ-ray spectroscopy.

*pushpendrapsingh@gmail.com
†bpsinghamu@gmail.com

TABLE I. List of reactions, identified characteristic γ rays, half-lives, branching ratios, and their Q values.

Reaction	Residue	J^{π}	Half-life	γ-ray energies (keV)	Branching ratio	Q value (MeV)
^{58}Ni(α, p)	^{61}Cu	$3/2^-$	3.33 h	283.0, 656.0	12.5, 10.7	−3.1
^{58}Ni(α, pn)	^{60}Cu	2^+	23.7 min	826.3, 1332.5	21.9, 88.0	−14.8
^{60}Ni(α, $p2n$)	^{61}Cu	$3/2^-$	3.33 h	283.0, 656.0	12.5, 10.7	−23.5
^{60}Ni(α, n)	^{63}Zn	$3/2^-$	38.47 min	669.86, 926.27	8.4, 6.6	−7.9
^{60}Ni(α, $2n$)	^{62}Zn	0^+	9.186 h	548.4, 596.7	15.2, 25.7	−17.0
^{61}Ni(α, $3n$)	^{62}Zn	0^+	9.186 h	548.4, 596.7	15.2, 25.7	−24.8
^{61}Ni(α, $2n$)	^{63}Zn	$3/2^-$	38.47 min	669.86, 926.27	8.4, 6.6	−15.7

The experiment has been performed at the Variable Energy Cyclotron Center (VECC), Kolkata, India. The ^{nat}Ni samples (prepared by rolling) of thickness ≈3.32 mg/cm^2 (measured by the α-transmission method) were pasted onto Al holders. A collimated α beam of ≈40 MeV has been allowed to fall on a stack of eight targets (each backed by an Al degrader of thickness ≈6.75 mg/cm^2) for ≈12 h with a beam current ≈100 nA. The average beam energy on a given target foil and degrader was calculated by using the code SRIM based on stopping power and range calculations. Post-irradiation analysis has been performed by using a high resolution, large volume (100 c.c.), precalibrated HPGe detector coupled with a data-acquisition system. The activities induced in various samples were recorded, leading to the production probability measurement of individual evaporation residues. Various standard sources of known strength were used to determine the efficiency of the detector at various source-detector separations. The sample-detector separations were suitably adjusted to minimize the dead time to ⩽10%. The residues produced from different reaction channels were identified by their characteristic γ rays, Q values, and decay-curve analysis. Further details of the experimental arrangement, formulation used, and data reduction procedure are similar to those in Ref. [23].

In the present work, the EFs for ^{58}Ni(α, p)^{61}Cu, ^{58}Ni(α, pn)^{60}Cu, ^{60}Ni(α, $p2n$)^{61}Cu, ^{60}Ni(α, n)^{63}Zn, ^{60}Ni(α, $2n$)^{62}Zn, ^{61}Ni(α, $3n$)^{62}Zn, and ^{61}Ni(α, $2n$)^{63}Zn reactions have been measured by using the activation technique followed by off-line γ spectroscopy. The reaction products identified on the basis of decay-curve analysis and Q-value systematics are given in Table I. In Table II the experimentally deduced production cross sections of identified residues are given. The errors quoted in the production cross sections are expected and are caused by several factors: (i) The statistical errors in counting of standard sources may introduce error in detector efficiency, which was minimized by accumulating the large number of counts for considerably longer time (≈5000 s). The geometry-dependent efficiency of γ-ray counting at various source-detector separations has been deduced and fitted with a fourth-order polynomial function, where the uncertainty from the fitting is found to be ⩽3% for the energy range of interest. (ii) The solid-angle effect is also expected to introduce some uncertainty in efficiency. This may be because the irradiated samples were not point sources like the standard sources. The errors in efficiency on account of the solid-angle effect have been calculated as demonstrated by Gardner *et al.* [24] and are found to be ⩽2%. (iii) The inaccurate determination of foil thickness and the nonuniformity of the foil may give rise to an uncertainty in the total number of target nuclei in the sample. The errors expected in the number of nuclei on account of the nonuniform thickness of the sample may be deduced by measuring the thickness at different positions of the sample and are found to be ≈1%. (iv) Proper care was taken to keep the beam current constant; however, all the fluctuations were noted during the entire irradiation time and the beam flux was individually calculated for the duration of fluctuations. The error from the fluctuations in the beam current was found to be ≈3%. (v) During irradiation of the stack, the beam traverses the thickness of the material, thus reducing the initial beam intensity. It is estimated that the error from this decrease in beam intensity is ⩽2%, as suggested by Ernst *et al.* [25]. The overall errors in the present measurement

TABLE II. List of reactions with their cross section and error.

Energy (MeV)	Cross section (mb)						
	^{58}Ni(α, p)	^{58}Ni(α, pn)	^{60}Ni(α, $p2n$)	^{60}Ni(α, n)	^{60}Ni(α, $2n$)	^{61}Ni(α, $3n$)	^{61}Ni(α, $2n$)
9 ± 1	150 ± 17	–	–	–	–	–	–
14 ± 0.9	360 ± 38	–	–	–	–	–	–
17 ± 0.9	401 ± 60	–	–	–	–	–	–
23 ± 0.8	201 ± 32	–	–	–	–	–	–
25 ± 0.8	95 ± 15	148 ± 22	–	–	11 ± 1.4	–	–
29 ± 0.8	46 ± 5	270.1 ± 40	–	21 ± 3	25 ± 4	–	124 ± 18
36 ± 0.7	16 ± 2	251 ± 38	64 ± 13	4 ± 0.9	28 ± 4	2 ± 0.8	151 ± 27
40 ± 0.7	13 ± 2	111 ± 17	191 ± 33	1 ± 0.3	17 ± 2	10 ± 0.7	75 ± 11

are found to be $\leqslant$15%. However, the uncertainties in the branching ratio, decay constant, half-lives, etc., which are taken from the table of isotopes [26], have not been taken into account in the measured cross sections. The experimentally measured EFs are compared with the calculations performed with the theoretical model code ALICE-91 [27], which takes both equilibrium and PE decay processes into account, and are shown in Figs. 1 and 2. The code ALICE-91 is frequently used for the analysis of experimental data [23,28]. This may be because of the fact that the input parameters of this code are few and are rather well defined. Moreover, the theoretical analyses with ALICE-91, in general, are found to give reasonably good agreement with the experimental data. The CN calculations in this code are performed by using the Weisskopf-Ewing model [29], whereas the PE component is simulated by using the geometry-dependent hybrid model [27]. The Myers-Swiatecki/Lysekil mass formula [30] is used for calculating Q values and binding energies of all the nuclei in the evaporation chain. Calculations for PE emission in this

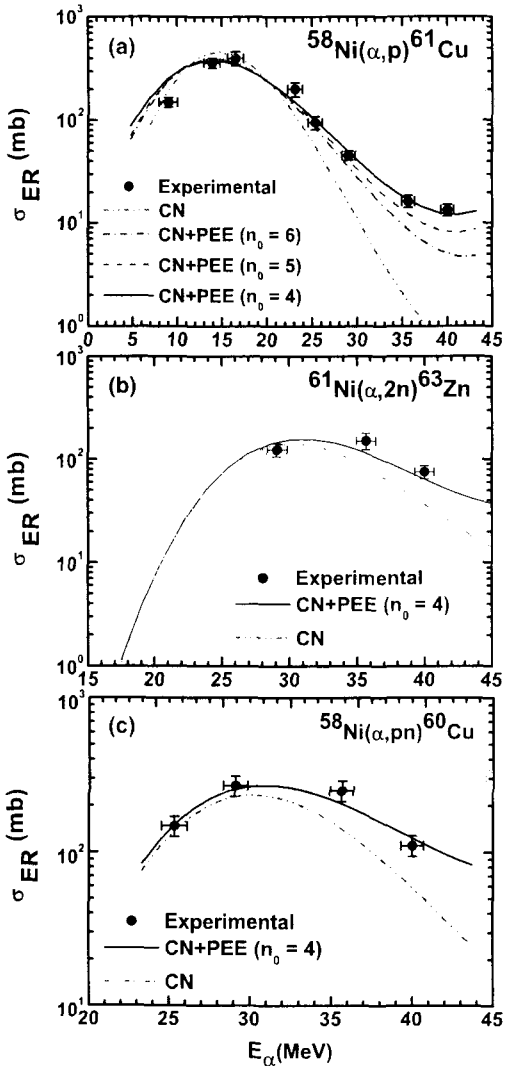

FIG. 1. (Color online) Experimentally measured and theoretically calculated EFs using the code ALICE-91.

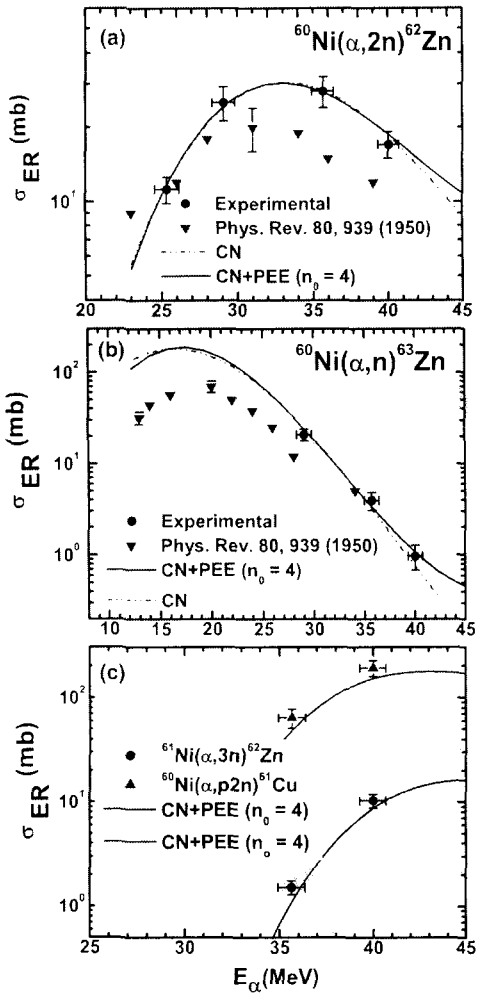

FIG. 2. (Color online) Experimentally measured and theoretically calculated EFs using code the ALICE-91.

code are done by assuming equipartition of energy among the initially excited particles and holes. The mean free path for intranuclear transition rates may be calculated either from the optical potential parameters of Becchetti and Greenlees [31] or from Pauli-corrected nucleon-nucleon cross sections [32,33].

In this code the level density parameter a, initial exciton number n_0, and the mean free path multiplier MFP are the important parameters that may be varied to reproduce the experimental data. The parameter a mainly affects the equilibrium component, whereas n_0 and MFP largely govern the pre-equilibrium component. In the hybrid model, the intermediate states of the system are characterized by the excitation energy E and number n_p of excited particles and number n_h of excited holes. Particles and holes are defined relative to the ground state of the nucleus and are called excitons. The initial configuration of the compound system defined by initial exciton number $n_0 = (n_p + n_h)$ is an important parameter of PE formalism. To find the value of the initial exciton number n_0, calculations for different values of n_0 were performed. As a representative case, calculated EFs for different values of n_0 ranging from 4 to 6 with configurations $n_0 = 4(2p +$

$2n + 0h$), $n_0 = 5(3p + 2n + 0h)$, and $n_0 = 6(3p + 2n + 1h)$ for the reaction ^{58}Ni(α, p)^{61}Cu are shown in Fig. 1(a). It may be pointed out that, in PE emission, the initial exciton number n_0 is a crucial quantity and determines the shape of the PE component. For α-induced reactions, values of initial exciton number $n_0 = 4$ or 5 have been justified by Blann [27] since a lower value of n_0 means a larger number of two-body interactions prior to the equilibration of the composite system, resulting in a large PE contribution. In the present work, a set of $a = A/8$, $n_0 = 4$, and $MFP = 1$ is found to satisfactorily reproduce the experimental data, in general. In the present work the same data set has been consistently used to obtain the cross-section values from the code. As shown in Figs. 1 and 2, the CN theoretical calculations satisfactorily reproduce the experimental data up to the peak portion of the EFs only. However, at higher energies (i.e., in the tail portion of the EFs) the admixture of CN and PE emission reproduce the experimental data to a satisfactory level.

Further, in some cases the same residual nucleus is produced through different reaction channels and hence the observed count rate may be the sum of contributions from different reaction paths. The residual nuclei ^{61}Cu, ^{62}Zn, and ^{63}Zn are found to be populated via equilibrium and/or pre-equilibrium decay of the CN formed through the interaction of $\approx$8–40 MeV α particles with various nickel isotopes. For example, the residual nucleus ^{61}Cu may be produced via both ^{58}Ni(α, p) and ^{60}Ni(α, $p2n$) reactions, where the Q values of these reactions are -3.1 and -23.5 MeV, respectively. Thus, for a projectile energy above 3.1 MeV, the production of ^{61}Cu will be entirely due to the ^{58}Ni(α, p) channel up to 23.5 MeV. However, at energies above 23.5 MeV the intensity of the γ rays from ^{61}Cu will make a contribution from both these reaction channels. From the measured cross section for ^{61}Cu above $\approx$24 MeV, the contribution of the theoretically calculated cross section was subtracted to obtain the contribution of ^{61}Cu populated via the ^{60}Ni(α, $p2n$)^{61}Cu reaction. The cross sections deduced for ^{60}Ni(α, $p2n$)^{61}Cu in this way are plotted in Fig. 2(c). As can be seen from this figure, the cross sections for the ^{60}Ni(α, $p2n$)^{61}Cu channel are very nicely reproduced by theoretical model predictions, which gives us confidence in the data-reduction procedure. Similarly, the cross section for ^{62,63}Zn populated via two different reaction channels as given in Table I have been obtained by using Q-value systematics. While deducing the cross section ratios proper care is taken for the threshold of each channel, isotopic abundance, half-life of the residual nucleus, and the branching ratio for the observed γ rays. Furthermore, the comparison of measured cross sections for the residues ^{62}Zn($2n$) and ^{63}Zn(n) has also been made with the pioneering measurements of Ghoshal [34] and are given in Figs. 2(a) and 2(b). As can be seen from Figs. 2(a) and 2(b), the data points of the present measurement are not in good agreement with the literature values [34]. In fact, the activities of ^{62}Zn and ^{63}Zn isotopes reported in Ref. [34] were deduced by a chemical separation method, which may involve quite large uncertainties because the activities were recorded by detecting energetic positrons with the help of a thin window counter. However, in the present work a much better high-resolution γ spectroscopy technique employing an HPGe detector has been used to provide a more reliable data set. Moreover, the trends of Ghoshal's data [34] are quite similar to the present measurements. It may further be pointed out that the present experimental data are very well fitted with the predictions of the code ALICE-91.

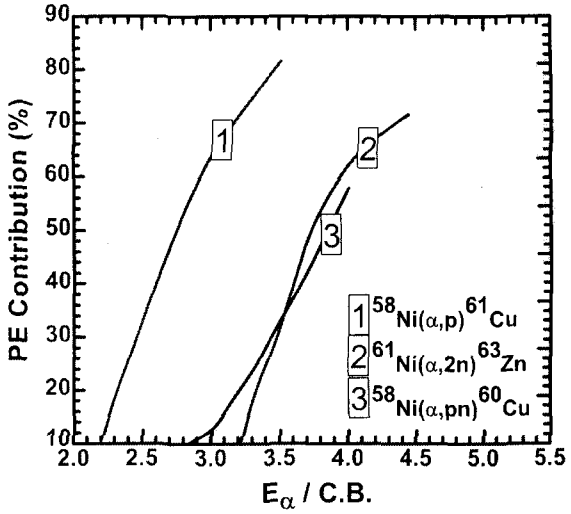

FIG. 3. (Color online) Estimated PE contribution as a function of normalized projectile energy (E_α/CB).

In the present work, the PE emission is significantly observed in some cases. Therefore, an attempt has been made to estimate the PE contribution at a given energy for a particular channel. It may be defined as the ratio of the pre-equilibrium cross section ($\sigma_{PE} = \sigma_{ER} - \sigma_{CN}$) to the evaporation residue cross section (σ_{ER}). The percentage PE contribution deduced from the analysis of data for different reaction channels has been plotted in Fig. 3 as a function of projectile energy normalized with the Coulomb barrier (E_α/CB). As can be observed from Fig. 3, in general, the percentage PE contribution is found to increase with normalized projectile energy. Furthermore, the threshold of PE emission for the different reaction channels is found to be different, depending on the associated Q value. It may, however, be pointed out that the PE contribution is found to be greater for the channels that consist of fewer PE particle(s)/nucleon(s) even at small projectile energy. This may be because the probability of single-nucleon emission is greater in the PE emission process. Moreover, it may not be out of place to mention that the PE contribution shows a dependence on initial excitation energy and/or Q value.

In summary, it may be inferred that the experimental data and the predictions of the statistical model code ALICE-91 reveal a significant contribution from the PE emission process at the studied energies. Furthermore, the input parameters—level density parameter $K = 8$, initial exciton number $n_0 = 4$ (with configuration $2p + 2n + 0h$), and $MFP = 1.0$—are found to be a suitable set of parameters to fit the experimental data in the present work. The percentage PE contribution for individual reaction products in different projectile-target combinations is found to be sensitive to the Q value of the reactions and/or the PE particle multiplicity. As such, it may be concluded that the PE emission is an important mode

of reaction in LI-induced reactions at the studied energies. Additional information about the PE emission may be obtained by PE particle(s) multiplicity and energy spectra measurement in equilibrium and PE emission processes, leading to the estimation of the entry point from PE emission to equilibrium processes.

The authors thank the Chairman, Department of Physics, and Director, VECC, Kolkata, India, for providing all the necessary facilities to carry out the experiment and analysis. A.Y. thanks the UGC, M.K.S. thanks the DST, and R.P. thanks the UGC and DST for providing financial support.

[1] N. Patronis *et al.*, Phys. Rev. C **75**, 034607 (2007).
[2] T. E. Rodrigues, M. N. Martins, C. Garcia, J. D. T. Arruda-Neto, J. Mesa, K. Shtejer, and F. Garcia, Phys. Rev. C **75**, 014605 (2007).
[3] J. Pal *et al.*, Phys. Rev. C **71**, 034605 (2005).
[4] W. Bauer and A. Botvina, Phys. Rev. C **52**, R1760 (1995).
[5] H. Feshbach, Rev. Mod. Phys. **46**, 1 (1974).
[6] H. Ejiri *et al.*, Nucl. Phys. **A305**, 167 (1978).
[7] E. Gadioli, E. Gadioli-Erba, J. J. Hogan, and B. V. Jacak, Phys. Rev. C **29**, 76 (1984).
[8] J. Ernst *et al.*, Z. Phys. A **328**, 333 (1987).
[9] M. Blann, Phys. Rev. Lett. **28**, 757 (1972); Phys. Rev. C **21**, 1770 (1980); M. Blann and H. Vonach, Phys. Rev. C **28**, 1475 (1983).
[10] H. Sakai, H. Ejiri, T. Shibata, Y. Nagai, and K. Okada, Phys. Rev. C **20**, 464 (1979).
[11] B. Strohmaier, M. Fassbender, and S. M. Qaim, Phys. Rev. C **56**, 2654 (1997).
[12] J. R. Wu and C. C. Chang, Phys. Rev. C **17**, 1540 (1978).
[13] M. L. Goldberger, Phys. Rev. **74**, 1269 (1948).
[14] K. Chen *et al.*, Phys. Rev. C **4**, 2234 (1971).
[15] A. Mignerey, M. Blann, and W. Scobel, Nucl. Phys. **A273**, 125 (1976).
[16] J. J. Griffin, Phys. Rev. Lett. **17**, 478 (1966).
[17] M. Blann, Annu. Rev. Nucl. Sci. **25**, 123 (1975).
[18] D. Agassi, H. A. Weidenmüller, and G. Mantzouranis, Phys. Rep. **22**, 145 (1975).
[19] E. Gadioli, E. Gadioli-Erba, and P. G. Sona, Nucl. Phys. **A217**, 570 (1973).
[20] E. P. Gavathas, A. D. Frawley, R. C. Kline, and L. C. Dennis, Phys. Rev. C **51**, 1991 (1995).
[21] C. Rubbia *et al.*, Report CERN/AT/95-94 (ET), 1995.
[22] B. P. Singh *et al.*, Nucl. Instrum. Methods Phys. Res. A **562**, 717 (2006).
[23] M. K. Sharma *et al.*, Eur. Phys. J. A **31**, 43 (2007), and references therein.
[24] R. P. Gardner *et al.*, Nucl. Instrum. Methods **93**, 163 (1971).
[25] J. Ernst *et al.*, Z. Phys. A **308**, 301 (1982).
[26] E. Browne and R. B. Firestone, *Table of Radioactive Isotopes* (Wiley, New York, 1986).
[27] M. Blann, NEA Data Bank, Report No. PSR-146, Gif-sur-Yvette, France (1991).
[28] M. K. Sharma *et al.*, Phys. Rev. C **70**, 044606 (2004); Nucl. Phys. **A776**, 83 (2006).
[29] V. F. Weisskopf and D. H. Ewing, Phys. Rev. **57**, 472 (1940).
[30] M. L. Goldberger, Phys. Rev. **74**, 1269 (1948).
[31] F. D. Becchetti and G. W. Greenlees, Phys. Rev. **182**, 1190 (1969).
[32] K. Kikuchi and M. Kawai, *Nuclear Matter and Nuclear Reactions* (North-Holland, Amsterdam, 1968).
[33] M. Blann, Nucl. Phys. **A213**, 570 (1973).
[34] S. N. Ghoshal, Phys. Rev. **80**, 939 (1950).

Reaction mechanism in the $^{16}O+^{27}Al$ system: Measurements and analysis of excitation functions and angular distributions

Manoj Kumar Sharma,[1,*] Unnati,[1] Devendra P. Singh,[1] Pushpendra P. Singh,[1] B. P. Singh,[1,†] H. D. Bhardwaj,[2] and R. Prasad[1]

[1]*Department of Physics, Aligarh Muslim University, Aligarh-202002, India*

[2]*Department of Physics, DSN, College, Unnao, India*

(Received 26 January 2007; published 12 June 2007)

To study the dynamics of heavy ion fusion reactions in the lower mass region, experiments were carried out to measure the cross sections of radioactive residues produced in the interaction of the ^{16}O ion with ^{27}Al target nucleus at 19 different energies in very close intervals covering the energy range from $\approx$58 to 94 MeV, using the well-known recoil catcher off-line γ-ray spectroscopy technique. The simulation of experimental data was performed using statistical-model-based computer codes, viz., CASCADE, PACE2, and ALICE-91. The analysis of measured excitation functions indicates that these residues are likely to be produced by complete fusion, incomplete fusion, and direct reaction processes. Furthermore, to confirm the contribution of different reaction channels, a complementary experiment was performed that measured the angular distributions of the residues produced in the $^{16}O+^{27}Al$ system at 85 MeV beam energy. The analysis of the results of both experiments indicates that at these energies, the direct reactions compete with complete fusion and incomplete fusion reaction processes.

DOI: 10.1103/PhysRevC.75.064608 PACS number(s): 25.70.Gh

I. INTRODUCTION

During the last couple of decades, efforts have been made to understand the dynamics of nuclear interaction in light and heavy particle induced reactions. In light particle induced reactions, two apparently different mechanisms such as the compound nucleus (CN) and the direct reactions appear to be dominant. In the CN mechanism, the interaction between projectile and target nucleus takes place in such a way that the excitation energy is shared statistically among all the constituent nucleons of the composite system so that memory of its formation is lost. The time scales involved in these reactions are typically $\approx 10^{-16}$ s. The CN reactions are important at relatively low energies and remain a fruitful source of information about nuclear structure. On the other hand, in a direct reaction (DR), the projectile interacts with a single or a few nucleons of the target nucleus. The time taken by the projectile to traverse the target nucleus is very short ($\approx 10^{-22}$ s), thus the energy required for the DR process is relatively high, suggesting only a few degrees of freedom are involved.

Furthermore, at energies between those of the compound nucleus and direct reactions, the preequilibrium (PE) emission of nucleons has been observed, reflecting the dynamics of an excited composite system formation leading to the equilibrated CN [1,2]. In PE emission, the particle emission is assumed to take place after the first projectile target interaction but prior to the establishment of the equilibrated compound nucleus. Some of the important features of PE emission are (1) slowly descending tails of excitation function, (2) forward peaked angular distribution of emitted particles, and (3) relatively large number of high energy particles than predicated by the CN mechanism.

To explain the mechanism of such reactions, several models have been proposed. At present, model-based computer codes are available that include preequilibrium emission to explain the complete features of the experimental data. It is now possible to theoretically describe the sequence of processes, which has led to the comprehensive description of a large set of cross section data for different projectile-nucleus interactions.

In recent years, with the availability of medium energy heavy ion (HI) accelerators, it has become possible to study the nuclei at higher excitation energies and angular momenta, where, along with complete fusion (CF) processes, such processes as incomplete fusion (ICF) or breakup fusion, deep-inelastic collision (DIC), quasielastic collision (QEC), direct reaction (DR), transfer reaction (TR), PE emission, etc., are also likely to occur [3]. Thus, in HI reactions, the cross section is shared predominantly among the following processes: those leading to complete fusion, deep-inelastic collision, and quasielastic collision.

As the energy increases, one observes, in addition to light particles, beam like particle also, evidently emitted at an early stage of the reaction known as ICF particles. This emission is referred to as breakup fusion or ICF. The interplay between fusion and breakup fusion processes takes place at beam energies as low as just above the Coulomb barrier [4–9]. This observation led to a renewed interest to the study of the dynamics of HI reactions. Furthermore, the different behaviors of HI interactions, which depend on the energy regime, entrance channel mass asymmetry, etc., are still some of the unanswered and important open questions.

There are several ways to classify HI interactions. One of them is in terms of the impact parameter [3]. At higher values of impact parameter, the DR may take place, leading to few nucleon transfer processes. However, at smaller impact parameter values, the CF, ICF, and DIC processes may be dominant. In complete fusion reactions, the incident ion is

*mks_amu@rediffmail.com

†bpsinghamu@gmail.com

completely absorbed by the target nucleus, forming an excited composite system from which particles and/or γ rays may be emitted after the formation of the equilibrated compound nucleus.

However, in the case of ICF, the projectile is assumed to break up in the vicinity of the nuclear field of the target nucleus into the fragments called projectile-like fragments (PLFs), and only one of the PLFs fuses with the target nucleus, while the remaining PLFs continue to move in the forward direction with approximately the same velocity as that of the incident ion. The ICF reactions have been reported to have the following characteristics: (1) a forward peaked angular distribution of PLFs, which are predominantly emitted at the beam velocity and are generally viewed as fast breakup of the projectile, (2) a linear momentum transfer less than that of complete fusion, resulting in a smaller range of the evaporation residues, (3) a relatively higher measured cross section than that predicted by statistical models, and (4) a higher energy of the direct α particles than that of the evaporation α particles from the equilibrated compound nucleus. Various models have been proposed to describe the dynamics of ICF reactions, but none of them is able to explain the experimental data over a large energy range and mass region as well. It may not be out of place to mention that there is no satisfactory theoretical support so far for ICF reactions that can be used to simultaneously explain complete and incomplete fusion processes.

Furthermore, DICs may also be likely at these energies, in which the mass of the resulting nuclei are close to the mass of the projectile and target nuclei. The deep-inelastic collision may be characterized by substantial dissipation of initial kinetic energy and angular momentum. The time scale at which DICs are expected to occur is less than the CN lifetime, but long enough for the exchange of a significant number of nucleons between the target and the projectile. One may get the information about the mechanism through the measurement and analysis of cross section data, recoil range, and angular distributions of the residues produced in the interaction of two heavy nuclei. The cross section data obtained for such channels have a wide range of applications. Therefore, the above study is not only an important subject in its own right, but also significant for its impact on related fields of investigation and for its rich variety of applications. In this context, a program of measurement and analysis of the cross sections of nuclear reactions induced by HI has been undertaken [10].

In the present work, the excitation functions (EFs) for radioactive residues produced in the interaction of ^{16}O ion with ^{27}Al have been measured in order to study the reaction dynamics, particularly in the low mass region. Most of the studies in which the occurrence of ICF was observed were carried out generally with heavier mass target nuclei. Though initial studies on incomplete fusion have been carried out at energies $\approx$10 MeV/nucleon using rare-earth targets [11], there are very few studies with lower mass target nuclei. One advantage of using a lighter mass system is to avoid the possibility of fission, which is one of the competing modes in HI reactions on heavier target nuclei at these energies. Furthermore, if heavier targets are used, the emission of α particles from the fused excited system is likely to be substantially reduced [12] because of the high Coulomb barrier. As a result, the emission of α particles in incomplete fusion channels may give rise to residues which may have very little contribution from complete fusion channels. Measurement and analysis of EFs [4,5] in HI reactions for heavier target nuclei have indicated that ICF is an important component of the reaction mechanism at these energies.

With the motivation to determine the contribution of incomplete fusion processes in light mass target nuclei, the measurement and analysis of the cross sections for the reaction channels $(2\alpha n)$, $(3\alpha 3p)$, $(3\alpha 3pn)$, $(4\alpha 2pn)$, and $(4\alpha 3p)$ produced in the ^{16}O+^{27}Al system have been carried out at 19 different energies at very close intervals covering the energy range from $\approx$58 to 94 MeV. There are mainly two experimental methods which are widely used to study the dynamics of HI reactions: (1) off-beam γ-ray spectrometry by the measurement and analysis of the excitation functions (EFs), recoil range distributions, and angular distributions of the residues produced in the projectile-target interaction using the activation technique and (2) in-beam γ-ray spectrometry by detecting the breakup α particles of the projectile, i.e, projectile-like fragments, in coincidence with the prompt γ rays of the populated residues using the particle-γ coincidence technique. The former is based on the measurement of the activity produced in radioactive residues using off-line γ-ray spectroscopy.

In the literature [13], the measurement of cross section data exists for the ^{16}O+^{27}Al system using the activation technique. Landenbaurer-Bellis *et al.* [13] measured the cross section for the reactions in the above system employing the activation technique in the energy range 10.5–1 MeV/nucleon, using a NaI (Tl) detector to identify γ rays of interest and an end-window gas flow proportional counter to resolve β decay. The energy spread of the data points are substantially large. It may, however, be pointed out that no theoretical interpretation of the data was made [13]. Furthermore, it has been mentioned that observed trend of the data indicates a CN mechanism. However, more recently, McKenna *et al.* [14] tried to reproduce the experimental data [13] in an experiment using a high intensity laser produced plasma beam. They also performed theoretical calculations [14] using the Monte Carlo code PACE2 [15]. They reported that residue ^{34}Cl is produced by the evaporation of two α particles and one neutron from the compound nucleus. Furthermore, the production of other radioisotopes, viz., ^{27}Mg, ^{24}Na, and ^{24}Ne, was attributed to the compound nucleus as well as to direct reactions. It is not out of place to mention here that incomplete fusion and deep-inelastic collision are also dominant mechanisms in HI reactions at these energies, and hence the contributions of these reaction channels are also required to be taken in to account.

In the present work, an attempt has been made to explain the experimentally measured cross sections using statistical-model-based computer codes, viz., CASCADE [16], PACE2 [15], and ALICE-91 [17]. To obtain complementary information about the processes involved in lighter mass symmetric systems, angular distributions of the residues produced in the ^{16}O+^{27}Al system have also been measured at 85 MeV beam energy. Experimental details are discussed in Sec. II of the paper; the analyses of the excitation functions and angular distributions are presented in Secs. III and IV, respectively. Conclusions are given at the end of the paper.

II. EXPERIMENTAL DETAILS

The experiments were performed at the Inter University Accelerator Centre (IUAC) formerly known as Nuclear Science Center (NSC), New Delhi, India, using the 15 UD Pelletron accelerator facility. The experiments for excitation functions and angular distribution measurements were carried out in the general-purpose scattering chamber (GPSC) of 1.5 m diameter dedicated for such studies, having an in-vacuum transfer facility. The time interval between the end of irradiation and the beginning of counting was minimized using in-vacuum transfer of samples from the scattering chamber to the counting system. Details of the measurements of excitations functions and annular distributions are given in the following subsections.

A. Excitation functions

The spectroscopically pure self-supporting foils of ^{27}Al (purity ≈99.999%) were rolled to obtain samples of the desired thickness. Target thickness plays a crucial role in each measurement. Therefore, measurement of target thickness must be as accurate as possible to obtain accuracy in the measured cross section data. In the present case, the thicknesses of the target as well as the catcher foils were determined using the α-transmission method. This method is based on the measurement of the energy lost by 5.485 MeV α particles obtained from a ^{241}Am source while passing through the target thickness. For thickness determination, the stopping power values were calculated using the program SRIM-2006. The measured thickness of ^{27}Al foils were ≈1.8 mg/cm^2. The Al samples and the degrader/catcher foils were cut into 1.2 × 1.2 cm^2 squares and pasted onto rectangular target holders having concentric holes of 1.0 cm diameter. In the present work, two stacks containing five alternating samples of natural Tm and Al and another two stacks containing five and four alternating samples of natural Tb and Al, respectively, were used for the EF studies. The samples of Tm and Tb served as energy degraders and catchers. In separate communications [18,19], the activations of the Tb and Tm samples were studied for the measurement of cross sections for a large number of channels. The calculations of energy loss in the stack were done using the energy range program SRIM-2006. Four stacks containing in all 19 ^{27}Al samples and an equal number of energy degraders were irradiated by the $^{16}O^{7+}$ beam at four different energies, i.e., 86, 88, 92, and 95 MeV. The irradiation of these four stacks covered the desired energy range ≈58 to 95 MeV. As the beam traverses the samples of the stack, the energy spread goes on increasing toward the last sample. As a typical example, the energy spread at ≈58 MeV is ≈2%. Keeping in mind the half-lives of interest, the irradiation of each stack was carried out for ≈8 h duration. The beam currents were ≈50 nA. The total charge collected in the Faraday cup was used to calculate the flux of the incident beam. Furthermore, to monitor the flux of the incident beam, in an auxiliary experiment, two Rutherford monitor detectors kept at ±30° with respect to the beam direction were used. The two readings of the flux agreed with each other within an uncertainty of about 5%. It may, however, be pointed out that the unreacted beam is dumped in the Faraday cup about 1 m away from the samples.

In the present work, the analysis of the $^{16}O+^{27}Al$ system is being presented which provides a data set of 19 points at very close energy intervals. The stacked foil activation technique followed by off-line γ-ray spectroscopy was employed to determine the cross sections for various reaction residues. In the stacked foil technique, the energetic beam traverses through all the samples with degrading beam energies; as such, it is possible to bombard different samples of the stack at different energies. The activities induced in the various samples were recorded by counting the Al samples as well as the degrader/catcher foils using a high-purity Ge γ-ray spectrometer coupled to a personal-computer-based multichannel analyzer setup employing the FREEDOM software [20]. The counts under photo peaks of interest were taken for the determination of cross section after proper background correction. The HPGe γ-ray spectrometer (resolution ≈2 keV for 1.33 MeV γ ray of ^{60}Co) was precalibrated for both energy and efficiency employing various standard γ sources such as ^{22}Na, ^{54}Mn, $^{57,60}Co$, ^{133}Ba, ^{137}Cs, and ^{152}Eu. To determine the geometry-dependent efficiency G_ϵ for γ rays of different energies, a standard source of ^{152}Eu of known strength was used. A typical plot of G_ϵ at 2 cm distance from the sample to the detector system is shown in Fig. 1. Relevant portions of the observed γ-ray spectrum of the irradiated ^{27}Al sample at 82 MeV ^{16}O beam are shown in Fig. 2.

The peaks in the observed γ-ray spectrum were assigned to different reaction residues on the basis of their characteristic energy of γ lines as well as measured half-lives. A typical curve used to determine the half-life of the residue ^{34m}Cl is shown in Fig. 3. A list of reactions, energies of the identified γ rays, and their branching ratios [21] are given in Table I.

The measured intensities of the characteristic γ rays were used to compute the reaction cross sections using the formula [22]

$$\sigma_r(E) = \frac{C_a \lambda \exp(\lambda t_l)}{N_o \phi P K(G_\epsilon)[1-\exp(-\lambda t_i)][1-\exp(-\lambda t_a)]}, \quad (1)$$

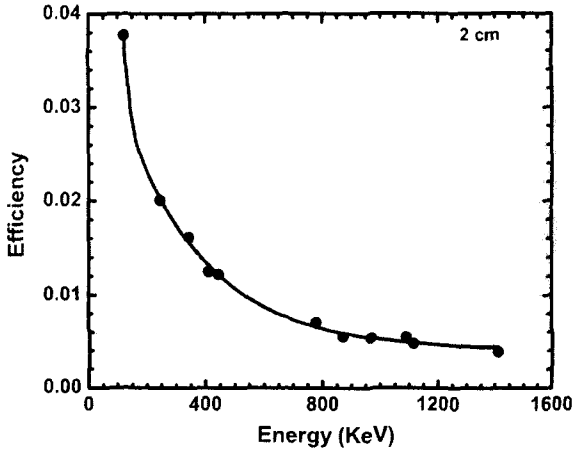

FIG. 1. Typical plot of photo peak efficiency of HPGe detector as a function of γ-ray energies of the ^{152}Eu source.

TABLE I. Reactions, measured half-lives, identified γ rays, and their branching ratios.

Sample no.	Reaction	Half-life	E_γ (keV)	Branching ratio (%)
1	^{27}Al(^{16}O, $2\alpha n$)^{34}Cl	32.2 min	146.5	40.5
2	^{27}Al(^{16}O, $3\alpha 3p$)^{28}Mg	20.9 h	400.5, 1342.3	36.0, 54
3	^{27}Al(^{16}O, $3\alpha 3pn$)^{27}Mg	9.4 min	843.7	73.0
4	^{27}Al(^{16}O, $4\alpha 2pn$)^{24}Na	14.6 h	1368	100
5	^{27}Al(^{16}O, $4\alpha 3p$)^{24}Ne	3.8 min	472.2	100

where C_a is the observed counts under the photo peak during the accumulation time t_a of the induced activity of decay constant λ, N_o the number of target nuclei irradiated for time t_i with a particle beam of flux ϕ, t_l the time lapse between the stop of irradiation and the start of counting, P the branching ratio of the characteristic γ ray, and G_ϵ the geometry-dependent efficiency of the detector for the γ ray of a given energy. Proper correction for the geometry-dependent efficiency was taken into account for each case. The factor $[1 - \exp(-\lambda t_i)]$, known as the saturation correction, takes care of the decay of evaporation residues during the irradiation. The corrections for the decay of the induced activity due to the delay between the stop of irradiation and the start of counting and during the data accumulation are taken into account via the factors $\exp(\lambda t_l)$ and $[1 - \exp(-\lambda t_a)]$, respectively. $K = [1 - \exp(-\mu x)/\mu x]$ is the correction for the self-absorption of the γ radiation in the sample thickness itself, where x is the thickness of the sample and μ is the energy-dependent γ-ray absorption coefficient.

The experimentally measured values of cross sections at different energies for the reactions ^{27}Al(^{16}O, $2\alpha n$)^{34}Cl, ^{27}Al(^{16}O, $3\alpha 3p$)^{28}Mg, ^{27}Al(^{16}O, $3\alpha 3pn$)^{27}Mg, ^{27}Al(^{16}O, $4\alpha 2pn$)^{24}Na, and ^{27}Al(^{16}O, $4\alpha 3p$)^{24}Ne are given in Table II.

B. Angular distributions

A separate experiment has also been carried out to measure the angular distribution of recoiling residues produced in the ^{16}O+^{27}Al system at 85 MeV beam energy. In this experiment, an Al target supported by Tm material of thickness $\approx$0.48 mg/cm^2 followed by a stack of thick annular concentric Al catcher foils was mounted in the irradiation chamber normal to the beam direction. Concentric annular aluminum catchers of thickness $\approx$0.3 mm with diameters 0.81, 1.29, 1.95, 2.64, 3.27, 5.46, and 6.4 cm were used to trap the recoiling nuclei emitted at different angles. A typical arrangement of the target and catcher assembly used for the angular distribution measurements is shown in Fig. 4. The arrangement of annular catchers was placed 1.8 cm behind the target for collecting the residues emitted in seven different angular ranges, viz., 0°–13° (most forward cone), 13°–21°, 21°–30°, 30°–39°, 39°–45°, 45°–60°, and 60°–64°. The irradiation was carried out for about 11 h with a beam current of $\approx$7 pnA. The activities induced in each catcher were followed off line for a couple of days. Typical γ spectra indicating the region of interest for different annular Al catcher rings covering the angular range from 0°–13° to 45°–60° is shown in Fig. 5. For identification of the reaction residues, the similar procedure is adopted, as discussed in Sec. II A. Further,

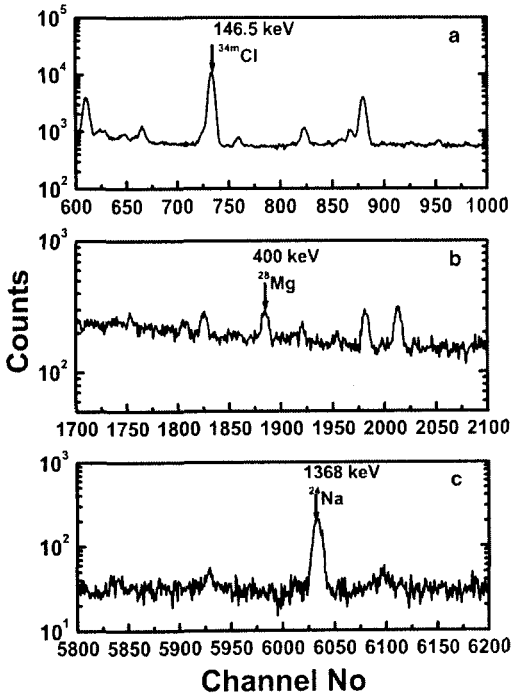

FIG. 2. Observed γ-ray spectrum of irradiated ^{27}Al sample at 82 MeV.

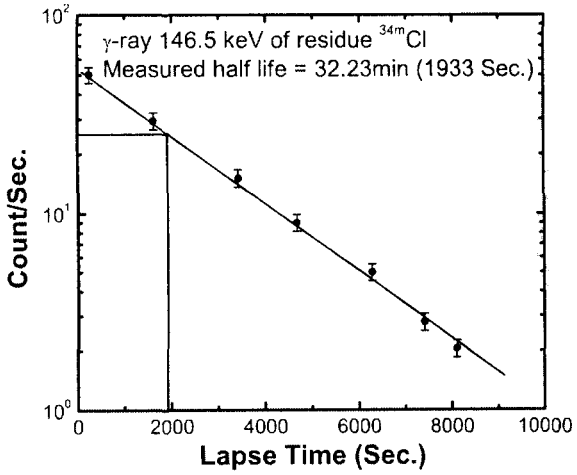

FIG. 3. Typical curve used to determine the half-live of the residue ^{34m}Cl.

TABLE II. Experimentally measured cross sections.

Lab energy (MeV)	$\sigma(^{34}Cl)$ (mb)	$\sigma(^{28}Mg)$ (mb)	$\sigma(^{27}Mg)$ (mb)	$\sigma(^{24}Ne)$ (mb)	$\sigma(^{24}Na)$ (mb)
58.0 ± 1.3	9.40 ± 1.69	–	–	–	0.46 ± 0.08
58.7 ± 1.3	14.57 ± 2.62	–	–	–	1 ± 0.18
66.5 ± 1.2	57.72 ± 10.39	–	–	–	0.94 ± 0.17
68.0 ± 1.2	62.70 ± 11.29	–	–	–	0.96 ± 0.17
68.2 ± 1.2	154.09 ± 27.74	–	–	–	0.275 ± 0.05
71.6 ± 1.1	115.49 ± 20.79	–	–	–	0.63 ± 0.11
75.4 ± 1.1	169.53 ± 30.52	–	–	–	0.89 ± 0.16
76.2 ± 1.1	100.98 ± 18.18	0.08 ± 0.01	–	–	1.35 ± 0.243
77.1 ± 1.0	126.40 ± 22.75	0.09 ± 0.01	–	–	1.17 ± 0.21
78.8 ± 1.0	95.32 ± 17.16	–	–	–	1.2 ± 0.22
81.8 ± 1.0	81.96 ± 14.75	2.48 ± 0.44	–	–	2.35 ± 0.42
82.0 ± 0.9	120.91 ± 21.76	–	–	–	1.37 ± 0.25
85.5 ± 0.6	84.79 ± 15.26	2.21 ± 0.4	–	0.12 ± 0.03	7.88 ± 1.41
85.9 ± 0.9	140.79 ± 28.26	3.11 ± 0.5	–	0.11 ± 0.02	5.15 ± 0.9
88.2 ± 0.6	15.53 ± 2.80	1.53 ± 0.26	0.22 ± 0.05	0.36 ± 0.09	1.03 ± 0.18
88.5 ± 0.8	–	0.42 ± 0.05	0.2 ± 0.05	–	1.58 ± 0.28
91.4 ± 0.6	5.43 ± 0.98	–	0.08 ± 0.02	0.22 ± 0.05	1.15 ± 0.20
93.4 ± 0.8	8.26 ± 1.48	0.4 ± 0.08	0.11 ± 0.02	0.12 ± 0.05	1.5 ± 0.27
94.4 ± 0.6	4.74 ± 0.85	0.2 ± 0.06	0.1 ± 0.03	0.1 ± 0.03	1.33 ± 0.24

the intensities of the characteristic γ rays were used to compute the reaction cross sections at different angular ranges, using Eq. (1), given in Sec. II A of this paper. The efficiency of the detector was obtained for a point source. However, the annular catchers used for trapping the reaction residues had a finite area; therefore, a proper correction [23] was applied to deduce the cross sections for the residues of interest.

III. ANALYSIS

To obtain information regarding the mechanism involved in these reactions, the comparison of measured excitation functions was performed using three computer codes: CASCADE [16], PACE2 [15], and ALICE-91 [17]. Brief details of these codes along with their important parameters, etc., are discussed in the following sections.

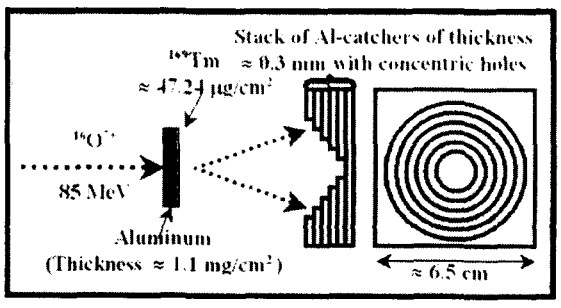

FIG. 4. Typical arrangement of target-catcher assembly used for the angular distribution measurements covering the annular range from 0–13° to 45–60°.

A. Calculations with CASCADE

The code CASCADE [16] is based on Hauser-Feshbach theory [24] and is generally used to obtain the theoretical estimates of cross sections using the CN mechanism. It does not consider the possibility of incomplete fusion (ICF) and PE emission. The main advantage of this code is that it provides the option of scaling the default parameters (i.e., fission barrier, rigid-body momentum of inertia) to obtain cross section values in the mass region of interest. The decay probabilities are

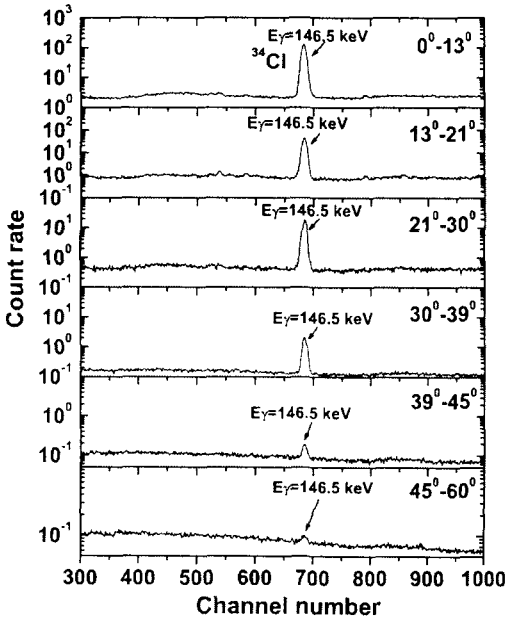

FIG. 5. Typical γ-spectra Al-catcher rings covering the annular range from 0°–13° to 45°–60°.

determined by the level densities of the daughter nuclei and the barrier penetrabilities for the various channels. The optical model potentials of Becchetti and Greenlees [25] are used for calculating the transmission coefficients for protons and neutrons, and the optical model potential of Satchler [26] is used for α particles. The Fermi gas model is used for calculating the level densities for the product nuclei.

The partial cross section for the formation of the compound nucleus of spin J and parity π from a projectile and a target nucleus of spins J_P and J_T, respectively, at center-of-mass energy E is given by [27]

$$\sigma(J,\pi) = \frac{\pi\lambda^2}{4\pi^2}\frac{(2J+1)}{(2J_P+1)(2J_T+1)}\sum_{S=|J_P-J_T|}^{J_P+J_T}\sum_{L=|J-S|}^{J+S} T_L(E), \tag{2}$$

where T_L are the transmission coefficients, which depend on the energy and the orbital angular momentum L, and $S(=J_P+J_T)$ is the channel spin.

The total fusion cross section for the maximum angular momentum L_c of the compound nucleus is given by

$$\sigma_L = \frac{\pi\lambda^2}{4\pi^2}\sum_{L=0}^{L_c}(2L+1)T_L(E). \tag{3}$$

In statistical model calculations, the critical angular momentum L_c for compound nucleus fusion may be sharp, or it may have some overlap from L_c to higher L. The effective moment of inertia I may be obtained from the low-lying states of the isotope using the relation

$$I = \frac{2}{5}mr^2, \tag{4}$$

where r is the radius of spherical nucleus given by $r_o A^{1/3}$.

The level density formula implies a yrast line,

$$E_{\rm rot}(J) = \frac{J(J+1)\hbar^2}{2I} + \Delta, \tag{5}$$

where Δ is the pairing energy which determines the zero point of the effective excitation energy. In this code, the level density parameter constant K and the ratio of actual moment of inertia to the rigid-body moment of inertia of the excited system F_θ are the two important parameters which may be varied to match the experimental data. In HI induced reactions, the high angular momentum and excitation energy are expected to have considerable influence on the deexcitation cascade. Because in HI reactions, the increasing excitation energy also increases the angular momentum; therefore, the deformation of the nucleus due to the angular momentum effect may also be quite substantial. In calculations, the deformation effects may be included by using an angular momentum dependent moment of inertia, which results in the deviation of the yrast line from that calculated assuming the nucleus to be a rigid sphere. The level density parameter a_f at the saddle point, which may be obtained from the relation $a_f = A/D_{AF}$, where A is the mass number of the compound nucleus and D_{AF} is a free parameter, may be varied to match the experimental data. It has been observed that the parameter D_{AF} has considerable influence on calculated EFs in the higher energy region.

It may, however, be pointed out that a value of $K > 10$ may give rise to the anomalous effects in particle multiplicity [28]. In the present work, the calculations were performed consistently using the set of parameters which are widely accepted and were used in our recent publication [19]. Here, calculations have been performed taking a value of $K = 8$.

It may also be pointed out that the residue ^{34}Cl produced via the ^{27}Al(^{16}O, $2\alpha n$) channel has metastable as well as ground states. In the present work, the metastable state of the residue ^{34m}Cl was observed through the 146.3 keV γ ray of intensity 40.5%. Since the intensity of the ground state of the residue ^{34g}Cl is very low, the ground state of ^{34g}Cl could not be observed. The production cross sections of the residue ^{34m}Cl were converted into the total cross section of the residue ^{34}Cl by using the standard radioactive decay method. Since the code CASCADE gives the total production cross section of the residue, it is reasonable from a physics point of view to compare the total cross section of the residue ^{34}Cl with the calculations.

The experimentally measured and theoretically calculated EF for the reaction ^{27}Al(^{16}O, $2\alpha n$)^{34}Cl is shown in Fig. 6. The measured values of the cross sections for the residue ^{34}Cl by Landenbaurer-Bellis *et al.* [13], which has some contribution from the residue ^{38}Cl, are also shown. As can be seen from this figure, the measured values [13] of the cross sections of the residue ^{34}Cl have large uncertainties in the energy scale. In the present work, the energy uncertainty resulting from the finite thickness of the sample is much smaller. Furthermore, in the energy range of interest, Landenbaurer-Bellis *et al.* [13] have effectively three data points, whereas in the present work, the measurements were carried out giving 19 data points, indicating a precise measurement at a very close energy interval, as indicated in Fig. 6. As has already been mentioned, the code CASCADE does not take into account the possibility of incomplete fusion processes; therefore, the enhancement of measured cross sections as compared with the calculated EFs for the reaction ^{27}Al(^{16}O, $2\alpha n$)^{34}Cl may be attributed to the ICF process.

The experimentally measured EFs for the reactions ^{27}Al(^{16}O, $3\alpha 3p$)^{28}Mg, ^{27}Al(^{16}O, $3\alpha 3pn$)^{27}Mg, ^{27}Al(^{16}O, $4\alpha 2pn$)^{24}Na, and ^{27}Al(^{16}O, $4\alpha 3p$)^{24}Ne are shown in Figs. 7–10, where the solid curves guide the eye to

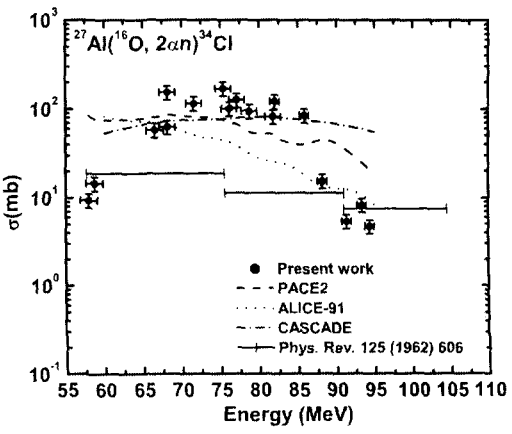

FIG. 6. Experimentally measured and theoretically calculated EFs. Literature values [13] are also shown.

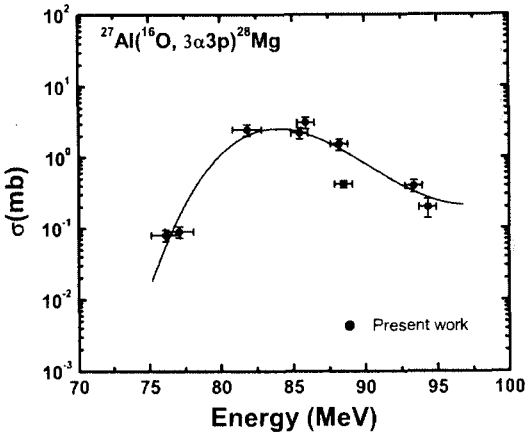

FIG. 7. Experimentally measured EFs. Solid curve guides the eye to the experimental data by curve fitting.

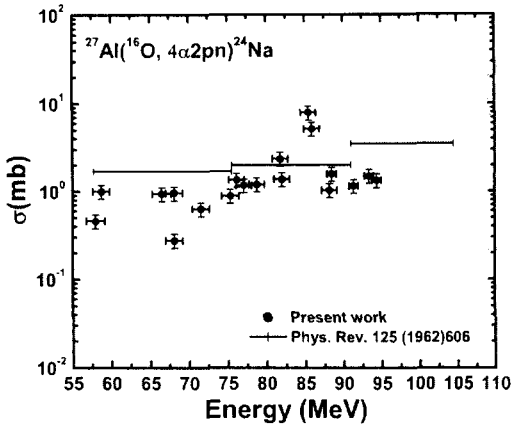

FIG. 9. Experimentally measured EFs. Literature values are also shown.

the experimental data by curve fitting. In Fig. 9, the literature values [13] of the cross sections of the residue ^{24}Na are also shown. On the basis of the trends of these curves, Landenbaurer-Bellis *et al.* [13] concluded that these reactions are formed by evaporation processes referred to as the compound nucleus mechanism. Landenbaurer-Bellis *et al.* [13] in their study of the $^{16}O+^{27}Al$ system did not compare the data with theoretical simulations. Since the calculated values of EFs using code CASCADE for these reactions are negligibly small, they are not shown in Figs. 7–10, thus the observed enhancement by several orders of magnitude over their negligible theoretical predictions for these channels may be attributed to the fact that these reactions are likely to be populated by some processes other than CN processes. Furthermore, to confirm whether these reactions are formed by CF or ICF processes, the angular distributions of these recoiling residues produced in the $^{16}O+^{27}Al$ system have also been measured, as discussed in Sec. IV of the paper.

B. Calculations with PACE2

The theoretical estimate of the cross sections for the evaporation residues has also been obtained using code PACE2 [15], which is based on a statistical approach. It uses a Monte Carlo procedure to determine the decay sequence of an excited nucleus using the Hauser-Fechbach formalism. The angular momentum projections are calculated at each stage of deexcitation, which enables the determination of the angular distribution of the emitted particles. The main advantage of Monte Carlo calculations is that they provide correlations between various quantities, such as particles and γ rays or angular distribution of particles. The evaporation cross sections of the residues are calculated using the Bass formula [29]. The code provides the ability to have an event-by-event traceback of the entire decay sequence from the CN system into any one of the exit channels. The optical model parameters for neutron, proton, and α emission were taken from Perey and Perey [15]. The γ-ray strength functions for $E1$, $E2$, and $M1$ transitions were taken from tables of Endt [30]. This code has been modified to take into account the excitation energy dependence of the level density parameter using the prescription of Kataria *et al.* [31]. In this code, the level density parameter $a = A/K$ is one of the important parameters, where

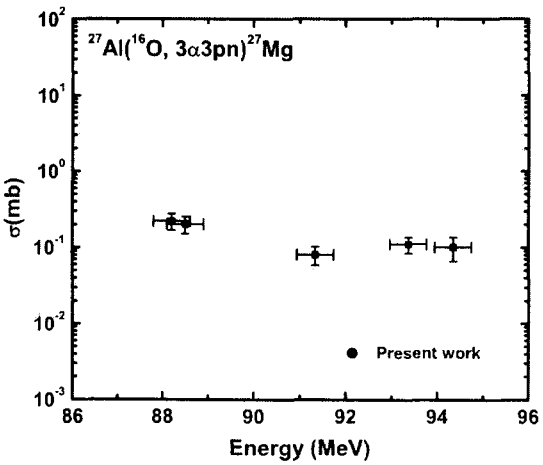

FIG. 8. Experimentally measured EFs.

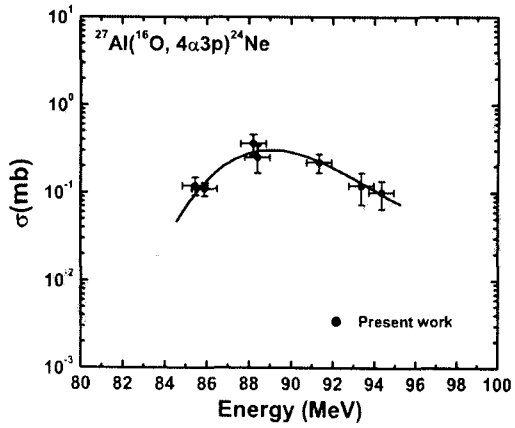

FIG. 10. Experimentally measured EFs. Solid curve guides the eye to the experimental data by curve fitting.

A is the mass number of the compound nucleus and K is a free parameter. The value of K may be varied to match the experimental data. In the present work, a value of $K = 8$ has been taken.

The theoretically calculated EFs using the code PACE2 for the reaction ^{27}Al(^{16}O, $2\alpha n$)^{34}Cl are also shown in Fig. 6 as the dashed curve. The observed enhancement of the measured EFs as compared with the theoretical calculations again indicates that the residue ^{34}Cl may not be produced only by the complete fusion process, but also by some other process such as incomplete fusion. The theoretical calculations for the reactions ^{27}Al(^{16}O, $3\alpha 3p$)^{28}Mg, ^{27}Al(^{16}O, $3\alpha 3pn$)^{27}Mg, ^{27}Al(^{16}O, $4\alpha 2pn$)^{24}Na, and ^{27}Al(^{16}O, $4\alpha 3p$)^{24}Ne give cross sections which are negligibly small, and hence no comparison of the experimental data with the simulations of this code is made in Figs. 7–10. Thus, it may be concluded that the significant contribution to these reaction channels comes from processes other than complete fusion.

C. Calculations with ALICE-91

The code ALICE-91 [17], developed by M. Blann, may be used to calculate the equilibrium as well as preequilibrium (PE) emission cross sections in light and heavy ion induced reactions. The compound nucleus calculations in this code are performed using the Weisskopf-Ewing model [32], while the PE component is simulated using the geometry-dependent hybrid model [33]. In this code, the possibility of incomplete fusion is not taken into account. The particles that could be emitted are neutron, proton, deuteron, and α particles. The code can calculate the reaction cross sections for the residual nuclei up to mass 11 and 9 a.u. away from the compound nucleus. The Myers-Swiatecki/Lysekil mass formula [34] is used for calculating Q values and binding energies of all the nuclei in the evaporation chain. The inverse reaction cross sections used in the code are calculated using the optical model [35] subroutines, although there is also an option of using the classical sharp cutoff model. The transmission coefficients are calculated using the parabolic model of Thomas [36] for heavy ions. Calculations for PE emission in this code are done assuming equipartition of energy among the initial excited particles and holes. The mean free path (MFP) for intranuclear transition rates may be calculated either from the optical model potential parameters of Becchetti and Greenlees [25] or from Pauli-corrected nucleon-nucleon cross sections [37,38]. In the present calculations, the optical potentials of Becchetti and Greenlees [25] were used.

Level densities of the residue in code ALICE-91 may be calculated either from the Fermi gas model or from the constant temperature form. The Fermi gas model gives [39]

$$\rho(U) = (U - \delta)^{-5/4} \exp\left[2\sqrt{a(U - \delta)}\right] \tag{6}$$

where δ is the pairing term and U is the excitation energy of the nucleus. The level density parameter a is taken as A/K, A being the mass number of the nucleus and K is an adjustable parameter. The level density $\rho(U)$ in constant temperature form is given as [40]

$$\rho(U) \propto \frac{1}{T}\varepsilon^{U/T}. \tag{7}$$

The differential cross section for emitting a particle with channel energy ε may be written as (cross section per unit energy to emit a particle of type ν)

$$\frac{d\sigma}{d\varepsilon_\nu} = \frac{\pi\lambda^2}{4\pi^2}\sum_{I=|0|}^{\infty}(2I+1)T_I(2S_\nu+1) \times \sum_{l=|0|}^{\infty}T^l{}_\nu(\varepsilon)\sum_{J=|I-l|}^{I+l}\rho(\varepsilon, J)/D, \tag{8}$$

where λ is the de Broglie wavelength of the incident ion, T_l the transmission coefficient of the lth partial wave of the incident ion, $\rho(\varepsilon, J)$ the spin-dependent level density for the residual nucleus, D the integral of numerator over all particles and emission energies, and ε the excitation energy of the compound nucleus. S_ν is the intrinsic spin of the particle ν, and $T^l_\nu(\varepsilon)$ is the transmission coefficient for the particle ν with kinetic energy ε and orbital angular momentum l.

In the Weisskopf-Ewing calculations, the nuclear moment of inertia is infinite; hence there is no energy tied to rotation, thus no level density cutoff at high spin. This code does not take into account the angular momentum involved in heavy ion reactions. However, the heavy ion projectile imparts large angular momentum to the composite system having a finite moment of inertia and hence greater rotational energy. Due to nuclear rotation, a nucleus with a given angular momentum J cannot have energy below a minimum value $E_J^{\min}$, that is,

$$E_J^{\min} \approx J(J+1)\frac{\hbar^2}{2I}. \tag{9}$$

Here, I is the moment of inertia of the composite nucleus.

In this code, the level density parameter a, the MFP multiplier COST, and initial exciton number n_0 are some of the important parameters. a largely affects the equilibrium component, while n_0 and COST govern the preequilibrium component. a is calculated from $a = A/K$. In code ALICE-91, the intermediate states of the system are characterized by the excitation energy E and number n_p of excited particles and n_h of excited holes. Particles and holes are defined relative to the ground state of the nucleus and are called excitons. The initial configuration of the compound system defined by the exciton number $n_0 = (n_p + n_h)$ is an important parameter of PE formalism. In the present work, a value of $n_0 = 16$ with configuration $(8p + 8n + 0h)$ has been found to satisfactorily reproduce the experimental data, where p, n and h represent the number of excited protons, neutrons, and holes, respectively. The code ALICE-91 calculates two-body nuclear transition rates using Pauli-corrected free nucleon-nucleon scattering cross section data. The actual MFP inside the nucleus may be quite different from the one calculated using free nucleon-nucleon scattering data. To compensate for this difference, a parameter COST is provided in the code ALICE-91. A value of COST greater than zero means a smaller value of the actual MFP for nucleon-nucleon scattering inside the composite excited nucleus. In the present work, a value

of COST = 2 is found to reproduce the experimental data satisfactorily.

When ALICE-91 calculations with the above-mentioned parameter values were compared with their experimental counterparts, it was observed that the maxima of the measured EFs were at higher energies than those of the calculated EFs. This is to be expected, because in ALICE-91 calculations the angular momentum effects are not taken into account. In HI induced reactions, the incident particle imparts relatively larger angular momentum to the composite system. If, in the last stages of nuclear deexcitation, higher angular momentum inhibits particle emission more than it does γ emission, then the peak of the excitation function corresponding to the particle emission mode will be shifted to higher energies [41]. The effect is more pronounced in heavy ion reactions than in light ion reactions, since the rotational energy is much greater in HI reactions. An estimate of the possible shift due to angular momentum effects may be made from the nuclear rotational energy. For a rigid body, the rotational energy is given by $E_{\rm rot} \approx (m/M)E_{\rm lab}$. Here, m/M is the ratio of the projectile and target nucleus masses and $E_{\rm lab}$ is the incident energy [41]. Since the angular momentum effects have not been considered in the Weisskopf-Ewing calculations of the present version of the ALICE-91 code, it is desirable to shift the calculated EFs by the amount approximately equal to $E_{\rm rot}$ as calculated above. In the present work, the calculated EFs have been shifted by $E_{\rm rot}$ on the energy scale. The experimentally measured and theoretically calculated EFs for the reaction $^{27}Al(^{16}O, 2\alpha n)^{34}Cl$ are shown in Fig. 6, where the dotted curve shows the theoretical calculation done using code ALICE-91. The observed enhancement of the measured EFs compared with the theoretical calculations for the reaction $^{27}Al(^{16}O, 2\alpha n)^{34}Cl$ done by this code indicates that the residue ^{34}Cl may not be produced by complete fusion but by some other processes such as ICF. Furthermore, the measured EFs for the reactions $^{27}Al(^{16}O, 3\alpha 3p)^{28}Mg$, $^{27}Al(^{16}O, 3\alpha 3pn)^{27}Mg$, $^{27}Al(^{16}O, 4\alpha 2pn)^{24}Na$, and $^{27}Al(^{16}O, 4\alpha 3p)^{24}Ne$ are shown in Figs. 7–10. The theoretical calculations for these reactions give cross sections that are negligibly small, similar to the codes CASCADE and PACE2, while the measured EFs for these channels have substantial cross sections. As such, it may be concluded that after including PE emission, which is one of the dominant mode of reaction mechanisms in heavy ion reactions, the experimental data could not be reproduced, indicating the presence of a reaction mechanism other than CF and PE processes.

IV. ANGULAR DISTRIBUTIONS

The analysis of EFs for the presently measured reactions, as mentioned in Secs. III A–III C, clearly indicates that these reactions have significant contributions other than those of CF and ICF processes. To confirm the reaction mechanism involved, a specially designed experimental setup was used as shown in Fig. 4. In this experiment, an Al target supported by a natural thulium material of thickness $\approx$0.48 mg/cm^2 followed by a stack of thick annular concentric Al catcher foils was used. Depending on the momentum transfer from the projectile to the composite system, the residues formed by CF and ICF processes will be trapped in the concentric annular aluminum catchers at different angles. The residues that are expected to be populated by a mechanism such as a direct reaction may be stopped within the thulium layer. The measured angular distributions for the reaction $^{27}Al(^{16}O, 2\alpha n)^{34}Cl$ is shown in Fig. 11. Two peaks are observed: one around 0°–13° can be assigned to the residues populated by complete fusion, and the other peak in the angular range 45°–60° can be assigned to the residues populated by ICF processes.

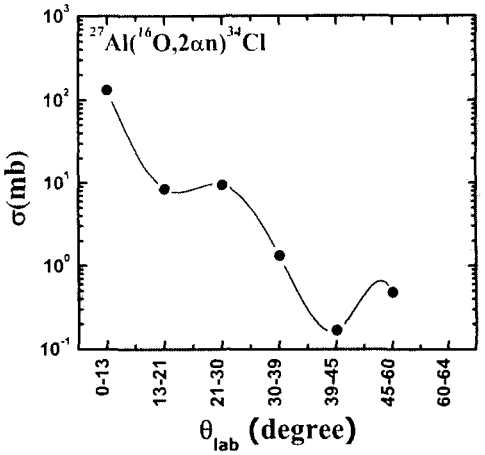

FIG. 11. Measured angular distributions for reaction $^{27}Al(^{16}O, 2\alpha n)^{34}Cl$.

Note that out of the five reactions identified in the EF measurements, only the γ ray of 146.5 keV corresponding to the reaction $^{27}Al(^{16}O, 2\alpha n)^{34}Cl$ could be identified from its energy as well as the half-life of residue ^{34}Cl in the angular distribution measurements. The residues formed by CF are likely to recoil in the forward cone, as such peaking of angular distribution around 0° indicates the population of residue ^{34}Cl via CF. However, the same residue ^{34}Cl when populated by ICF of residue ^{16}O will show peaks at much higher angles. Therefore, it may be concluded that the basic mechanism of population of ^{34}Cl may be based on both CF and ICF processes. However, the EF analysis has clearly indicated that the other reactions, i.e., $^{27}Al(^{16}O, 3\alpha 3p)^{28}Mg$, $^{27}Al(^{16}O, 3\alpha 3pn)^{27}Mg$, $^{27}Al(^{16}O, 4\alpha 2pn)^{24}Na$, and $^{27}Al(^{16}O, 4\alpha 3p)^{24}Ne$, are not likely to be populated via the CF process. The same is reflected from the angular distribution measurements, since no peak corresponding to these residues is identified in the γ-ray spectra of the angular distribution data. Thus, those residues are not likely to be populated via either complete or incomplete fusion processes. In direct reactions, the ejectile takes away a large fraction of the energy; hence, the residues formed may have ranges much smaller than those of residues formed by CF and/or ICF processes and may be trapped in the thulium layer.

V. CONCLUSIONS

Excitation functions for the reactions $^{27}Al(^{16}O, 2\alpha n)^{34}Cl$, $^{27}Al(^{16}O, 3\alpha 3p)^{28}Mg$, $^{27}Al(^{16}O, 3\alpha 3pn)^{27}Mg$, $^{27}Al(^{16}O, 4\alpha 2pn)^{24}Na$, and $^{27}Al(^{16}O, 4\alpha 3p)^{24}Ne$ produced in the $^{16}O+^{27}Al$ system have been measured in the energy range

≈58–94 MeV. Theoretical calculations based on three different computer codes have been carried out using well-accepted parameters. The codes PACE2 and CASCADE used in the present work are based on Hauser-Feshbach theory for compound nucleus calculations; however, the code ALICE-91 is based on the Weisskopf-Ewing model for compound nucleus calculations and the geometry-dependent hybrid model for simulating preequilibrium emission. Though preequilibrium emission may have considerable influence on the measured cross sections at relatively higher energies, even the ALICE-91 calculations which include preequilibrium emission are not found to reproduce the experimental data. The present analysis indicates that the residues ^{27,28}Mg, ^{24}Na, and ^{24}Ne are not populated either via complete or incomplete fusion processes, because theoretical calculations based on all these codes give negligible value of cross sections for their production. At present, we have no satisfactory explanation for the observed high cross sections for these channels; however, Landenbaurer-Bellis *et al.* [13] have attributed their production to a direct reaction mechanism. From the study of the angular distributions of these residues, we have concluded that in the case of complete fusion, the residues are emitted in the forward cone along the beam direction; while for incomplete fusion, the recoiling residues emerge at relatively large angles with respect to the beam direction, as expected. As such, angular distributions of residues with respect to the beam direction may also provide complementary information about the complete and incomplete fusion processes. The analysis of angular distribution data has clearly indicated the significant contribution of the ICF process in the ^{27}Al(^{16}O, $2\alpha n$)^{34}Cl reaction.

ACKNOWLEDGMENTS

The authors are thankful to the Director, NSC, New Delhi, for extending all the facilities for carrying out the experiment. We are also thankful to Dr. R. K. Bhaumik, for all his support during the experiment. We also thank the Chairman, Department of Physics, AMU for providing all the necessary facilities. One of the authors (MKS) thanks the Department of Science and Technology, New Delhi, for providing financial support through Project No. SR/FTP/PS-46/2003.

[1] M. Blann, Nucl. Phys. **A235**, 211 (1974).
[2] M. Blann, Annu. Rev. Nucl. Sci. **25**, 123 (1975).
[3] P. E. Hodgson, *Nuclear Heavy Ion Reactions* (Clarendon, Oxford, 1978).
[4] P. Vergani, E. Gadioli, E. Vaciago, E. Fabrici, E. Gadioli Erba, M Galmarini, G. Ciavola, and C. Marchetta, Phys. Rev. C **48**, 1815 (1993).
[5] M. Crippa, E. Gadioli, P. Vergani, G. Ciavola, C. Marchetta, and M. Bonardi, Z. Phys. A **350**, 121 (1994).
[6] M. Cavinato, E. Fabrici, E. Gadioli, E. Gadioli Erba, P. Vergani, M. Crippa, G. Colombo, I. Redaelli, and M. Ripamonti, Phys. Rev. C **52**, 2577 (1995).
[7] I. Tserruya *et al.*, Phys. Rev. Lett. **60**, 14 (1988).
[8] D. J. Parker, J. Asher, T. W. Conlon, and N. Naqib, Phys. Rev. C **30**, 143 (1984).
[9] D. J. Parker, J. J. Hogan, and J. Asher, Phys. Rev. C **35**, 161 (1987).
[10] Manoj Kumar Sharma, Ph.D. thesis, Aligarh Muslim University, 2002.
[11] J. Wilczynaski, K. Siwek-Wilczynaski, J. VanDriel, S. Gonggrip, D. C. J. M. Hangeman, R. V. F. Janssens, J. Lukasiak, R. H. Siemssen, and S. Y. Van der Werf, Nucl. Phys. **A373**, 109 (1982).
[12] S. Chakrborty, B. S. Tomar, A. Goswami, S. K. G. K. Gubbi, S. B. Manohar, Anil Sharma, B. B. Kumar, and S. Mukherjee, Nucl. Phys. **A678**, 355 (2000).
[13] Inge-Maria Ladenbaurer-Bellis, Ivor L. Preiss, and C. E. Anderson, Phys. Rev. **125**, 606 (1962).
[14] P. McKenna *et al.*, Phys. Rev. Lett. **91**, 075006 (2003).
[15] A. Gavron, Phys. Rev. C **21**, 230 (1980).
[16] F. Puhlhofer, Nucl. Phys. **A280**, 267 (1977).
[17] M. Blann, NEA Data Bank, Gif-sur-Yvette, France, Report PSR-146, 1991 (unpublished).
[18] M. K. Sharma, Unnati, B. K. Sharma, B. P. Singh, H. D. Bhardwaj, R. Kumar, K. S. Golda, and R. Prasad, Phys. Rev. C **70**, 044606 (2004).
[19] M. K. Sharma, Unnati, B. P. Singh, H. D. Bhardwaj, R. Kumar, K. S. Golda, and R. Prasad, Nucl. Phys. **A776**, 83 (2006).
[20] FREEDOM, Data acquisition and analysis system designed to support the accelerator-based experiments at the Nuclear Science Centre, New Delhi, India.
[21] E. Browne and R. B. Firestone, *Table of Radioactive Isotopes* (John Wiley & Sons, New York, 1986).
[22] M. K. Sharma, B. P. Singh, S. Gupta, M. M. Muthafa, H. D. Bhardwaj, and R. Prasad, J. Phys. Soc. Jpn. **72**, 1917 (2003).
[23] R. P. Gardner and K. Verghese, Nucl. Instrum. Methods **93**, 163 (1971).
[24] W. Hauser and H. Feshbach, Phys. Rev. **87**, 336 (1952).
[25] F. D. Becchetti and G. W. Greenlees, Phys. Rev. **182**, 1190 (1969).
[26] G. R. Satchler, Nucl. Phys. **70**, 177 (1965).
[27] J. M. Blatt and V. F. Weisskopf, *Theoretical Nuclear Physics* (John Wiley & Sons, New York, 1952).
[28] J. P. Lestone, Phys. Rev. C **53**, 2014 (1996).
[29] R. Bass, Nucl. Phys. **A231**, 45 (1974).
[30] P. M. Endt, At. Data Nucl. Data Tables **26**, 47 (1981).
[31] S. K. Kataria, V. S. Ramamurthy, and S. K. Kapoor, Phys. Rev. C **18**, 549 (1978).
[32] V. F. Weisskopf and D. H. Ewing, Phys. Rev. **57**, 472 (1940).
[33] M. Blann, Phys. Rev. Lett. **27**, 337 (1971).
[34] W. D. Myers and W. J. Swiatecki, Ark. Fys. **36**, 343 (1967).
[35] M. Blann, Phys. Rev. C **21**, 1770 (1980).
[36] T. D. Thomas, Nucl. Phys. **53**, 577 (1964).
[37] K. Kikuchi and M. Kawai, *Nuclear Matter and Nuclear Reactions* (North-Holland, Amsterdam, 1968).
[38] M. Blann, Nucl. Phys. **A213**, 570 (1973).
[39] M. Blann and H. Vonach, Phys. Rev. C **28**, 1475 (1983).
[40] M. Blann, G. Reffo, and F. Fabbri, Nucl. Instrum. Methods A **265**, 490 (1988).
[41] D. Bodansky, Annu. Rev. Nucl. Sci. **12**, 79 (1962).

Eur. Phys. J. A **31**, 43–51 (2007)
DOI 10.1140/epja/i2005-10318-5

THE EUROPEAN PHYSICAL JOURNAL A

Regular Article – Nuclear Structure and Reactions

A study of pre-equilibrium emission of neutrons in ^{93}Nb(α, xn) reactions

Manoj Kumar Sharma[1,a], H.D. Bhardwaj[2], Unnati[1], Pushpendra P. Singh[1], B.P. Singh[1,b], and R. Prasad[1]

[1] Department of Physics, Aligarh Muslim University, Aligarh (UP)-202 002, India
[2] Department of Physics, DSN College, Unnao (UP)-209 801, India

Received: 20 June 2005 / Revised: 13 October 2006
Published online: 22 January 2007 – © Società Italiana di Fisica / Springer-Verlag 2007
Communicated by C. Signorini

Abstract. With a view to study the pre-equilibrium emission mechanism in α-induced reactions the excitation functions for ^{93}Nb$(\alpha, n)^{96m}$Tc, ^{93}Nb$(\alpha, n)^{96}$Tc, ^{93}Nb$(\alpha, 2n)^{95m}$Tc, ^{93}Nb$(\alpha, 2n)^{95g}$Tc and ^{93}Nb$(\alpha, 3n)^{94}$Tc reactions have been measured in the energy range threshold to $\approx$ 10 MeV/nucleon using the activation technique. The measured excitation functions have also been compared with theoretical predictions based on the semi-classical code, which takes into account compound nucleus as well as pre-equilibrium emission. The analysis of the data indicates significant contribution from pre-equilibrium emission at these energies particularly in the high-energy tail portion of EFs. The effect of the variation of the parameters used in the code has been studied. The isomeric cross-section ratios have also been measured. It has been observed that the pre-equilibrium fraction increases rapidly with the increase in α-particle bombarding energy.

PACS. 25.55.-e ^{3}H-, ^{3}He-, and ^{4}He-induced reactions – 27.60.+j $90 \leq A \leq 149$

1 Introduction

The availability of medium-energy particle accelerators has made possible the study of charged-particle–induced reactions, which are important in large-scale developments. Applications of measured cross-section data may be found in the nuclear-energy generation and waste management and also in nuclear medicine. The knowledge of cross-sections for neutron emission channels is important in reactor technology, particularly in the recently proposed accelerator driven sub-critical (ADS) reactors, typically known as energy amplifiers. For all these applications, an improved understanding of charged-particle interaction is needed for transport calculations and radiation effects. The charged-particle–induced reactions are also important for the fundamental understanding of the reaction mechanism and to test the validity of various available nuclear-reaction models. The nuclear data required for the above applications come mainly from nuclear scattering and reaction model calculations, which depend on optical models, whose parameters are determined by elastic scattering and the total cross-section data. The measurement and analysis of the EFs is particularly interesting, because the features of the EFs at low, medium and high energies can reveal the reaction mechanism involved. The low-energy portion of EF is dominated by the compound-nucleus (CN) mechanism, however, with increasing the projectile energy, the PE processes become important [1–4]. The high-energy tail portion of the excitation functions (EFs) of the nuclear reactions induced by light-ion medium-energy projectiles has been one of the important signatures of pre-equilibrium (PE) emission. It may, however, be pointed out that considerable data is available in the literature on nucleon– and light-ion–induced reactions but the cross-section values measured by different groups of workers for the same reaction, generally, do not agree. Several authors [3–8] have reported a variety of data for α-induced activation reactions on niobium (Nb) in the energy range from threshold to well above it. Matsuo *et al.* [5] have measured the EFs for (α, n), $(\alpha, 2n)$ and $(\alpha, 3n)$ reactions on ^{93}Nb and have used chemical separation of radioactive residues followed by activity measurement employing the low-resolution NaI(Tl) crystal. In their work Bond and Jha [7] have measured EFs for these reactions employing the solid-state Ge(Li) γ-ray spectrometer. The measurements were mainly carried out [7] with a view to obtain the yield information as a function of energy. Gadioli *et al.* [8], however, have done more detailed measurements and theoretical description has been given in terms of several kinds of reaction mechanism at relatively higher energies in the range $\approx$ 40–140 MeV. As

[a] e-mail: mks_amu@rediffmail.com
[b] e-mail: bpsinghamu@gmail.com

such, their data is above the energy range of interest in the present work. Ernst *et al.* [9] in their paper on "Investigation of α-induced reactions on Niobium and Tantalum" have given the experimentally measured excitation functions for several reactions, however, they have not compared the measured excitation functions with calculated ones using statistical codes. Further, Mukherjee *et al.* [4] have carried out the measurement of isomeric cross-section ratio in the reaction ^{93}Nb$(\alpha, 2n)^{95m+g}$Tc only in the energy range upto 120 MeV with a view to study the PE emission. In order to test the theoretical models, Mukherjee *et al.* [4] have compared the measured EFs with calculations done using various codes [10,11]. It may not be out of place to mention that theoretically it may be possible to reproduce the measured EFs for the prominent reaction channels accurately and separately than trying to describe all open reaction channels simultaneously. It may improve the description of the data for the partial channel at the cost of other open channels, however, it appears unacceptable from the point of view of physics. Several phenomenological as well as quantum-mechanical models have been launched to explain the pre-equilibrium reaction mechanism. These models describe the way in which projectile energy gradually gets redistributed among the constituent nucleons of the composite system through a series of residual two-body interactions. These models have been quite successful in reproducing both the energy spectra of emitted particles and the EFs for the specific product nuclide in a wide range of reactions, but primarily for reactions involving mostly nucleons in the entrance and exit channels in the energy range up to 100 MeV or so. It is interesting to obtain in the analysis, simultaneously, a best description of all existing experimental data for all open channels, as this approach is internally consistent, detailed and complete. Further, the information on the isomeric cross-section ratio of a residual nucleus and its dependence on the incident particle is far from abundant. The study of the isomeric cross-section ratio is of importance from the viewpoint of understanding the reaction mechanism and to test the nuclear models. Several models like ALICE-91 [12], CASCADE [13], PACE2 [14], ACT [15], COMPLETE [10] etc., are available in the literature and are generally used for theoretical calculations of EFs for light- and heavy-ion-induced reactions. In all the codes except ACT [15], the configuration of the codes is such that they predict the total cross-section only for the population of the residual nuclei. However, the code ACT [15] calculates the cross-sections for the production of both the ground as well as isomeric states. As such, in order to obtain theoretical predictions of the population of the isomeric states, in particular, the code ACT [15] based on the lines of codes STAPRE [11] has been used in the present work using consistently the same set of parameters.

In light of the above and with a view to study PE emission in a consistent and systematic way, a programme of precise measurement and analysis of EFs for a large number of α-induced PE-dominated reactions has been undertaken. As a part of this programme, in the present work, EFs for the reactions ^{93}Nb$(\alpha, n)^{96m}$Tc, ^{93}Nb$(\alpha, n)^{96}$Tc, ^{93}Nb$(\alpha, 2n)^{95m}$Tc, ^{93}Nb$(\alpha, 2n)^{95g}$Tc, and ^{93}Nb$(\alpha, 3n)^{94g}$Tc have been measured in the excitation energy range from threshold to $\approx$ 40.8 MeV, using the stacked-foil activation technique and γ-ray spectrometry. One of the applications of technetium isotopes is that it is an excellent corrosion inhibitor for steel. In all these reactions the isotopes of Tc are formed and as such the measured EF may be used for deciding the optimum beam energy for the production of these isotopes. In the present work, the analysis of the measured EFs has been performed within the framework of CN and PE formalisms employing the Hauser-Feshback (HF) [16] and exciton models [17], respectively. The experimental details and errors are given in sect. 2, while, sects. 3 and 4 deal with the results and discussion. The conclusions are given in sect. 5 of the paper.

2 Experimental details

Experiment has been carried out at the Variable Energy Cyclotron Centre (VECC), Kolkata, India, using a collimated α-particle beam of $\approx$ 40 MeV. Self-supporting spectroscopically pure foils of natural niobium have been used as targets. The thickness of these commercially supplied Nb foils was $\approx$ 5 mg/cm^2. The target stack containing 12 Nb samples having aluminium degraders in between them was bombarded by α-particles in the irradiation chamber dedicated to this purpose in *cave one* for about half an hour. A beam current $\approx$ 100 nA was monitored from current integrator count rate. The average beam energy on a given target foil and degrader was calculated using the stopping-power values given in the tables of Northcliffe and Schilling [18]. Post-irradiation analysis has been performed using a high-resolution large-volume (100 c.c.) Ge(Li) detector coupled to a multichannel analyzer CANBERRA-88. The activities induced in various sample foils were recorded using a Ge(Li) detector, which was pre-calibrated using various standard γ-sources. A ^{152}Eu point source was used to determine the efficiency of the detector for different γ-ray energies at various source-detector distances. The sample and detector distances were suitably adjusted so as to minimize the dead time $< 10\%$. Pertinent decay data [19] used in the present work for yield calculations are given in table 1. The residues produced due to different reaction channels were identified by their characteristic γ-rays and measured half-lives. From the observed activities of the residual nuclei, the cross-sections were determined for a given reaction channel using the standard formulation as given below [20]:

$$\sigma_r(E) = \frac{A\lambda \exp(\lambda t_2)}{N_0 \phi \theta K(G\varepsilon)[1-\exp(-\lambda t_1)][1-\exp(-\lambda t_3)]}, \quad (1)$$

where, A is the observed counts (area under the photo peak of the characteristic gamma ray of the particular residues) during the accumulation time t_3 of the induced activity of the decay constant λ, N_0 the number of target nuclei being exposed under the geometrical shadow of the beam irradiated for duration t_1 with a particle beam of

Table 1. List of reactions, identified γ-rays, half-lives and their branching ratios.

Serial No.	Reaction	J^{π}	Half-life	E_{γ} (keV)	Branching ratio (%)
1.	^{93}Nb$(\alpha, n)^{96m}$Tc	4^{+}	51.5 min	1200	1.09
2.	^{93}Nb$(\alpha, n)^{96}$Tc	7^{+}	4.28 d	778.1	99.79
				812.5	82
				849.9	98
				1126.8	15.20
3.	^{93}Nb$(\alpha, 2n)^{95m}$Tc	1/2	61.0 d	204.0	66.20
4.	^{93}Nb$(\alpha, 2n)^{95g}$Tc	$9/2^{+2}$	20.0 h	765.7	93.00
				947.6	2.14
				1073.3	3.75
5.	^{93}Nb$(\alpha, 3n)^{94g}$Tc	7^{+}	4.8 h	702.0	99.60
				916.0	7.60

flux ϕ, t_2 the time lapse between the stop of irradiation and the start of counting, θ the branching ratio of the characteristic γ-ray and $G\varepsilon$ the geometry-dependent efficiency of the detector. The factor $[1 - \exp(-\lambda t_1)]$ takes care of the decay of evaporation residue during the irradiation and is typically known as the saturation correction. The correction for the decay of the induced activity due to the delay between the stop of irradiation and the start of counting and during the data accumulation is taken into account via the factors $\exp(\lambda t_2)$ and $[1 - \exp(-\lambda t_3)]$, respectively. $K = [1 - \exp(-\mu d)]/\mu d$ is the correction for the self-absorption of the γ radiation in the sample thickness itself, where d is the thickness of the sample and μ is the γ-ray absorption coefficient.

Various factors which may introduce uncertainties in the present measurements are discussed here. There may be uncertainty in determining the geometry-dependent detector efficiency. The statistical errors of the counting of the standard sources may give rise to the error in efficiency, which was minimized by accumulating large number of the counts for comparatively larger times (≈ 5000 s). Experimental data on the variation of geometry-dependent efficiencies with the γ-ray energy at different source-detector distances has been fitted with the power law curve. The uncertainty due to fitting of the efficiency curve is estimated to be $< 3\%$. Uncertainty in determining the efficiency may also come up due to the solid-angle effect, because the irradiated samples were not point sources like the standard source, but they had a diameter of ≈ 3 mm. It is estimated that the error in the efficiency on account of solid-angle effect is $< 5\%$. The inaccurate estimate of the foil thickness and non-uniformity of foil may give rise to uncertainty in determining the number of target nuclei in the sample. It is estimated from the thickness measurements at different positions of the sample foils that errors due to non-uniform deposition are expected to be $< 1\%$. Errors may come up due to fluctuations in beam current during the irradiation. Although, care was taken to keep the beam current constant within 10%. It is estimated that beam fluctuations may introduce an error of $< 3\%$. During irradiation of the stack, the beam traverses the thickness of the material, thus the initial beam intensity reduces. It is estimated that the error due to decrease in beam intensity is expected to be $< 2\%$. In all these measurements the dead time is kept less than 10% by suitably adjusting the sample-detector distance and the corrections for it were applied in the counting rate. Further, the uncertainties in the branching ratio, decay constant, half-lives etc., which are taken from the table of isotopes have not been taken into account. The overall error due to all these factors is expected to be $< 15\%$ of the measured cross-section values.

3 Results and discussion

The measured excitation functions for the reactions ^{93}Nb$(\alpha, n)^{96m}$Tc, ^{93}Nb$(\alpha, n)^{96}$Tc, ^{93}Nb$(\alpha, 2n)^{95m}$Tc, ^{93}Nb$(\alpha, 2n)^{95g}$Tc, and ^{93}Nb$(\alpha, 3n)^{94g}$Tc have been shown in figs. 1-4 and 6, respectively. In fig. 5, the total cross-section for the Nb$(\alpha, 2n)$ reaction, obtained from the sum of isomeric and ground-state cross-sections, is plotted. The experimental results are presented in table 2 of the paper. The uncertainties reported are the statistical errors of counts and the discrepancies between the independent measurements (different gamma rays) of given nuclei. The horizontal bars in figs. 1-6, represent the beam energy spread obtained from the energy loss in sample thickness. The size of the circle includes the magnitude of statistical errors in cross-section values, if no error bar is plotted. In all the neutron exit channel reactions both the ground state as well as the isomeric states are populated. All the above-mentioned reactions are described separately in the following parts.

3.1 ^{93}Nb(α, n) reaction

The EFs for the reactions ^{93}Nb$(\alpha, n)^{96m}$Tc and ^{93}Nb$(\alpha, n)^{96}$Tc are plotted in figs. 1 and 2, respectively. The isomer ^{96m}Tc produced in the (α, n) reaction decays (98%) to ^{96}Tc via internal transition. The half-life of ^{96}Tc is 4.35 d which is much larger than that of the metastable state ^{96m}Tc ($t_{1/2} = 51.5$ min). As such, the

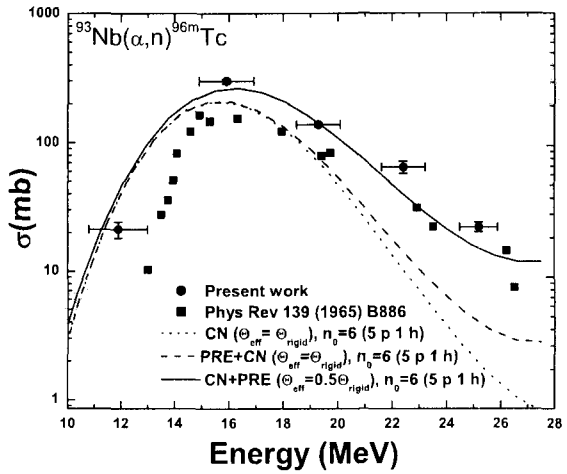

Fig. 1. The experimentally measured and theoretically calculated EFs for the reaction ^{93}Nb$(\alpha, n)^{96m}$Tc. The effect of the variation of the effective momentum of inertia on calculated EFs is also shown.

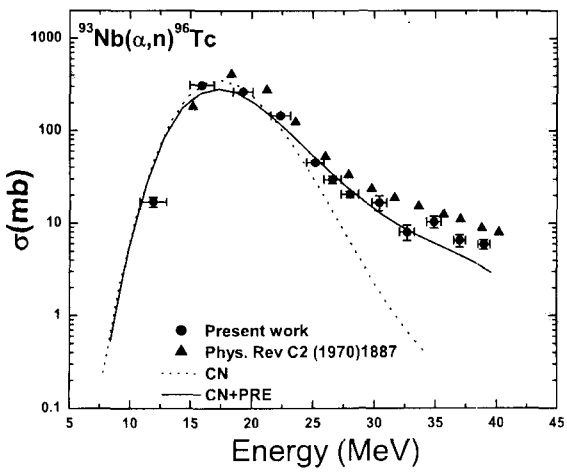

Fig. 2. The experimentally measured and theoretically calculated EFs for the reaction ^{93}Nb$(\alpha, n)^{96}$Tc.

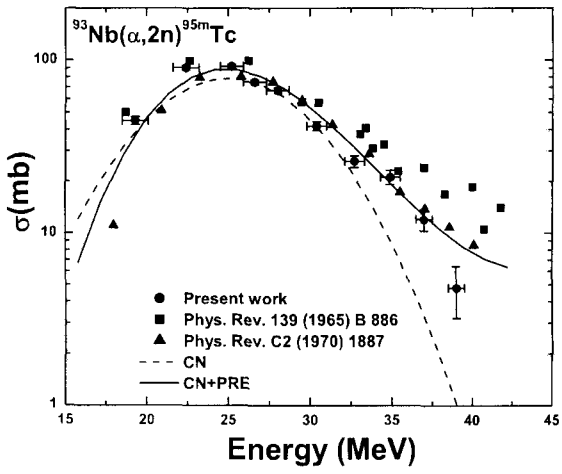

Fig. 3. The experimentally measured and theoretically calculated EFs for the reaction ^{93}Nb$(\alpha, 2n)^{95m}$Tc.

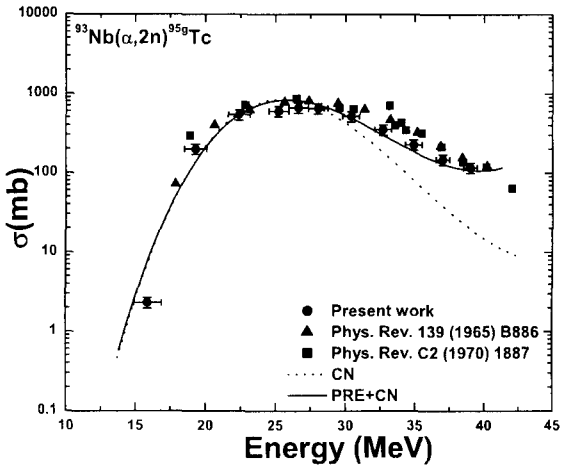

Fig. 4. The experimentally measured and theoretically calculated EFs for ^{93}Nb$(\alpha, 2n)^{95g}$Tc.

observed activity for the residue ^{96}Tc has contribution for both the isomeric and ground-state cross-sections. In fig. 1, the cross-sections for the ^{93}Nb$(\alpha, n)^{96m}$Tc reaction measured by Matsuo *et al.* [5] have also been plotted for comparison. As can be seen from this figure, the measurements of Matsuo *et al.* [5] are lower than the present work in the low-energy region. In fig. 2, presently measured EF for ^{93}Nb$(\alpha, n)^{96}$Tc reaction is shown along with literature data [7]. As can be seen from this figure, the measurements of Bond *et al.* [7] agree with the present work within statistical errors.

3.2 ^{93}Nb$(\alpha, 2n)$ reaction

The EFs for the reactions ^{93}Nb$(\alpha, 2n)^{95m}$Tc and ^{93}Nb$(\alpha, 2n)^{95g}$Tc are given in figs. 3 and 4, respectively. In the ^{93}Nb$(\alpha, 2n)$ reaction, both the ground and metastable states are populated. The metastable state ^{95m}Tc is longer lived with a half-life of 61 d, while the half-life of the ground state ^{95g}Tc is $\approx$ 20 h. The isomeric transition is only 3.9%. The cross-sections for both the states are determined by taking proper account of the isomeric transition. The measurements of Matsuo *et al.* [5] and Bond *et al.* [7] are also presented for both these reactions *i.e.*, ^{93}Nb$(\alpha, 2n)^{95m}$Tc and ^{93}Nb$(\alpha, 2n)^{95g}$Tc and are shown in figs. 3 and 4, respectively. As can be seen from fig. 3, the measurements of Matsuo *et al.* [5] are in general higher than the present work ones, particularly in the tail portion of EF. However, in case of ^{93}Nb$(\alpha, 2n)^{95g}$Tc the literature values agree with the present work. In fig. 5, the excitation function for the reaction ^{93}Nb$(\alpha, 2n)^{95}$Tc, obtained from the sum of cross-sections for isomeric and ground states is shown.

Table 2. Experimentally measured cross-sections.

E_α (MeV)	$\sigma(^{96m}$Tc) (mb)	$\sigma(^{96}$Tc) (mb)	$\sigma(^{95m}$Tc) (mb)	$\sigma(^{95g}$Tc) (mb)	$\sigma(^{95T}$Tc) (mb)	$\sigma(^{94g}$Tc) (mb)
11.9 ± 1.1	21.1 ± 3	16.9 ± 2.0				
15.9 ± 1.0	298.7 ± 11.9	310.8 ± 1		2.3 ± 0.1		
19.3 ± 0.8	138.1 ± 5.3	265.4 ± 2.3	44.9 ± 2.3	199.1 ± 1.5	244 ± 2.7	
22.4 ± 0.8	64.3 ± 7.1	146.1 ± 5.9	90.3 ± 2.6	541.8 ± 0.5	632.1 ± 2.6	
25.2 ± 0.7	22 ± 1.9	45.5 ± 1.9	92.1 ± 2.7	600.15.8	692.1 ± 6.4	
26.6 ± 0.7		29.5 ± 2.7	74.9 ± 2.6	666.6 ± 6.3	741.5 ± 6.8	2.3 ± 0.3
28 ± 0.7		20.5 1.6	67 ± 2.5	651.7 ± 5.8	718.7 ± 6.3	55.9 ± 0.2
30.4 ± 0.6		16.6 ± 3.1	41.8 ± 2.4	516.5 ± 3.7	558.3 ± 4.4	205.7 ± 3.7
32.7 ± 0.6		8 ± 1.5	26.1 ± 2.1	352.1 ± 1.7	378.2 ± 2.7	345.1 ± 1.4
34.9 ± 0.6		10.3 ± 1.5	21.1 ± 2	226.8 ± 1.4	247.9 ± 2.4	483.6 ± 17.8
37 ± 0.5		6.5 ± 1	12 ± 1.7	147.1 ± 0.9	159.1 ± 1.9	477.2 ± 2.9
39 ± 0.5		5.9 ± 0.7	4.8 ± 1.6	116.2 ± 1.0	121 ± 1.9	549.4 ± 2.3

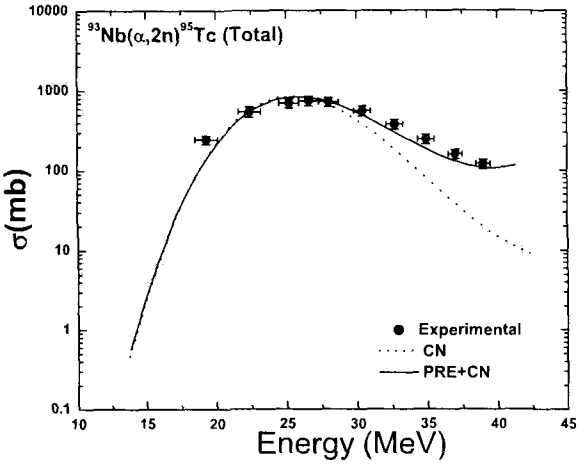

Fig. 5. The experimentally measured total cross-sections (sum of meta + ground states) and theoretically calculated EFs for the reaction ^{93}Nb$(\alpha, 2n)^{95}$Tc.

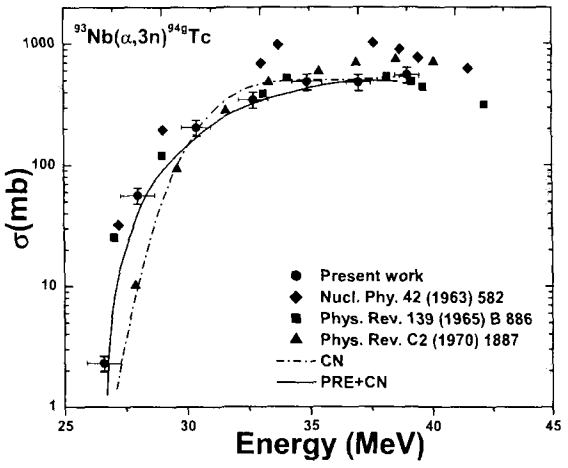

Fig. 6. The experimentally measured and theoretically calculated EFs for the reaction ^{93}Nb$(\alpha, 3n)^{94g}$Tc.

3.3 ^{93}Nb$(\alpha, 3n)$ reaction

In this reaction, both the ground state (^{94g}Tc) as well as the isomeric (^{94m}Tc) states are populated. The decay of these isomers is independent and the half-life of ^{94m}Tc (52.5 min) is smaller than that of the ground state ^{94g}Tc (293 min). The γ-rays of 702, 871 and 916 keV are emitted by the isotope ^{94g}Tc. However, ^{94m}Tc also emits 871 keV γ-rays. These two states of ^{94}Tc decay independently and thus the intensity of the 871 keV γ-ray has contributions due to both these states, hence the separate contribution of the metastable and ground states of ^{94}Tc could not be obtained. The excitation function for the reaction ^{93}Nb$(\alpha, 3n)^{94g}$Tc is shown in fig. 6, along with the literature values. As can be seen from fig. 6, the measurements of Matsuo *et al.* [5] and Bond *et al.* [7] agree to the present measurements in the whole energy range. However, the measurement of Matuszek *et al.* [21] are slightly higher at energies greater than 37 MeV.

Some times the residual nucleus of two different reactions emit γ-rays of nearly the same energy. The γ-ray of 849 keV is emitted in the decay of both the residues ^{96}Tc and ^{94g}Tc produced via ^{93}Nb(α, n) and ^{93}Nb$(\alpha, 3n)$ reactions, respectively. The cross-sections for the ^{93}Nb(α, n) reaction were determined from the observed intensities of the 778 keV, 812 keV and 1126 keV γ-rays coming from ^{96}Tc and the activity of the 849 keV γ-ray was used only up to below the threshold of the ^{93}Nb$(\alpha, 3n)$ reaction. The thresholds for ^{93}Nb$(\alpha, 2n)$ and ^{93}Nb$(\alpha, 2p)$ reactions are very close to each other *i.e.*, $\approx$ 13.1 MeV and $\approx$ 15.5 MeV, respectively. The residual nuclei ^{95m}Tc ($t_{1/2}$ = 61 d) and ^{95m}Nb ($t_{1/2}$ = 3.6 d) produced by the reactions ^{93}Nb$(\alpha, 2n)^{95m}$Tc and ^{93}Nb$(\alpha, 2p)^{95m}$Nb, respectively, both emit γ-rays of 204 keV. As such, the observed intensity of the 204 keV γ-ray will have contribution from both these reaction channels. Since the absolute intensity of 204 keV γ-rays in ^{95m}Tc is 66.2%, while in ^{95m}Nb it is only 2.34%, as such, the contribution of the $2p$ channel to

the $2n$ channel is expected to be negligibly small. In order to check this, the counting of the samples was performed for several days and the intensity of the 204 keV γ-ray was monitored. The activity of ^{95m}Nb ($t_{1/2} \approx 3.61$ d) was found to drop to the background level after $\approx$ 4–5 half-lives. As such, the remaining activity in the samples was attributed only to the ^{95}Tc and the contribution of the $2p$ channel is negligibly small.

4 Model calculations

Various semi-classical models [17,22–24] are available for theoretical calculations. Quantum-mechanical (QM) theories [25–28], which treat the reaction in terms of statistical multi-step compound (SMC) and statistical multi-step direct (SMD) processes have also been proposed. However, QM theories at present are mostly applicable to the nucleon-induced reactions because for a complex particle in the entrance channel the QM treatment of the initial projectile target interaction becomes very much intricate [29]. In view of the above mentioned fact, the calculations in the present work have been performed employing the semi-classical approach using the code ACT [15].

4.1 Calculations with the code ACT

The theoretical calculations for the excitation functions have been performed using the code ACT [15] which is based on the lines of the code STAPRE [11]. In this code, each evaporation step is treated within the framework of the statistical model with consideration of angular momentum and parity conservation. For the emission of the first particle, PE decay is also taken into the account. The cross-section for the population of both the ground and isomeric states may be calculated using this code. The compound-nucleus calculations are performed using the HF model [16], while the exciton model is employed for the simulation of PE emission. The γ-competition with particle emission is taken into account from the second compound system and onwards. The maximum γ-ray multipolarity of two (dipole) is considered, both for electric and magnetic transitions.

The code ACT [15] first generates a table containing for each CN, the HF denominator $N_i(U, J, \Pi)$ for all excitation energies U in steps of 0.5 MeV bin size and all values of angular momentum J and parity Π, which are required for the subsequent evaporation calculations. These quantities are used for all incident energies for the calculation of excitation functions. The HF denominator is defined as the sum of transmission coefficients for all open channels. The excited state of the residual nucleus is described by the level density $\rho(U, J, \Pi)$. At low excitation energies, the complete information on the quantum numbers of the discrete levels is available. However, in the energy region above the discrete levels, which is referred to as continuum, the level densities are calculated within the framework of the backshifted Fermi gas model by the spin-dependent Lang expression [30]. In this model, it is assumed that the levels with positive and negative parities have the same density. Some of the important parameters of the code are the level density parameter a, the effective moment of inertia Θ_{eff}, and the backshift Δ. In the present calculations, the level density was calculated from the backshifted formula and the level density parameters given in ref. [31] are used. In the cases when the level density parameters a are not known, they were selected for the calculation by interpolating the data of the neighboring isotopes, taking into account the odd-even systematics [31,32]. In some cases the level density parameters were required to be varied within 20% in order to get a better description of the data. As a typical example, the effect of variation of the level density parameters a on calculated EFs is discussed elsewhere [33]. In the present work, a value of $a = 13.07$ of the first compound nucleus ^{97}Tc gives a satisfactorily representation of the experimental data, however, its interpolation value was 11.37 [31]. This variation of the level density parameters is justified, since these parameters are empirical in nature and are valid [31] in the energy range up to 20 MeV only. Further, any change in the effective value of the moment of inertia (Θ_{eff}), and the temperature (T) of the nucleus may influence the spin cut-off parameter (σ) given by the expression [32]

$$\sigma^2 = \Theta_{eff} \frac{T}{\hbar^2}. \tag{2}$$

In the present calculations, the effective moment of inertia Θ_{eff}, has been taken equal to the rigid-body value (Θ_{rig}), assuming the nucleus to be as a solid sphere, *i.e.*

$$\Theta_{rig} = \frac{2}{5} mA(r_0 A^{1/3})^2, \tag{3}$$

where, $r_0 = 1.25$ fm, A is the mass number and m the nucleon mass. The transmission coefficients required in the calculations are generated by a code TLK, which uses the global optical model potentials [34]. The transmission coefficients are assumed to depend on the orbital angular momentum and on the energy of the relative motion only. The separation energies needed in these calculations are taken from the tables of Wapstra and Bos [35], and the decay scheme of various nuclei from the table of isotopes [19].

The equilibration of the compound system is treated within the framework of the exciton model [17]. Starting from a simple configuration, the composite system is assumed to equilibrate through a series of two-body interactions and may emit particles from all intermediate stages. The states of the system are classified according to the number of excitons or more specifically to the numbers n_p and n_h of the excited particle and hole degrees of freedom, respectively. The application of a two-body interaction to the state of a (n_p, n_h) configuration leads to states with $(n_p + 1, n_h + 1)$, (n_p, n_h) or $(n_p - 1, n_h - 1)$ excited particles and holes. In competition with these internal transitions, particles can be emitted from each stage. For all these processes transition rates averaged over all states of a configuration are calculated. These transition rates λ_+, λ_0 and λ_- are related by the Williams expression [36],

corrected for Pauli principle by Cline [37] to $|\bar{M}|^2$, the absolute value of the square of the average effective matrix element for two-body residual interactions:

$$\lambda_+ = \frac{2\pi}{\hbar}|\bar{M}|^2 \frac{g^3}{U^2}(n+1), \quad (4)$$

$$\lambda_0 = \frac{2\pi}{\hbar}|\bar{M}|^2 g n_p n_h (n-2), \quad (5)$$

$$\lambda_- = \frac{2\pi}{\hbar}|\bar{M}|^2 g^2 U \frac{(3n-2)}{4}. \quad (6)$$

In order to evaluate internal transition rates, it is necessary to calculate $|\bar{M}|^2$. However, at present no microscopic calculations for $|\bar{M}|^2$ are available [38]. As such, the expression $|\bar{M}|^2 = F_M \cdot A^{-3}U^{-1}$ proposed by Kalbach-Cline [39], where A is the mass number and U the excitation energy of composite system, is used for calculating the value of the matrix element. Here, F_M is a constant and is treated as an adjustable parameter to match the experimental data. In the literature, values of F_M ranging from 95–7000 MeV^3 are proposed [28,40] for reproducing the experimental data. The average rates for the emission of particle are calculated from the principle of detailed balance considerations. The single-particle state density g, used in the transition rate calculations, is obtained from the level density parameter a using the relation $g = 6\pi^{-2}a$.

For PE decay the initial number n_0 of excited particles and holes and the parameter F_M, which is given by equation $|\bar{M}|^2 = F_M \cdot A^{-3}U^{-1}$ and defines the matrix for internal transition rates, are required to be given in the first input data and may be treated as parameters of the model. In the literature, the values of the initial exciton number n_0 ranging from 4 to 6 are used for α-induced reactions. In some of our earlier analysis [15,41, 42] of excitation functions for α-induced reactions on several targets (A = 55, 59, 63, 65, 121, 128, 130, 165, 197 and 209) where measurements were done to cover the tails of the excitation functions, a value of $n_0 = 6$ along with $F_M = 430$ MeV^3 was found to give a satisfactory reproduction of the experimental data. In the present analysis also, the same value of the initial exciton number $n_0 = 6$ ($n_p = 5$, $n_h = 1$) and $F_M = 430$ MeV^3 has been retained and found to give a satisfactory reproduction of the excitation functions, in general, for all the reactions studied presently as shown in figs. 1-6. In all these calculations the value of the effective moment of inertia Θ_{eff} has been taken equal to the rigid-body value, *i.e.* Θ_{rig}. The experimentally measured EFs agree well with these calculations, in general, except for the reaction ^{93}Nb$(\alpha, n)^{96m}$Tc. The calculations for this reaction were again performed with the $\Theta_{eff} = 0.5\Theta_{rig}$ value and it is found that there is surprisingly a good agreement between calculation and experimental data. The same is again reflected in the isomeric cross-section ratio, as discussed in sect. 4.2.

The configuration of the 6-exciton state may be justified [15,41,42] as the first interaction may give rise to the excitation of one particle above the Fermi energy leaving behind a hole in the excited state, *i.e.* in all 5 particles and one hole. The amount of PE emission depends on how successfully particle decay competes with internal transition and, therefore, is determined by the respective rates and the initial exciton number. Figure 7 displays the influence of variation of F_M (*i.e.*, of internal transition rates) and the initial exciton number n_0 on the calculated excitation function for the ^{93}Nb$(\alpha, n)^{96}$Tc reaction. It may be observed from fig. 7 that a lower value of the exciton number gives, in general, higher pre-equilibrium contributions. This is evident as a smaller value of n_0 means larger number of two-body interactions prior to the establishment of equilibrium characteristic of compound nucleus resulting in the large pre-equilibrium contribution. Further, a lower value of F_M means a smaller value of $|\bar{M}|^2$ and hence lower internal transition rates. Consequently, continuum decay rates for a given value of n_0 will be relatively enhanced resulting in a large pre-equilibrium contribution. In the present work, the calculations have been performed using first only the compound-nucleus model and it has been observed that the high-energy tail portion of excitation functions was underestimated, as shown in fig. 2. However, when the PE contribution is added to these calculations with $n_0 = 6$ and $F_M = 430$ MeV^3, in general, a satisfactory reproduction of the experimental data for the presently measured excitation functions has been obtained. As such, it may be mentioned that there is significant contribution from PE emission for these channels at higher energies.

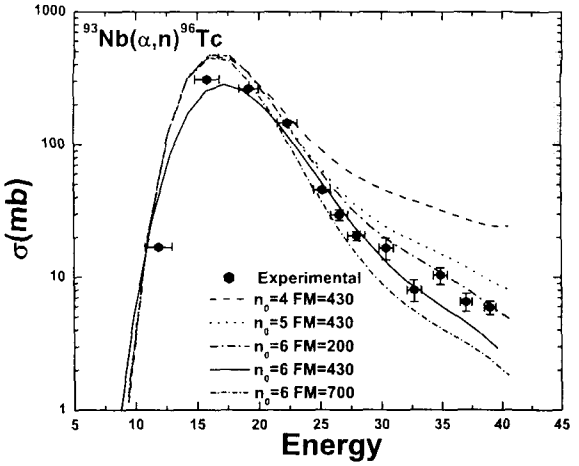

Fig. 7. The experimentally measured and theoretically calculated EFs for the reaction ^{93}Nb$(\alpha, n)^{96}$Tc. The effect of the variation of parameters n_0 and F_M on calculated EFs is also shown.

4.2 Isomeric cross-sections ratio

Isomeric states of a given nucleus have relatively long half-lives, they slightly differ in their energies and have large difference in their spins. Some nuclear reactions populate both the isomeric and the ground states. The ratio of the population of these states is generally called "isomeric cross-section ratio". Since the model used in the

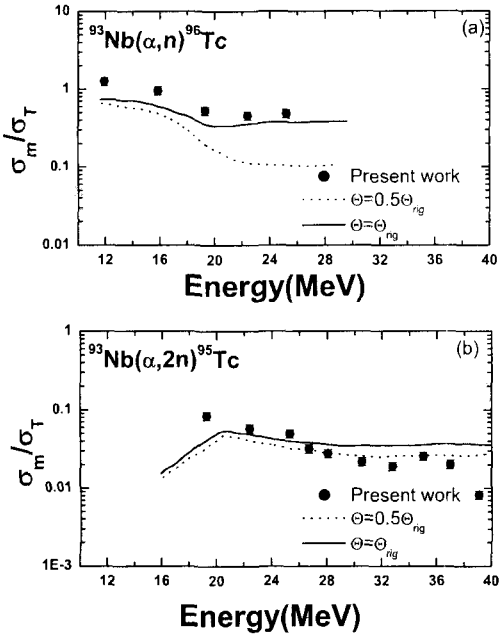

Fig. 8. The experimentally measured and theoretically calculated isomeric cross-section ratios for the reactions ^{93}Nb$(\alpha, n)^{96}$Tc and ^{93}Nb$(\alpha, 2n)^{95}$Tc. The effect of the variation of the moment of inertia on calculated isomeric ratios is also shown.

present work gives a satisfactory representation of the experimental data, it may be considered that the assumptions used in the code ACT [29] are correct. If the ratio σ_m/σ_T, *i.e.* the ratio of the high-spin product to the low-spin product in an (α, xn) reaction is plotted, it should invariably increase with bombarding energy as higher l-waves are admitted and average spin $\langle J_c \rangle$ of the compound nucleus increases. The isomeric ratio in residual nuclei from nuclear evaporation processes cannot increase indefinitly because of the effect of competing reactions. It is possible to calculate the EFs for both the ground as well as isomeric states separately using the code ACT [29]. In all the presently studied reactions both these states are populated. In the following discussion, the isomeric cross-section ratio is defined as the ratio of the cross-section for the population of the isomeric state σ_m to the total cross-section σ_T for the population of both isomers $\sigma_T = \sigma_m + \sigma_g$. The study of the isomeric cross-section ratio (σ_m/σ_T) may give information on the angular-momentum effects in nuclear reactions. The experimental isomeric cross-section ratios σ_m/σ_T for the reactions ^{93}Nb(α, n) and ^{93}Nb$(\alpha, 2n)$ are determined at different α-particle bombarding energies and are shown in fig. 8(a-b). Since higher partial waves participate in reactions with higher bombarding energy, the isomeric cross-section ratio is expected to be a function of the incident projectile energy. The spins of the isomeric states ^{96m}Tc $(J = 4^+)$ and ^{95m}Tc $(J = 1/2^-)$ are lower than the respective ground-state spins ^{96}Tc $(J = 7^+)$ and ^{95g}Tc $(J = 9/2^+)$. It is known that the PE particles carry away the significant amount of angular momentum from the compound system, hence, the isomeric cross-section ratio is expected to depend strongly on the initial spin distribution of the CN. The isomeric cross-section ratio initially decreases with the increase in α-particle bombarding energy and soon levels off. It may be due to the fact that, with further increase in excitation energy, more channels open up, as a result, larger angular momentum will be carried away by the ejectiles and hence the ratio does not increase above a certain energy. Thus the isomeric ratio becomes nearly constant. The isomeric ratios in ^{96}Tc and ^{95}Tc are observed to become nearly constant above α-energies of ≈ 20 and ≈ 30 MeV, respectively. In fig. 8(a-b), the experimental isomeric cross-section ratios are also compared with the ones calculated theoretically with two options of the moment of inertia using the code ACT. In the first option the effective moment of inertia Θ_{eff} is taken equal to the rigid-body value, while in the second option the effective moment of the inertia $\Theta_{eff} = 0.5\Theta_{rig}$ is taken. It may be observed from fig. 8, that the experimental isomeric cross-section ratios for the reactions ^{93}Nb$(\alpha, n)^{96m}$Tc and ^{93}Nb$(\alpha, n)^{96}$Tc are better reproduced when the calculations are performed with the effective moment of inertia equal to the rigid-body value, however the theoretical isomeric cross-section ratios are close to the experimental ones for the reactions ^{93}Nb$(\alpha, 2n)^{95m}$Tc and ^{93}Nb$(\alpha, 2n)^{95g}$Tc, when $\Theta_{eff} = 0.5\Theta_{rig}$ is taken. The effective moment of inertia at low excitation energies is expected to be less than to the rigid-body value and should approach towards the rigid-body value with increase in excitation energy [43].

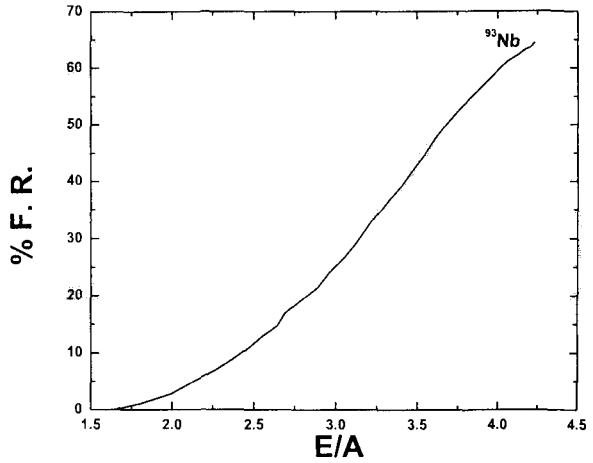

Fig. 9. Pre-equilibrium fraction as a function of excitation energy per nucleon.

4.3 Pre-equilibrium fraction

The total pre-equilibrium fraction "FR", which is a measure of the relative strength of the PE component needed to reproduce the experimental EFs has also been calculated [3]. FR reflects the relative importance of equilibrium and PE processes. The total FR at a given excitation

energy may be defined as the ratio of the sum of the cross-sections for PE emission of all emitted particles (restricted to n, p, d and α) to the total cross-section. The PE fraction for the target ^{93}Nb is calculated and is shown in fig. 9. As can be seen from this figure, the pre-equilibrium fraction increases rapidly with the increase in α-particle bombarding energy per nucleon, which indicates the dominance of PE emission at relatively higher energies.

5 Conclusions

The excitation functions and the isomeric cross-section ratios for α-induced reactions in ^{93}Nb are presented in the energy range threshold to ≈ 40 MeV. It may be concluded that the high-energy tails of the EFs of α-induced reactions cannot be accounted for by the pure compound-nucleus mechanism and they have contributions from the PE emission. The proper admixture of EQ and PE processes is needed for a better reproduction of the experimentally measured excitation functions. An attempt has been made to fix the two important free parameters of the exciton model and a value of $n_0 = 6$ along with $F_M = 430\,\mathrm{MeV}^3$ is found to give the best fit to the experimental data. The pre-equilibrium fraction has been found to be energy dependent.

The authors are thankful to the Chairman, Department of Physics, A.M.U. Aligarh for extending the necessary facilities. Further, we would like to acknowledge the VECC personnel for all its help during the experiments. One of the authors (MKS) thanks the Department of Science and Technology (DST), New Delhi, India, for providing financial support vide the project no. SR/FTP/PS-46/2003.

References

1. M. Blann, Ann. Nucl. Sci. **25**, 123 (1975).
2. J. Pal, C.C. Dey, P. Banerjee, S. Bose, B.K. Sinha, M.B. Chatterjee, Phys. Rev. C **71**, 03605 (2005).
3. B.P. Singh, Manoj K. Sharma, M.M. Muthafa, H.D. Bhardwaj, R. Prasad, Nucl. Instrum. Methods Phys. Res. A **562**, 717 (2006).
4. S. Mukherjee, N.L. Singh, G. Kiran Kumar, L. Chaturvedi, Phys. Rev. C **72**, 014609 (2005).
5. T. Matsuo, J.M. Matuszek jr., N.D. Dudey, T.T. Sugihara, Phys. Rev. B **139**, 886 (1965).
6. C.L. Branquihno, S.M.A. Hoffmann, G.W.A. Newton, V.J. Robinson, H.Y. Wang, I.S. Grant, J. Inorg. Nucl. Chem. **41**, 617 (1970).
7. P. Bond, S. Jha, Phys. Rev. C **2**, 1887 (1974).
8. E. Gadioli, E. Gadiolli-Ebra, J.J. Hogan, B.V. Jacab, Phys. Rev. C **29**, 76 (1984).
9. J. Ernst, W. Friedland, H. Stockhorst, Z. Phys. A **308**, 301 (1982).
10. J. Ernst, W. Friedland, H. Stockhorst, Z. Phys. A **328**, 333 (1987).
11. M. Uhl, B. Strohmair, Report IRK 76/01 (1981) NEA Data Bank (Cedex) France.
12. M. Blann, NEA Data Bank, Gif-sur-Yvette, France, Report PSR-146 (1991).
13. F. Puhlhofer, Nucl. Phys. A **280**, 267 (1977).
14. A. Garvon, Phys. Rev. C **21**, 230 (1980).
15. H.D. Bhardwaj, PhD Thesis, A.M.U. Aligarh, India (1985).
16. W. Hauser, H. Feshbach, Phys. Rev. **87**, 366 (1952).
17. J.J. Griffin, Phys. Rev. Lett. **17**, 478 (1966)
18. L.C. Northcliffe, R.F. Schilling, Nucl. Data Tables A **7**, 256 (1970).
19. C.M. Lederer, V.S. Shirley, *Table of Isotopes VII* (John Wiley, New York, 1978).
20. N.L. Singh *et al.*, Can. J. Phys. **67**, 870 (1989).
21. J.M. Matuszek jr., T.T. Sugihara, Nucl. Phys. **42**, 582 (1963).
22. R. Serber, Phys. Rev. **72**, 1114 (1947).
23. M. Blann, Phys. Rev. Lett. **27**, 337 (1971).
24. M. Blann, Phys. Rev. Lett. **28**, 757 (1972).
25. H. Feshbach, A. Kerman, S. Koonin, Ann. Phys. **125**, 429 (1980).
26. Klaus Debertin, Richard G. Helmer *Gamma-and X-Ray spectrometry with semiconductor detector* (Elsevier Science Publisher B.V., Amsterdam, 1988).
27. D. Agassi, H.A. Weidenmuller, G. Mantzouranis, Phys. Rep. **22**, 145 (1975).
28. T. Udagawa, K.S. Low, T. Tamura, Phys. Rev. C **28**, 1033 (1983).
29. H. Gruppelaar, P. Nagel, P.E. Hodgson, Riv. Nuovo. Cimento **9**, No. 1 (1986).
30. D.W. Lang, Nucl. Phys. **77**, 545 (1966).
31. W. Dilg, W. Schantl, H. Vonach, Nucl. Phys. A **217**, 269 (1973).
32. S. Sudar, S.M. Qaim, Phys. Rev. C **73**, 034613 (2006).
33. B.P. Singh, H.D. Bhardwaj, R. Prasad, Can. J. Phys. **69**, 1376 (1991).
34. M. Blann, H.K. Vonach, Phys. Rev. C **28**, 1475 (1983).
35. A.H. Wapstra, K. Bos, At. Data Nucl. Data Tables **19**, 215 (1977).
36. F.C. Williams jr., Phys. Rev. Lett. B **31**, 184 (1970).
37. C.K. Cline, Nucl. Phys. A **186**, 273 (1972).
38. H. Jahn, *Nuclear Theory for Applications*, IAEA-SMR 93 report (1982) p. 39.
39. C. Kalbach-Cline, Nucl. Phys. A **210**, 590 (1973).
40. K.K. Gudima, S.G. Mashnik, V.D. Toneev, Nucl. Phys. A **401**, 329 (1983).
41. B.P. Singh, M.G.V. Sankaracharyulu, M. Afzal Ansari, H.D. Bhardwaj, R. Prasad, Phys. Rev. C **47**, 2055 (1993).
42. B.P. Singh, PhD Thesis, Aligarh Muslim University, India (1992).
43. N.D. Dudey, T.T. Sugihara, Phys. Rev. B **139**, 886 (1969).

PROBING OF INCOMPLETE FUSION DYNAMICS AT ENERGIES $\approx$ 4-7 MeV/nucleon

A thesis submitted for the award of
DOCTOR OF PHILOSOPHY
in
PHYSICS
(Experimental Nuclear Physics)

by
PUSHPENDRA P. SINGH

under the supervision of
DR. B. P. SINGH

Department of Physics
Aligarh Muslim University, Aligarh (UP)-202 202, INDIA

2008

Thesis Supervisor: Dr. B. P. SINGH*,[1]

Experimental Collaborators:
Prof. R. Prasad[1]
Dr. R. K. Bhowmik[2]
Mr. S. Muralithar[2]
Mr. R. P. Singh[2]
Mr. Rakesh Kumar[2]
Dr. M. K. Sharma[1]
Prof. M. A. Ansari[1]
Dr. (Mrs.) Unnati Gupta[1]
Mr. Devendra P. Singh[1]
Mr. Abhishek Yadav[1]
Ms. K. S. Golda[2]
Dr. H. D. Bhardwaj[1]

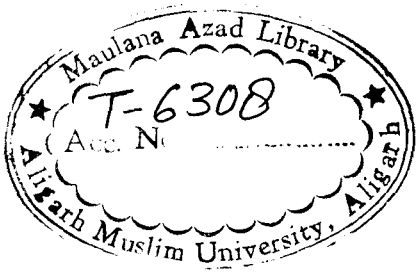

*email: bpsinghamu@gmail.com
[1]*Acc. Lab., Department of Physics, A. M. University, Aligarh-202 002, India*
[2]*NP-Group, Inter-University Accelerator Center, New Delhi-110 067, India*

The experimental work presented in this thesis has been carried out at the Inter-University Accelerator Center (IUAC), New Delhi-67, India, using 15UD-Pelletron accelerator facilities (http://www.iuac.ernet.in)

I dedicate this thesis to,
My parents *.....for their love, affection & inspiration, and*
All my teachers *.....for architecting my career*

DEPARTMENT OF PHYSICS
ALIGARH MUSLIM UNIVERSITY
ALIGARH-202 002 (UP), INDIA

Dr. B. P. Singh
Reader

Phone & Fax : +91-571-2701001, Cell : +91-9412133929, e-mail: bpsinghamu@gmail.com

Certificate

Certified that the work presented in this thesis entitled **"Probing of Incomplete Fusion Dynamics at Energies ~4-7 MeV/ nucleon"** is the original work of **Mr. Pushpendra P. Singh** done under my supervision.

(Dr. B. P. Singh)

Acknowledgements

The work presented in this thesis resulted from the help and support of many people. I would, thus, like to utilize this opportunity to express my sincere indebtedness towards all of them.

Firstly, I thank my thesis supervisor Dr. B. P. Singh for his inspiring guidance, analytical and critical suggestions. He has been a patience bearer of my mistakes and always supported my efforts in this project as an intellectual creative faculty. A respectful acknowledgment is due to Prof. R. Prasad for numerous scientific discussions and to convert mysterious things into marvelous simplicities. He has always been a constant source of inspiration for me throughout the course of this work.

I am equally thankful to Dr. R. K. Bhowmik, who enabled me to force my will to learn several things with his expertise, his unwavering support and commitment particularly for in-beam experiments always inspired me to work hard to meet his expectations. Nonetheless, I warmly thank Mr. Rakesh Kumar for his enthusiasm, and for always being ready to discuss instrumentation. He has been more than an experimental collaborator for me during my thesis work.

I am very much thankful to Mr. S. Muralithar and Mr. R. P. Singh for their help in setting up the experimental arrangement, and always being available with their comments and suggestions for the improvement of the present work. My sincere thank also goes to Mr. J. J. Das, Mr. N. Madhavan, Ms. K. S. Golda, Mr. Subir Nath, Mr. Jagdish Gehlot for their immense help and encouraging attitude. Mr. E. T. Subramanium, Mr. P. Barua, Mr. R. Abhilash and Ms. Kusum Rani are also thankfully acknowledged for their help in various capacities.

I also would like to thank all my teachers, particularly (late)Prof. C. V. K. Baba, Dr. S. K. Datta, Prof. S. K. Sammadar, Prof. J. N. De, Dr. A. K. Sinha, Dr. S. Bhattacharya, Prof. A. Chibhi, Prof. P. Chomaz, Dr. Subendu Ghosh, Prof. S. B. Patel for being kind to hear my problems and several discussions during my stay at IUAC, New Delhi and in SERC06 school (held at VECC, Kolkata). Thanks are also due to Prof. Zoran Basrak, Prof. Hans-Juergenan Wollersheim, Prof. Adam Maj, Prof. P. R. S. Gomes, Prof. Roman Caplar for several discussions, encouragement and help in various capacities.

I especially thank all my university colleagues, in particular, Dr. Manoj K. Sharma, Dr. (Mrs.) Unnati, Mr. Devendra P. Singh, Mr. Abhishek Yadav and Mr. Akshay Kumar Behera, for their constant support and co-operation during the course of this work. I am also thankful to all my friends, Mr. Pankaj Kumar, Dr. P. D. Shidling, Dr. Pradeep Datta, Dr. Vijay K. Sai, Dr. R. G. Shankar, Mr. Dinesh Negi, Mr. T. Trivedi, Mr. Sugam Kumar, Mr. Praveen Kumar, Mr. Subhash Pokhriyal, Dr. Ritesh Kshetri

and Dr. Vivek Chandel for their moral support which they extended with their humorous and good-natured approach to life.

I am highly indebted to Prof. Amit Roy, Director, IUAC for providing necessary facilities for carrying out the experiments. I also thank Pelletron crew at IUAC for providing good quality beams for experiments. Thanks are also due to the Chairman, Department of Physics, for providing all the necessary departmental facilities. I also thank Dr. H. D. Bhardwaj, Dr. Avinash Agrawal for their valuable moral support during this work.

I am forever indebted to all my family members and relatives, in particular, Mrs. Vimlesh Chaudhary, Mr. G. S. Chaudhary, Mrs. Meena Yadav, Er. V. S. Yadav, Mrs. Mamata Yadav, and Mr. Rajendra K. Singh, for their affection and patience. It would not have been possible to complete this work without their loving support and blessings. I don't want to confine the support and endearment in words, which I received from Shilpi through out this work. Saving the best for last, I thank Priyanka, Nitin, Nikhil, Tanuj, Anuj, Tanvi and Manu for continuous, unwavering support and their love that have always been a reason to smile.

Last but not the least, I am also thankful to all those who remembered and wished me on every success, with out of their endless strife and blessings, it would have been impossible for me to pursue this work.

Pushpendra P. Singh

(Pushpendra P. Singh)

List of Publications

(*a*) International Journals[1]

1. *Probing of incomplete fusion dynamics by spin distribution measurement*

Pushpendra P. Singh, B. P. Singh, Unnati, Manoj Kumar Sharma, R. Kumar, D. Singh, R. P. Singh, S. Muralithar, M. A. Ansari, R. Prasad and R. K. Bhowmik.

Phys. Lett. **B** (2008), **doi:10.1016/j.physletb.2008.11.035** (in press).

2. *Spin distribution studies: A sensitive probe for incomplete fusion reaction dynamics*

Pushpendra P. Singh, B. P. Singh, Manoj Kumar Sharma, Unnati, R. Kumar, K. S. Golda, D. Singh, R. P. Singh, S. Muralithar, M. A. Ansari, R. Prasad and R. K. Bhowmik.

Phys. Rev. C **78**, 017602 (2008).

3. *Influence of incomplete fusion on complete fusion: Observation of large incomplete fusion fraction at E/A ≈5-7 MeV*

Pushpendra P. Singh, B. P. Singh, Manoj K. Sharma, Unnati, Devendra P. Singh, Rakesh Kumar, K. S. Golda and R. Prasad.

Phys. Rev. C**77**, 014607 (2008).

4. *Observation of complete- and incomplete-fusion components in ^{159}Tb, $^{169}Tm(^{16}O,x)$ reactions: Measurement and analysis of forward recoil ranges at E/A≈6 MeV.*

Pushpendra P. Singh, Manoj K. Sharma, Unnati, Devendra P. Singh, Rakesh Kumar, B. P. Singh, and R. Prasad.

Euro. Phys. J. A **34**, 29-39 (2007).

5. *Production of fission like events after complete and/or in-complete fusion of ^{16}O with ^{159}Tb and ^{169}Tm at E/A≈6 MeV.*

Pushpendra P. Singh, B. P. Singh, Bhavna Sharma, Unnati, Manoj K. Sharma, H. D. Bhardwaj, Rakesh Kumar, K. S. Golda and R. Prasad.

Int. J. Modern Phys. E**17**, No.3, 549-566 (2008).

6. *Observation of a large incomplete fusion in $^{16}O+^{103}Rh$ system at ≈40-85 MeV*

Unnati, **Pushpendra P. Singh**, Devendra P. Singh, Manoj K. Sharma, B. P. Singh, and R. Prasad

Nucl. Phys. A 811, 77-92 (2008).

7. *Large pre-equilibrium emission in $\alpha+^{nat}Ni$ interaction at ≈ 8-45 MeV*

[1]This thesis is based on the work presented in the first four publications

Abhishek Yadav, **Pushpendra P. Singh**, M. M. Musthafa, Devendra P. Singh, Unnati, Manoj K. Sharma, B. P. Singh, and R. Prasad

Phys. Rev. C 78, 044606 (2008).

8. *A study of reaction mechanism in ^{16}O+^{27}Al system: Measurement and analysis of excitation functions and angular distributions.*

Manoj K. Sharma, Unnati, Devendra P. Singh, **Pushpendra P. Singh**, B. P. Singh, and R. Prasad.

Phys. Rev. C**75**, 064608 (2007).

9. *A study of pre-equilibrium emission of neutrons in $^{93}Nb(\alpha, xn)$ reactions*

Manoj K. Sharma, H.D. Bhardwaj, Unnati, **Pushpendra P Singh**, Devendra P. Singh, B.P. Singh and R. Prasad.

Euro. Phys. J. A**31**, 43-51 (2006).

(*b*) International/national Conferences/Symposia

1. *Complete versus incomplete fusion in ^{159}Tb (^{16}O,x) reactions: Forward recoil ranges measurement of heavy slow residues at $E_{recoil} \leq 0.05$ MeV/nucleon*

Pushpendra P. Singh, Devendra P. Singh, Unnati, Manoj K. Sharma, Rakesh Kumar, K. S. Golda, H. D. Bhardwaj, B. P. Singh, and R. Prasad

DAE-BRNS, Nucl. Phys. Symp., V**51** (2007) 403.

2. *Spin distribution and feeding intensity measurement: Disentangling of fusion and incomplete fusion reaction dynamics at E/A≈4-7MeV*

Pushpendra P. Singh, B. P. Singh, Unnati, Manoj K. Sharma, Rakesh Kumar, D. Singh, R. Ali, P. D. Shidling, D. Negi, R. P. Singh, S. Muralithar, H. D. Bhardwaj, M. A. Ansari, B. P. Singh, R. Prasad and R. K. Bhowmik.

DAE-BRNS, Nucl. Phys. Symp., V**52** (2007) 327.

3. *Spin distribution studies: a sensitive probe for in-complete fusion reaction dynamics*

Pushpendra P. Singh, Unnati, Manoj K. Sharma, Rakesh Kumar, D. Singh, K. S. Golda, S. Muralithar, R. P. Singh, H. D. Bhardwaj, M. A. Ansari, B. P. Singh, R. Prasad and R. K. Bhowmik.

DAE-BRNS, Nucl. Phys. Symp., V**51** (2006) 361.

4. *Influence of in-complete fusion on complete fusion: Observation of large fusion suppression at ≈5-7 MeV/nucleon.*

Pushpendra P. Singh, Devendra P. Singh, Unnati, Manoj Kumar Sharma, Rakesh Kumar, K. S. Golda, H. D. Bhardwaj, B. P. Singh and R. Prasad.

DAE-BRNS, Nucl. Phys. Symp., V**51** (2006) 359.

5. *In-complete fusion of ^{16}O with ^{159}Tb: Measurement and analysis of excitation functions*

Pushpendra P. Singh, Unnati, Manoj Kumar Sharma, Rakesh Kumar, K. S. Golda, H. D. Bhardwaj, B. P. Singh and R. Prasad.

DAE-BRNS, Nucl. Phys. Symp., V51 (2006) 435.

6. *Investigation of fractional momentum transfer: Measurement of forward recoil ranges in* ^{16}O+^{169}Tm *collisions*

Pushpendra P. Singh, Unnati, Manoj Kumar Sharma, Rakesh Kumar, K. S. Golda, H. D. Bhardwaj, B. P. Singh and R. Prasad.

DAE-BRNS, Nucl. Phys. Symp., V51 (2006) 437.

7. *Incomplete fusion studies using particle-gamma coincidence technique*

Pushpendra P. Singh, Bhavna Sharma, Unnati, Manoj K. Sharma, B. P. Singh, H. D. Bhardwaj, Rakesh Kumar, K. S. Golda and R. Prasad.

DAE-BRNS, Nucl. Phys. Symp., V50 (2005) 337.

8. *Investigation of fission like events at energy 6 MeV/nucleon*

Pushpendra P. Singh, Bhavna Sharma, Unnati, Manoj K. Sharma, B. P. Singh, H. D. Bhardwaj, Rakesh Kumar, K. S. Golda and R. Prasad.

DAE-BRNS, Nucl. Phys. Symp., V50 (2005) 335.

9. *Study of incomplete fusion dynamics: Analysis of excitation functions*

Pushpendra P. Singh, Bhavna Sharma, Unnati, Manoj K. Sharma, B. P. Singh, H. D. Bhardwaj, Rakesh Kumar, K. S. Golda and R. Prasad.

DAE-BRNS, Nucl. Phys. Symp., V50 (2005) 336.

10. *Life time measurement of* ^{75}Br *with inverse kinematics reaction*

D. Negi, V. Kumar, T. Trivedi, S. A. Babu, Ranjeet, V. Kumar, **Pushpendra P. Singh**, S. Muralithar, Rakesh Kumar, R. P. Singh, S. C. Pancholi, A. K. Bhati, and R. K. Bhowmik

DAE-BRNS, Nucl. Phys. Symp., V51 (2007) 292.

11. *Spin distribution studies for incomplete fusion reactions in* ^{16}O+^{124}Sn *collision*

D. Singh, R. Ali, M. Afzal Ansari, K. S. Babu, **Pushpendra P. Singh**, Manoj K. Sharma, Unnati, B. P. Singh, R. K. Sinha, Rakesh Kumar, S. Muralithar, R. P. Singh, and R. K. Bhowmik

DAE-BRNS, Nucl. Phys. Symp., V51 (2007) 321.

12. *Isotopic mass distribution of fission products in* ^{16}O+^{197}Au *reactions at* $\approx$*6 MeV/nucleon*

Manoj K. Sharma, Devendra P. Singh, Unnati, **Pushpendra P. Singh**, B. P. Singh, K. S. Golda and R. Prasad

DAE-BRNS, Nucl. Phys. Symp., V51 (2007) 433.

13. *Complete and incomplete fusion studies for the* ^{16}O+^{181}Ta *system using x-ray detection technique*

Devendra P. Singh, Unnati, Manoj K. Sharma, **Pushpendra P. Singh**, B. P. Singh, K. S. Golda, A. K. Sinha, and R. Prasad

DAE-BRNS, Nucl. Phys. Symp., V**51** (2007) 379.

14. *Measurement and analysis of radio-active nuclides produced in the interaction of* ^{16}O+^{130}Te *system over the energy range* $\approx$*3.8-5.6MeV/A*

Unnati, Manoj K. Sharma, Devendra P. Singh, **Pushpendra P. Singh**, Sunita Gupta, H. D. Bhardwaj, Rakesh Kumar, B. P. Singh, and R. Prasad

DAE-BRNS, Nucl. Phys. Symp., V**51** (2007) 343.

15. *Study of incomplete fusion reaction of* ^{16}O*-ion beam with* ^{124}Sn *using particle-gamma coincidence technique.*

D. Singh, R. Ali, M. Afzal Ansari, K. Surendra Babu, **Pushpendra P. Singh**, M. K. Sharma, Unnati, B. P. Singh, R. K. Sinha, R. Kumar, S. Muralithar, R. P. Singh, and R. K. Bhowmik.

DAE-BRNS, Nucl. Phys. Symp., V**51** (2006) 439

16. *Measurement and analysis of cross-sections for some residues produced in* ^{16}O+^{27}Al *system.*

Manoj Kumar Sharma, Unnati, Devendra P. Singh, **Pushpendra P. Singh**, Rakesh Kumar, K. S. Golda, H. D. Bhardwaj, B. P. Singh and R. Prasad.

DAE-BRNS, Nucl. Phys. Symp., V**51** (2006) 431.

17. *Measurement and analysis of excitation functions in* ^{16}O+^{103}Rh *system at* E^* = *2-4MeV/nucleon*

Devendra P. Singh, Unnati, Manoj Kumar Sharma, **Pushpendra P. Singh**, Sunita Gupta, B. P. Singh, Rakesh Kumar, H. D. Bhardwaj and R. Prasad

DAE-BRNS, Nucl. Phys. Symp., V**51** (2006) 365.

18. *A study of energy dependence of complete and in-complete fusion in* ^{16}O+^{169}Tm *system below 6 MeV/nucleon using recoil range distribution technique*

Unnati, Manoj Kumar Sharma, B. P. Singh, **Pushpendra P. Singh**, Devendra P. Singh, Rakesh Kumar, K. S. Golda, H. D. Bhardwaj, Sunita Gupta and R. Prasad

DAE-BRNS, Nucl. Phys. Symp., V**51** (2006) 441.

19. *Signature of fission in 16O+159Tb system at energy 5 MeV/nucleon*

B. Sharma, **Pushpendra P. Singh**, Unnati, Manoj K. Sharma, B. P. Singh, H. D. Bhardwaj, Rakesh Kumar, K. S. Golda and R. Prasad

DAE-BRNS, Nucl. Phys. Symp., V**50** (2005) 313.

20. *Measurement of recoil range distribution for some evaporation residues of the system* ^{16}O+^{169}Tm *at* $\approx$*81 MeV beam energy*

Unnati, Manoj Kumar Sharma, B. Sharma, **Pushpendra P. Singh**, B. P. Singh, Rakesh Kumar, K. S. Golda, Sunita Gupta, H. D. Bhardwaj and R. Prasad

DAE-BRNS, Nucl. Phys. Symp., V**50** (2005) 315.

21. *Measurement of excitation functions (EFs) for some residues produced in* $^{16}O+^{159}Tb$ *system below 7MeV/nucleon energies*

Unnati, Manoj Kumar Sharma, **Pushpendra P. Singh**, Bhavna Sharma, B. P. Singh, Sunita Gupta, H. D. Bhardwaj, Rakesh Kumar and R. Prasad.

DAE-BRNS, Nucl. Phys. Symp., V**47B** (2004) 208.

22. *Measurement of excitation functions (EFs) for* $^{16}O+^{103}Rh$ *system in the energy range 56-85MeV*

Unnati, Manoj Kumar Sharma, Bhavna Sharma, **Pushpendra P. Singh**, B. P. Singh, Sunita Gupta, H. D. Bhardwaj, Rakesh Kumar and R. Prasad

DAE-BRNS, Nucl. Phys. Symp. V**47B** (2004) 254.

23. *Absorptive break-up of* ^{16}O *projectile in interaction with* ^{nat}Tm*: Observation of fast projectile-like fragments in forward cone*

Pushpendra P. Singh, B. P. Singh, Unnati, Manoj K. Sharma, Devendra P. Singh, Rakesh Kumar, P. D. Shidling, D. Singh, P. S. Rao, S. Muralithar, R. P. Singh, K. S. Golda, M. A. Ansari, H. D. Bhardwaj, R. Prasad and R. K. Bhowmik

International Nuclear Physics Conference 2007 (INPC07), 3-8th June 2007, Tokyo, Japan.

24. *Complete and incomplete fusion in reactions induced by heavy ions*

Manoj K. Sharma , B. P. Singh, Unnati, **Pushpendra P. Singh**, Rakesh Kumar, K. S. Golda, H. D. Bhardwaj and R. Prasad

5Th Conference on Nuclear and Particle Physics (NUPPAC'05), 19 - 23 Nov. 2005 Cairo, Egypt

25. *Pre-equilibrium emission studies in some light ion induced reactions*

B. P. Singh, Manoj K. Sharma, Unnati, **Pushpendra P. Singh**, D. P. Singh, H. D. Bhardwaj and R. Prasad

International Workshop on "Physics for ADS for Energy and Transmutation" held at University of Rajasthan, Jaipur, India. 23rd-26th Feb. 2006.

26. *A study of reaction mechanism in heavy ions at energies* $\approx$*5-7MeV/A*

Manoj Kumar Sharma, Unnati, **Pushpendra P. Singh**, Devendra P. Singh, B. P. Singh and R. Prasad

11th International Conference on Nuclear Reaction Mechanisms, Varenna (Italy), Villa Monastero, June12-16, 2006.

27. *A study of* $^{16}O+^{159}Tb$ *system: Complete and Incomplete Fusion*

Manoj Kumar Sharma, B. P. Singh, Unnati, **Pushpendra P. Singh**, Bhavna Sharma, H. D. Bhardwaj, Rakesh Kumar, K. S. Golda and R. Prasad

International Conference on Contemporary Issues in Nuclear and Particle Physics, Nuclear and Particle Physics Research Centre, Jadavpur, Kolkata (2005) 50.

(c) Scientific/Technical Reports

1. *Disentangling of fusion and incomplete fusion: spin distribution measurement at ≈4-7 MeV/nucleon*

Pushpendra P. Singh, B. P. Singh, Unnati, Manoj K. Sharma, D. P. Singh, Rakesh Kumar, P. D. Shidling, D. Singh, Abhishek Yadav, R. Ali, R. P. Singh, S. Muralithar, M. A. Ansari, H. D. Bhardwaj, R. Prasad and R. K. Bhowmik

Annual Report, Inter-University Accelerator Center (IUAC), New Delhi, India, year 2007-08, page no. 124

1. *Disentangling of fusion and incomplete fusion: spin distribution measurement at ≈4-7 MeV/nucleon*

Pushpendra P. Singh, B. P. Singh, Unnati, Manoj K. Sharma, D. P. Singh, Rakesh Kumar, P. D. Shidling, D. Singh, Abhishek Yadav, R. Ali, R. P. Singh, S. Muralithar, M. A. Ansari, H. D. Bhardwaj, R. Prasad and R. K. Bhowmik

Annual Report, Inter-University Accelerator Center (IUAC), New Delhi, India, year 2007-08, page no. 124

2. *Spin distribution studies at E/A ≈4-7MeV: a sensitive probe for in-complete fusion dynamics*

Pushpendra P. Singh, B. P. Singh, Unnati, Manoj K. Sharma, D. P. Singh, Rakesh Kumar, P. D. Shidling, D. Singh, J. K. Rana, P. S. Rao, R. Ali, R. P. Singh, S. Muralithar, M. A. Ansari, H. D. Bhardwaj, R. Prasad and R. K. Bhowmik

Annual Report, Inter-University Accelerator Center (IUAC), New Delhi, India, year 2006-07, page no. 133

3. *Study of incomplete fusion reaction dynamics: Observation of fast alpha particles in forward cone*

Pushpendra P. Singh, Bhavana Sharma, Unnati, D. Singh, M. K. Sharma, B. P. Singh, M. A. Ansari, H. D. Bhardwaj, R. Prasad, Rakesh Kumar, K. S. Golda, R. P. Singh, S. Muralithar and R. K. Bhowmik

Annual Report, Inter-University Accelerator Center (IUAC), New Delhi, India, year 2005-06, page no. 141

4. *Reaction mechanism studies in some medium mass nuclei below ≈7 MeV/nucleon*

Unnati, **Pushpendra P. Singh**, Bhavana Sharma, M. K. Sharma, B. P. Singh, Sunita Gupta, H. D. Bhardwaj, K. S. Golda, Rakesh Kumar and R. Prasad

Annual Report, Inter-University Accelerator Center (IUAC), New Delhi, India, year 2005-06, page no. 118

Contents

List of Figures

List of Tables

Chapter 1

Nuclear Phenomena at High Angular Momenta

1.1 Prelude

The present knowledge of nuclear interactions and the properties of nuclei is based on the phenomenal progress of an idea of *"atomism"*, i.e., *"all the matter of the universe is made up of a set of tiny, indivisible particles called atom"*. In 1898, British physicist J. J. Thomson conceived the atom as consisting of electrons embedded in a spherical matrix of positive charge[1]. Later, in 1911, Rutherford modified the above hypothesis on the basis of the results of large angle α-scattering experiment[2], which indicate that all the positive charge and most of the mass of atom is concentrated in a very small central part of the atom named as *'nucleus'*. The electrons are assumed to revolve around the nucleus in nearly circular orbits and make the atom electrically neutral. The discovery of natural radioactivity, in 1896, by Henri Becquerel led to contemplate the nature of the nucleus[3]. In 1919, Rutherford achieved the first artificial radioactivity[4]. The nuclear transmutation experiments of Rutherford, Cock-Croft & Walton, Curie & Juliet and Fermi suggested new experimental methods to solve basic problems regarding the nuclear structure, nuclear properties, nuclear forces, energy states of nuclei, transition probabilities etc., which considerably motivated nuclear reaction studies[4, 5]. Soon after the establishment of the presence of neutron inside the nucleus, nuclear reactions were used as a tool to understand the properties of nuclear interactions in various physical conditions. Some of the basic aims of nuclear physics research are to investigate the nature of interactions, decay characteristics of excited nuclei and more recently to explore the possibilities of sizing up the heavy nuclei[6]. In general, a nuclear reaction takes place, when a particular chosen nuclide (target nucleus) is bombarded by a pro-

jectile of sufficient kinetic energy which can overcome the fusion barrier (B_{fus}) between interacting partners. As a consequence of such an interaction, the components of the initial system (projectile and target nucleus) come close to each other within the range of nuclear forces, eventually transforming into a final system, consisting of reaction products, like; light emitted particle(s) and a residual nucleus followed by the emission of characteristic radiations [7]. In general, a nuclear reaction may be represented as;

$$ {}^{A_a}_{Z_a}a \;+\; {}^{A_X}_{Z_X}X \;\longrightarrow\; {}^{A_Y}_{Z_Y}Y \;+\; {}^{A_b}_{Z_b}b \;+\; \gamma \tag{1.1} $$

Here; ${}^{A_a}_{Z_a}a$ is the projectile and ${}^{A_X}_{Z_X}X$ is the target nucleus. While, ${}^{A_Y}_{Z_Y}Y$ and ${}^{A_b}_{Z_b}b$ are the residual nucleus and the ejectiles (light and/or heavy nuclear particle), respectively.

An important parameter involved in nuclear reactions is the Q-value of the reaction, which refers to energy balance of a nuclear reaction and may be written as;

$$ Q = (M_a + M_X)c^2 - (M_b + M_Y)c^2 \tag{1.2} $$

Where, M_a and M_X are the masses of particles in the initial system, M_b and M_Y are the masses of particles in the final system in a binary reaction of the type X(a,b)Y, and c is the speed of light in vacuum.

On the basis of Q-value, the nuclear reactions may be of two types; (a) Exoergic reaction (Q>0), in which energy is evolved, and (b) Endoergic reaction (Q<0), in which energy is absorbed. Since, there is a net deficit of energy in the later case (b), therefore, energy must be supplied to initiate such a nuclear reaction, which usually comes from the kinetic energy of the projectile. Further, the nuclear reactions have been used to produce new isotopes & elements, and today it has become possible to synthesize the super heavy elements[8, 9]. In the field of accelerated charged particles, the growth from the Cockcroft and Walton's machine to todays TeV machines has been phenomenal. There is a huge development in the detection systems and high speed computation facilities. As such, with the availability of advanced accelerators and sophisticated auxiliaries, the present day nuclear physics stands where it has not been imagined several decades ago. These new developments in nuclear physics gave birth to the several new branches. Based on the energy region of interest, there are three broad classifications of nuclear reaction studies; (i) Low Energy Nuclear Reactions, (ii) Medium Energy Nuclear Reactions, and (iii) High Energy Nuclear Reactions. This thesis deals with some of the interesting problems associated with Heavy Ion (HI) induced Low Energy Nuclear Reactions, which has been a topic of resurgence interest for HI nuclear physics community since last decade or so.

The nuclear reactions can be categorized as '*elastic*' and '*inelastic*' reactions. The elastic nuclear reactions are those in which interacting partners only change their direction of motion. In above case, the particles in the exit channel are exactly same as that in entrance channel. While, in case of inelastic nuclear reactions, one or both of the interacting partners may change their internal states alongwith their nuclear properties. In an inelastic nuclear reaction the properties of initial and final systems are well defined but it is not known what exactly happens at the time of projectile-target interaction. Since, the nuclear reaction takes place in a very short time $\approx 10^{-22}$-10^{-16} sec, therefore, it is not possible to visualize intermediate stage directly. In 1936, Bohr proposed the compound nucleus (CN) theory [10] to explain the nuclear reaction dynamics. According to CN theory, the reaction mechanism is considered as a two stage process. When a projectile (E$>B_{fus}$) interacts with the target nucleus, in first stage, the projectile is captured by the target nucleus, eventually, the total kinetic energy and driving input angular momenta of the projectile are equally shared among all the constituent nucleons of the composite system leading to the establishment of thermodynamic equilibrium. However, in the second stage, after a long time ($\approx 10^{-16}$sec), some how sufficient amount of energy may be accumulated on a nucleon or on a group of nucleons to emit from the CN, leaving behind a residual nucleus. The CN theory is also known as the *'Bohr's independent hypothesis'*. As a matter of fact, the lapse time between the formation of composite system and its decay is too large, and hence, no trace is left to decide its mode of formation [10]. In 1950, the validity of *'Bohr's independent hypothesis'* has been experimentally verified by S. N. Ghoshal [11], where the reaction cross-sections of almost same orders of magnitude (within the experimental uncertainties) have been observed for particular reaction products formed via different entrance channels. On the other hand, the direct reactions occur promptly, on a time scale of the same magnitude as the time taken by a projectile to traverse through the target nucleus (i.e.,$\approx 10^{-22}$sec). Hence, the CN and direct reaction processes may be distinguished on the basis of interaction time required for the completion of the reaction. The direct reactions may, further, be classified into two categories viz; (i) knock-out, and (ii) stripping/pick-up reactions. In case of stripping reactions, the projectile splits up into two fragments, one of them may merge with the target nucleus and the other may continue to move on, more or less undisturbed. The inverse of the stripping reaction would be a pick-up reaction; in which the projectile pick(s) up a nucleon/nucleons from the target nucleus. Direct reactions are likely to occur at relatively large projectile velocity, where the time of contact of two interacting nuclei is expected to be very small.

Further, in CN reactions it is assumed that the emission of light nuclear particle(s)/cluster(s) takes place, after the establishment of thermodynamic equilibrium. However, it has been inferred from the results of a large number of experiments that the

emission of light nuclear particle(s)/cluster(s) may also take place even before the establishment of thermodynamic equilibrium of the composite system from its intermediate stages [12]. The particles which are emitted before the equilibration of composite system are called pre-equilibrium (PE) particle(s) and the process is referred to as PE-emission and the mechanism is referred to as pre-compound reaction mechanism [13]. It may not be out of place to mention that the PE-emission serves as a bridge between the direct and the CN reactions. Further, with the availability of modern accelerators, it has now become possible to accelerate heavy ions (from α-particle, the lightest heavy ion to ^{235}U) at energies varying from few MeV/nucleon to many GeV/nucleon. Thereafter, the study of heavy ion (HI)-induced reactions acquired central place in nuclear physics research. The HI-induced reactions are significantly different from light ion induced reactions. This is because of the fact that the charge and mass of HI's are larger than the light ions, thus energy and momentum carried in by the HI's are relatively large, which makes the HI-induced reactions more complex. A detailed discussion on HI-induced reactions and how they differ from light ion induced reactions is given here.

1.2 Heavy Ion Induced Reactions

The study of HI-induced reactions is quite intricate due to the involvement of many nucleons interacting partners having large fusion barrier (B_{fus}). Therefore, a certain amount of projectile energy E>B_{fus}, is required to initiate a heavy ion (HI) reaction. Further, the de-Broglie wavelength (λ) involved in HI-induced reactions is very small, i.e., of the order of nuclear dimensions (compared to the radius of the target nucleus) and can be expressed as;

$$\lambda = \frac{1}{2\pi}\left[\frac{h^2}{2mE_{lab}}\right]^{1/2} \tag{1.3}$$

Since, the associated de-Broglie wavelength (λ) of the HI's is very small, therefore, the HI-induced reactions can be described using semi-classical approach. In semi-classical approach, one considers radial motion of ions classically and angular motion in central force field quantum mechanically. The semi-classical nature of HI-induced reactions makes it possible to give general description of their classical characteristics, particularly their relative motion along quite well defined orbits in terms of the distance of closest approach between interacting nuclei (r_{min}), which is related to the impact parameter b, and may be expressed as;

$$r_{min} = \frac{b}{\sqrt{[1 - \frac{V(r_{min})}{E_{CM}}]}} \tag{1.4}$$

where, V(r_{min}) is the nuclear potential acting between the interacting nuclei and E_{CM} is the center of mass energy of the interacting system.

The classical trajectories of projectile leading to the different modes of reactions may be classified on the basis of impact parameter, as schematically represented in Fig.1.1.

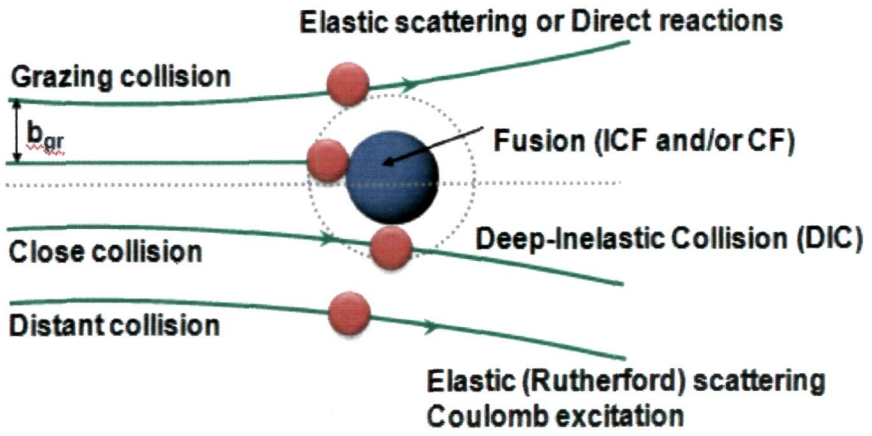

Figure 1.1: A typical representation of heavy ion interaction trajectories.

As can be seen from the Fig.1.1, at projectile energies deep below the fusion barrier (B_{fus}), the projectile does not touch the target nucleus and is assumed to be elastically scattered through the Coulomb field, at large values of impact parameter, leading to the *'distant collisions'*. In these *'distant collisions'* no mass is transferred from projectile to target nucleus and/or vice-versa, and the Coulomb forces exclusively determine the process *(elastic scattering, Coulomb excitation)*. However, when the projectile and target nucleus come into close contact then the nuclear interactions will set in. Meaning thereby, if the impact parameter is comparable to the sum of the radii of interacting partners, *'grazing collision'* takes place and the projectile can be elastically or inelastically scattered, in which the projectile smoothly grazes along the outer surface of target nucleus. In this process, the system keeps its original asymmetry in kinetic energy, mass, etc. Moreover, when the projectile interacts with the target nucleus at smaller values of impact parameter with relatively high bombarding energies (just enough to enter in the nuclear field range of target nucleus) then *'deep inelastic collision' (DIC)* dominates, in which the projectile interacts strongly with the target nucleus. In such a case, the nuclear densities rise very rapidly in the surface region of target nucleus, and a few nucleons may get transferred from projectile to target nucleus, which is also called as *'massive transfer reaction'*. Further, if the projectile interacts with the target nucleus

very strongly at still smaller values of impact parameters, the projectile fuses with target nucleus to form a compound nucleus (CN). The ranges of impact parameters associated with different processes are summarized in Table.1.1.

Table 1.1: Ranges of impact parameter and angular momentum associated with different types of heavy-ion interactions

Impact parameter (b)	Angular momentum (ℓ)	Types of interaction
$b > R_N = (R_1 + R_2)$	$\ell > \ell_N$	Rutherford (Elastic) scattering or Coulomb excitation
$b \approx R_N$	$\ell_N > \ell > \ell_{DIC}$	Elastic and inelastic scattering Few-nucleon transfer reactions
$b \leq R_N$	$\ell_{DIC} > \ell > \ell_F$	Deep inelastic scattering or close collision
$b << R_N$	$\ell < \ell_F$	Fusion (CN formation)

(*Where,* $R_N = R_1 + R_2$ *is the sum of radii of interacting partners, b=impact parameter.)*

As has already been mentioned, in a HI-induced reactions, when the center of mass energy of the interacting partners is greater than the B_{fus}, they overcome the barrier and may lose some of the relative energy through nuclear friction to get trapped in the pocket of the potential and ultimately, it may lead to the CN formation. In general, the angular momentum dependent partial reaction cross-section $\sigma_\ell^R(E)$ at a given energy for these reactions may be given as,

$$\sigma_\ell^R(E) = \pi\lambda^2(2\ell + 1)T_\ell(E) \tag{1.5}$$

where, $T_\ell(E)$ is the transmission coefficient for a particular ℓ-wave.

In the simplest form, one may assume a nuclear potential which depends on the relative separation (r) of two nuclei. The nucleon-nucleon interaction is the key for the proper understanding of any nuclear phenomenon. In nuclear reactions, emphasis is laid on the interaction between incident particle and the target nucleus, since the nuclear scattering processes are more sensitive to the $V_{eff}(r)$ in the nuclear surface region. The $V_{eff}(r)$ as a function of distance and relative angular momenta consists of the sum of Coulomb, centrifugal and nuclear potential terms and may be given as,

$$V_{eff}(r) = V_{Coul}(r) + V_{nucl}(r) + V_{cent}(r) \tag{1.6}$$

Where; $V_{Coul}(r)$ is the repulsive Coulomb potential, $V_{cent}(r)$ is centrifugal potential and $V_{nucl}(r)$ is the attractive nuclear potential. As a representative case, the effective potential $V_{eff}(r)$ for ^{16}O+^{169}Tm system as a function of separation (r) between interacting ions is shown in Fig.1.2, for different ℓ-values.

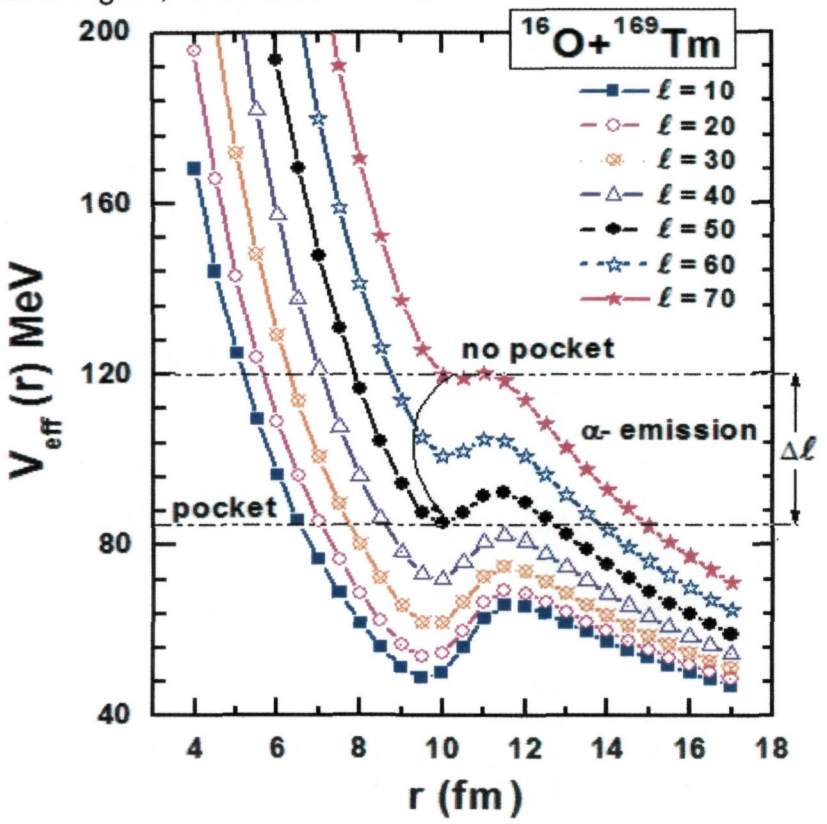

Figure 1.2: Plots of effective potential $V(r)$ as a function of relative separation (r) between the interacting ions for the system $^{16}O +^{169} Tm$.

The repulsive Coulomb potential $V_{Coul}(r)$ may be expressed as follows;

$$V_{Coul}(r) = \frac{1}{4\pi\varepsilon_o}\frac{Z_P\ Z_T\ e^2}{r}, \qquad \text{for} \quad r \geq (R_P + R_T) \tag{1.7}$$

Here, Z_P and Z_T are the atomic numbers R_P and R_T are the radius of the projectile and the target nuclei, respectively.

Several forms of the complex short ranged attractive nuclear potential $V_{nucl}(r)$ have been used in literature. One of the commonly used forms for the nuclear potentials is

the Wood-Saxon form which may be given as;

$$V_{nucl}(r) = \frac{V_o}{1 + exp(\frac{r-R}{a})} \tag{1.8}$$

Where, $R = r_o(A_T^{1/3} + A_P^{1/3})$, $V_\circ$ is the depth of the potential, *'a'* the diffuseness parameter and $r_\circ$=1.31 fm.

The repulsive centrifugal potential $V_{cent}(r)$ is given by;

$$V_{cent}(r) = \frac{\hbar^2}{2\mu}\frac{\ell(\ell+1)}{r^2} \tag{1.9}$$

Here; ℓ is the angular momentum and μ is the reduced mass of the interacting partners. .

It may, further, be pointed out that at low bombarding energies and at relatively large impact parameters, when two ions pass through each other at distances larger than the range of the nuclear interaction, they interact only through their Coulomb fields, where only elastic scattering may take place as only V_{Coul} and V_{cent} potentials are important. There is nearly no dissipation of kinetic energy, and the nuclear interaction is only a small perturbation of Coulomb interaction. For grazing impact parameter 'b'_{gr}', processes like inelastic scattering and a (few) nucleon may get transferred from projectile to target nucleus. This may be due to the overlapping of the extreme tails of nuclear matter densities. On further reduction of impact parameter, the wave functions of the two interacting nuclei overlap considerably and a part of the relative kinetic energy may be converted into internal excitation before the two separate out into target and projectile like systems. These deep inelastic collisions take place at energies of the order of a few MeV/nucleon above the B_{fus}. At still lower values of impact parameters the interacting partners may come close within the range of nuclear forces, where a large dissipation of energy takes place leading to a fully equilibrated CN.

The dependence of the reaction probability for different types of collisions on the impact parameter 'b', can be converted into a dependence on the driving input angular momenta, using the relation $\ell = m_p v_p b$. In this expression $m_p v_p$ denotes the asymptotic initial momentum of the projectile nucleus relative to the target nucleus. A qualitative picture of the reaction probability (σ_ℓ) as a function of entrance channel angular momentum (ℓ) is given in Fig.1.3, for the collision types discussed above. As can be observed from Fig.1.3, the area below the solid curve gives the reaction cross-section for CN formation (σ_{CN}), deep inelastic collision (σ_{DIC}), direct reactions (σ_D) to the right area of elastic collisions and/or Coulomb excitation follow. As indicated in this figure, different regions are overlapping in different ℓ-values. At present, it is not clear,

how large the overlapping regions are for a individual mode of reaction. Moreover, the different modes of reactions can also be understood on the basis of contact duration of projectile and target nuclei, depending upon the relative velocity of projectile.

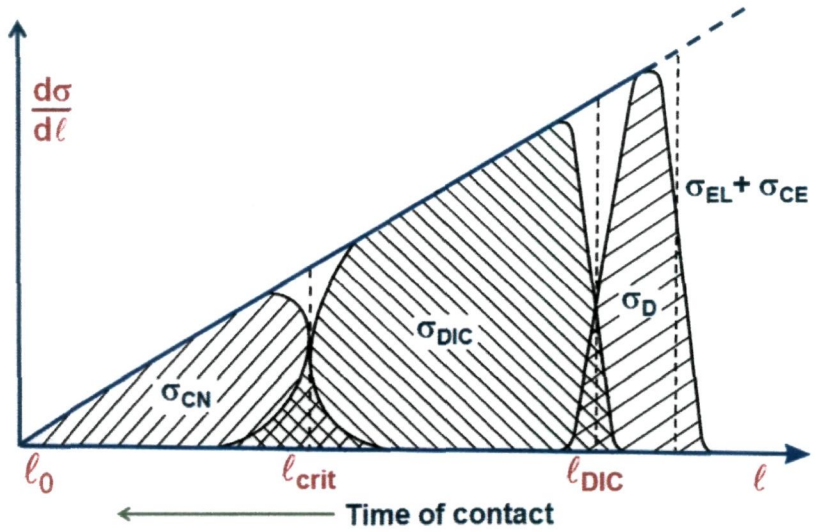

Figure 1.3: A qualitative picture of the reaction probability for fusion (CN-formation), deep inelastic collisions, direct reactions, etc., as a function of entrance channel input angular momentum and time of contact of interacting partners. The higher partial waves and smaller time of contact with target nucleus at higher relative velocity mainly contribute to elastic scattering (σ_{EL}) and Coulomb excitation (σ_{CE})

Further, for sufficiently large time of contact corresponding to the small relative velocity, CN formation is more likely to takes place. However, at high relative velocity of projectile where the time of contact is supposed to be very small, other reactions like DIC, direct reactions etc., follow. It is now well established that, in HI-induced reactions at energies near and above the B_{fus}, the most dominating fusion processes are; (i) complete, and (ii) incomplete fusion. Brief description of these processes is given in the following sub sections.

1.2.1 Complete Fusion

In complete fusion (CF) reaction, a composite system is expected to be formed after an intimate contact and transient amalgamation of projectile and target nucleus lead-

ing to the formation of fully equilibrated *"compound nucleus"*(CN). For CN formation several conditions must be fulfilled, such as;

- The projectile energy must be sufficient enough to overcome the B_{fus} of the projectile-target system. The B_{fus} in the center of mass frame may be given as;

$$B_{fus}(r) = \frac{1.44 Z_T Z_P}{r_\circ (A_T^{1/3} + A_P^{1/3})} \tag{1.10}$$

  Where; the symbols used have their usual meaning.

- The projectile and target should have maximum mass overlap for amalgamation to occur.

- The CN can not be formed, if the entrance-channel introduces more input angular momenta than the composite system can sustain.

Further, for CF to occur, the entrance channel angular momentum should be $\leq \ell_{crit}$, the upper limit of sustainable angular momentum. In such a case, the attractive nuclear potential overcomes the sum of repulsive Coulomb and centrifugal potentials during the projectile-target interaction. This implies large transmission probability, even for higher partial waves ($\ell \leq \ell_{crit}$) and smaller mean-free path. Consequently, the target nucleus hugs the projectile with the involvement of all nucleonic degrees of freedom essentially at projectile energy comparable to their B_{fus} or well above it. Absorption of projectile and target nucleus means that, after a while, nucleons from both the projectile and the target lose their previous collective and individual characteristics and take on a set of new characteristics in a single nuclear potential leading to the formation of the composite system. A typical representation of CF reaction dynamics in given in Fig.1.4. The CF reactions are said to occur probably at zero/small values of impact parameters and for the input angular momenta range $0 \leq \ell \leq \ell_{crit}$, where the probability of CF is supposed to be maximum. In case of CF, the total linear momentum of the projectile is given to the composite system and hence the nuclei recoil at angles very close to the beam direction. The mass of the composite system is nearly equal to the sum of the projectile and the target nucleus masses [7, 14]. It may, further, be pointed out that the kinetic energy of projectile in the center of mass frame is converted into the excitation energy of the CN. All the kinetic energy which is allowed by momentum conservation is distributed statistically among all accessible internal degrees of freedom until the memory of its mode of formation is lost, except that required by the conservation of energy, total angular momentum, and parity.

Moreover, the CN is only formed if the life-time of the merged system (projectile plus target nucleus) is long enough to attain thermodynamic equilibrium. The CN thus formed de-excites by the evaporation of light nuclear particle(s) alongwith characteristic γ-radiations. Each particle takes away a definite amount of excitation energy from the equilibrated system, but only a small amount of angular momentum. With the stipulation that fission is also an acceptable means of de-excitation in favorable conditions. The CN in case of CF, is assumed to be formed via essentially a single route with pre-determined mass and charge, excitation energy, angular momentum, etc. The angular distribution of the emitted particle(s) from a CN may be obtained by simple classical considerations. In such a case, evaporation residues (target-like fragments) are expected to be concentrated in forward cone.

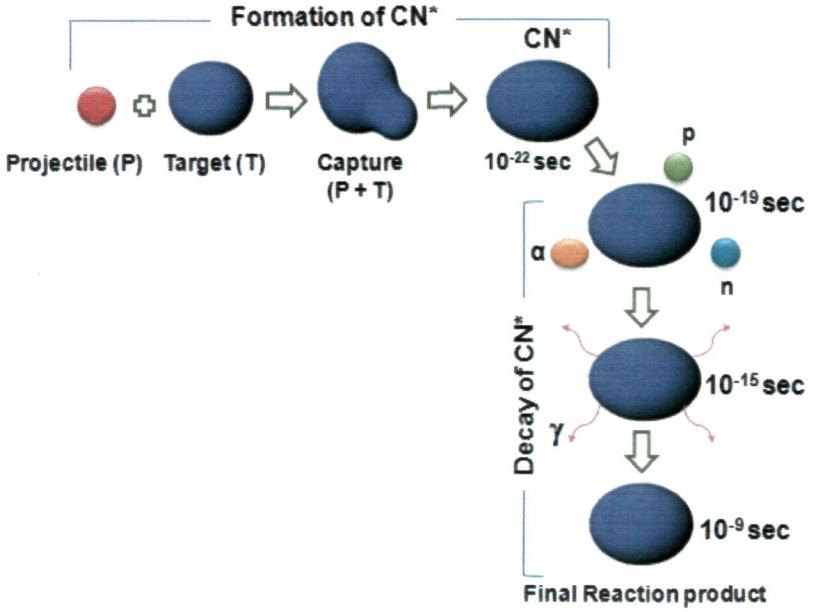

Figure 1.4: A typical representation of CN formation and its decay via CF-process. The accelerated projectile nucleus collides and fuses with target nucleus involving all nucleonic degrees of freedom, which may leads to excited compound nucleus (CN*). The CN* first cools by evaporation of neutrons, protons and/or α-particles. Eventually, it may lose the rest of its excitation energy and almost all of its initial angular momentum by emission of γ-rays. The total decay process is completed very quickly in about 10^{-9} seconds

Further, it has been experimentally observed that the total CF cross-section (σ_{CF}) is smaller than the total reaction cross-section (σ_R) at a given projectile energy [16]. As a matter of fact, large angular momenta inhibit CF, which is expressed as a ℓ cut-off for CF (ℓ_{crit}), above which the centrifugal potential is so large which prevents fusion between two colliding nuclei. Starting with usual expression (equation-1.5), the sharp-cut-off model calculates the cross-section for CF as a summation of contributing ℓ-values from ℓ=0 upto a limiting value ℓ=ℓ_{crit}, where the probability of CN formation is assumed to be maximum. Since, ℓ-values are related to the interaction trajectories, therefore, at higher ℓ-values beyond ℓ_{crit} or at relatively higher values of impact parameters, minimum mass overlap between projectile and target nuclei takes place. This is obvious when a grazing collision involves only the tails of nuclear matter, where fusion incompleteness may take place, the details of such a process is given in subsection-1.2.2

1.2.2 Incomplete Fusion

Incomplete fusion (ICF) corresponds to the reaction dynamics where a "hot" metastable incompletely fused composite system is formed as a result of partial linear momentum transfer (LMT) from projectile to target nucleus. In case of ICF relatively less nucleonic degrees of freedom are expected to be involved as that in CF. A typical representation of ICF dynamics is given in Fig.1.5. As already mentioned, at relatively higher projectile energies and at finite values of impact-parameters, CF gradually gives way to ICF, where the centrifugal potential (V_{cent}) increases due to projectile-target interaction. Under the influence of centrifugal force field, the driving angular momenta exceed its critical limit (ℓ_{crit}) for CF, as such, the attractive nuclear potential (V_{nucl}) is no more strong enough to capture entire projectile by the target nucleus. As can be seen from Fig.1.2, at relatively small centrifugal potentials, a pocket remains in the potential energy curve in the vicinity of critical distance of approach. However, the pocket in the entrance channel potential almost vanishes at high input angular momentum (depends on projectile energy and the value of impact parameter). As such, no fusion can occur unless a part of projectile is emitted to release excess driving angular momenta. After the prompt emission of a part of projectile (predominantly α-cluster in case of ^{16}O and ^{12}C beams) allows a loss of input angular momenta($\Delta\ell$), so that another curve is attained corresponding to a lower ℓ-value where the pocket does exist, as shown in Fig.1.2. As such, the remnant is now supposed to have input angular momentum less than or equal to its own critical limit for fusion with the target nucleus as is shown in Fig.1.2. Eventually, an incompletely fused composite (IFC) system (a part of projectile plus target nucleus) appears with less charge and mass as that of CF population. Further, the ICF is associated with the ℓ-bins above the ℓ_{crit}. The statement about the ℓ-window

in the entrance channel for ICF reaction dynamics, is based on the comparison of the population of 'yrast' states (spin distribution) in final nuclei populated via CF and/or ICF [14].

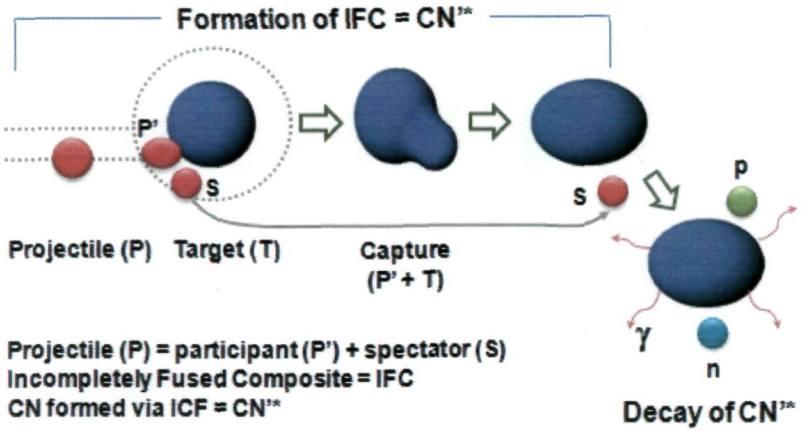

Figure 1.5: A typical representation of ICF process. As shown, one of the fragments fuses with target nucleus called participant leading to the formation of IFC system, while the remnant moves in forward cone as spectator, with almost projectile velocity. The IFC de-excites in the similar fashion as the CN decay in CF.

It may, however, be pointed out that in case of ICF, most of the time either α-particle or cluster of α-particles (i.e., ^{8}Be or ^{12}C) depending on the incident ion, escape as unfused spectator. Nonetheless, the viscous forces between interacting partners also play an important role in the occurrence of fusion and fusion-like (ICF) processes [15]. At relatively higher projectile energies (or at large relative velocities) the viscous force between interacting partners decreases, which may significantly reduces the sticking probability of projectile with target nucleus. However, it has experimentally been observed that there is no such boundary of input angular momentum for CF and ICF, both the processes are found to contribute significantly below and above their input angular momentum limits. Some most prominent features of ICF dynamics, which have emerged from a qualitative inspection of more recent experimental results are summarized below.

Characteristics of incomplete fusion

- ICF processes mainly occur for the ℓ-values above the ℓ_{crit} for CF, meaning thereby the lower ℓ-values don't contribute to ICF [14].

- The fused system is formed with less mass and charge as compared to the total mass and charge of interacting partners [16].
- The contribution of ICF is found to increase with projectile energy. Relatively large yield comes from fast-α-particles, which increases the production cross-section of residues populated via α-emitting channels as compared to the fusion-evaporation model codes. At higher beam energies ICF is found to contribute a significant fraction to the total reaction cross-section [16, 19].
- The forward recoil velocity of the reaction products formed via ICF has been observed to be less than those populated via CF, due to partial linear momentum transfer [21].
- The angular distribution of ejectiles in case of ICF (outgoing projectile-like fragments) is found to be peaking at forward angles, where the α-particle(s) are emitted with a velocity centered nearly to the projectile velocity. The ejectiles behave like spectator and assumed to have no significant interaction with target nucleus.
- The composite system formed via ICF has a narrow angular momentum distribution than in case of CF, i.e., the spin-distribution and side-feeding pattern of evaporation residues (ER's) are likely to have distinctly different nature for ICF than that observed for CF [23].
- The ICF has been observed to be more prominent for relatively more mass asymmetric systems (or Z_1 and Z_2 effect) as compared to mass symmetric systems[24, 25, 26].

1.3 Motivation and review of literature

Incomplete fusion in HI-induced (A$\leq$20) reactions has been a topic of renewed interest after the observation of such processes even at energies near and/or just above the B_{fus} [32, 33, 34]. Large-scale efforts in the field of interest have been made to understand the multitude of ICF processes at energies $\approx$ 4-7 MeV/nucleon, where only complete fusion (CF) is expected to be dominant. The first evidence of ICF reaction dynamics also referred to as massive transfer reactions was presented by Kauffmann and Wolfgang [17] in 1961 by studying ^{12}C+^{nat}Rh system at $\approx$ 7-10 MeV/nucleon, where strongly forward peaked angular distribution of various light nuclear particles have been observed. In the same year, Britt and Quinton [37] found similar observations in the reaction ^{16}O+^{209}Bi

at energies from ≈ 7-10 MeV/nucleon. In these measurements, significantly large yield of direct emitting α-particles of mean energy roughly corresponding to the projectile velocity at forward angels has been observed. The results of this pioneering experiment suggested that the principal process involved in the production of fast-α-particles is the projectile break-up, in the nuclear field of target nucleus, in a hard grazing interaction through the surface of target nucleus. Later, similar experimental evidences have also been obtained by Galin *et al.* [38] in the interaction of ^{14}N with ^{103}Rh, where it has been observed that ICF processes compete with CF at the bombarding energies above 7 MeV/nucleon. Since then, the question of fast projectile-like-fragment(PLF) production has been studied quite intensively. Moreover, ICF processes have, predominantly, been observed in case of projectiles having α-cluster structure such as; ^{12}C and ^{16}O projectiles at energies ≈7-10 MeV/nucleon, and well above it [22]. The advances in the study of ICF reaction dynamics took place after spin distribution study by Inamura *et. al.* [23], using particle-γ-coincidence technique for the identification of CF and ICF channels.

As of now, several dynamical models viz; SUMRULE model[14], Break-Up Fusion (BUF) model[40], Promptly Emitted Particles (PEP's) model[41], Exciton model[12], HOT SPOT model[39], etc., have been proposed to explain some of the characteristics of ICF reaction dynamics. The SUMRULE model of Wilczynski *et al.*[14], considers that ICF processes mainly originate from peripheral interactions and are localized in the angular momentum space above the critical angular momentum (ℓ_{crit}) for the CF. The peripheral nature of ICF reaction dynamics has also been emphasized by Trautmann *et al.*[42], and Inamura *et al.*[43, 44]. The BUF-model of Udagawa and Tamura[40], is based on the Distorted Wave Born Approximation (DWBA) formalism for elastic break-up, where the projectile is supposed to break-up into its constituent α-clusters (e.g., ^{16}O may break-up into ^{12}C+α and/or ^{8}Be+^{8}Be) as it approaches the nuclear field of target nucleus. One of the fragments of the projectile is assumed to fuse with target nucleus to form an incompletely fused composite system and unfused fragment continues to move nearly undeflected or less deflected in the forward cone with almost projectile velocity. However, in PEP's model[41], the particles are assumed to be transferred from the projectile to target nucleus and get accelerated in the nuclear field of target nucleus and hence, acquire extra velocity to escape from the surface of composite system before the establishment of thermodynamical equilibrium. Moreover, the leading-particle model of Natowitz *et al.*[45], Hybrid model of Blann *et al.*[13], Fermi-jet model[46, 47, 48], and Moving-Source model[49] have also been proposed and seem to explain some of the experimental data related to ICF at relatively higher projectile energies. As a matter of fact, the above existing models qualitatively explain the experimental data particularly at E/A $\geq$ 10.5 MeV, however, none of the proposed models is able to reproduce the experimental data obtained at energies as low as ≈4-7 MeV/nucleon[50].

Further, in several HI-reactions, significant ICF contribution has been observed even at energies just above the B_{fus}, which has become the motivation to study ICF dynamics at relatively low bombarding energies[51, 52, 53]. Apart from that, Parker *et al.*[54], observed forward α-particles in low-Z heavy ion interactions on ^{51}V target at E/A $\approx$ 6 MeV. Morgenstern *et al.* [24], observed the velocity spectra of evaporation residues in the interaction of ^{40}Ar with Boron and Carbon targets. Morgenstern *et al.*[25, 26], have also showed that, ICF reactions significantly contribute to the total reaction cross-section for mass asymmetric systems as compared to mass symmetric systems at the same relative velocity. Later studies by Vineyard *et al.* [55], and Beck *et al.* [56], also supported the systematics presented by Morgenstern *et al.*,[25, 26]. Further, it has also been observed that both the processes contribute significantly below and above their input angular momentum limits[27]. Gerschel[82] suggested that the localization of ℓ-window depends on target deformation at energies $\leq$10MeV/nucleon. Where, in case of deformed targets peripheral collisions are observed with ℓ-values in the vicinity of ℓ_{crit} for CF, while for spherical targets, the ℓ-window is found to be centered around values $\leq 0.5\ell_{crit}$. Since then, the ICF reaction dynamics has been extensively studied, nevertheless, no clear picture regarding the multiplicity of linear momentum transfer, effect of mass asymmetry, role of different ℓ-values associated with different reaction processes could not be drawn, and/or such studies are still limited for a few projectile-target combinations in medium mass region i.e., A $\approx$ 150. As such, in order to have better understanding of reaction dynamics, it is required to further investigate the underlying processes for above mentioned aspects. Moreover, Dracoulis *et. al.*[83], Lane, *et al.*,[84] and Mullins, *et al.*,[85] reported that ICF can selectively populate high spin states in final reaction products even at low bombarding energies, and can be used as a spectroscopic tool. However, the perfect modeling of the ICF processes is still lacking. Nonetheless, a better understanding of the underlying processes can also provide an insight into the production of radio-active ion beams (RIBs) [57, 58] and may be used to determine optimum irradiation conditions to produce radio-isotopes of interest. In the HI-induced reactions, the final state is expected to be a heavy residual nucleus which may also lead to the synthesis of super heavy nucleus in favorable conditions, but presence of ICF may play a negative role in the super heavy synthesis due to significant fusion incompleteness.

In the present work, in order to explore some of the important issues related to the ICF reaction dynamics at energies near and just above the B_{fus}, i.e., 4-7MeV/nucleon, the information of considerable value have been obtained from the measurements of;

- Excitation functions (EFs): as an indication of ICF reaction dynamics in which the relative contributions of CF and ICF processes have been deduced [59],

- Forward recoil range distributions (RRDs): as a proof of fractional linear momentum transfer in which significant fusion incompleteness, associated with fractional degree of linear momentum transfer (LMT) has been observed [60], and
- Spin-distributions and feeding intensity profiles of evaporation residues (ERs): to probe the entirely different entry state populations in CF and ICF reaction processes [61, 62].

The experiments for all the above measurements have been performed at the Inter-University Accelerator Center (IUAC), New Delhi, India. In the first set of experiments, the excitation functions (EFs) and forward recoil range distributions (RRDs) measurements have been carried out using General Purpose Scattering Chamber (GPSC). In these experiments activation technique followed by off-line γ-spectroscopy have been used to measure the EFs for several radio-nuclides produced in $^{16}O+^{159}Tb$ and $^{16}O+^{169}Tm$ systems via CF and/or ICF at the energies $\approx$ 5-7 MeV/nucleon[59, 60]. The experimentally measured EFs for various radio-nuclides produced in the given systems are compared with the predictions of statistical model code PACE2. The experimental details for the measurement of EFs, results and their interpretations are given in Chapter-2 of this thesis, where the significant information on the dependence of ICF on projectile energy and mass asymmetry of interacting partners have been obtained. Further, in order to confirm the findings of the measurement and analysis of EFs presented in Chapter-2, and also to have proof of fusion incompleteness associated with the various degrees of linear momentum transfer (LMT) from projectile to target nucleus, a complementary experiment has been carried out for the same systems to measure forward recoil ranges of different reaction products produced via CF and/or ICF processes at energies $\approx$87 and 82 MeV, respectively[60]. The forward recoil range distributions have been used to separate out the relative strengths of CF and ICF components. The detailed discussion on experimental set-up, measurement and analysis, results obtained and their interpretations are given in the Chapter-3. While, in the second set of experiments, the Gamma Detector Array (GDA) set-up together with the Charged Particle Detector Array (CPDA) has been used to investigate the multitude of driving input angular momenta associated with different CF and/or ICF processes. Two particle-γ-coincidence experiments for $^{16}O+^{169}Tm$ and $^{12}C+^{169}Tm$ systems at energies $\approx$5.6MeV/nucleon and $\approx$4-7 MeV/nucleon, respectively, have been performed. In these experiments, the de-excitation pattern in the framework of spin population of different reaction products have been studied and the information about the driving input angular momenta involved in various CF and ICF channels have been obtained [61, 62]. In order to understand the results obtained from spin-distribution measurements, feeding intensity of γ-transitions for different reaction products have been deduced from spin-distribution of residues. However, in order to

have confidence in the spin-distribution data, relative production yields of different CF and/or ICF products have been compared with the predictions of theoretical model code PACE4. The detailed discussion of the experimental and electronic set-ups, the method of analysis, findings etc., are given in Chapter-4 of this thesis. The conclusions and future perspectives of the present work are given in the last Chapter of this thesis.

$=*=*=*=$

Chapter 2

Influence of Incomplete Fusion on Complete Fusion

This chapter deals with the measurements carried out to understand the influence of incomplete fusion on complete fusion at energies near and above the Coulomb barrier. Excitation functions for ^{168m}Lu, ^{167}Lu, ^{167}Yb, ^{166}Tm, ^{179}Re, ^{177}Re, ^{177}W, ^{178}Ta *and* ^{177}Hf *radio-nuclides populated via complete and/or incomplete fusion of* ^{16}O *with* ^{159}Tb *and* ^{169}Tm *have been measured and analyzed over a wide projectile energy range i.e.,* $E_{proj} \approx 75$*-95 MeV. Recoil-catcher technique followed by off-line* γ*-spectrometry has been employed in the present measurements. The radio-nuclide* ^{177}W *is found to have contribution coming from its pre-cursor decay, which has been separated out from its cumulative cross-section. Experimental data have been compared with the predictions of statistical model code PACE2. Sizable enhancement in the experimentally measured production cross-sections has been observed in case of* α*-emitting channels over the theoretical ones, which has been attributed to coming from incomplete fusion of projectile at these energies. During the analysis of experimental data, incomplete fusion has been found to be in competition with complete fusion, and is observed to be more at higher energies. As such, an attempt has been made to estimate the fraction of incomplete fusion for both the systems, and has been found to be sensitive to the projectile energy and mass asymmetry of interacting partners.*

In HI-induced reactions, at energies near and above the B_{fus} a large number of reaction channels are expected to open up, where the measurement and analysis of excitation functions may provide significant information about the involved reaction mechanism. Since, the mechanism of CF reactions (CN-mechanism) is well established and several theoretical codes based on CN-mechanism are available, it is expected that model based calculations of EFs for CF channel will agree rather well with their corresponding experimental data. Therefore, if one compares the experimentally measured EFs with the predictions of theoretical model codes, the experimentally measured EFs are expected to agree well with the theoretical model predictions in case of fusion-evaporation channels. However, as has already been mentioned in the Chapter-I, at relatively higher projectile energies corresponding to the critical limit of driving input angular momenta for CF (above ℓ_{crit}), the CF gives way to the ICF, where α-particles are emitted in forward cone as spectator. As such, due to the presence of this type of reaction process i.e., the ICF processes, the production cross-section of reaction products may get enhanced as compared to the predictions of theoretical models codes. It may, further, be pointed out that this enhancement in the production cross-section is expected to be more at relatively higher projectile energies. It may be because of the fact that, the break-up probability significantly increases with projectile energy and driving input angular momenta. As such, in order to investigate the presence of contribution coming from ICF in the production of different α-emitting channels, excitation functions(EFs)[1] for nine radio-nuclides produced in $^{16}O+^{159}Tb$ and $^{16}O+^{169}Tm$ systems at energies $\approx$ 5-7 MeV/nucleon have been measured [59]. The experimentally measured EFs have been compared with the predictions of theoretical model code PACE-2. Experiments have been carried out using 15-UD Pelletron accelerator facility [63, 64] of the Inter-University Accelerator Center (IUAC), New Delhi, India. Activation technique followed by off-line gamma-spectroscopy has been used [65]. Since, ICF is found to contribute significantly to the production cross-section of residues associated with α-emitting channels, as such, in order to have better understanding of ICF contribution, the percentage incomplete fusion fraction has been estimated from the comparison of experimentally measured and theoretically calculated EFs. This Chapter is organized as follows; the details of technique used in the measurement of EFs are given in section 2.1. However, the experimental details like; sample preparation, experimental set-up, calibration of the spectrometer, irradiation of target samples and post irradiation analysis, detection of residues and/or identification of populated reaction products are given in the following sections/sub-sections, respectively.

[1]**Pushpendra P. Singh** *et al.*, Physical Review **C77**, 14607 (2008)

2.1 Stacked Foil Activation Technique

Activation technique [65] is one of the simplest and powerful methods for measuring the EFs to deduce important information about the nuclear reaction dynamics, and has been extensively used. In this technique, a stack of targets backed by Al-catchers may be irradiated by an energetic beam. After the irradiation, the activities induced in the target-catcher foil assembly are recorded off-line for a considerably long time depending on the half-lives of reaction products of interest. Some of the important advantages of the activation technique are following;

- Measurement of induced activity may be done after the irradiation. Therefore, there is no possibility of contamination from beam background.
- When a sample is irradiated, several nuclear reactions take place simultaneously. Many of these reactions leave radioactive nuclides. Each radioactive nuclide has its characteristic half-life and decay mode. The stacked foil activation technique provides the possibility of measuring cross-sections for several reactions at different projectile energies in a single irradiation, hence the beam-time requirements can be minimized.
- With the availability of high resolution detectors, it is, now, possible to separate out the activities of different reaction products decaying by γ-rays of nearly same energies, accurately. As a result, errors in these measurements are expected to be quite low.

2.2 Target preparation and irradiation

The self supporting, spectroscopically pure, ^{159}Tb (abundance = 99.99 %) targets of thickness $\approx$ 0.83 mg/cm^2 were prepared by rolling method and the ^{169}Tm (abundance = 100 %) targets of $\approx$ 0.65 mg/cm^2 thickness were deposited on Al-backing of $\approx$ 1.5 mg/cm^2 thickness, using high vacuum-evaporation technique. The Al-backing of ^{169}Tm targets served both as energy degrader as well as catcher for residues recoiling out of the target foil during the irradiations. In the present experiment, the ^{159}Tb targets were backed by thick Al-catchers of thickness $\approx$ 2 mg/cm^2 to trap recoiling reaction products. Since, a precise knowledge of the target thickness is an essential part of the absolute cross-section measurement of different reaction products, therefore, the thickness of each target was determined by α-transmission method. This technique is based on the measurement of the energy lost by 5.487 MeV α-particles obtained from standard ^{241}Am

source, while passing through the material of target. The targets were cut into the size of 1.2×1.2 cm^2 and were pasted on Al-holders having concentric hole of 1.0 cm diameter. The Al-holders were used for rapid dissipation of heat produced during the irradiations.

The irradiations have been carried out in the General Purpose Scattering Chamber (GPSC) having an Invacuum Transfer Facility (ITF) using recoil-catcher activation technique. A photograph of GPSC and ITF are shown in Figs.2.1. The ITF has been used to minimize the lapse time between the stop of irradiations and beginning of the counting. Two stacks, each containing 4 and 5 samples of ^{159}Tb were irradiated at the beam energies $\approx$ 87 and 95 MeV, while, two stacks of ^{169}Tm targets having 4 and 3 samples each were irradiated at the beam energies $\approx$ 92 and $\approx$ 95 MeV by $^{16}O^{7+}$ beam. Typical target-catcher foil arrangement for the measurement of EFs is given in Fig.2.2.

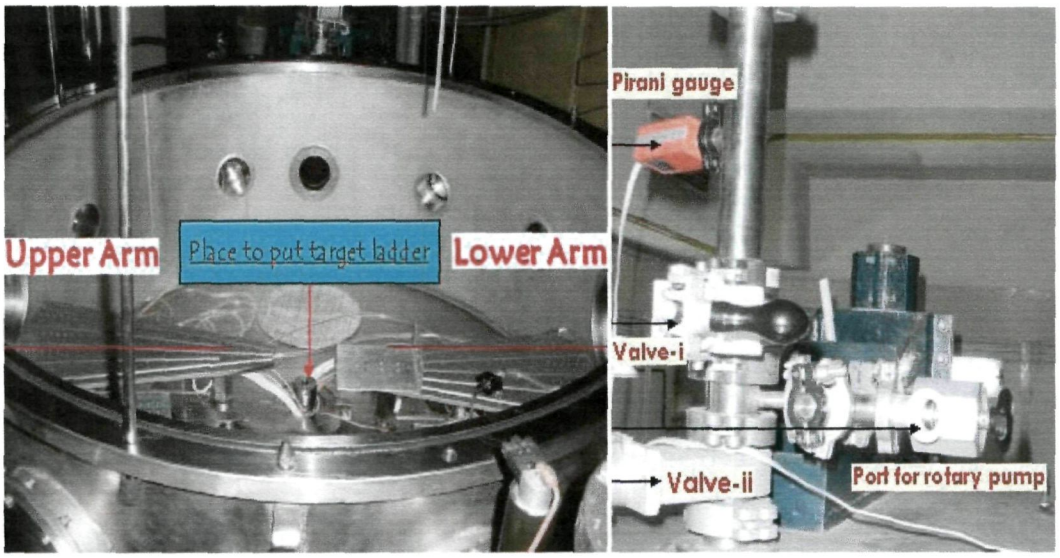

Figure 2.1: Inside view of the General Purpose Scattering Chamber (GPSC), and typical arrangement of an Invacuum Transfer Facility (ITF), used for invacuum transfer of irradiated samples.

As can be seen from this figure, catcher foils of sufficient thicknesses are placed just after each target to stop the recoils produced in the reaction. The beam current in all irradiations was $\approx$ 30-50 nA. However, extra care has been taken to keep the beam current constant during the irradiations. The stack of targets along with Al-catcher foils was placed normal to the beam direction so that the recoiling nuclei, which have been populated during the interaction of projectile and target nuclei may be trapped in

the catcher foil thickness. Keeping in view the half-lives of interest, irradiations have been carried out for ≈ 8-10 hrs. The beam flux was calculated by the total charge collected in the Faraday cup, placed behind the target-catcher foil assembly, using a current integrator device.

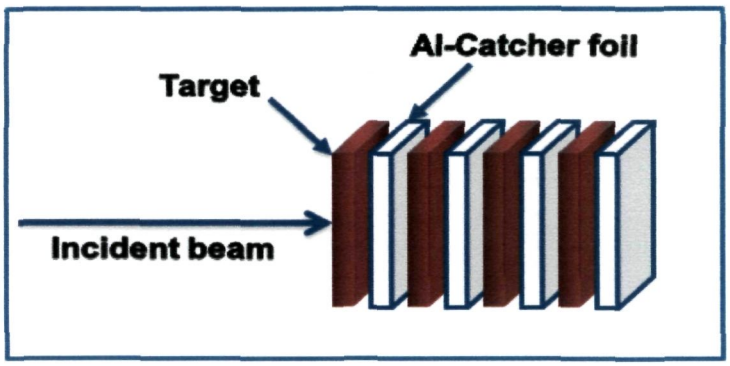

Figure 2.2: Typical target-catcher foil arrangement for the measurement of EFs.

Moreover, in a separate experiment done earlier, the determination of the incident flux was checked by putting two Rutherford monitors at 30^0 with respect to the beam direction. As the incident beam passes through the stack, it loses its energy. As such, successive targets of the stack get irradiated at different energies. The energies of the incident ion on successive targets have been calculated using stopping power code SRIM06 based on the range-energy formulations [66].

2.3 Post irradiation analysis

2.3.1 Calibration and efficiency of HPGe-detector

After the irradiation the stack of targets along with catcher foils was taken out from the GPSC with the help of ITF. The evaporation residues populated in each target-catcher foil assembly via complete and/or incomplete fusion of ^{16}O were identified by counting the induced activities (characteristic γ-rays) in a complex γ-ray spectra. The activities induced in the irradiated samples were recorded using high resolution (resolution ≈2 keV for 1.33 MeV γ-ray of ^{60}Co) HPGe γ-ray spectrometer of 100 c.c. active volume coupled to a PC through CAMAC based FREEDOM software [67]. The HPGe detector was pre-calibrated both for energy as well as efficiency by using various standard γ sources i.e., ^{60}Co and ^{152}Eu of known strengths.

The geometry dependent efficiency ($G\varepsilon$) of the HPGe detector at a given energy has been calculated using the following expression;

$$G\varepsilon = \frac{N_o}{N_{ao}e^{(-\lambda t)}\theta} \tag{2.1}$$

Where, N_o is the disintegration rate of the standard γ source at the time of measurement, N_{ao} is the disintegration rate at the time of manufacture of the source, λ is the decay constant, t is the time lapse between the manufacture of the source and the start of counting and θ is the branching ratio of the characteristic γ-ray. The prominent γ-rays of the standard ^{152}Eu source given in Table 2.1, have been used in the present measurements, both for energy calibration of the γ-ray spectrometer and for the determination of detector efficiency for different energies.

Table 2.1: The energy and absolute intensities of some predominant γ-rays from standard γ source ^{152}Eu

γ ray energy (keV)	Absolute Intensity(%)
121.78	28.40
244.69	7.51
344.29	26.60
443.89	2.80
778.92	12.98
867.58	4.21
964.11	14.50
1089.71	1.71
1112.08	13.60
1212.90	1.40
1299.16	1.63
1408.00	20.80

In order to keep the geometry dependent detector efficiency same for both standard γ-sources and samples/catchers, the standard γ-sources and the irradiated samples and/or catcher foils were counted in the same geometry. However, the source-detector separations for various irradiated samples were kept different depending on the intensity of the induced activities in order to keep the dead time of counting less than 10%. The geometry dependent efficiency curves for the γ-rays of different energies and for various

source-detector separations were plotted using the ORIGIN graphics software and are given in Fig.2.3(a-b).

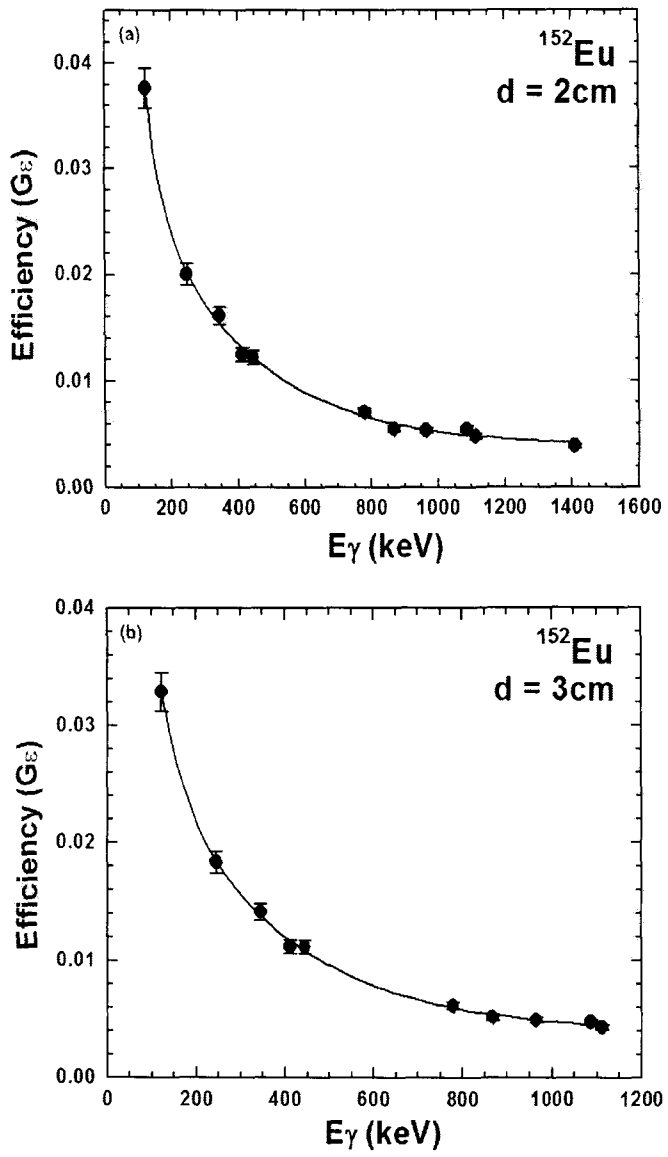

Figure 2.3: Typical geometry dependent efficiency curves of HPGe detector for different γ-energies at source-detector separations (a) d=2cm, and (b) d=3cm. Solid line represents the best polynomial fit.

Further, the geometry dependent efficiency of HPGe spectrometer is found to be best fitted with a 5th order polynomial function of following type;

$$G\varepsilon = a_0 + a_1X + a_2X^2 + a_3X^3 + a_4X^4 + a_5X^5 \tag{2.2}$$

Where, X being the energy of the characteristic γ-ray and a_0, a_1, a_2, a_3, a_4 and a_5 being the coefficients having different values for different source-detector distances. Further, the activities induced in the target-catcher foil assembly were recorded at increasing times, so that the recorded activity at different times may be used for the decay curve analysis.

2.3.2 Identification of radio-nuclides

The radio-nuclides populated by beam-target interactions are likely to decay to the ground state by emitting characteristic γ-rays. As typical examples, the γ-ray spectrum of $^{16}O+^{159}Tb$ and $^{16}O+^{169}Tm$ bombarded at $\approx$ 95 MeV are shown in Fig.2.4 and Fig.2.5, respectively.

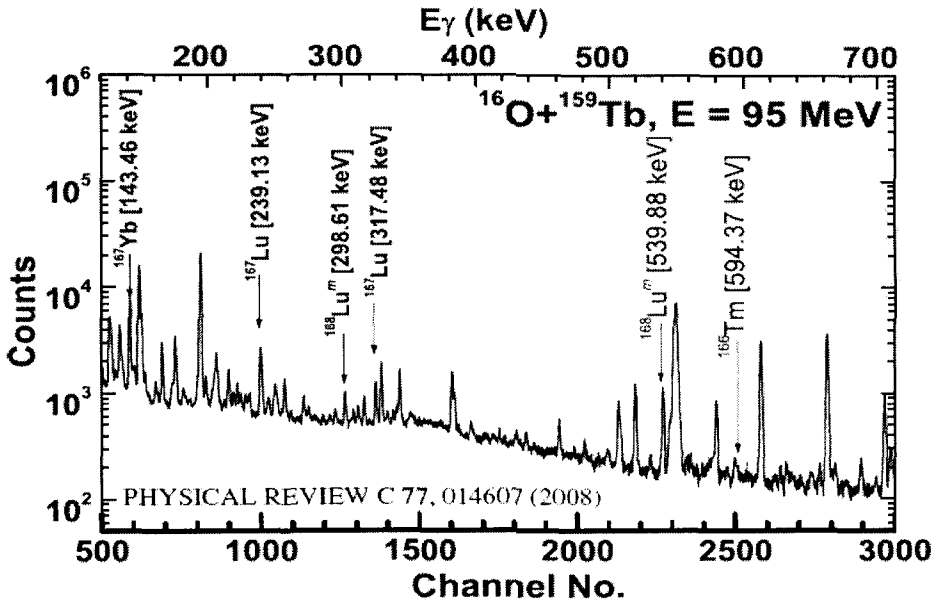

Figure 2.4: Typical γ-ray spectrum showing γ-lines of different radio-nuclides populated via CF and/or ICF in ^{16}O+^{159}Tb system at projectile energy $\approx$ 95MeV.

In order to determine the production cross-section of these residues, first of all it is desirable to identify characteristic γ-rays corresponding to the various reaction products.

The assigned γ-lines of the various residues have also been identified in the spectra recorded at increasing times by decay curve analysis. The identification of residues has been performed by identifying characteristic γ-rays of reaction products and also by measuring their half-lives. This is a very specific way for the identification of reaction residues because each radio-active isotope has a unique decay mode. Thus, the observed intensity of induced activity is a measure of the production cross-section of that particular reaction residue.

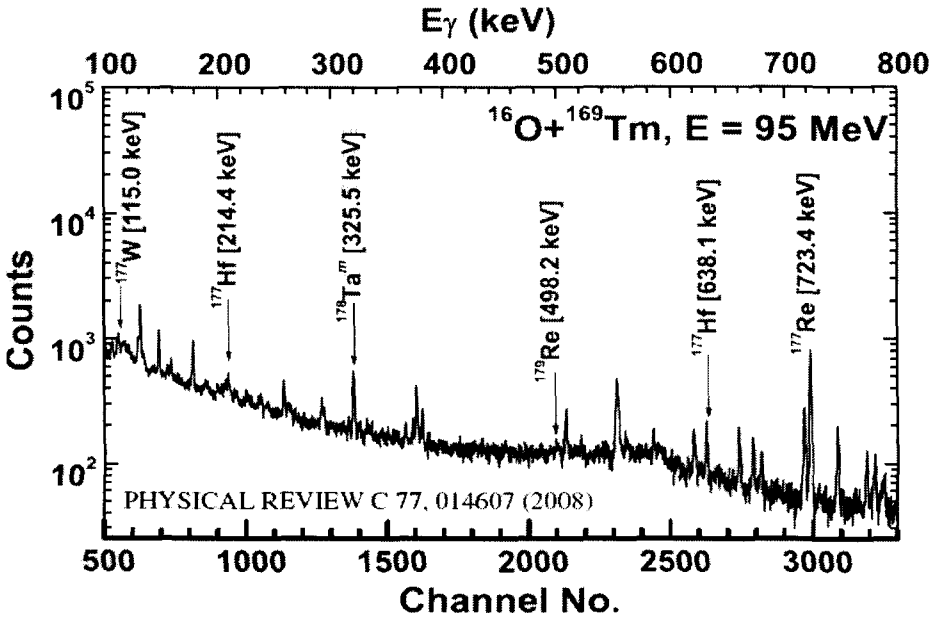

Figure 2.5: Typical γ-ray spectrum showing γ-lines of different radio-nuclides populated via CF and/or ICF in ^{16}O+^{169}Tm system at projectile energy $\approx$ 95MeV.

However, since there may be several residues which may emit γ-ray of nearly same energies, in such a case only γ-ray identification may not be enough. As such, the intensity of the photo-peaks were plotted as a function of time to get the half-lives of the residues to confirm the identification. As a representative case, the observed decay curve of ^{177}Hf having half-life $t_{1/2}$ = 51.4min is shown in Fig.2.6. As can be seen from this figure, the minimum counts at the time just after the irradiation $C_{t=0}$ is found to be 606 which reduces by half i.e. 303 at the time 50 min after the stop the irradiation. Thus, different peaks have been assigned to various residues that may be produced via

CF and/or ICF reaction channels.

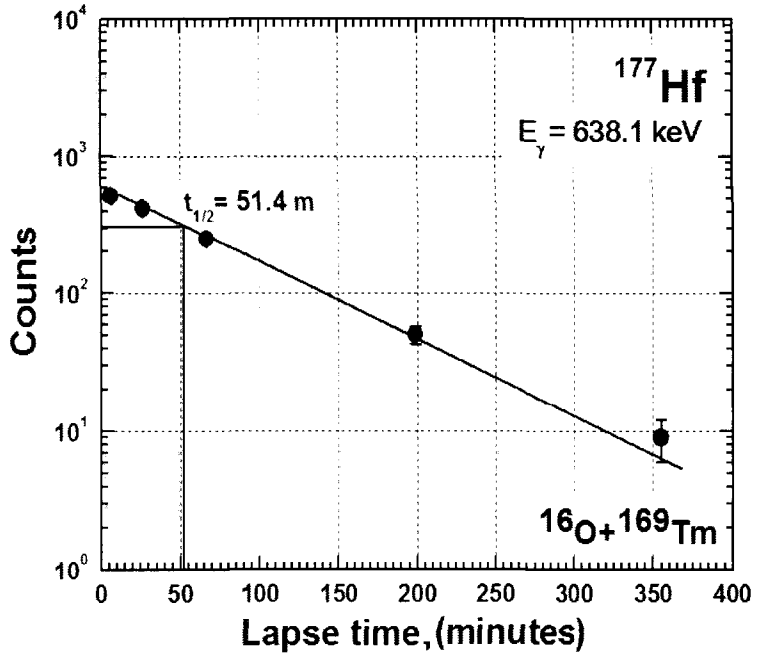

Figure 2.6: Experimentally observed counts have been plotted as a function of lapse time, which indicates half live of 51.4 min corresponding to ^{177}Hf residue produced in $^{16}O+^{169}Tm$ system at γ-ray energy $E_\gamma = 638.1$ keV.

The reaction products identified using the assignment of characteristic γ-radiations and decay curve analysis are given in Tables-2.2 & 2.3, alongwith their spectroscopic properties which has been taken from the Table of Isotopes[68] and Nuclear Wallet Card[69].

2.3.3 Production cross-section measurement

The production cross-section σ_r(E) is a measure of the probability of the formation of a particular reaction product. Experimentally, the cross-section for a reaction $X(a,b)Y$ may be defined as the number of events of a given type $X(a,b)Y$ per unit area per unit target nucleus per unit time. The cross-section is generally expressed in units of barn which is equal to $10^{-24}cm^2$. As such, the reaction cross-section may be represented as,

Table 2.2: List of identified evaporation residues produced in ^{16}O+^{159}Tb system via complete and/or in-complete fusion.

Reactions	Residues	E_γ(keV)	half-life	J_π	$a_\gamma(\%)$
$^{159}Tb(^{16}O, \alpha 3n)$	$^{168m}_{71}Lu$	298.61	6.7 m	3+	17
		539.88			47
$^{159}Tb(^{16}O, \alpha 4n)$	$^{167}_{71}Lu$	239.13	57.5 m	7/2+	8.2
		317.48			1.5
$^{159}Tb(^{16}O, \alpha p3n)$	$^{167}_{70}Yb$	143.46	17.5 m	5/2-	2.10
$^{159}Tb(^{16}O, 2\alpha n)$	$^{166}_{69}Tm$	594.37	7.7 h	2+	3.08
		1176.68			8.4

$$\sigma_r(E) = \frac{Number\ of\ events\ of\ a\ given\ type\ X(a,b)Y/area}{N_0\ \phi\ t} \tag{2.3}$$

Where, N_0 is the number of nuclei in the target, ϕ is the flux of incident beam and t is the time of bombardment. In order to determine the cross-section of a particular reaction, the quantities given in the denominator of the above equation are known and the quantities in the numerator i.e., the number of events of a given type $X(a,b)Y$ are required to be measured. The number of events of a given type may be obtained from (a)On-line measurements, by recording the outgoing particles directly using particle telescopes accommodated in the irradiation chamber, and/or by (b)Off-line measurements, by following the activities induced in the irradiated samples, only in case the radio-active residues (Y) are of measurable half-lives. As has already been mentioned, the irradiation of a sample by a particle beam may initiate various reactions in it and many isotopes are formed by the process of transmutation. The rate of formation (N) of a particular activation product may be given by the following expression,

$$N = N_0 \phi \sigma_r \tag{2.4}$$

where; ϕ is the flux of incident beam, N_0 is the initial number of nuclei in the target/sample and σ_r is the reaction cross-section for that particular channel.

The disintegration rate of the induced activity in a sample after a time t from the stop of irradiation may be given as,

$$\left[\frac{dN}{dt}\right]_t = N\frac{[1 - exp(-\lambda t_1)]}{exp(\lambda t)} \tag{2.5}$$

Table 2.3: List of identified evaporation residues produced in ^{16}O+^{169}Tm system via complete and/or in-complete fusion.

Reactions	Residues	E_γ(keV)	half-life	J_π	a_γ(%)
$^{169}Tm(^{16}O, \alpha p3n)$	$^{177}_{74}W$	115.0	2.21 h	1/2-	59
		426.94			13.1
$^{169}Tm(^{16}O, \alpha 2pn)$	$^{178}_{73}Ta$	325.5	2.36 h	7-	94.1
		331.6			32
$^{169}Tm(^{16}O, \alpha 3pn)$	$^{177}_{72}Hf$	214.4	51.4 m	7/2-	8.3
		638.1			20.0
$^{169}Tm(^{16}O, \alpha 4n)$	$^{177}_{75}Re$	1118.4	14.0 m	5/2-	25
		723.4			15
$^{169}Tm(^{16}O, \alpha 2n)$	$^{179}_{75}Re$	221.9	19.5 m	5/2+	3.6
		401			7.3
		498.2			5.7

where; t_1 is the time of irradiation and λ is the decay constant of the induced activity given as,

$$\lambda = \frac{ln2}{t_{1/2}} \tag{2.6}$$

The factor $[1 - exp(-\lambda t_1)]$ is called the saturation correction. It should also be considered that some radio nuclei produced may also decay during the irradiation time, therefore, the number of decays of the induced activity in a very small time dt may be given as,

$$dN = N\frac{[1 - exp(-\lambda t_1)]}{exp(\lambda t)}dt \tag{2.7}$$

If the activity induced in the irradiated sample is recorded for time duration t_3 after a lapse time t_2, then the number of nuclei decayed in time between t_2 to (t_2+t_3) may be given as,

$$C = N\frac{[1 - exp(-\lambda t_1)][1 - exp(-\lambda t_3)]}{\lambda.exp(\lambda t_2)} \tag{2.8}$$

If the activity induced in the sample is recorded by a γ-ray spectrometer of efficiency G_ε, then, absolute count rate C and observed counting rate may be related as,

$$C = \frac{A}{G_\varepsilon.\theta.K} \tag{2.9}$$

Where, θ is the branching ratio of the characteristic γ-ray and K=$[\{1 - exp(-\mu d)\}/\mu d]$ is the self absorption correction factor for the material of the sample of thickness d (gm/cm^2) and of absorption coefficient μ (cm^2/gm). Thus, σ_r can be written as,

$$\sigma_r = \frac{A.\lambda.exp(\lambda t_2)}{N_0.\theta.\phi.G_\varepsilon.K.[1 - exp(-\lambda t_1)][1 - exp(-\lambda t_3)]} \tag{2.10}$$

Also, the count rate at the time of stop of irradiation $C_{t=0}$ can be given as,

$$C_{t=0} = \frac{A.\lambda.exp(\lambda t_2)}{[1 - exp(-\lambda t_3)]} \tag{2.11}$$

The reaction cross-section σ_r may be written with the help of above equations as,

$$\sigma_r(E) = \frac{C_{t=0}}{N_0.\theta.\phi.G_\varepsilon.K.[1 - exp(-\lambda t_1)]} \tag{2.12}$$

A FORTRAN program EXP-SIGMA based on the above formulations has been used for the determination of the reaction cross-sections of the populated reaction products.

In the present work, excitation functions for nine radio-nuclides (expected to be populated via CF and/or ICF processes) ^{168m}Lu(α3n), ^{167}Lu(α4n), ^{167}Yb(αp3n) and ^{166}Tm(2αn) produced in ^{16}O+^{159}Tb system, and ^{179}Re(α2n), ^{177}Re(α4n), ^{177}W(αp3n), ^{178}Ta(α2pn), and ^{177}Hf(α3pn) produced in ^{16}O+^{169}Tm system have been measured. Experimentally measured production cross-sections of identified radio-nuclides are given in Tables-2.4 & 2.5.

2.3.4 Uncertainties in the measurements

The errors in the measured production cross-sections may arise mainly due to following reasons;

- The non-uniform thickness of samples may lead to the uncertainty in the determination of the number of target nuclei. To check the uniformity of the sample, thickness of the each sample was measured at different positions by α-transmission method. It is estimated that the error in the thickness of the sample material is less than 1%.

Table 2.4: Experimentally measured production cross-sections for evaporation residues populated via ICF and/or CF in $^{16}O+^{159}Tb$ system along with the projectile energies.

Lab Energy (MeV)	$\sigma(^{168m}Lu)$ (mb)	$\sigma(^{167}Lu)$ (mb)	$\sigma(^{167}Yb)$ (mb)	$\sigma(^{166}Tm)$ (mb)
75.2±0.9	3±0.59	-	-	-
78.7±0.9	12±1.86	-	-	1.93±0.36
83.2±0.9	57±6.81	5±1.12	9±1.23	7±1.24
87.2±0.8	69±9.8	46±6.54	28±4.22	28±3.11
89.6±1.0	87±11.67	59±9.61	49±5.94	31±5.69
94.6±0.4	145±16.93	118±17.52	21±3.63	49±7.56

- Fluctuations in the beam current may result in the variation of incident flux. Proper care has been taken to minimize the beam current fluctuations as far as possible and, correction in flux determination has been applied.

- Uncertainty in the determination of geometry dependent efficiency of γ-spectrometer. The error in the efficiency determination due to the statistical fluctuations in counts is estimated to be less than 2% for the present measurements.

- The loss of the product nuclei recoiling out of the sample may introduce large errors in the measured cross-sections. In order to reduce it, the thickness of the catcher foils was kept sufficient to stop even the most energetic residues. Moreover, in the present measurements both the sample and the catcher foils were counted together and hence, the losses due to the recoiling of nuclei is further avoided.

- The dead time of the recording system may also introduce errors in the measured cross-sections. The dead time of the spectrometer in present measurements has been kept $\leq$10% by suitably adjusting sample-detector distance and corrections for it were applied.

The overall errors from all the aforementioned factors are estimated to be $\leq$ 15 %, including statistical errors. These errors exclude the uncertainty of the nuclear data like branching ratio, decay constant etc., which have been taken from the Table of Isotopes[68, 69].

Table 2.5: Experimentally measured production cross-sections for evaporation residues populated via ICF and/or CF in ^{16}O+^{169}Tm system along with the projectile energies.

E_{beam} (MeV)	$\sigma_{cum}(^{177}\mathrm{W})$ (mb)	$\sigma_{ind}(^{177}\mathrm{W})$ (mb)	$\sigma(^{178}\mathrm{Ta})$ (mb)	$\sigma(^{177}\mathrm{Hf})$ (mb)	$\sigma(^{177}\mathrm{Re})$ (mb)	$\sigma(^{179}\mathrm{Re})$ (mb)
74.9±0.9	-	-	-	-	-	3±0.89
78.7±0.9	17±2.49	-	36±4.58	8±0.89	-	14±1.24
82.0±0.8	41±4.3	35±3.17	87±8.91	11±1.27	5±1.09	19±3.02
85.8±0.8	36±5.9	28±4.63	106±7.61	28±2.32	7±1.04	39±4.64
88.9±1.0	73±6.2	58±5.31	143±13.57	37±2.59	13±1.96	46±5.36
91.6±0.4	79±8.3	62±6.48	149±12.81	40±3.71	15±2.97	37±6.98
94.6±0.4	96±9.5	61±7.19	194±18.41	63±6.51	31±3.17	32±3.71

2.4 Analysis of EFs with code PACE2

In order to examine the extent to which the observed quantities are described in terms of the equilibrated decay of excited compound nuclei $^{175}Ta^{\star}$ and $^{185}Ir^{\star}$ produced in the interaction of ^{16}O with ^{159}Tb and ^{169}Tm target nuclei at projectile energies $\approx$ 5-7 MeV/nucleon, the presently measured EFs have been compared with the predictions of theoretical model code PACE2 (based on Hauser Feshbach theory)[71]. The code PACE2 is based on statistical approach of CN de-excitation by Monte Carlo procedure. This code does not take ICF into consideration. In code PACE2 the angular momentum projections are calculated at each step of de-excitation. The angular momentum conservation is explicitly taken into account, and the CF cross-sections are calculated using BASS formula[72].

The partial cross-section (σ_ℓ) for the formation of compound nucleus at a particular angular momentum ℓ and specific bombarding energy, E is given by,

$$\sigma_\ell = \frac{\lambda^2}{4\pi}(2\ell+1)T_\ell \tag{2.13}$$

where, λ is reduced wavelength. Transmission coefficients T_ℓ may be given by the expression,

$$T_\ell = \left[1 + exp\left(\frac{\ell - \ell_{max}}{\Delta}\right)\right]^{-1} \tag{2.14}$$

where, Δ is the diffuseness parameter, while ℓ_{max} the maximum amount of ℓ determined by total fusion cross-section,

$$\sigma_F = \sum_{\ell=0}^{\infty} \sigma_\ell \tag{2.15}$$

The optical model potentials of Becchetti and Greenlees[73] have been used for calculating the transmission coefficients for neutron and proton, and optical model potential of Satchler[74] for α-particle emission. In the description of γ-ray competitions, emission of E1, E2, M1 and M2 γ-ray are included and the γ-ray strength functions for different transitions, are taken from tables of Endt[75]. In code PACE-2, the level density parameter $a(= A/K)$, is an important parameter, where, A is the mass number of the nucleus and K is a free parameter. The value of K may be varied to match the experimental data.

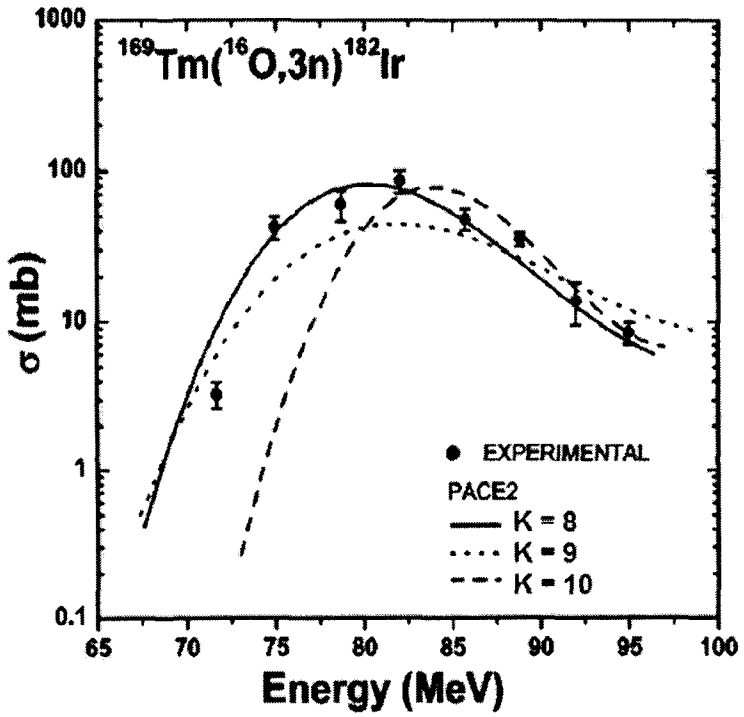

Figure 2.7: Experimentally measured and theoretically calculated EFs for ^{182}Ir produced via CF in ^{16}O+^{169}Tm system. The lines represent the PACE2 calculations for different values of parameter K.

In the present work, the experimental data has been tested using different values of level density parameters. It may, however, be pointed out that a value of $K \geq 10$, may give rise to the anomalous effect in particle multiplicity, and compound nucleus temperature[76]. Although, it is possible to explain all the excitation functions with different values of parameters of the code for individual channels, however, from the physics point of view, it is quite unreasonable. As such, in the present work all the calculations have been performed consistently using same set of parameters for all the channels. The value of level density parameter (a) was taken as A/8 MeV^{-1} i.e., K=8, as suggested by Gilbert and Cameron[77]. The theoretical calculations done by adopting the given set of parameters is found to agree well with the experimentally measured EF for CF-channels. As a representative case, the EFs for ^{182}Ir produced via CF through 3n-channel is shown in Fig.2.7, where the effect of variation of 'K' on calculated EFs is presented. As can be seen from this figure, the above choice reproduces the experimental data for xn-channel, predominantly populated via CF process.

2.4.1 Excitation Functions: ^{16}O+^{159}Tb system

As has already been pointed out, ICF is not taken into consideration in the theoretical model code PACE2. Hence, if there is any enhancement in the experimentally measured production cross-sections as compared to PACE2 calculations, it may be attributed to ICF processes [16, 19]. In Figs.2.8 and Fig.2.9, the experimentally measured and theoretically calculated EFs for four radio-nuclides ^{167,168m}Lu, ^{167}Yb and ^{166}Tm produced in ^{16}O+^{159}Tb system in the energy range ≈70-95 MeV are shown. The reaction products ^{167,168m}Lu have ground and metastable states of half-lives 51.5 m and 6.7 m, respectively. The reaction products ^{167,168m}Lu may be formed both via complete and/or incomplete fusion of ^{16}O with ^{159}Tb. In case of complete fusion, composite system ^{175}Ta* is formed, which may decay via the emission of an α-particle and 3 or 4 neutrons leaving behind the above residues. Since, no choice of physically accepted input parameters is able to fit the experimental data [as shown in Fig. 2.8(a)&(b)], the enhancement of measured EFs over the theoretical predictions based on CF model may be attributed to ICF. As such, it may be inferred that the same residues may also be populated via ICF. It may, further, be explained by assuming the break-up of ^{16}O-nucleus into its fragments e.g., ^{12}C and ^{4}He(α-particle) in the nuclear force field of target nucleus. One of the fragments ^{12}C fuses with ^{159}Tb, forming an incompletely fused composite system ^{171}Lu*, which may decay by the emission of three neutrons forming ^{168m}Lu and four neutrons forming ^{167}Lu. Similarly, the reaction product ^{167}Yb, which has ground state of half-life 17.5 m, is expected to be populated via complete fusion (αp3n) channel and/or incomplete fusion. In case of ICF population the ^{16}O may be assumed to break-up in to ^{12}C and

an α-particle, and one of the fragments ^{12}C fuses with ^{159}Tb followed by subsequent emission of one proton and three neutrons from ^{171}Lu*.

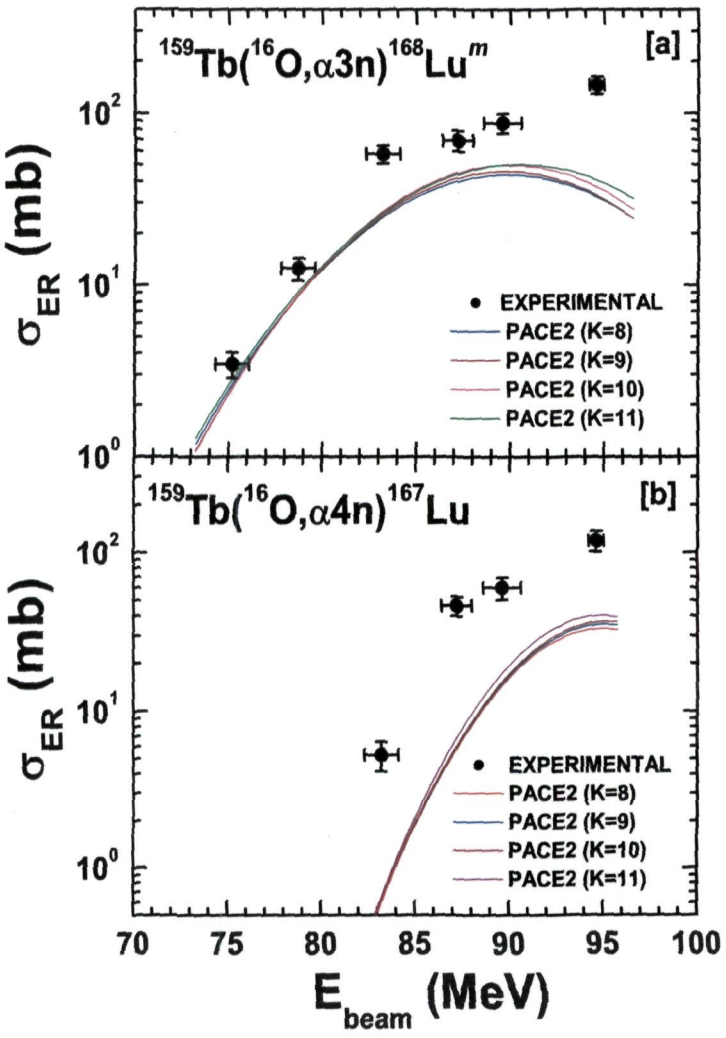

Figure 2.8: Experimentally measured and theoretically calculated EFs for ^{167,168m}Lu isotopes, populated, respectively via α4n and α3n channels in ^{16}O+^{159}Tb system.

However, the remaining α-fragment (^{4}He) of the incident ion is assumed to go on moving with beam velocity in forward direction without any significant interaction with target nucleus. Similarly, the evaporation residue ^{166}Tm ($t_{1/2}$ = 7.7 hours), is expected to be populated via fusion of ^{8}Be and subsequent emission of one neutron from ^{167}Tm*. However, the remaining part ^{8}Be may be assumed to behave like a spectator. Further, it may be observed from the Fig.2.8(a), the experimentally measured production cross-sections are almost matching with PACE-2 calculations in the energy range $\approx$ 75-80 MeV. However, in the higher energy region the measured cross-sections are some what under predicted by PACE-2 calculations. As shown in Fig.2.8(a), the enhancement as compared to theoretical model predictions may be explained by assuming that only complete fusion contributes to the formation of ^{168m}Lu in the energy range $\approx$ 75-80 MeV, while, as the energy increases both complete and incomplete fusion contribute to the production probability. In the similar way, the theoretical values of cross-sections for most of the α-emitting channels are found to be some what underpredicted than that of experimental data, as indicated in Fig.2.8 and Fig.2.9.

In order to see the effect of the variation of input parameters of Code PACE-2 on theoretical EFs, the calculations have been performed using different values of level density parameters for Lu isotopes produced in ^{16}O+^{159}Tb system and are shown in Figs.2.8(a)-(b). As can be observed from this figure, the theoretical predictions with different input parameters are almost similar or a very small change comes into picture for higher value of level density parameters at relatively higher projectile energies. Since, ICF is not taken into consideration in code PACE-2, therefore, substantially large values of experimental cross-sections (in case of ^{167,168m}Lu and ^{167}Yb evaporation residues) as compared to the theoretical ones can not be the uncertainty in measurement and hence may be attributed to the contribution coming from ICF process of the type;

$$^{16}\mathrm{O}\ (^{12}\mathrm{C}+^{4}\mathrm{He}) \Rightarrow {}^{12}\mathrm{C}+{}^{159}\mathrm{Tb} \Rightarrow {}^{171}\mathrm{Lu}^{*} + {}^{4}\mathrm{He}$$
(α as spectator)

Moreover, in case of reaction product ^{166}Tm(2αn), the theoretical predictions of PACE-2 give almost negligible cross-section and hence are not shown in Fig.2.9(b). This indicates that, the major contribution for the production of ^{166}Tm comes from ICF process of the type;

$$^{16}\mathrm{O}\ (^{8}\mathrm{Be}+^{8}\mathrm{Be}) \Rightarrow {}^{8}\mathrm{Be} + {}^{159}\mathrm{Tb} \Rightarrow {}^{167}\mathrm{Tm}^{*}+{}^{8}\mathrm{Be}$$
(Beryllium as spectator)

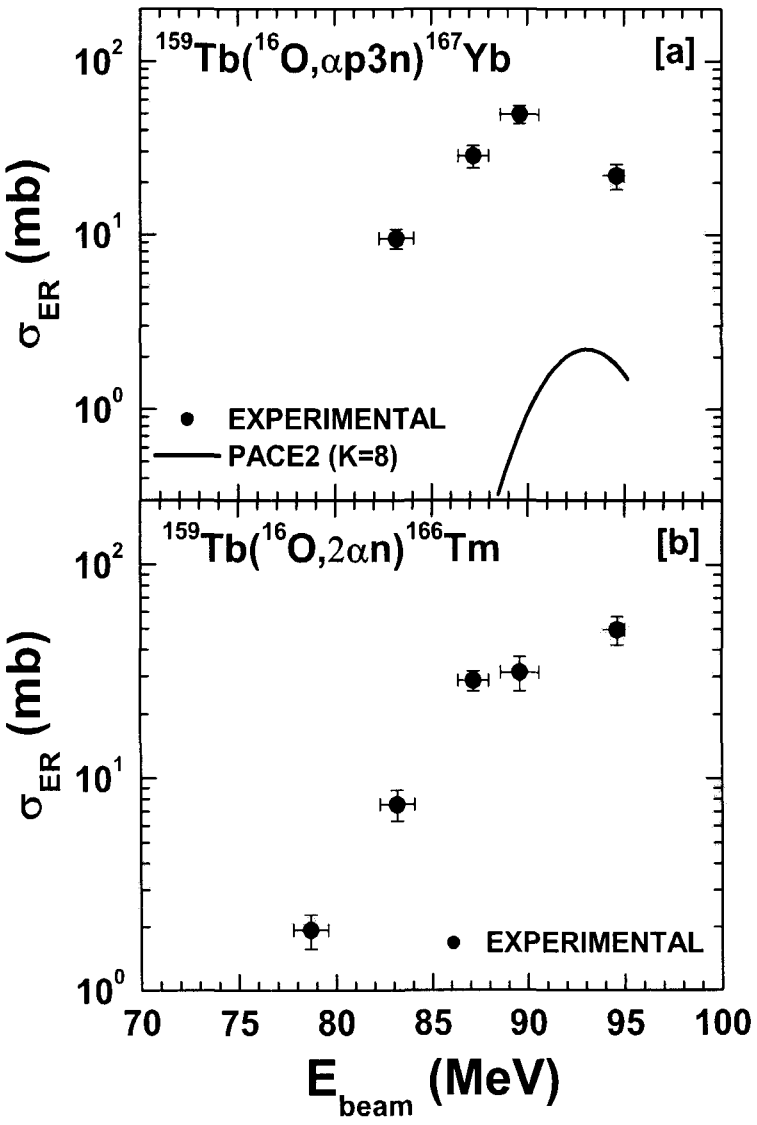

Figure 2.9: Experimentally measured and theoretically calculated excitation functions for (a) ^{167}Yb populated via αp3n channel, and (b) ^{166}Tm populated via 2αn channel in the interaction of ^{16}O with ^{159}Tb

2.4.2 Excitation Functions: $^{16}O+^{169}Tm$ system

The EFs for five radio-nuclides $^{177,179}Re$, ^{177}W, ^{178}Ta and ^{177}Hf populated in the interaction of ^{16}O with ^{169}Tm at energies ≈5-7 MeV/nucleon are shown in Figs.2.10 and Fig.2.11. The above residues may be populated via CF and/or ICF of ^{16}O with ^{169}Tm. The production of these residues via α-emission channels may also be explained in terms of the break-up of ^{16}O into ^{12}C and ^{4}He followed by fusion of ^{12}C with ^{169}Tm forming an incompletely fused composite system $^{181}Re^*$. The reaction products $^{177,179}Re$ having half-lives of 14 m and 19.7 m, are expected to be populated via the emission of four and two neutrons from $^{181}Re^*$. Thus, the evaporation residues ^{177}Re and ^{179}Re may not only be populated via in-complete fusion but may have significant probability of being formed via complete fusion of the projectile leading to the formation of $^{185}Ir^*$, which may decay by the emission of two and four neutrons along with an α particle. The complete fusion component calculated by PACE-2 code is shown in Fig.2.10(a)-(b) by solid lines. As can be seen from these figures, the calculated cross-section values by PACE-2 have lower magnitudes than the experimental data, which indicates the contribution from incomplete fusion at these energies. Similarly, the reaction products ^{178}Ta and ^{175}Hf have half-lives 2.45 h and 51.4 m, respectively and are expected to be populated via α2pn and α3pn-channels, respectively, in which α-particle behaves as spectator. Since, the theoretical predictions of code PACE2 are negligible in cases of ^{178}Ta, ^{177}Hf and ^{177}W residues, and are, therefore, not shown in the Fig.2.11(a)-(b). As such, it may be inferred that, the major contribution to these reaction channels comes from incomplete fusion processes of the type;

$$^{16}O\ (^{12}C{+}^{4}He) \Rightarrow {}^{12}C{+}^{169}Tm \Rightarrow {}^{181}Re^* + {}^{4}He$$
$$(\alpha \text{ as spectator})$$

It may be pointed out that the evaporation residue ^{177}W (half-life of 2.21 h) may be populated via three different reaction channels, viz;

(i) complete fusion of ^{16}O: where subsequent emission of an α-particle, a proton and three neutrons from $^{185}Ir^*$ leaving behind ^{177}W residual nucleus, i.e.,

$$^{16}O + {}^{169}Tm \Rightarrow {}^{185}Ir^* \Rightarrow {}^{177}W + \alpha + p + 3n$$

(ii) incomplete fusion of ^{16}O: where only ^{12}C is assumed to fuse with target nucleus, while ^{4}He behaves as a spectator. In such a case, ^{177}W may be formed after emission of a proton and three neutrons from an excited IFC $^{181}Re^*$, i.e.,

$$^{16}O\ (^{12}C{+}^{4}He) + {}^{169}Tm \Rightarrow {}^{181}Re^* + {}^{4}He \text{ (spectator)}$$
$$^{181}Re^* \Rightarrow {}^{177}W + p + 3n$$

and,

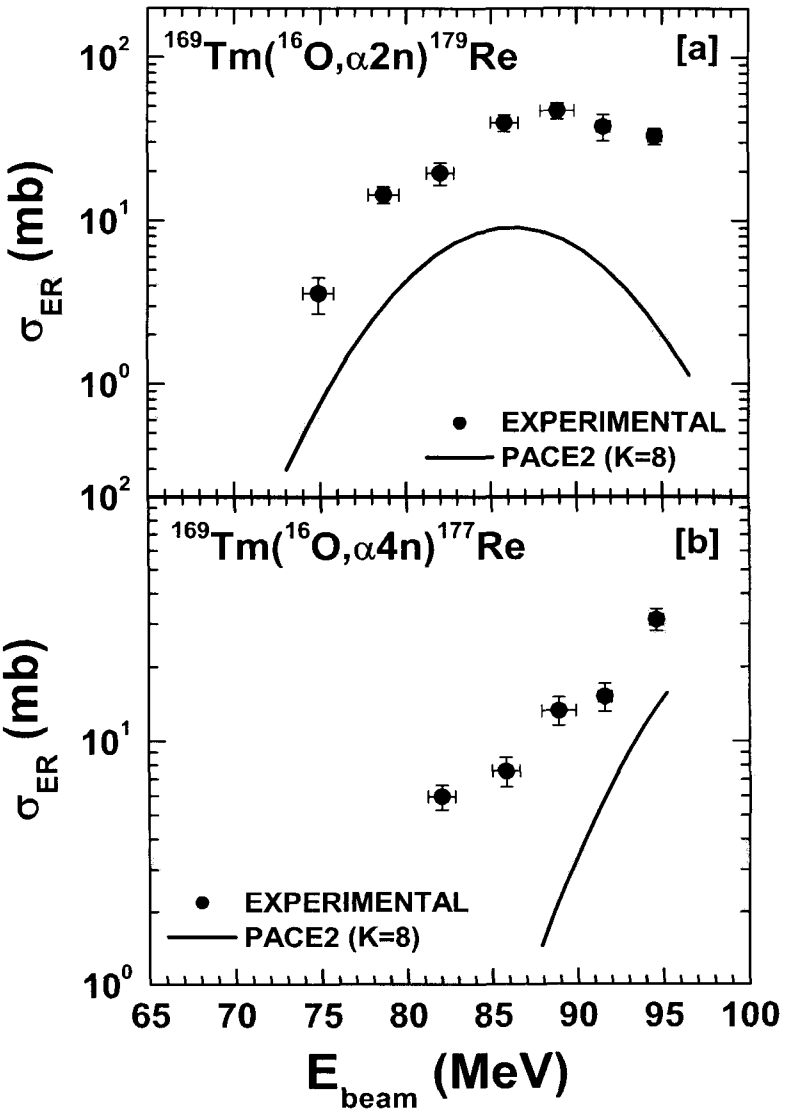

Figure 2.10: Experimentally measured and theoretically calculated EF's for ^{177,179}Re isotopes expected to be populated, respectively via α4n and α2n channels in ^{16}O+^{169}Tm system.

(iii) β^+ emission and/or EC decay of higher charge pre-cursor, i.e.,

$$^{16}O + {}^{169}Tm \Rightarrow {}^{177}Re^* + {}^{4}He + 4n$$
$$^{177}Re^* \Rightarrow {}^{177}W + \beta^+/EC$$

It may, further, be pointed out that the theoretical calculations (PACE2) for the CF channel (i) gives negligible cross-section and hence not shown in Fig.2.11(a)-(b). As such, it may be inferred that the residue ^{177}W is populated predominantly via ICF (channel '(ii)') and the pre-cursor decay (channel '(iii)'). Since, the residue ^{177}W is assumed to be populated via ICF and pre-cursor decay, hence, it is required to separate out the independent (σ_{ind}) and pre-cursor decay (σ_{pre}) contributions from cumulative cross-section (σ_{cum}).

2.4.3 Estimation of independent cross-section (σ_{ind}) from cumulative cross-sections (σ_{cum})

It has been pointed out that the cumulative cross-section (σ_{cum}) of ^{177}W may have contribution coming from its higher charge isobar pre-cursor through β^+-emission and/or electron capture(EC). For such a case, if the half-life of the pre-cursor is considerably smaller than that of the daughter residue, the independent production cross-sections (σ_{ind}) may be estimated from the cumulative production cross-sections (σ_{cum}). As such, an attempt has been made to separate out the contribution due to its pre-cursor from the cumulative activity of ^{177}W. Therefore, the σ_{cum} of a given residue is expected to be the sum of σ_{ind} and the cross-section for the independent production of its pre-cursor σ_{pre} multiplied by a numerical coefficient F_p[78] i.e.,

$$\sigma_{cum} = \sigma_{ind} + F_{pre}\sigma_{pre} \tag{2.16}$$

Where; σ_{cum} and σ_{ind} represent, respectively, the cumulative and independent yields of the residue and σ_{pre} stands for the independent contribution of the pre-cursor. The value of pre-cursor fraction (F_{pre}) depends on the branching ratio P_p for pre-cursor decay to the residue and is given by;

$$F_{pre} = P_p \frac{T_{ind}^{1/2}}{T_{ind}^{1/2} - T_{pre}^{1/2}} \tag{2.17}$$

Here, $T_{pre}^{1/2}$ and $T_{ind}^{1/2}$ are the half-lives of the pre-cursor and the daughter residues, respectively. Thus, the cumulative cross-section may be given as;

$$\sigma_{cum} = \sigma_{ind} + P_p \frac{T_{ind}^{1/2}}{T_{ind}^{1/2} - T_{pre}^{1/2}} \sigma_{pre} \tag{2.18}$$

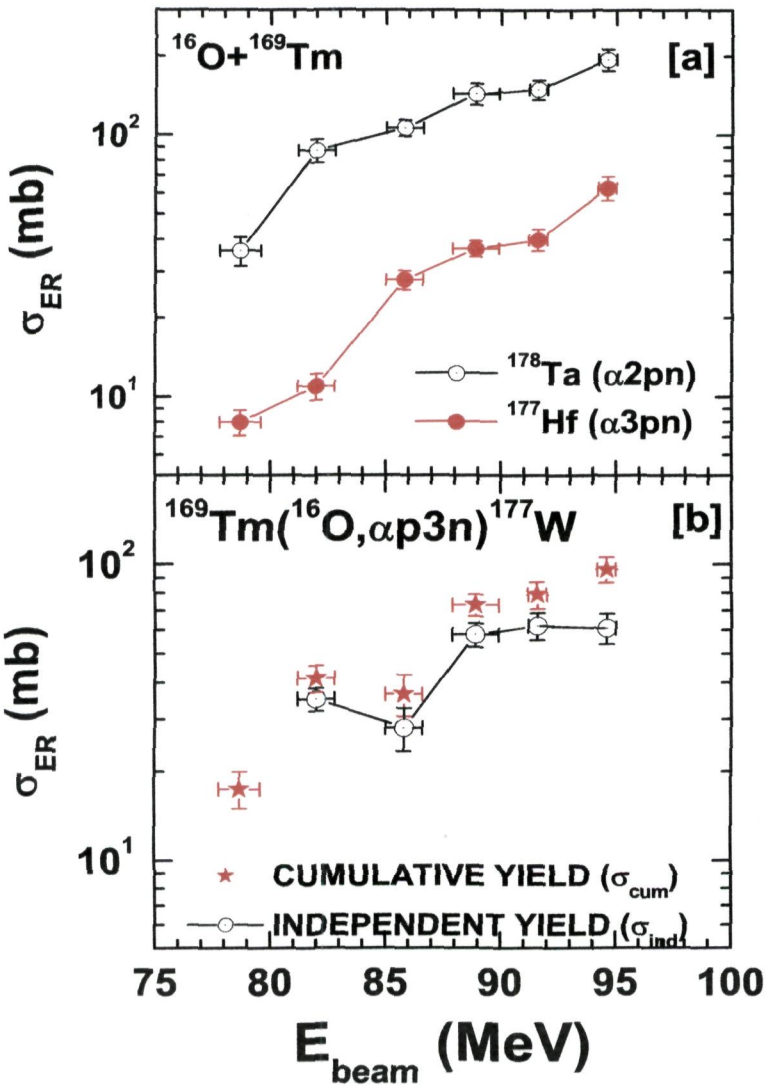

Figure 2.11: Experimentally measured excitation functions for (*a*) ^{178}Ta & ^{177}Hf, and (*b*) ^{177}W, residues expected to be populated via, respectively, α2pn, α3pn and αp3n channels in ^{16}O+^{169}Tm system. The theoretical predictions are found to be negligible for these residues and hence are not shown here.

The values of branching ratio and the half-lives required for obtaining the coefficient F_{pre} are taken from the ref.[42,44]. Using the above formulation, in the present case, the cumulative yield (σ_{cum}) and independent yield (σ_{ind}) for ^{177}W are related as follows;

$$\sigma_{cum}(^{177}W) = \sigma_{ind}(^{177}W) + 1.118\sigma_{pre}(^{177}Re) \quad (2.19)$$

where, $\sigma_{pre}(^{177}$Re) is the independent yield of the pre-cursor.

The pre-cursor contribution of ^{177}W at different energies has been subtracted from cumulative yield for the determination of independent yield. The measured cumulative cross-sections (σ_{cum}) as well as independent cross-sections (σ_{ind}) for ^{177}W residue deduced in such a way are given in Table-2.5 (on page 33) and are also plotted in Fig.2.11(b). As can be seen from this figure, the pre-cursor (^{177}Re) of ^{177}W contributes a finite value of yield to the production of ^{177}W. Moreover, the pre-cursor (^{177}Re) starts contributing to the production probability at $\approx$ 82 MeV, which is found to increase with projectile energy. It may, however, be pointed out that the cumulative and independent yields of ^{177}W reaction product are almost same up to $\approx$ 87 MeV (within the error bars), which indicates a small contribution from the pre-cursor decay for the energies up to $\approx$87MeV, while as the energy increases the pre-cursor contribution increases as inferred from the data points at $\approx$ 95MeV. As shown in this figure, the solid stars represent the cumulative cross-section of the residue ^{177}W, while the open circles represent the independent yield of this residue. A closer look to Fig.2.11(b) indicates that σ_{cum} for ^{177}W and σ_{ind} for the independent production of ^{177}W have cross-sections with a very small difference at lower energies. However, as one moves towards the relatively higher energy the difference increases to a sizable value, indicating the influence of pre-cursor contribution in this case.

Although, it may not be possible to directly obtain the relative contribution of complete and incomplete fusion from the measurement of excitation functions, however, an attempt has been made to obtain the incomplete fusion contribution. The production cross-sections which have been measured experimentally may be attributed to both the CF and/or ICF. As already mentioned, the enhancement in the experimentally measured production cross-sections than that of PACE-2 predictions may be assumed to be attributed to the incomplete fusion processes. As such, the incomplete fusion contribution for individual channels has been deduced by subtracting complete fusion cross-sections (σ_{CF}) (obtained by PACE2) from the experimentally measured cross-sections (σ_{EXP}) at respective projectile energies. The incomplete fusion contributions (σ_{ICF}), for presently measured evaporation residues are plotted in Fig.2.12(a)-(b) along with the sum of all incomplete fusion channels ($\Sigma\sigma_{ICF}$) as a function of projectile energy for ^{16}O+^{159}Tb and ^{16}O+^{169}Tm systems, respectively. The lines drawn in these figures are just to guide the eyes. As can be seen from these curves, in general, the incomplete fusion contri-

bution increases with projectile energy, which is expected as the break-up probability of the incident ion significantly increases with projectile energy.

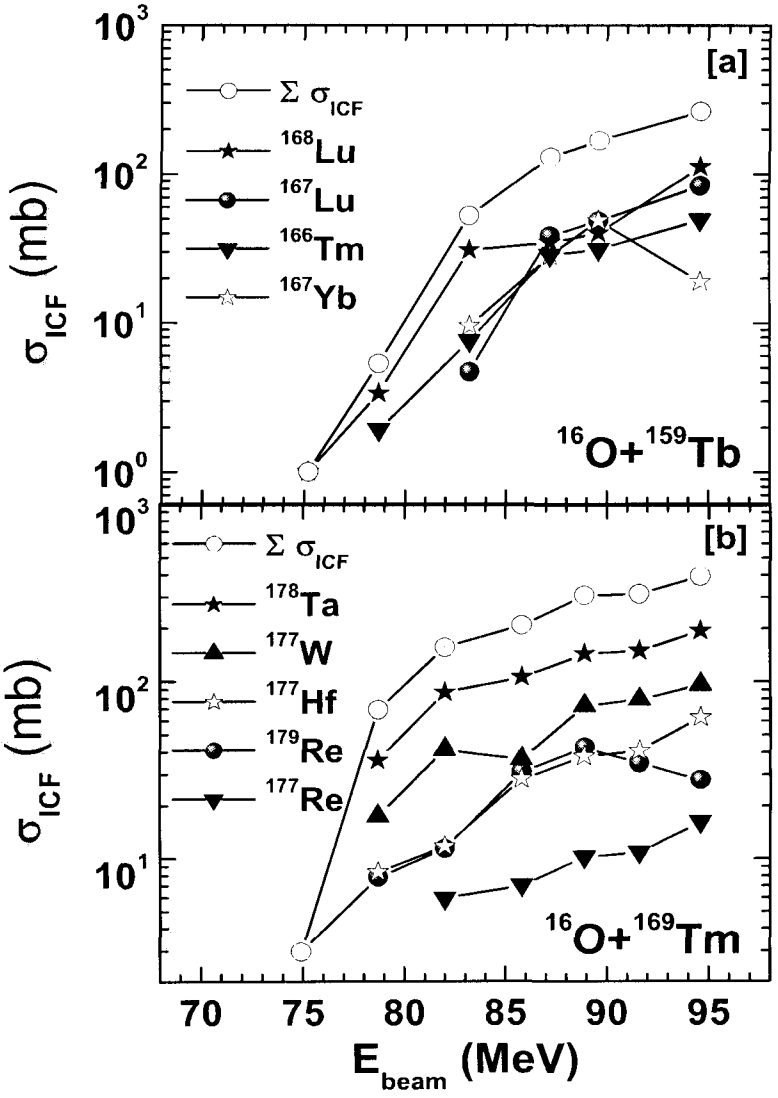

Figure 2.12: Deduced ICF contribution as a function of projectile energy for (*a*) ^{16}O+^{159}Tb, and (*b*) ^{16}O+^{169}Tm systems. Open circles represent the sum of all $\Sigma\sigma_{ICF}$.

In the present work, the cross-sections for CF and/or ICF channels have also been calculated using SUMRULE model [14], which is based on the generalized concept of critical angular momentum. In these calculations, it is assumed that, ICF channels open only for those partial waves which have ℓ-values$\geq\ell_{crit}$. On the other hand, partial waves with $\ell\leq\ell_{crit}$ contribute to CF process. In these calculations, the input parameters like; temperature (T) of the contact zone of interacting partners, the diffuseness parameter (Δ) of transmission probability distribution (T_ℓ), and the Coulomb interaction radius (R_c) are taken as 3.5MeV, 1.7 unit of angular momentum and 12fm, respectively, as suggested by Wilczynski *et al.*[14]. In the present work, it has been observed that the experimental cross-section for fusion-evaporation channels agree reasonably well with the predictions of SUMRULE model. However, there is a large discrepancy between measured and calculated cross-section values for ICF channels. As a typical example for ICF channels producing Lu isotopes in ^{16}O+^{159}Tb system, and Re isotopes in ^{16}O+^{169}Tm system, the SUMRULE calculations are lower by a factor of more than 100, in general. Similar discrepancy has also been observed in case of ^{13}C+^{181}Ta system studied by Babu *et al.*[79] in their experiment at projectile energy ≈6MeV/nucleon. As a matter of fact, Wilczynski *et al.*[14] tested the SUMRULE model for the reactions at 8-10MeV or higher energies and found satisfactory agreement in calculated and experimental cross-sections. One of the possible reasons for the above disagreement in case of ICF channels may be the non-validity of the generalized concept of critical angular momentum at energies in the range of ≈5-7MeV/nucleon. Further, the cluster structure of incident ion may also play an important role in ICF reactions.

2.5 Fraction of Incomplete Fusion (F_{ICF})

As already mentioned in the earlier section, the sum of all incomplete fusion components is taken as the total incomplete fusion contribution ($\Sigma\sigma_{ICF}$). The experimentally measured contribution coming from all incomplete fusion channels ($\Sigma\sigma_{ICF}$) and the sum of all complete fusion channels ($\Sigma\sigma_{CF}$) obtained from PACE-2 calculations are plotted along with the total fusion cross-section (σ_{TF}=$\Sigma\sigma_{CF}$+$\Sigma\sigma_{ICF}$) for presently studied systems ^{16}O+^{159}Tb and ^{16}O+^{169}Tm in Figs.2.13(a)-(b). As can be observed from these figures, the CF component has measurable contribution even at ≈70MeV, while ICF contribution seems to start from ≈75MeV, in case of presently studied systems. Further, as can be observed from the Figs.2.13(a)-(b), the separation between the plots for σ_{TF} (solid stars) and σ_{CF} (solid circles) increases with projectile energy, which indicates that, the ICF contributes larger production yield at relatively high projectile energies. This may be on account of the increasing probability of the break-up of incident ion into

α-clusters (^{12}C+α and/or ^{8}Be+^{8}Be) as the projectile energy increases.

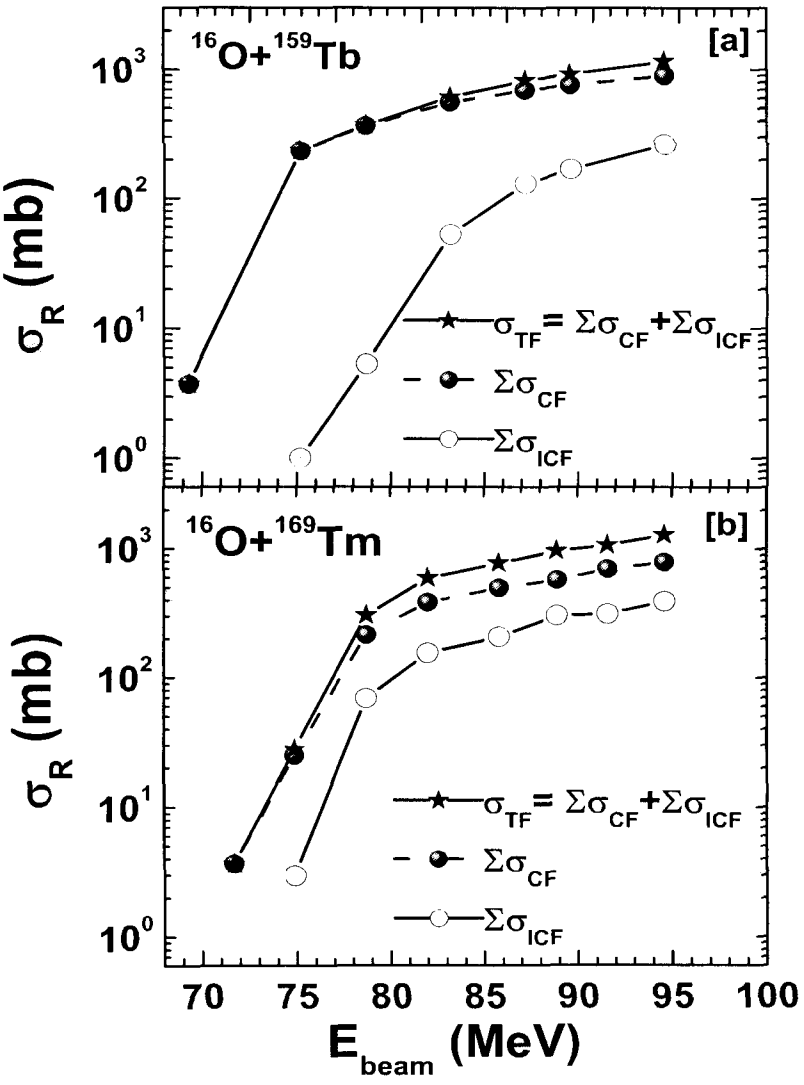

Figure 2.13: Total fusion probability (σ_{TF}) along with the sum of complete ($\Sigma\sigma_{CF}$) and incomplete fusion contributions ($\Sigma\sigma_{ICF}$) at different energies for (a) ^{16}O+^{159}Tb, and (b) ^{16}O+^{169}Tm systems.

It may, however, be pointed out that the difference between the plots for $\Sigma\sigma_{CF}$ (solid stars) and σ_{TF} (solid circles) is more for ^{16}O+^{169}Tm system as compared to ^{16}O+^{159}Tb system at different energies. This observation may be because of the fact that, ^{16}O+^{169}Tm system is more mass asymmetric as compared to ^{16}O+^{159}Tb system, indicating the dependence of underlying process on mass asymmetry of interacting partners. Further, the data seems to support the sensitiveness of incomplete fusion on projectile energy and mass asymmetry of interacting partners, as inferred by Morgenstern *et al.* [24, 25, 26]. An attempt has been made to investigate the effect of above variables on the relative contributions of complete and incomplete fusion fraction. The percentage incomplete fusion fraction (F_{ICF}) for both the systems has been estimated from the experimentally measured production cross-sections, as given below;

$$F_{ICF} = \frac{\Sigma\sigma_{ICF}}{\sigma_{TF}} \times 100 \tag{2.20}$$

The F_{ICF} for both the systems has been deduced at different energies and is plotted as a function of reduced projectile energy (E_{beam}/V_b, where V_b is Coulomb barrier of respective systems) in Fig.2.14(a)-(b). The reduced projectile energy (E_{beam}/V_b) has been used to incorporate the effect of Coulomb barrier while comparing different projectile-target combinations in a plot. As can be seen from Fig.2.14(a), at the threshold of ICF (i.e., $\approx$ 75 MeV in case of ^{16}O+^{169}Tm system) the relative percentage F_{ICF} is found to be $\approx$ 10 % of the total fusion cross-section (σ_{TF}), which increases with projectile energy. At the highest studied energy (i.e., $\approx$ 95 MeV) the relative percentage of ICF fraction approaches to $\approx$ 30 % of σ_{TF}. Similar energy dependence of ICF fraction for ^{16}O+^{159}Tb system has also been observed, where ICF fraction at $\approx$ 75 MeV is found to be $\leq$ 1 % of σ_{TF}, but at $\approx$ 95 MeV, it approaches to $\approx$ 20 % of the total fusion cross-section.

Further, it may be observed that the percentage ICF contribution is an order of magnitude higher for ^{16}O+^{169}Tm system as compared to ^{16}O+^{159}Tb system at $\approx$ 75 MeV. However, it almost approaches to nearly the same value at higher energies. This may be because of the fact that as the beam energy increases, the effect of Coulomb barrier goes on diminishing. An attempt has also been made to estimate the similar energy dependence of F_{ICF} for ^{12}C+^{128}Te and ^{12}C+^{165}Ho systems [36, 53], and is shown in Fig.2.14(b). The data for these systems is taken from our earlier publications. The percent F_{ICF} for ^{12}C+^{165}Ho system is shown in the inset of Fig.2.14(b) in order to see the variation more clearly. As can be seen from this figure, the incomplete fusion fraction for these systems also increases with the projectile energy. It may, however, be pointed out that on the basis of Fig.2.14(b) the ICF fraction for ^{12}C and ^{16}O induced

reactions increases with the charge and mass of target nucleus.

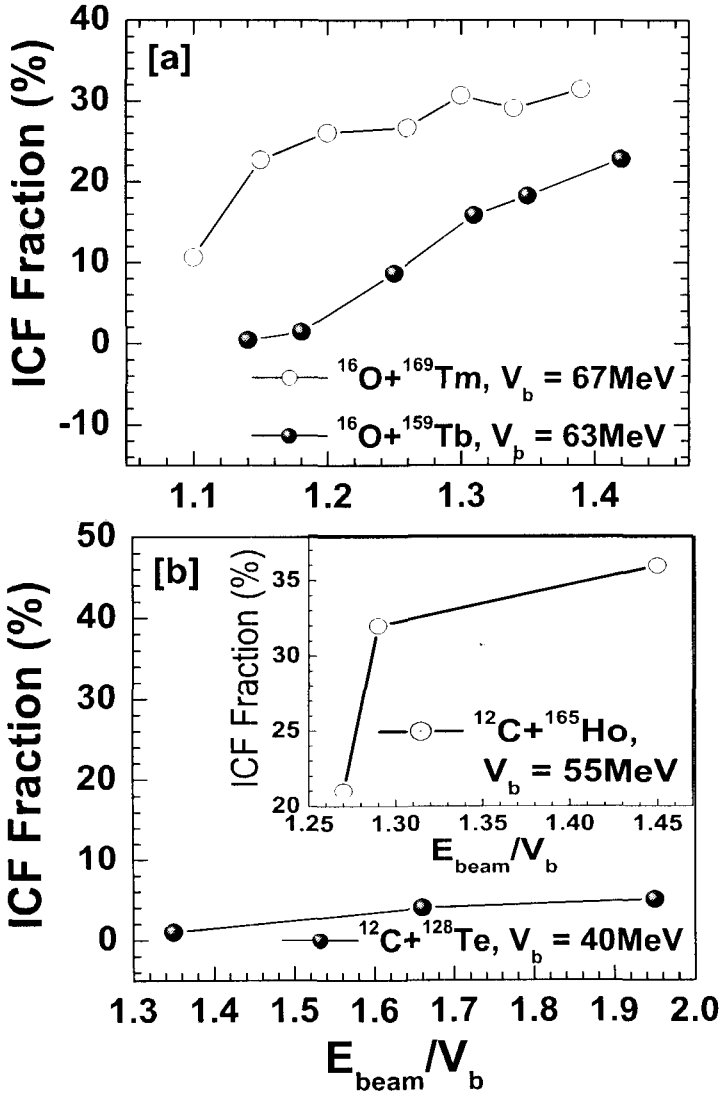

Figure 2.14: Percentage incomplete fusion fraction (F_{ICF}) as a function of reduced projectile energy (E_{beam}/V_b) for (a) ^{16}O+^{159}Tb, ^{16}O+^{169}Tm, and (b) ^{12}C+^{128}Te and ^{12}C+^{165}Ho (inset) systems.

Further, the difference between two systems at different projectile energies can be seen quite clearly, where the ICF fraction is found to be more for ^{16}O+^{169}Tm system than that for ^{16}O+^{159}Tb system, which shows the sensitiveness of ICF fraction to the mass asymmetry of interacting partners.

Mogenstern *et al.*[24], suggested that the onset of incomplete fusion is governed by the relative velocity ($v_{relative}$) of projectile (i.e., $\sqrt{2(E_{c.m.} - V_b)/\mu}$, here; V_b is the CB between the interacting partners, $E_{c.m.}$ is the projectile energy in center of mass system and μ is the reduced mass of the system) and mass asymmetry of the interacting partners. With this in view, the percentage F_{ICF} for ^{16}O+^{159}Tb, ^{16}O+^{169}Tm, ^{12}C+^{128}Te and ^{12}C+^{165}Ho systems have been deduced at a constant value of $v_{relative}$. The mass asymmetry dependent percentage ICF fraction is shown in Fig.2.15.

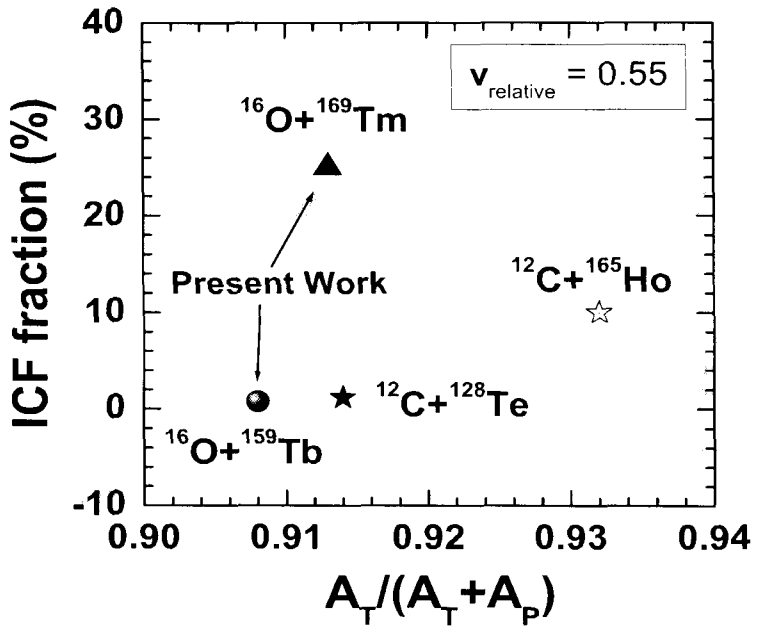

Figure 2.15: Percentage incomplete fusion fraction (F_{ICF}) as a function of mass asymmetry at a constant normalized projectile energy.

As can be seen from Fig.2.15, in general, the data points suggest more ICF probability for more mass asymmetric systems than relatively mass symmetric system, which support the systematics presented by Morgenstern *et al.*,[25, 26]. However, the percentage ICF

fraction for ^{16}O+^{169}Tm system is not following the general trend as inferred from the plot (Fig.2.15). The above descrepency may be attributed to the projectile structure effects. It can be pointed out that, for ^{16}O-induced reactions with ^{159}Tb and ^{169}Tm, percentage ICF fraction is more for mass asymmetric systems. Further, for ^{12}C-induced reactions with ^{128}Te and ^{165}Ho, the percentage F_{ICF} also indicates similar trends as that of ^{16}O-induced reactions. As such, it may not be out of order to state that, mass asymmetry is also a function of projectile structure. However, for better understanding of underlying processes, detailed measurements for various projectile-target combinations are required. In order to see the effect of projectile structure on the ICF fraction, one may look separately for reactions induced by differnt incident beams. For example, as can be seen from Fig.2.15, ICF fraction for all reactions induced by ^{16}O-beam increases with beam energy. Similarly, the ICF fraction for all reactions induced by ^{12}C-beam also increases with beam energy, but at different rate.

2.6 Summary

In summary of the present work, it can be inferred that the fraction of incomplete fusion (F_{ICF}) has been deduced from the measurement and analysis of EFs for various radio-nuclides produced via CF and/or ICF in ^{16}O+^{159}Tb and ^{16}O+^{169}Tm systems at energies $\approx$ 75-95 MeV. As far as the projectile energy dependence of F_{ICF} is concerned, it may be pointed out that the F_{ICF} is found to be sensitive to the projectile energy. In case of ^{16}O+^{159}Tb system, the F_{ICF} has been observed to be $\leq 1\%$ at $\approx$75 MeV, while, it approaches to $\approx 20\%$ of the total fusion cross-section (σ_{TF}) at the highest measured energy i.e., $\approx$95 MeV. However, the F_{ICF} is found to be $\approx 10\%$ at $\approx$75 MeV and is observed to be $\approx 30\%$ of σ_{TF} at $\approx$95 MeV for ^{16}O+^{169}Tm system. Further, the percentage F_{ICF} is also found to be sensitive to the mass-asymmetry of interacting partners, where F_{ICF} is found to be larger for more mass asymmetric system. Moreover, in order to have better understanding of underlying processes and to have perfect modeling for ICF dynamics, it would be quite interesting to perform more detailed experiments for various projectile-target combinations. As such, complementry experiments have been performed to measure the forward recoil ranges of evaporation residues as a direct indication of fractional linear momentum transfer in ICF processe(s), and are presented in the next Chapter.

=*=*=*=

Chapter 3

Investigation of Fusion Incompleteness

In order to investigate fusion incompleteness due to fractional linear momentum transfer from projectile to target nucleus, most probable forward recoil ranges of various radio-nuclides produced via CF and/or ICF in $^{16}O+^{159}Tb$ and $^{16}O+^{169}Tm$ systems have been measured at $\approx$ 90 MeV and $\approx$ 87 MeV, respectively. In this chapter, the measurement and analysis of forward mean recoil ranges for different radio-nuclides have been performed in the framework of degree of linear momentum transfer from projectile to the target nucleus by adopting break-up fusion model considerations. Different full and fractional linear momentum transfer components corresponding to the fusion of ^{16}O and/or ^{12}C and ^{8}Be transfer from ^{16}O projectile to the target nucleus have been observed. Further, the experimentally measured recoil range distributions can be used to deduce the relative strengths of full and fractional linear momentum transfer components. As such, an attempt has been made to separate out the relative percentage contributions of CF and ICF by the analsysis of experimentally measured forward recoil ranges.

The ERs produced in heavy ion-induced reactions may originate via two different processes viz; (i) from the compound nucleus (full linear momentum transfer), after the statistical emission of light nuclear particles and/or characteristics radiations, and (ii) from the statistical decay of incompletely fused composite (IFC) system formed after the direct emission of α-cluster(s) at the initial stages of nuclear reaction. For incident energies near and a little above B_{fus}, the observed ERs predominantly originate from the first mechanism, i.e, from the de-excitation of compound nucleus. However, at relatively higher projectile energies, both the processes contribute to the production probability. As already mentioned, with the increase of incident projectile energy, the ICF becomes more and more dominant. Therefore, the question comes, how one can estimate the relative contributions of CF and ICF processes in the energy regime where both the processes are believed to co-exist. An attempt has been made in Chapter-2, to extract the relative contributions of CF and ICF from the analysis of experimentally measured EFs and by comparing them with the predictions of theoretical model code PACE2, where it has been concluded that as the projectile energy increases, influence of incomplete fusion comes into play with an increasing probability.

Further, one of the straightforward methods, to tackle this problem experimentally or to get information about involved linear momentum transfer (LMT), is to measure the Recoil Range Distributions (RRDs)[1] of the residues. The forward recoil ranges of CF and ICF reaction products depend on the recoil velocity of composite system associated with the various degrees of linear momentum transfer (ρ_{LMT}) from projectile to the target nucleus. The ρ_{LMT} may be defined by the following equation;

$$\rho_{LMT} = \frac{P_{frac}}{P_{proj}} \tag{3.1}$$

where; P_{frac} is the linear momentum of fused fraction of projectile and P_{proj} is the entire linear momentum of the projectile. The ρ_{LMT} depends on the fused mass of the projectile, i.e., maximum LMT may give maximum recoil velocity to the reaction products. This is supposed to be a promising way of investigating the full momentum transfer in case of complete fusion process, and a relatively small recoil velocity in partial momentum transfer reactions (ICF). In case of complete fusion, entire projectile fuses with the target nucleus, hence the ρ_{LMT} is expected to be unity. For a given entrance channel the CN has predetermined mass, energy, linear momentum and angular momentum. However, for incomplete fusion, only a part of projectile fuses with target nucleus, and the above mentioned quantities (mass, energy linear momentum and angular momentum of incompletely fused composite system) may be different than in CN reactions. This may

[1]**Pushpendra P. Singh** *et al.*, Europeon Physical Journal **A34**, 29-39 (2007)

be because of the fluctuations in the fused mass from projectile to target nucleus and interaction trajectories. For a given reaction product formed via particle evaporation from a recoiling intermediate with a well defined velocity v_0, the velocity distribution will be symmetric about v_0 with a width which depends on the evaporation process and, in particular upon the number of alpha particles evaporated in case of incomplete fusion processes. For the CN formed via complete fusion the velocity v_0, may be written as;

$$v_0 = v_{CN} = \frac{\sqrt{2mE}}{M} \tag{3.2}$$

Where, m is the projectile mass, M is the total mass of the system (projectile + target), and E is the projectile energy. Further, as already mentioned, any intermediate complex which is supposed to be formed via partial fusion of projectile, the recoil velocity will be less than that achieved by complete momentum transfer population. Therefore, the reaction products populated via incomplete fusion will show relatively smaller range in the stopping medium as compared to complete fusion reaction products. In principle, by measuring the forward recoil ranges, one can predict the linear momentum transferred in the associated reaction channel. It is possible to characterize CF and ICF by the measurement of forward recoil ranges of heavy residues in the stopping medium. This technique is also applicable even when a reaction product is produced via different modes of reaction. Further, the RRD measurements can also be used to separate out the relative contributions of various partial fusion components to the formation of particular evaporation residue. The radio-nuclides populated via less degree of LMT, show relatively smaller depth (momentum transfer component) in the stopping medium as compared to the entire LMT populations. For a different ρ_{LMT}, the residues may have different recoil ranges in the stopping medium.

Further, some of the important and unaddressed issues associated with ICF dynamics at energies ≈5-7MeV/nucleon are; (i) The degree of fusion incompleteness i.e., the degree of LMT associated with ICF at different energies, and (ii) the relative contributions of CF and ICF processes have not yet been fully explored or limited upto a few projectile-target combinations. As such, in order to have better understanding of fusion incompleteness and to give the complement to the EF measurements presented in Chapter-2, forward recoil ranges of several residual nuclei ^{168m}Lu, ^{167}Lu, ^{167}Yb, ^{166}Tm, ^{179}Re, ^{177}Re, ^{177}W, ^{178}Ta and ^{177}Hf populated via complete and/or incomplete fusion in ^{16}O+^{159}Tb,^{169}Tm systems have been studied at, respectively, ≈ 90 MeV and ≈ 87 MeV. An attempt has also been made to separate out the relative percentage contributions of CF and ICF components from the experimentally measured forward recoil ranges. In the present work, recoil-catcher technique followed by off-line gamma-spectroscopy has been used.

3.1 Target Preparation and Irradiations

In the measurement of forward recoils ranges, same projectile-target combinations have been used as in case of EF measurements presented in Chapter-2. In the present measurements, self-supporting sample of ^{159}Tb (Abundance = 99.99%) of thickness $\approx$ 0.80mg/cm ^{2} has been prepared by rolling method, while the sample of ^{169}Tm (Abundance = 100%) of thickness t $\approx$ 0.60 mg/cm^2 has been deposited employing electrodeposition technique on Al-foil (prepared by rolling method) of thickness $\approx$ 1.5 mg/cm^2. The thickness of samples have been estimated by the α-transmission method as discussed in Chapter-2, section 2.2. The irradiations have been performed using $^{16}O^{7+}$-beam in the GPSC (set-up is same as given in Chapter-2, Fig.2.1). Stacks of Al-catcher foils (sufficient to stop the most energetic residues formed by total linear momentum transfer) have been placed just after the target, so that the heavy slow residues populated via CF and/or ICF may be trapped at various Al-catcher foil thicknesses. A typical target-catcher foil set-up used for the measurement of forward recoil ranges is shown in Fig.3.1.

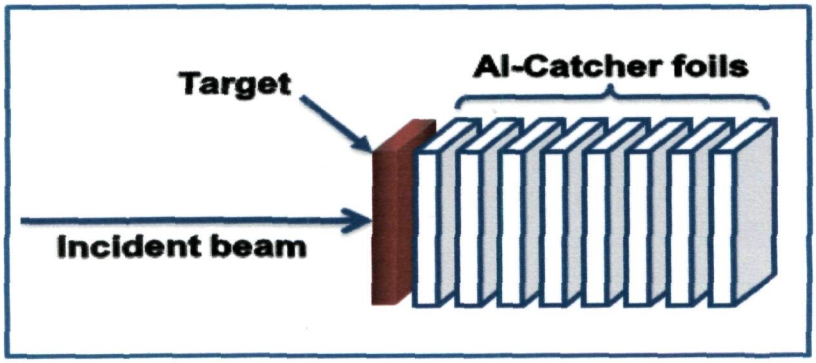

Figure 3.1: Typical target-catcher foil arrangement for forward recoil ranges measurements.

Further, the thickness of targets has been kept in such a way that the recoiling nuclei may not be stopped in the target thickness itself. The thicknesses of the catcher foils used in the experiment are given in the Table-3.1, alongwith the serial number from the target. The catchers used to stop the evaporation residues, which are very thin have been prepared by ultra-high vacuum evaporation technique. For the measurement of forward recoils ranges, it is quite essential that recoiling nuclei should flow in the medium provided in the forward cone i.e. the stack of Al-catchers.However, in case of ^{169}Tm target deposited on Al-foil, the target has been mounted in such a way that the

T-6308

Al-backing faced the beam so that the recoiling nuclei (if any of very short range) may not be stopped in the target backing itself. The effective projectile energy on the target has been estimated by calculating energy loss in the Al-backing of ^{169}Tm target. The irradiations have been carried out for the duration of ≈10-12 hrs, with beam currents ≈ 30 and 40 nA, respectively. The delay time between the stop of irradiation and the beginning of counting was minimized using invacuum transfer of target-catcher foil assembly.

Table 3.1: List of catcher-thicknesses used in RRD measurements.

S. No.	^{16}O+^{169}Tm thickness in $\mu g/cm^2$	^{16}O+^{159}Tb thickness in $\mu g/cm^2$
1	16.8	50.2
2	19.6	50.3
3	27.4	50.8
4	27.8	51.1
5	28.6	51.2
6	29.5	55.5
7	30.2	52.2
8	30.6	52.2
9	31.3	52.9
10	31.9	52.9
12	32.1	53.0
13	33.2	53.0
14	33.9	54.1
15	37.1	54.8
16	39.9	57.2
17	44.2	57.6
18	46.1	57.8
19	47.0	58.5

3.2 Post irradiation details and ERs identification

The target-catcher foil assembly (a target followed by a stack of Al-catchers) irradiated at a given energy was taken out from the scattering chamber after the irradiations

using an ITF. After taking it out from the scattering chamber, the target-catcher foil assembly was disassembled to count the activities produced in the irradiated catcher foils. The ERs populated via CF and/or ICF processes are expected to be trapped at different catcher foil thicknesses, depending on the ER's recoil velocity and/or on the degree of linear momentum transfer associated with the mode of formation. The activities produced in each catcher foil of the stack were counted separately using pre-calibrated, high resolution HPGe-spectrometer of 100 c.c. active volume coupled to a CAMAC based FREEDOM software [67]. The HPGe-spectrometer was pre-calibrated both for energy and efficiency. The resolution of γ-spectrometer was $\approx$ 2 keV, for 1.33 MeV γ-ray of ^{60}Co source. The residues decay to the ground state by emitting characteristic γ-radiations, that have been used for their identification. Thus, the induced activities has been used to measure the production probability of evaporation residues. The γ-ray spectra of each foil has been recorded at the increasing times and the decay curve analysis has been done to measure the half-lives of the residues. The measured half-lives of evaporation residues were found to be in good agreement with the literature values. Typical γ-ray spectra of irradiated ^{159}Tb and ^{169}Tm samples, respectively, at $\approx$ 90 and $\approx$ 87 MeV are shown in Figs.3.2 and Fig.3.3.

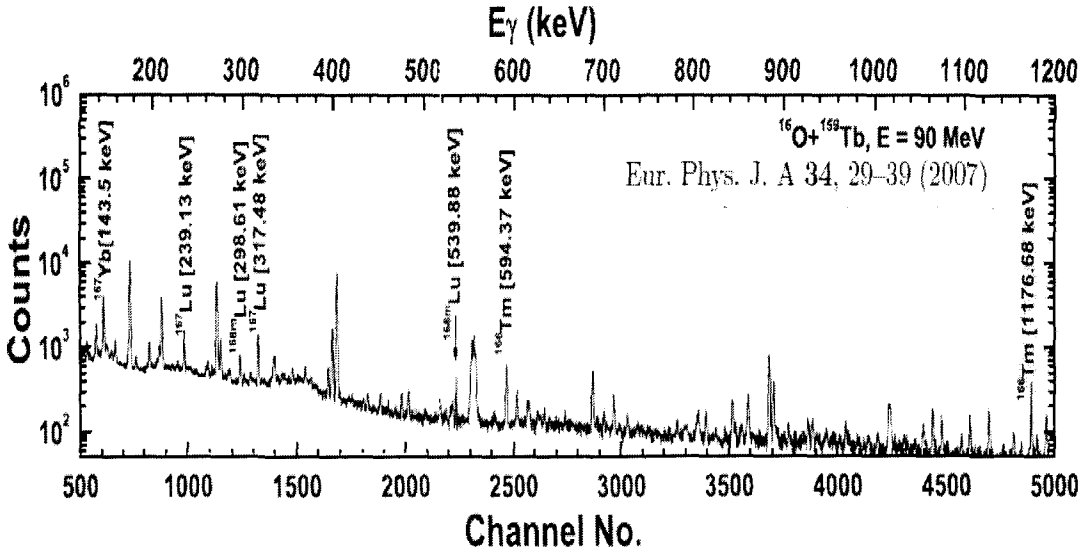

Figure 3.2: The observed γ-ray spectrum of ^{159}Tb sample irradiated by $^{16}O^{7+}$ beam at energy $\approx$ 90MeV. Peaks have been assinged to different reaction products populated via CF and/or ICF.

The various peaks which have been used for recoil range analysis are assigned to the different reaction products on the basis of their characteristic γ-ray energies and measured half-lives, and are indicated in the figures. Nuclear data like; half-lives, gamma-ray energies, etc., have been taken from the Table of Isotopes[68, 69]. The list of identified radio-nuclides populated in $^{16}O+^{159}Tb$ and $^{16}O+^{169}Tm$ alongwith their spectroscopic properties used for forward recoil range measurements are given in Chapter-2, Tables 2.2 and 2.3.

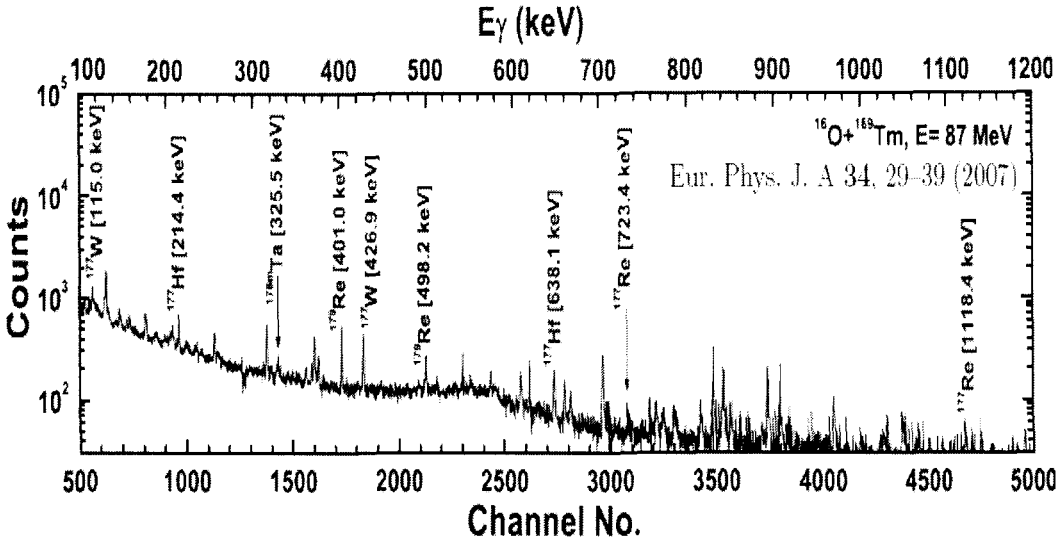

Figure 3.3: The observed γ-ray spectrum of ^{169}Tm sample irradiated by $^{16}O^{7+}$ beam at energy $\approx$ 87MeV.

The measured intensities of the characteristic γ-radiations were used to estimate the production yield of evaporation residues using formulations given in Chapter-2. In the present work, the production probability of ERs ^{168m}Lu(α3n), ^{167}Lu(α4n), ^{167}Yb(αp3n) and ^{166}Tm(2αn) produced in $^{16}O+^{159}Tb$ system, and ^{179}Re(α2n), ^{177}Re(α4n), ^{177}W(αp3n), ^{178}Ta(α2pn), and ^{177}Hf(α3pn) produced in $^{16}O+^{169}Tm$ system have been measured at different catcher foil thicknesses to estimate the recoil range distributions. In order to obtain the normalized yield (mb/mg/cm^2) as a function of cumulative depth in the catcher stack, the cross-section of the reaction products in each catcher foil was divided by its measured thickness. The resulting normalized yields of different reaction products have been plotted against cumulative catcher foil thicknesses to obtain the differential recoil range distributions and are shown in Figs.3.4 to Fig.3.8. The size of the circles in these figures includes the uncertainty in the yield values. The

overall errors in the measured production cross-sections including statistical error are estimated to be $\leq$ 15 % and the details of the factors responsible for errors in data are already given in subsection-2.3.4 of Chapter-2.

3.3 Estimation of most probable recoil range (R_P)

It is difficult to measure the precise form of the corresponding LMT component. The reason for such a difficulty is the recoil velocity distribution of evaporation residues due to straggling effects. In addition to this, the effects due to prompt particle(s) emission may also contribute extra broadening in the recoil range distributions. As such, in order to get a reliable form for the degree of linear momentum transfer from the experimental data a careful deconvolution is required. The relative contributions and precise form of linear momentum transfer in complete and incomplete fusion in the production of a particular reaction product may be computed by fitting the experimentally measured RRD data with Gaussian peaks using the ORIGIN software. The yield curves of evaporation residues obtained from RRDs are assumed to be Gaussian in nature and may be given as [70];

$$Y = Y_0 + \frac{A}{\sqrt{2\pi w_A^2}} e^{-(R-R_p)^2/2w_A^2} \tag{3.3}$$

Where; R_p is most probable mean range, w_A is the width parameter (FWHM) of the recoil range distribution, and A is the area under the peak. Further, the normalized yield Y may be estimated by chi square fit (χ^2) from the experimentally determined production yield at different catcher foil thicknesses and may be represented as follows;

$$\chi^2 = \frac{1}{m-p-1}\{Y(A) - Y_0(A)\}^2 \tag{3.4}$$

The value of χ^2 was minimized in this analysis using a non-linear least square fit routine, here w_A is the the width parameter and R_p is the most probable mean range of the evaporation residues. As indicated in the Figs.3.4-3.8, most of the residues show more than one LMT components. In such cases, the experimentally measured normalized yields have been fitted by assuming multi-peaks in the similar way as mentioned above. The contribution of different fusion components (^{16}O, ^{12}C and ^{8}Be - fusion) have been obtained by dividing the area under the peak of the corresponding fusion component by the total area associated with the distribution. The percentage contributions coming from different complete and/or incomplete fusion components deduced in such a way for the residues populated in both the systems are also indicated in Figs.3.4 to Fig.3.8, along with their corresponding channels.

3.4 Interpretation of experimental results

3.4.1 $^{16}O+^{159}Tb$ System

In Figs.3.4-3.5, the experimentally measured recoil range distributions for four reaction products ^{167,168m}Lu, ^{167}Yb and ^{166}Tm, populated via complete and/or incomplete fusion in $^{16}O+^{159}Tb$ system at ≈90 MeV are shown. The reaction products ^{167,168m}Lu have ground and metastable states of half-lives 51.5 m and 6.7 m, respectively. As can be seen from Figs.3.4(a)-(b), these reaction products ^{167,168m}Lu may be formed both via complete and/or incomplete fusion of ^{16}O with ^{159}Tb. In case of CF, the composite system ^{175}Ta* is formed, which may decay via the statistical emission of an alpha-particle and 3 or 4 neutrons leaving behind the above residues. The above residues may also be populated, if it is assumed that, as soon as the incident ^{16}O nucleus approaches the nuclear range of target nucleus, it may break-up into α-clusters viz; ^{12}C and ^{4}He(alpha). One of the fragments ^{12}C fuses with ^{159}Tb, forming an incompletely fused composite system ^{171}Lu*, which may decay by the emission of respectively three neutrons forming ^{168m}Lu and four neutrons forming ^{167}Lu. As can be observed from Fig.3.4(a), that the RRD for the residue ^{167}Lu show both complete and incomplete fusion components having two peaks at the cumulative catcher thicknesses at ≈ 239 $\mu g/cm^2$ (due to ^{12}C-fusion) and ≈ 426 $\mu g/cm^2$ (due to ^{16}O-fusion). The observed mean recoil range of ^{16}O-fusion with ^{159}Tb correspond to the expected recoil range of the compound system ^{175}Ta in Aluminum, calculated using code SRIM06 [66].

It may, however, be pointed out that, the relative contribution of ^{12}C-fusion for the reaction ^{159}Tb(^{16}O,α4n)^{167}Lu [Fig.3.4(a), indicated by dotted curve] is found to be ≈33%, while the contribution from ^{16}O-fusion [indicated by dashed curve] is ≈67%. The observation of a peak at relatively smaller cumulative depth clearly indicates relatively less degrees of LMT involved in the process. The reaction product ^{168m}Lu also shows two components in RRD data, respectively at ≈ 256 $\mu g/cm^2$ (due to ^{12}C-fusion) and at ≈ 451 $\mu g/cm^2$ (due to ^{16}O-fusion). Similarly, for the reaction ^{159}Tb(^{16}O,α3n)^{168m}Lu, the contribution of ^{12}C (ICF) and ^{16}O (CF)-fusion [Fig.3.4(b), indicated by dotted and dashed curves] are found to be ≈74% and ≈26%, respectively. The above description clearly indicates that depending on the degree of linear momentum transfer (ρ_{LMT}) two components are well separated giving a clear indication of the population of the same residue via two different processes. Further, the reaction product ^{167}Yb, which has ground state of half-life 17.5 m, is expected to be populated via complete fusion (αp3n) channel and/or incomplete fusion i.e., the fusion of ^{12}C with ^{159}Tb followed by subsequent emission of one proton and three neutrons from ^{171}Lu*. The remaining alpha fragment (^{4}He) of the incident ion is assumed to go on moving with the beam velocity

in forward direction without any significant interaction with target nucleus.

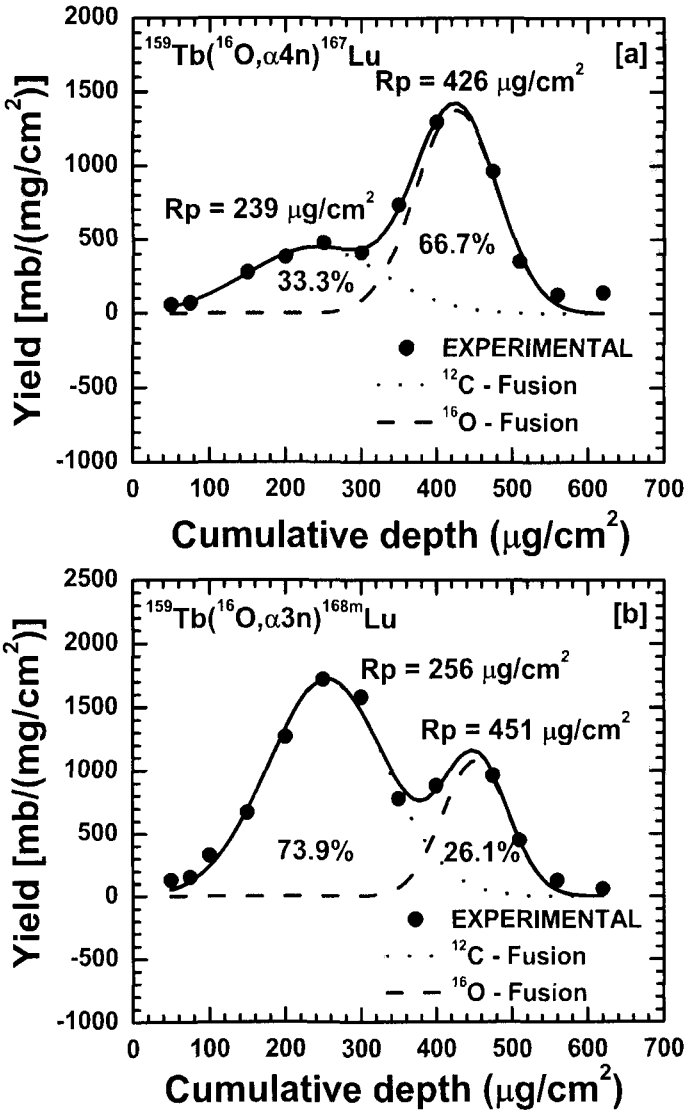

Figure 3.4: The experimentally measured recoil range distributions for (*a*) ^{167}Lu(α4n), and (*b*) ^{168m}Lu(α3n) produced in ^{16}O+^{159}Tb system at $\approx$ 90 MeV.

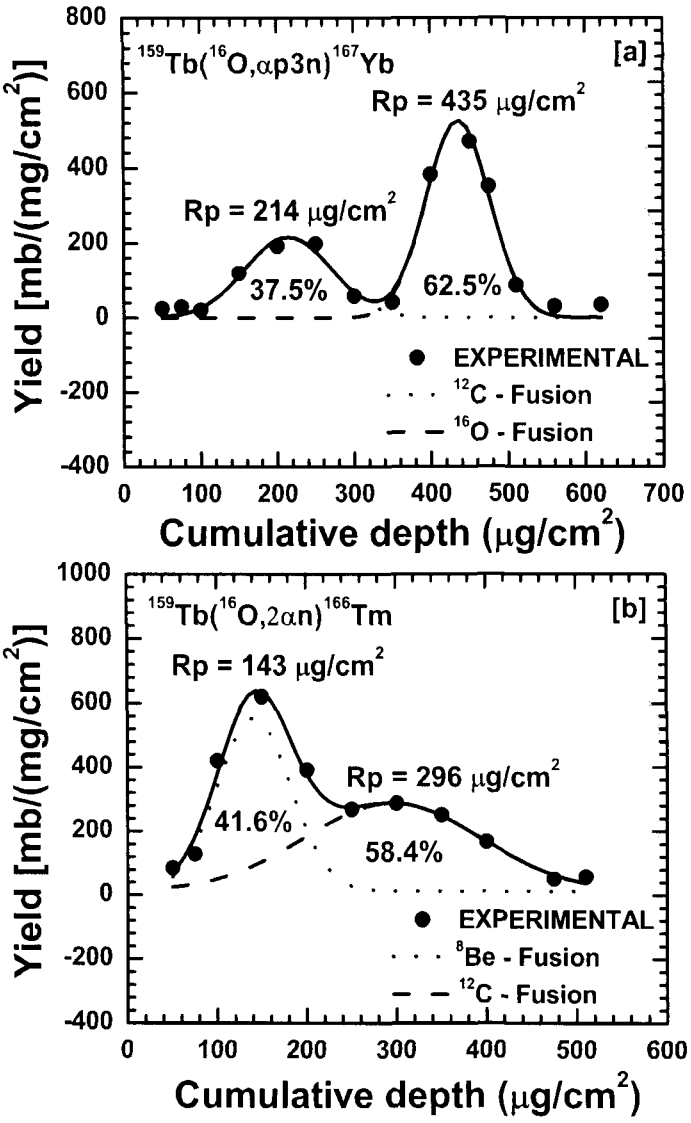

Figure 3.5: The experimentally measured recoil range distributions for (a) ^{167}Yb(αp3n), and (b) ^{166}Tm(2αn) produced in ^{16}O+^{159}Tb system at $\approx$ 90 MeV.

As indicated in the Fig.3.5(a), there are two LMT components, respectively at $\approx$ 214 $\mu g/cm^2$ (corresponds to ^{12}C-fusion) and $\approx$ 435 $\mu g/cm^2$ (due to ^{16}O-fusion). The relative contribution of ICF (due to ^{12}C-fusion) and CF (^{16}O-fusion) for the reaction

^{159}Tb(^{16}O,αp3n)^{167}Yb are found to be ≈37.5% and ≈62.5% respectively, as indicated in the Fig.3.5(a) by dotted and dashed curves. While, the evaporation residue ^{166}Tm(2αn) of half-life $t_{1/2} = 7.7$ hours), is expected to be populated via fusion of ^{8}Be and subsequent emission of one neutron from ^{167}Tm*. However, the remaining part ^{8}Be (two α-particles) is assumed to behave like a spectator. Further, it may be observed from the Fig.3.5(b), that there are two LMT components, at ≈ 143 $\mu g/cm^2$ and ≈ 296 $\mu g/cm^2$, due to ^{8}Be and ^{12}C-fusion, respectively, indicating the major contribution for the population of the above residue only from the two incomplete fusion channels.

Table 3.2: Experimentally measured most probable ranges $R_{p(exp)}$ deduced from RRD curves, and theoretically estimated forward mean ranges $R_{p(the)}$ for CF and ICF components using range-energy relation along with the reaction products produced in ^{16}O+^{159}Tb system at ≈90MeV.

Residues	$R_{p(exp)}$ ^{16}O	$R_{p(the)}$ ^{16}O	$R_{p(exp)}$ ^{12}C	$R_{p(the)}$ ^{12}C	$R_{p(exp)}$ ^{8}Be	$R_{p(the)}$ ^{8}Be
^{167}Lu(α4n)	426±18	432	239±15	245	-	-
^{168m}Lu(α3n)	451±25	432	256±13	245	-	-
^{167}Yb(αp3n)	435±14	432	214±21	245	-	-
^{166}Tm(2αn)	-	-	296±27	245	143±19	126

Table 3.3: Experimentally measured cumulative (CF+ICF) production cross-sections, deduced (using RRD's) cross-section for ICF and CF components and the theoretically calculated (PACE) cross-sections for the residues produced in ^{16}O+^{159}Tb system at ≈ 90 MeV.

Residues	σ_{exp}(mb) CF+ICF	σ_{exp}(mb) ICF	σ_{exp}(mb) CF	σ_{the}(mb) CF
^{167}Lu	46±6.6	15±2.2	30±4.4	26.50
^{168m}Lu	146±18.5	108±13.7	37±4.8	42.46
^{167}Yb	49±7.6	18±3.2	30±4.4	27.18
^{166}Tm	31±5.7	31±5.7	-	-

It may, however, be pointed out that, the relative contribution coming from ^{8}Be and ^{12}C-fusion [Fig.3.5(b), indicated by dotted and dashed curves] are found to be ≈42%

and ≈58%, respectively. In order to get confidence in the experimentally measured RRD, an attempt has been made to estimate most probable ranges R_p theoretically using range-energy relation. The experimentally measured most probable ranges $R_p(exp)$, and theoretically estimated forward mean ranges $R_p(the)$ for CF and/or ICF components using range-energy relation for the reaction products produced at ≈ 90 MeV are given in Table-3.2. As can be seen from this table, the experimentally measured most probable ranges for both CF and/or ICF components agree well with the theoretical ones within the experimental uncertainties. The errors shown in $R_p(exp)$ indicates the fitting errors of the Gaussian distribution to the experimental data. Further, the experimentally measured production cross-sections for CF and ICF deduced from the fitting of RRD's have been compared with the theoretical predictions of PACE2 for the residues produced in ^{16}O+^{159}Tb system at ≈ 90 MeV. As can be seen from Table-3.3, the deduced cross-section from the fitting of RRDs for CF and ICF are in good agreement with the predictions of PACE2.

3.4.2 ^{16}O+^{169}Tm System

The recoil range distributions for ^{177,179}Re, ^{177}W, ^{178}Ta and ^{177}Hf reaction residues populated in the interaction of ^{16}O with ^{169}Tm at ≈ 87 MeV are shown in Figs.3.6 and Fig.3.7. As already indicated in the earlier section, the above residues may be populated both via complete and/or incomplete fusion of ^{16}O with ^{169}Tm. The population of these residues in α-emission channels may also be explained in terms of the break-up of ^{16}O into ^{12}C and ^{4}He(α-particle) followed by fusion of ^{12}C with ^{169}Tm forming an incompletely fused composite system ^{181}Re*. As shown in Fig.3.6(a), the reaction product ^{177}Re of half-life 14 m is expected to be populated via the emission of four neutrons from ^{181}Re* and show two peaks, respectively at ≈ 221 $\mu g/cm^2$ (belongs to ^{12}C-fusion) and ≈ 379 $\mu g/cm^2$ (belongs to ^{16}O-fusion). Thus, the evaporation residues ^{177}Re may not only be populated via in-complete fusion but may have significant probability of being formed by the CF of the projectile leading to the formation of ^{185}Ir*, which may decay by the emission of four neutrons along with an alpha particle. Similarly, the reaction product ^{177}W(α p3n) having half-life 2.21 h is also expected to be populated dominantly via ICF of ^{12}C with ^{169}Tm, leading to the formation of ^{181}Re*. The reaction product ^{177}W may come into picture after emission of a proton and three neutrons from ^{181}Re*. As can be seen from the Fig.3.6(b), there are two LMT components, respectively at ≈ 110 $\mu g/cm^2$ (due to ^{8}Be-fusion) and ≈ 214 $\mu g/cm^2$ (due to ^{12}C-fusion) associated with the incomplete fusion of following type;

$$^{16}\text{O}(^{12}\text{C} + ^{4}\text{He}) \Rightarrow ^{12}\text{C} + ^{169}\text{Tm} \Rightarrow ^{181}\text{Re}^* + ^{4}\text{He (Alpha as spectator)}$$

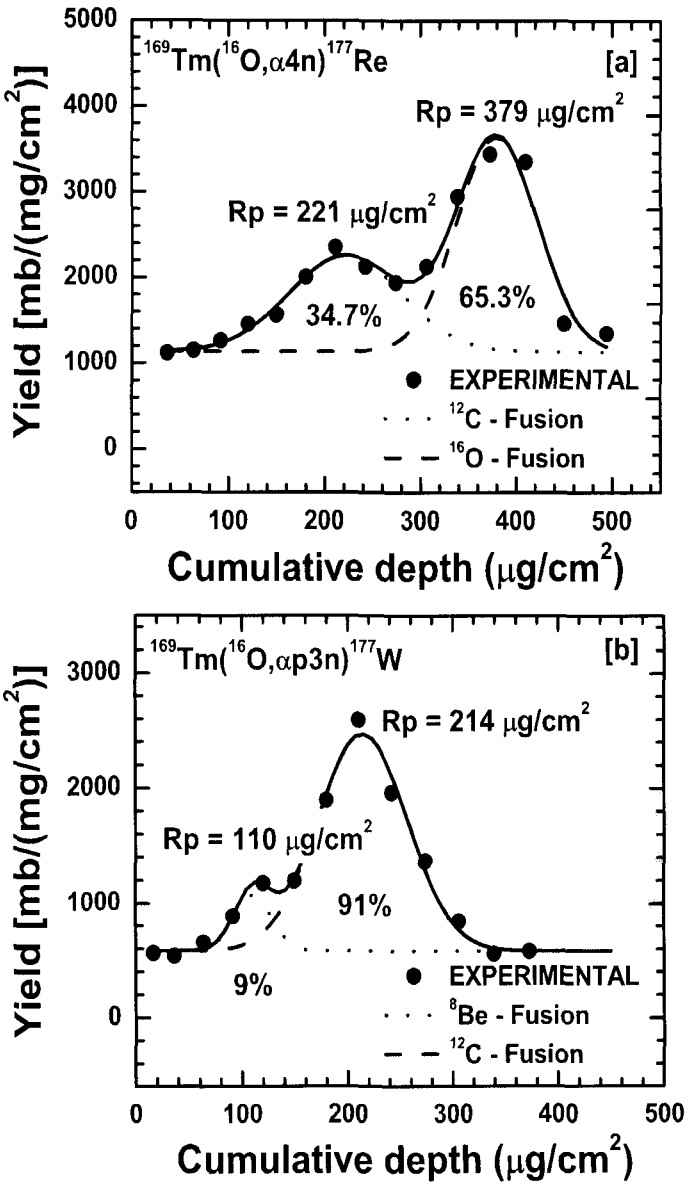

Figure 3.6: The experimentally measured recoil range distributions for (*a*) ^{177}Re(α4n), and (*b*) ^{177}W(αp3n) produced in ^{16}O+^{169}Tm system at $\approx$ 87 MeV.

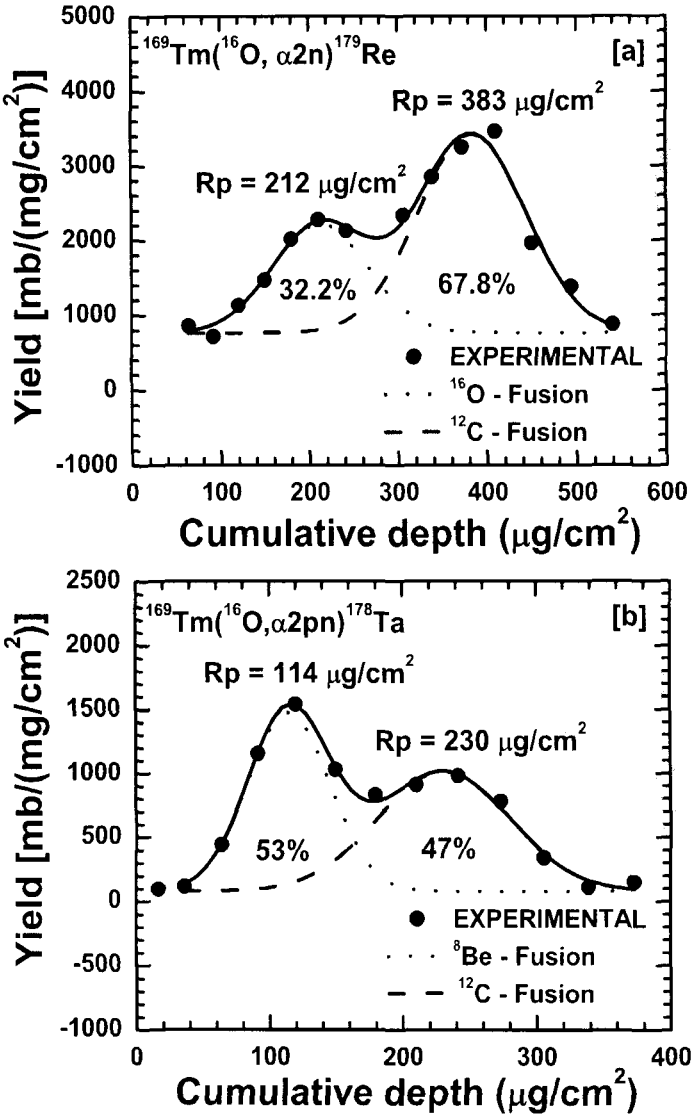

Figure 3.7: The experimentally measured recoil range distributions for (a) ^{179}Re(α2n), and (b) ^{178}Ta(α2pn) produced in ^{16}O+^{169}Tm system at $\approx$ 87 MeV.

It may however be pointed out that the LMT component at the relatively smaller depth i.e., $\approx$ 110 $\mu g/cm^2$ may be associated with the ICF of ^{8}Be with the target nucleus, which may lead to the formation of ^{177}Ta*. The final reaction product ^{177}W

may also be populated via β^+-emission and/or EC decay of higher charge precursor isobar ^{177}Ta* via incomplete fusion of ^{8}Be of following type;

$$^{16}\mathrm{O}(^{8}\mathrm{Be} + {}^{8}\mathrm{Be}) \Rightarrow {}^{8}\mathrm{Be} + {}^{169}\mathrm{Tm} \Rightarrow {}^{177}\mathrm{Ta}^{*} + {}^{8}\mathrm{Be}\ \text{(Beryllium as spectator)}$$

Similarly, the reaction products ^{178}Ta and ^{179}Re have the half-lives 2.36 h and 19.5 m, respectively and are expected to be populated via α2pn and α2n-channels respectively, in which α-particles may be assumed to behave as spectator. As indicated in Fig.3.7(a), ^{179}Re is expected to be populated via both complete and/or incomplete fusion and hence shows two LMT components, respectively at $\approx$ 212 $\mu g/cm^2$ (due to ^{12}C-fusion) and $\approx$ 383 $\mu g/cm^2$ (due to ^{16}O-fusion). While, ^{178}Ta is populated only via incomplete fusion and showing two LMT components, respectively at $\approx$ 114 $\mu g/cm^2$ (due to ^{8}Be-fusion) and $\approx$ 383 $\mu g/cm^2$ (due to ^{12}C-fusion), which is shown in Fig.3.7(b). Further, the RRD for reaction product ^{177}Hf($\alpha 3pn$) of $t_{1/2}$=51.4 m is found to have only one peak corresponding to the cumulative depth $\approx$ 216 $\mu g/cm^2$, indicating the population of this residue by incomplete fusion of ^{12}C only, as indicated in Fig.3.8.

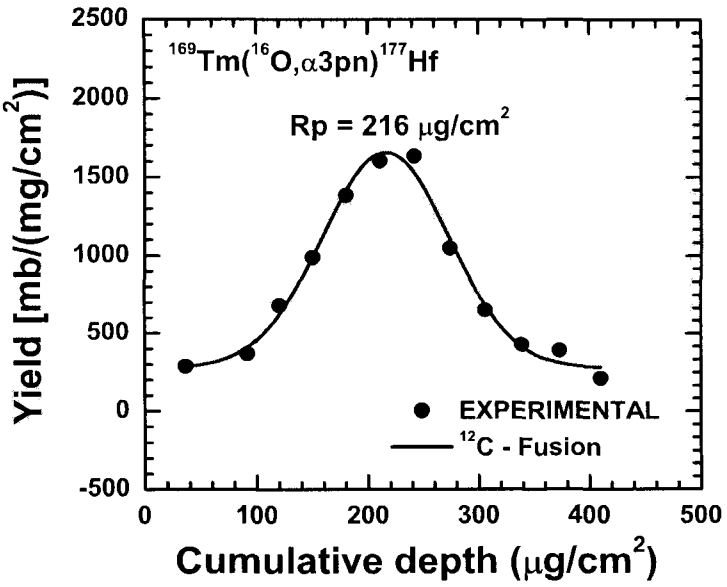

Figure 3.8: The experimentally measured recoil range distribution for ^{177}Hf(α3pn) produced in ^{16}O+^{169}Tm system at $\approx$ 87 MeV.

Further, for $^{16}O+^{169}Tm$ system, the experimentally measured most probable ranges $R_{p(exp)}$ for various residues deduced from RRD curves, and theoretically estimated forward mean ranges $R_{p(the)}$ for CF and ICF components using code SRIM06 based on range-energy formulation are given in Table-3.4. Moreover, the experimentally measured range integrated cross-sections have been compared with that of theoretical predictions based on PACE2 code. The CF contributions deduced from forward recoil range data σ_{exp}(CF) have been compared with the CF contributions deduced using fusion-evaporation model code PACE2. A comparison of the CF contributions is given in table-3.5 for various residues produced in $^{16}O+^{169}Tm$ system at ≈87MeV. It may be pointed out that the code does not take ICF process into account. As can be seen from these tables, the experimentally deduced contributions of CF and their forward ranges agree well with the theoretical values within the experimental uncertainties.

Table 3.4: Experimentally measured most probable ranges $R_{p(exp)}$ for various residues deduced from RRD curves, and theoretically estimated forward mean ranges $R_{p(the)}$ for CF and ICF components using range-energy relation along with the reaction products produced in $^{16}O+^{169}Tm$ system at ≈87MeV.

Residues	$R_{p(exp)}$ ^{16}O	$R_{p(the)}$ ^{16}O	$R_{p(exp)}$ ^{12}C	$R_{p(the)}$ ^{12}C	$R_{p(exp)}$ ^{8}Be	$R_{p(the)}$ ^{8}Be
$^{177}Re(\alpha 4n)$	379±22	402	221±13	228	-	-
$^{177}W(\alpha p3n)$	-	-	214±17	228	110±11	117
$^{179}Re(\alpha 2n)$	383±21	402	212±18	228	-	-
$^{178}Ta(\alpha 2pn)$	-	-	230±15	228	114±17	117
$^{177}Hf(\alpha 3pn)$	-	-	216±17	228	-	-

It has already been mentioned, the RRD for the residues ^{166}Tm, ^{177}W, ^{178}Ta and ^{177}Hf show the peaks corresponding to the ICF of ^{8}Be and/or ^{12}C only. As such, experimental CF contributions for these residues are not observed and are not shown in these tables. It may not be out of place to mention that the PACE-2 predictions also give negligible contribution for these residues as well. As such, it may again be inferred that these residues are predominantly produced in ICF processes. In the above description, it is assumed that the residues produced by CF of ^{16}O, ICF of ^{12}C and ICF of ^{8}Be would produce residues with the observed average recoil ranges. It has also been pointed out by Parker *et al.*,[54] on the basis of detailed theoretical calculations that the recoil range distributions of many residues produced in HI interactions can not be explained by assuming the pre-equilibrium emission of particles & clusters from the composite

system. As such, it may be inferred that inclusion of ICF is essential to explain the observed RRDs. The enhancement in cross-sections for the production of Re, W, Ta and Hf isotopes that are observed here may be attributed to the ICF processes. It may, further, be mentioned that observation of RRDs obtained in the present work may be considered as confirmation of ICF processes at the studied energies.

Table 3.5: Experimentally measured cumulative (CF+ICF) production cross-sections, deduced using RRD cross-section for ICF and CF components and the theoretically calculated (PACE) cross-sections for the residues produced in $^{16}O+^{169}Tm$ system at $\approx$ 87 MeV.

Residues	σ_{exp}(mb) CF+ICF	σ_{exp}(mb) ICF	σ_{exp}(mb) CF	σ_{the}(mb) CF
^{177}Re	26±4.1	9±1.5	17±2.6	19.8
^{177}W	39±5.9	39±5.9	-	-
^{179}Re	23±3.7	8±1.2	15±2.5	13.4
^{178}Ta	106±12.6	106±12.6	-	-
^{177}Hf	48±7.3	48±7.3	-	-

3.5 Summary

The RRDs of different reaction products populated via CF and/or ICF have been measured, which strongly revealed the significant contribution of ICF processes at energies ≈90 and 87 MeV. Different momentum transfer components have been observed and are found to be attributed to ^{12}C and/or ^{8}Be transfer from ^{16}O projectile to target nucleus. CF components in the above measurements are also found to be consistent with the theoretical predictions based on model code PACE2. In addition to the measurements presented in Chapters-2 and 3, information regarding CF and/or ICF have also been obtained using particle-γ-coincidence technique experiments discussed in the Chapter-4.

=*=*=*=

Chapter 4

Reaction Dependent Spin Population

Aiming to probe the incomplete fusion dynamics within the framework of input angular momenta, spin-distributions of various reaction products populated via xn,α/2αxn-channels have been measured for $^{16}O+^{169}Tm$ system at E≈5.6 MeV/nucleon and $^{12}C+^{169}Tm$ at E≈4-7 MeV/nucleon. Prompt γ-rays in coincidence with fast charged particles (Z=1,2) have been recorded to obtain the information about involved reaction processes on the basis of their experimentally observed spin-populations during de-excitation. The experimentally observed spin-distributions for direct-α-emitting channels (associated with incomplete fusion) have been found to be distinctly different than that observed for fusion-evaporation (complete fusion) channels. The mean value of driving input angular momenta associated with various direct-α/2αxn-channels have been found to be higher than that observed for fusion-evaporation xn/αxn-channels, and increases with direct-α-multiplicity in the forward cone. Experimentally measured production yields of fusion-evaporation xn/αxn-channels have been found to be in good agreement with the predictions of theoretical model code PACE4. Further, in order to understand the feeding probability in both complete and incomplete fusion reaction products, an attempt has been made to generate feeding intensity profiles from spin-distribution data for both the systems. It has been observed that the complete fusion products are strongly fed over a broad spin range, however, incomplete fusion products are found to be less fed and/or the population of lower spin states are strongly hindered.

It has already been inferred from the analysis of excitation functions and recoil range distributions data, that the significant fusion incompleteness play an important role in HI-induced reactions at projectile energies as low as E≈5-7MeV/nucleon. The related processes were interpreted as ICF on the basis of several observations, such as; (i) Most of the α-emitting channels were found to be produced with a large production cross-section as that predicated by fusion-evaporation model code PACE2. The observed enhancement has been assumed to be the contribution coming from the incomplete fusion of projectile. (ii) Reaction products are found to be associated with the partial degree of linear momentum transfer (ρ_{LMT}) from the projectile to target nucleus, where different mean recoil ranges of residues populated via ICF processes have been observed. However, the information about the multiplicity of driving input angular momenta associated with CF and ICF could not be obtained from the measurements presented in Chapters-2 and 3. As such, further measurements have been performed for the better understanding of underlying processes, where qualitative information about driving input angular momenta involved in CF and ICF processes have been obtained at energies as low as E≈4-7MeV/nucleon. In this chapter, an attempt has been made to show that the ICF processes most likely result from the peripheral collisions associated with large input angular momentum in HI induced reactions, where input angular momentum limit do not allow CF. As such, in order to obtain the experimental information on CF and/or ICF within the framework of driving input angular momenta involved in various channels, spin-distributions (SDs)[1],[2] and side-feeding intensity profiles of several reaction products have been measured [61, 62]. In these measurements, different reaction modes have been disentangled on the basis of entry state spin population during the de-excitation of excited/equilibrated complex nucleus produced via CF and/or ICF processes. It may further be pointed out that, an excited/equilibrated complex nucleus produced through CF and/or ICF processes, generally, leads to the final reaction product(s) via emission of characteristic γ-rays and/or light nuclear particle(s). In such a case, two type of decay steps may take place, viz;

- Those that cool the excited/equilibrated complex nucleus to/or towards the yrast line, and are expected to remove less angular momentum and more excitation energy called statistical transitions, and
- Those that are roughly parallel to the yrast line, and remove more angular momentum and relatively less excitation energy in comparison to statistical transitions called yrast-like transitions.

[1] **Pushpendra P. Singh** *et al.*, Physics Letters B, (2008)**doi:10.1016/j.physletb.2008.11.035**
[2] **Pushpendra P. Singh** *et al.*, Physical Review **C78**, 017602 (2008)

It may, further, be pointed out that, there is a competition between statistical and yrast-like transitions at each stage during the de-excitation. The competition between these two type of transitions depends on the available excitation energy (E*) which affect the level density, and also on the degree of collectivity above the yrast line which produces faster yrast-like transitions. The relative number of statistical and yrast-like transitions also depend strongly on the angular momentum left with the final reaction product. According to the definition of CF, as a result of projectile-target interaction a composite system is formed with definite mass, charge, E* and angular momenta, which may de-excite via light nuclear particles and/or characteristics γ-rays, isotropically, leading to more statistical transitions. In such a case, the yrast state may be predominantly fed by statistical γ-rays over a broad spin range, where a gradual monotonic increase in intensity is expected upto the band head, as expected for CF. However, ICF is assumed to be the result of fractional momentum transfer from projectile to the target nucleus after projectile break-up into α-clusters. In this case, the incompletely fused composite system (a part of projectile plus target nucleus) is formed with less excitation energy (due to the involvement of partial degrees of excitations), high angular momenta (relatively higher values of impact parameters contribute to the high spin states) at a given projectile energy. In case of high angular momenta, the de-excitation of excited nucleus favours more number of yrast-like transitions as compared to statistical ones, where less or no feeding is expected. Therefore, a rapid increase in the production yield (intensity) upto a certain value of spin is expected, thereafter, the production yield is expected to remain constant down to the band head. This production yield pattern may arise from the narrow ℓ-window, localized near and above to the critical angular momentum for CF.

As such, on the basis of aforementioned description, the spin-distribution of CF and ICF products are expected to be distinctly different in nature and may be used as a sensitive tool to probe reaction dynamics by looking into entry state spin population [23]. In this work, the involved dynamical processes such as CF and/or ICF in HI induced reactions have been investigated by two different approaches, such as;

- Spin-distribution studies i.e., the study of qualitative behaviour of intensity profiles with observed spin, and
- Side-feeding of γ-ray intensities for different reaction products, which have been deduced from experimentally measured spin-distributions.

Significant information about the multiplicity of driving input angular momenta involved in CF and ICF processes have been obtained from the spin-distribution and side-feeding intensity profiles. The details of experimental set-up & methodology, electronics & data collection, the data analysis and results with interpretations are given in the following subsections.

4.1 Experimental Details

In order to understand the multiplicity of driving input angular momenta involved in CF and ICF reactions, two particle-γ-coincidence experiments have been performed at the Inter-University Accelerator IUAC, New Delhi using Gamma Detector Array (GDA) alongwith charged particle detector array (CPDA) setup, for ^{16}O+^{169}Tm and ^{12}C+^{169}Tm systems at energy ≈4-7 MeV/nucleon. Coincidences were recorded between prompt γ-rays observed by HPGe detectors and charged particles (Z=1,2) detected by the charged particle detector system. The first experiment has been carried out for ^{16}O+^{169}Tm system, where spin-distribution and feeding intensity profiles of several evaporation residues have been measured at ≈5.6MeV/nucleon. However, for additional information on the multiplicity of driving input angular momenta, and to investigate the effect of projectile energy and structure on the entry state spin populations, another experiment has been performed to measure spin-distributions and side-feeding intensity profiles at 8 different energies ranging from ≈4 to 7MeV/nucleon. Brief description of target preparation, experimental setup and the description of used electronics, etc., is given in the following subsections.

4.1.1 Target Preparation

In these experiments for the spectroscopy of prompt γ-rays (in-beam spectroscopy), it is required to have spectroscopically pure and uniform target foils. As such, the targets have been prepared by rolling technique. In the first experiment, (i.e., ^{16}O+^{169}Tm system, where spin-distributions and feeding intensity profiles have been measured at E≈5.6MeV/nucleon) spectroscopically pure and self-supporting ^{169}Tm target of thickness ≈0.96 mg/cm^2 has been used. However, for the second experiment (i.e., ^{12}C+^{169}Tm system, where the spin-distributions and feeding intensity profiles have been measured at 8 different energies ranging from E≈4-7MeV/nucleon) ^{169}Tm target of thickness ≈ 1.85mg/cm^2 has been used. Thickness of the targets has been measured by α-transmission technique. The brief details of α-transmission technique have already been given in the Section-2.2 of Chapter-2. Further, the above projectile-target combinations have been chosen because of the fact that the possible reaction products are the well known rotational nuclei, and also the prompt γ-transitions are available in the literature.

4.1.2 Experimental Setup

For in-beam particle-γ-spectroscopy, a large improvement in the experimental technique has been achieved in recent years due to the availability of multi-detector systems, different energy filter detectors as well as anti-Compton spectrometers. This advance-

ment arrised as a large scale scientific efforts made to improve upon the spectroscopic limitations of single detector system, where the total counting rate is not, in general, allowed to exceed 10,000 counts per second due to the excessive pile up. However, it may be reduced to 3,000 counts per second after Compton scattering correction. The counting rate in a single HPGe detector may be calculated as;

$$N_s = \mathrm{N}_r(\Omega/4\pi)\mathrm{MG}_\varepsilon \tag{4.1}$$

Where; N_r is the number of residual nuclei produced per second. $\Omega/4\pi$ is the fraction of solid angle covered by each detector, M the number of photons emitted per event, and G_ε is the total γ-ray detection efficiency of the detector after Compton correction.

In case of in-beam γ-spectroscopy, it is required to collect the coincidence data to improve the resolving power. This technique is one of the most reliable criteria for assigning γ-transitions and/or cleaning up the spectrum considerably. The main disadvantage of coincidence experiments is that the count rate goes down drastically with the degree of coincidence or with the number of fold(s). For example, the data rate may be very less for an α-γ-coincidence as compared to proton-γ-coincidence in a nuclear reaction. As such, with any gating condition, the count rate in coincidence with one detector may be too small for analysis and/or to draw any significant conclusion. The count rate may be increased by increasing number of residual nuclei produced per second (N_r), which may be done by increasing beam current and/or target thickness. But, the above way of increasing the count rate may be constrained due to the pile-up events. Further, the coincidence count rate can not be increased much by increasing the solid angle of individual detector, since with this increase the Doppler broadening of γ-rays also increases. Therefore, the coincidence count rate can only be increased by using multi-detector system without affecting the quality of data. As such, in the present work, Gamma Detector Array (GDA) consisting of 12HPGe detectors has been used to record characteristic γ-rays. However, for particle identification and to generate particle-γ-coincidences, Charged Particle Detector Array (CPDA) set-up has been used alongwith Gamma Detector Array. A brief description of GDA and CPDA set-up, and their specifications are given in the following sections.

Gamma Detector Array (GDA)

Gamma Detector Array (GDA) is a multi-detector system of high counting efficiency, installed at the Inter-University Accelerator Center, New Delhi, India. This detector system is a dedicated array for γ-spectroscopy and reaction dynamics studies. With the advancement in the technology of the high-purity germanium material, the purity level of germanium crystal can be maintained as high as 10^9-10^{10}. The detectors used

in this array are made up of such high purity germanium and efficient in detecting γ-rays. This detector array consists of 12 n-type, intrinsic, HPGe-detectors. The n-type Ge-semiconductors are used almost universally as detector material for γ-spectroscopy, because of the good timing and high resistance to neutron damage. Further, in the mechanism of γ-ray detection, the photo-electric processes are important, as they result in full energy deposition. Generally, only 15-20% of photons result in full energy peak in a typical (100 C.C.) HPGe detector. For a particle-γ-coincidence experiment, the situation gets much worse, where only 4% events are expected to be full energy deposition events. Thus, it is required to improve the signal to background ratio for coincidence experiments. The signal to background ratio can be increased by detecting Compton scattered γ-rays coming out of the HPGe detector, by another scintillator and veto them out electronically. Such an array of scintillators surrounding an HPGe detector is known as Anti-Compton Shield (ACS). Both NaI and BGO crystals (which has absorption thickness about 2.2 times of NaI) have been used to construct an ACS. As an example, a typical schematic diagram of ACS is shown in Fig.4.1.

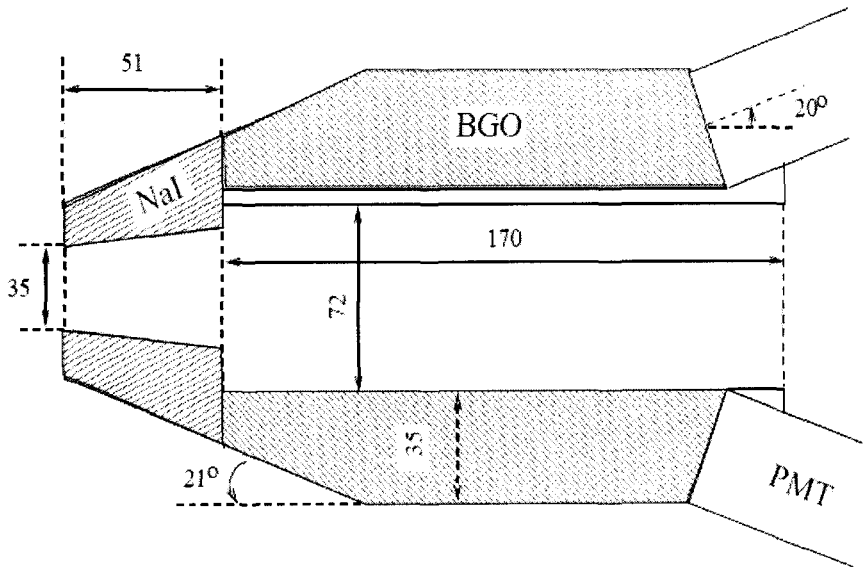

Figure 4.1: The symmetric Anti-Compton Shield (ACS) as used in GDA. The lengths are in mm.

As can be seen from this figure, the ACS is of symmetric design, and surrounded around each HPGe detector of the array. It has got two parts, i.e.,

- The main cylindrical body, which consists of eight optically separated 15cm long BGO crystals. To each of these BGOs, PMT is attached at an angle of 20°.
- A piece of NaI crystal is optically coupled to BGO crystals forming the front end of ACS.

Further, since, the energy of the back-scattered γ-rays from HPGe are $\leq$300 keV, the very high density material like BGO is not needed to detect those. Therefore, NaI crystal are used for the front part of ACS, which has a higher light output than BGO, particularly at lower γ-ray energies. Fig.4.2 gives the view of GDA set-up at the IUAC.

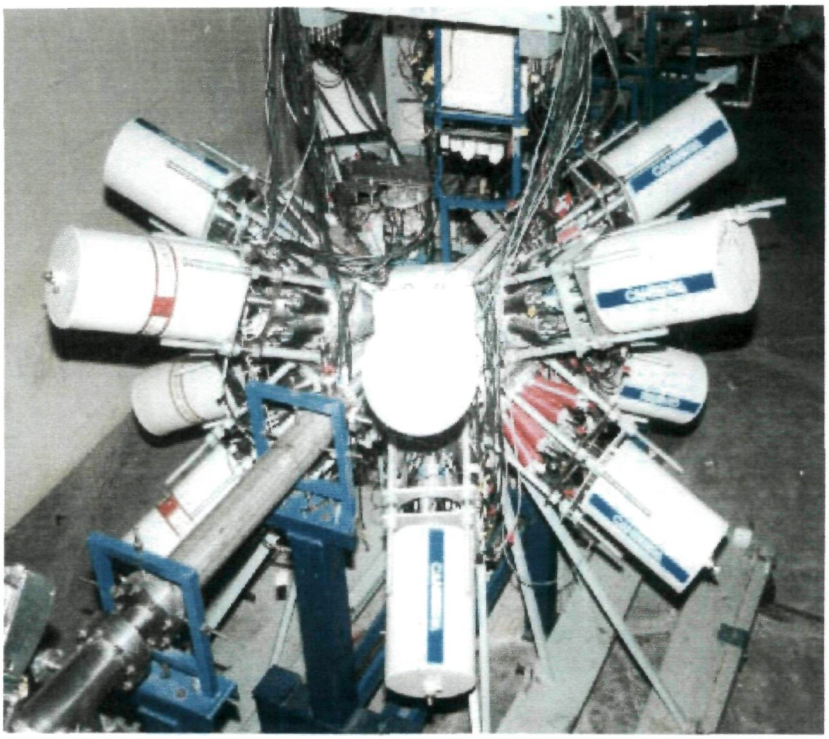

Figure 4.2: The Gamma Detector Array (GDA) in position

As shown in Fig.4.2, the HPGe detectors are inserted axially inside the ACS and are mounted on two rigid mechanical structures on either side of 30° beam line at the IUAC in Beam Hall-I. Each ACS is shielded from in-beam γ-rays from the target by 3 cm thick tantalum (Ta) collimator. The structures are movable with the help of rails fixed on the floor vertical to the beam line. Each of the structures consists of six HPGe detectors in

two rows, 25° above and below the horizontal plane with three detectors in each row at 45°, 99° and 153° in plane angles. This makes approximately 50°, 98° and 144° actual angles, respectively, with respect to the beam direction and there are four detectors at each of these angles. These detectors are cooled to liquid Nitrogen temperature (i.e., 77 K) to reduce the thermally generated leakage current.

Charged Particle Detector Array (CPDA)

In HI induced reactions a large number of reaction products are observed to be populated predominantly via CF and ICF processes at energies ≈4-7MeV/nucleon. As such, in order to distinguish between CF and/or ICF fusion processes, the detection of charged particles (Z=1,2) in coincidence with prompt-γ-rays becomes very important. Moreover, coincidences are also essential for selecting the desired reaction channels and/or for removing the unwanted background. As such, it is required to have a detector system for charged particle detection in a 4π-arrangement. The motivation of present work is to study the ICF reaction dynamics, where charged particle gating is an important tool for selecting the desired incompletely fused composites formed via ICF processes. In ICF reactions, the probability of projectile-like fragments emission is expected to be large as compared to CF reaction process, particularly in forward cone (as per the definition of ICF processes). Therefore, a device capable of particle (Z=1,2) identification is required to investigate the interplay of particle emission from different reaction processes, such as; CF and/or ICF fusion. The CPDA at IUAC consists of 14 charged particle detectors (CPD's) arranged in two truncated hexagonal pyramids. The bases of all pyramids lie in a horizontal plane with each other having trapezoidal shape. The remaining space at the top and bottom are filled by hexagonal detectors, which together with trapezoids cover nearly 90% of the total solid angle. The corner of the trapezoids are cut in V-shape for the entrance and exit of the beam and also for the target support (mounting) arrangement. The full CPDA is held in place from the top and bottom flanges of the scattering chamber, and is shown in Fig.4.3. There are four detector at the forward angles (F) covering 10°-60°, four in backward (B) covering 120°-180° and six sideway (S) at an angle around 90°. The specific features of CPDA are summarized in the Table.4.1. However, various stages of the installation of CPDA are shown in Fig.4.4. As can be seen from this figure, each CPD consists of the following components; (i) Phoswich detector made of plastic scintillator, (ii) Optical Guide, and (iii) Photo-multiplier Tube (PMT) with its base.

(i) **Phoswich Detector:**

The plastic scintillator is an organic scintillator, which is characterized by the presence of benzene ring structure in their constituent molecules. This particular structure possesses

chemical bonds in which the electron configuration can be distributed into a number of excited states by the absorption of radiation. These excited states then decay to their original ground state and emit light during the de-excitation. The entire process takes few nanoseconds in most of the orogenic scintillators. This is the principle used in the detection of charged particles in the Phoswich detectors. The combination of two dissimilar plastic scintillators optically coupled to a Photo-Multiplier Tube (PMT) is called Phoswich detector. One of the detectors (thin-BC400-0.1 mm) has a fast rise time giving information on the type of particle detected based on the energy deposited by a particle (ΔE) inside the detector material. However, the second (thick-BC444-5 mm) detector has a slow decay constant containing the total energy (E) deposited by the traversing particle(s). The scintillator (BC400, and BC444) of each CPD are having proper shapes (edges and sides) to match with the optical guide's trapezoidal face and the shape of the truncated hexagonal pyramid of full detector system. Each Phoswich detector is made by heat pressing the two plastic scintillators at constant temperature for about two hrs under pressure (sandwiched between two flanges tightened with a set of bolts). If the joining temperature and pressure is more, then the scintillator material may melt and cause drastic changes in the optical properties (and becomes opaque), where, the dimension changes will not allow the precise positioning of the detectors in the compact array. The front face of the Phoswich detector is having a layer of gold (100 μg/cm^2 deposition) for good collection efficiency.

(*ii*) Optical Guide:

The optical guide is the material which joins the scintillator and the PMT. The PMT converts the light signal into electrical signal for further processing. As the wavelength of the light (emitted by plastic scintillator) is of the order of Ultra-Violet (UV) region, the UV transmitting (UVT) lucite material (BC800 UVT acrylic) is there for better transmission of light. The length of the optical guide has to be kept minimum for maximum light collection efficiency at the PMT. For joining the optical guide to the Phoswich detector and also with PMT, an optical cement BC600 was used, which is a clear, optically transparent epoxy. The optical guide alongwith the Phoswich detector is covered with the aluminized mylar foil of 6 μg/cm^2 for the good transmission of light. The vacuum seal is used with the PMT, as it avoids the light leakage and vacuum problem to a large extent.

(*iii*) Photo-Multiplier Tube (PMT):

Considering the space availability in the scattering chamber, rise time compatibility between the scintillator and the Photo-Multiplier Tube (PMT), stability and low noise,

the HAMAMATSU PMT R1924 is used as the PMT for the charged particle detector. The working of the PMT is ensured by keeping the anodes and plates successively at a positive stable voltage with respect to photo-cathode. As the gain of the PMT is extremely sensitive to changes in voltage, it is very important that sources of high voltage be well regulated and free of ripples.

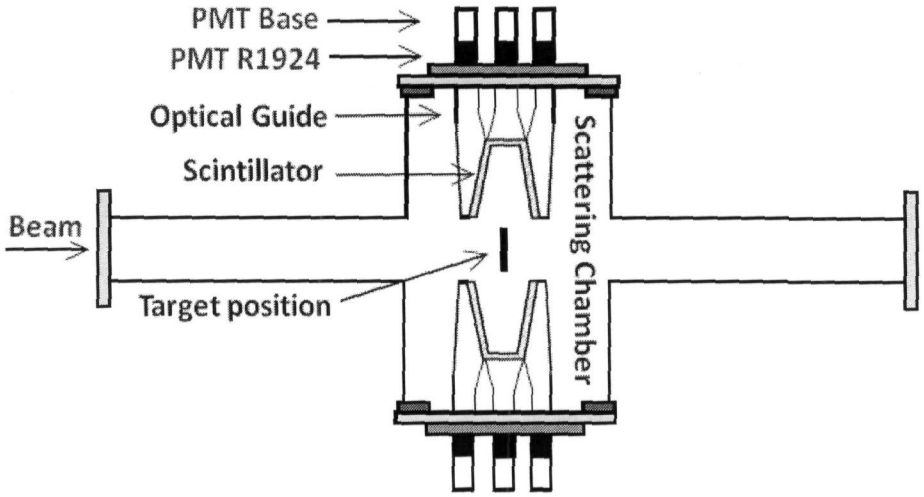

Figure 4.3: Charged particle detector array housed in a small scattering chamber, where target position is also shown

Table 4.1: Salient features of CPDA

Geometry of CPDA	Two truncated hexagonal pyramids
Detector material	Plastic scintillator
Solid angle covered	90 % of 4 π
Number of detectors	14
Count rate for each element	50,000 counts/sec
ΔE detector	BC400, thickness $\approx$ 100 μm
E detector	BC444, thickness $\approx$ 5 mm
Optical guide	BC800 UVT lucite material
PMT	1" diameter, R1924- HAMAMATSU
Glue for PMT & optical guide	Optical cement (BC600)

Figure 4.4: Different components of Charged particle detector array.

4.2 Irradiations

The scattering chamber of 16cm diameter (made up of Aluminum) housed the CPDA for the configuration of GDA+CPDA operation. This scattering chamber is made up of aluminum to minimize the absorption of emitted γ-rays from the target area. It also houses a special arrangement to mount the target, beam collimator (called CPDA collimator), and the current feed-through for the beam current monitoring. Special care has been taken so that the center of the CPDA and that of GDA coincide. This chamber has two rotatable flanges for the alignment purposes. As the CPDA is held and aligned by the top and bottom flanges of the target chamber, specially designed set of two flanges hold each set of seven charged particle detectors (CPD's) in a proper geometry to reliably reproduce the center.

In the present set of experiments, natural ^{169}Tm (100%) targets of given thicknesses have been bombarded with $^{16}O^{+7}$ and $^{12}C^{+5}$ projectiles, respectively, at projectile energies $\approx$90 MeV and $\approx$ 57-90MeV delivered from 15UD-Pelletron Accelerator at IUAC. As has already been mentioned, in these experiments, particle-γ-coincidences have been recorded using GDA alongwith CPDA set-up. The GDA is an assembly of 12 Compton suppressed, high resolution HPGe γ-detectors at angles 45°, 99°, 153° with respect to the beam axis and there are 4 detectors at each of these angles. However, the CPDA is a set of 14-Phoswich detectors, covering nearly 90% of total solid angle, so that the angular distribution of charged particles (Z=1,2) in $\approx 4\pi$-solid angle may be recorded. For coincidence purposes, all 14 detectors of CPDA have been divided into the three angular zones;

- Forward angles (F) $10° - 60°$,
- Sideways (S) $60° - 120°$, and
- Backward angle (B) $120° - 170°$.

Moreover, in order to remove the scattered beam during the experiment, CPD's have been covered by Al-absorber of appropriate thickness. The Al-absorber also reduces the number of random coincidences due to elastically scattered beams and prevents the detector array from the direct radiation damage. As a kinematical fact, in HI (e.g., ^{16}O, ^{12}C etc.) induced reactions, different α-components (fast and slow) are, generally, emitted, as;

- the fusion-evaporation (CF) α-particles i.e., the slow-α-component (CN-α) expected to be emitted after equilibration of composite nucleus, and

- the spectator α-particles i.e., the fast-α-component ($E_{direct-\alpha}$) after projectile break-up in an incomplete fusion reaction.

It may, further, be pointed out that the slow-α-component (CN-α) may be simulated by fusion-evaporation model code PACE. However, fast-α-component with a forward peaked angular distribution emitted in ICF process is expected to be peaking at the projectile velocity. The energy of fast-α-component ($E_{direct-\alpha}$) may be calculated as the energy of projectile times ejectile to projectile mass ratio ($E_{Direct-\alpha} = E_{projectile}$ x $M_{ejectile}/M_{projectile}$). As a typical example, spectra for slow-α-component simulated for ^{16}O+^{169}Tm system at ≈5.6MeV/nucleon using statistical model code PACE4 is shown in Fig.4.5.

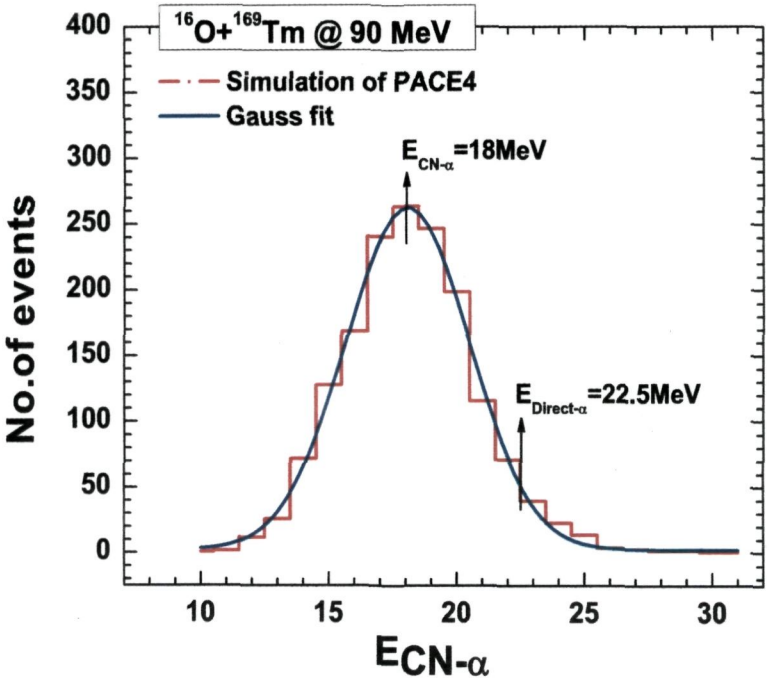

Figure 4.5: Typical spectra for slow-α-component (i.e., $E_{CN-\alpha}$≈18MeV) simulated by statistical model code PACE4.

As can be seen from the Fig.4.5, the slow-α-component (CN-α) emitted in ^{16}O+^{169}Tm system at ≈5.6MeV/nucleon indicates the most probable energy $E_{CN-\alpha}$≈

18MeV. However, as per the definition of ICF the $E_{Direct-\alpha}$ has been estimated to be $\approx$ 22.5MeV corresponding to $\approx$ 90MeV projectile energy. Since, there is a significant difference in the energy of fast and slow-α-components, therefore, it is possible to distinguish them by using the charged particle detector system. Moreover, in a nuclear reaction initiated by HIs, the charged particle detectors at forward angles (F) $10^{\circ} - 60^{\circ}$ are expected to detect both fast and slow-α-components. As such, in order to record only fast-α-particles originated from ICF processes in forward cone (F), an Al-absorber of appropriate thickness has been kept at forward cone (F) $10^{\circ} - 60^{\circ}$ CPDs to cut-off the low energy alpha component (i.e., $E_{CN-\alpha}$ $\approx$18 MeV). All HPGe γ-detectors of GDA set-up have been calibrated using various standard γ-sources of known strength. The efficiency of these high-resolution HPGe γ-detectors have been measured by putting ^{152}Eu and ^{133}Ba γ-sources at the target position. While, the ^{241}Am α-source has been used for CPDA gain matching.

4.3 Electronics set-up

4.3.1 Electronics for GDA

The electronics for the GDA consists of the following requirements;

- The rejection of γ-rays associated with Compton scattering. When a signal comes from the ACS, the corresponding signal from the HPGe detector should veto out electronically.

- Coincidence relation should be satisfied at the hardware level before recording the data.

- The energy and timing information from the valid signal obtained from HPGe detector after the suppression of the Compton background should also be recorded, which is very important for coincidence measurements.

As a matter of fact, the valid signals are those, which satisfy the first two requirements. The HPGe detectors have two signal outputs, i.e., 'fast' for deriving the timing, and 'slow' for γ-ray energy information, although both the signals are actually identical in nature while coming out from the Ge pre-amplifier. The pre-amplification of both the signals are achieved inside the detector housing itself. These 'slow' and 'fast' signals are sent to linear amplifier, and then fed to the analog to digital convertor (ADC) for recording of the energy information, proportional to the pulse height. The TFA output on the

other hand is used as timing and logic signals for generating master triggers. The block diagram of the electronics for the Compton suppression is shown in Fig.4.6.

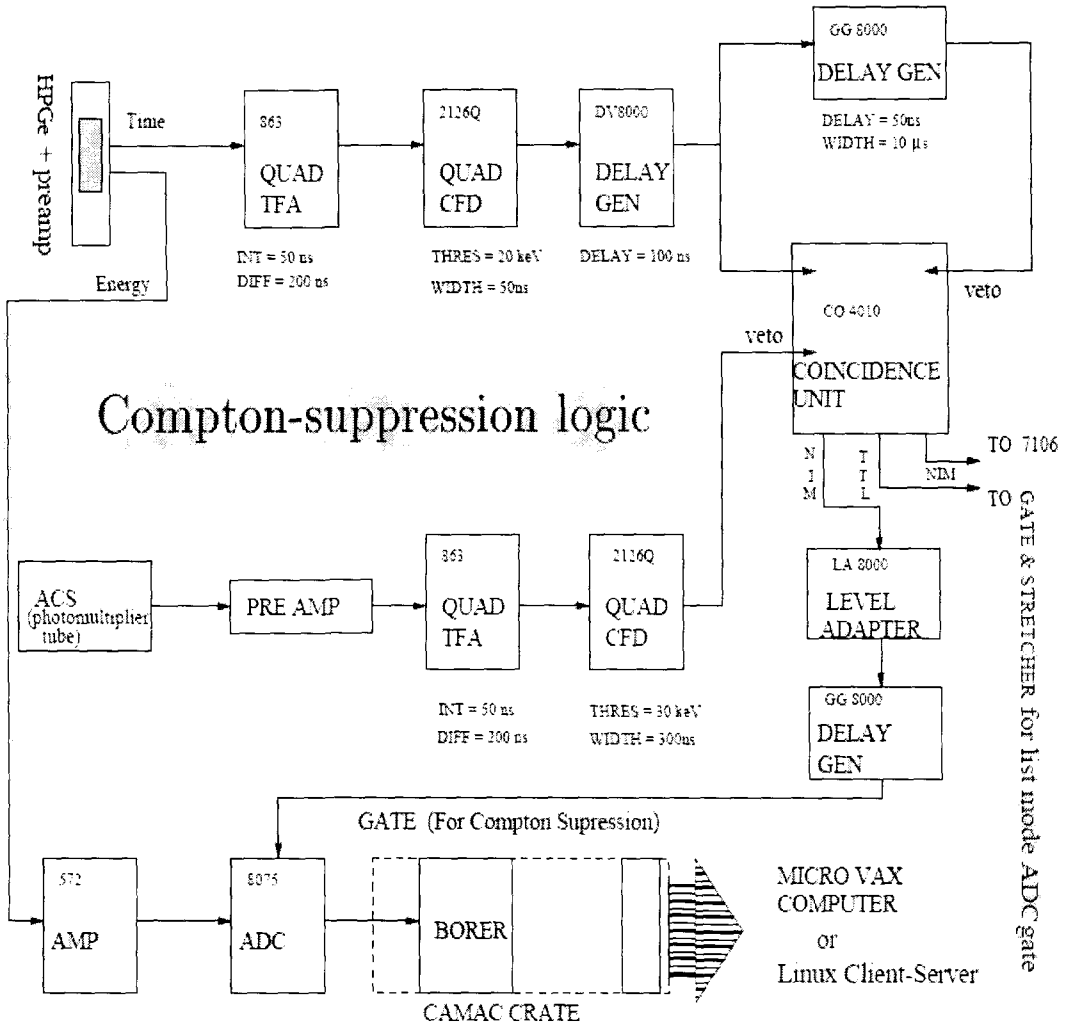

Figure 4.6: Block diagram of Compton suppression logic used in Gamma Detector Array Experiments.

As has already been pointed out that the 'fast' signal from HPGe is fed into a TFA and then the output of TFA is fed into a constant fraction discriminator (CFD) for deriving the timing signal. The CFD is used in slow rise time (SRT) mode for achieving better timing resolution. The thresholds of CFDs for the HPGe are set just above the noise by

looking at the linear amplifier output on an oscilloscope triggered by the CFD out-put. The CFD pulse width for HPGe is kept to 60 ns. The signals from the shield scintillator are summed up and the timing of this summed signal is also derived from a TFA-CFD combination. This signal is used to veto the HPGe CFD output in a coincidence module CO4010. Moreover, in order to ensure that the HPGe signal is at the center of the ACS signal or not, and to take care of pulse walk in the HPGe signal, the HPGe CFD output is delayed by 100ns before feeding into the coincidence unit CO4011. To remove the pile up signals, the signal A is further delayed by a delay generator, which is further fed into the same coincidence module and demanding an anti-coincidence with the first signal. The coincidence now generates a logic output which is Compton suppressed and is termed as GE.ACS(bar). The coincidence unit CO4010 has both TTL and NIM outputs. The TTL outputs, after proper delay and width adjustments, are used to gate the ADCs of individual HPGe detector.

4.3.2 Electronics for CPDA

In the present experiments, the particle identification has been done based on the pulse height of the signal. The same signal has been used for both protons and α-particles, where the buffer module takes the analog signal, priori shaped by the fast amplifier and give two outputs with 50Ω output impedance. Hence eight channel buffer module with each channel having one input and two outputs is used for this purpose. The count rate from the individual charged particle detector is quite high, i.e., 50,000 counts per second, therefore, the regular spectroscopic amplifier can not be used as they will choke the data flow. Hence, an amplifier cum attenuator is used which takes the input from buffer module, amplifies it and gives output alongwith twelve attenuated outputs. The block diagram of CPDA electronics is shown in Fig.4.7. The circuit diagram shown in this figure is used to record the particle(Z=1,2)-γ-coincidences. However, Fig.4.8 is used to record the multiplicity of charged particles (Z=1,2) detected in the various angular zones of CPDA.

As demonstrated in the figure, the signal from each charged particle detector is fed into 776 amplifier (16 channel-fixed gain amplifier), which amplifies the CPD signals with a constant rate. The output of the fast amplifiers are fed into the 777 amplifier (variable gain amplifiers), which are used to match the gain and for further amplification of all the signals. Moreover, two multi-unit constant fraction discriminators (ORTEC CF8000) are used to adjust the threshold of CPDA to differentiate the particles (Z=1,2 i.e., proton and α-particles respectively), and alpha are set by looking at the output of 777 amplifiers on an oscilloscope triggered by the CF8000 output. For the particles (Z = 1,2) and alpha-particle, the threshold of the CF8000 in the CPDA channels is set just

above the noise. The threshold of the α-particle(s) has been kept high in comparison to the particles. These modules give a multiplicity (M) signal and OR (ORed) signal, which is then fed into the modules 744 FIFO and the coincidence unit CO4010. The coincidence unit CO4010 generates a logic output. The output of CF8000 is delayed using delay generator GG8000.

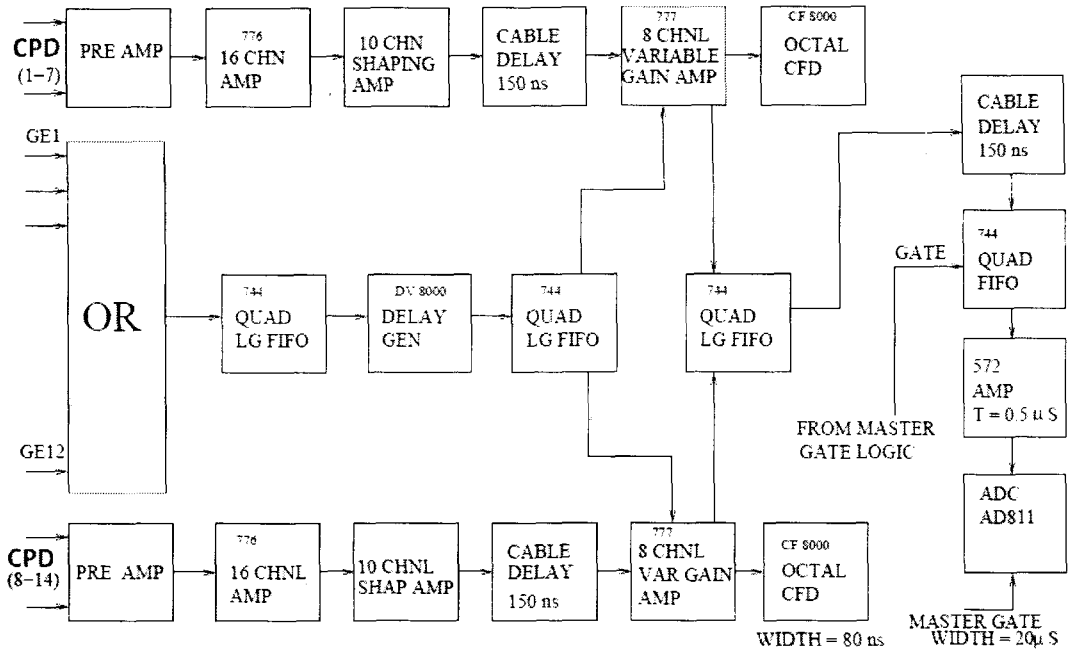

Figure 4.7: Block diagram for generating master-gate to record particle-γ-coincidences.

This signal is further fed into the same coincidence unit and master-coincidences in between particles (Z=1,2) and prompt γ-rays emitted are demanded as a course of projectile-target interactions. Further, the output of CF8000 is delayed by 130ns using delay unit and then the delayed output fed into FIFO744 module. The output from the coincidence unit CO4010 is fed into a DV8000 module. However, the NIM signal is fed into the trigger logic unit to generate the master gate. After proper delay and width adjustment the output of DV8000 is fed into FIFO744 unit, where output is further fed into the 572 ORTEC amplifier. The amplified signal from 572ORTEC amplifier is fed into the analog to digital converter (AD 418A QUAD 8k) for recording the α-multiplicity

and particle-multiplicity spectra.

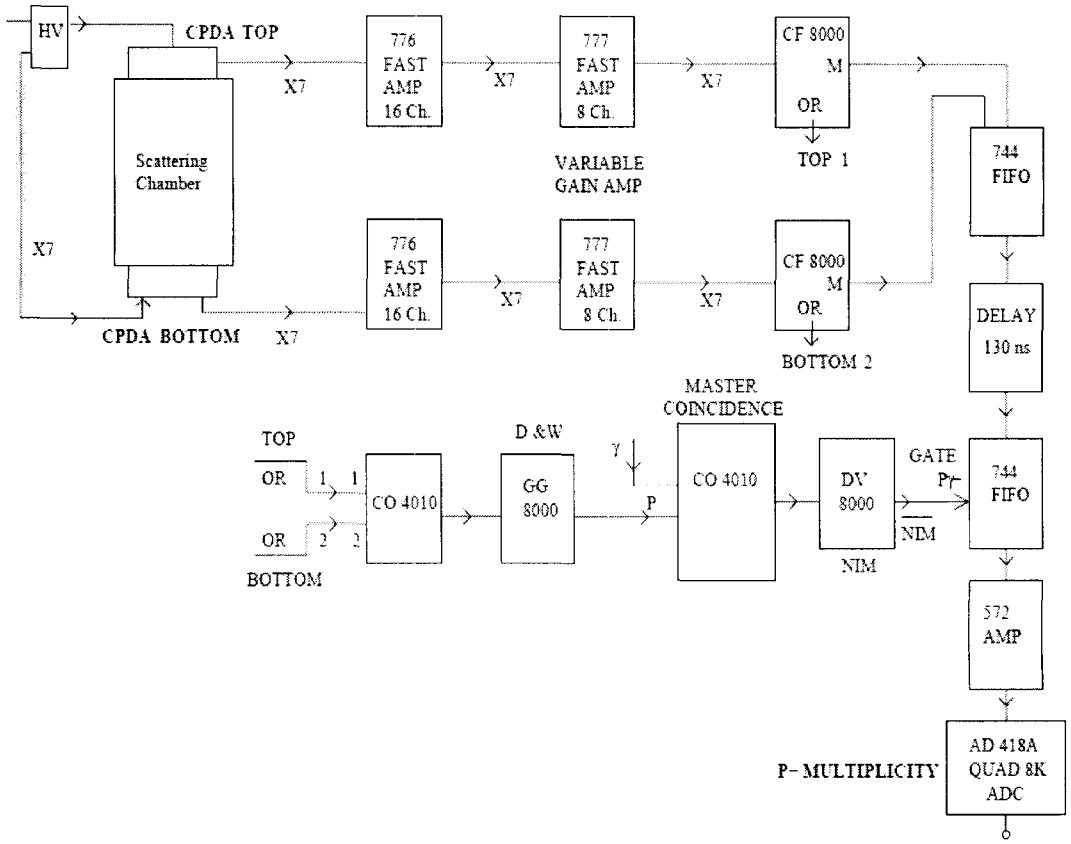

Figure 4.8: Block diagram for particle (Z=1,2) multiplicity

4.3.3 Data acquisition System

In the GDA+CPDA experiments, a LINUX based computer was used for data acquisition. The CAMAC (Computer Automated Measurement And Control) crates were used for the interfacing. The online data acquisition program CANDLE of IUAC, New Delhi was used to collect the multi-parameter data in event-by-event (LIST) mode. Each event has been recorded with following parameters;

- The bit-pattern from the 16-channel discriminator latch gives the information about the pair of detectors fired when coincidence conditions are satisfied.
- The twelve energy signals from twelve detectors which satisfy all the coincidence and anti-coincidence conditions.
- The timing of all the detectors from TDC module.
- The charged particles (Z=1,2) and α-particle multiplicity.

Moreover, in order to collect the coincidence information, the events for particle (Z=1,2)-γ-coincidences have been collected in three angular zones. As such, six AD's (one for each angular zone) have been assigned for particle (a sum of proton and α-particles), and α-gates, in the following manner;

- CPDA-P-F (CPDA-particle-forward) for $10^\circ - 60^\circ$ angular zone,
- CPDA-P-S (CPDA-particle-sideways) for $60^\circ - 120^\circ$ angular zone,
- CPDA-P-B (CPDA-particle-backward) for $120^\circ - 170^\circ$ angular zone,
- CPDA-α-F (CPDA-α-forward) for $10^\circ - 60^\circ$ angular zone,
- CPDA-α-S (CPDA-α-sideways) for $60^\circ - 120^\circ$ angular zone, and
- CPDA-α-B (CPDA-α-backward) for $120^\circ - 170^\circ$ angular zone.

Apart from the particle-γ-coincidence events in different gating conditions, data has also been collected in singles mode without any hard and/or soft gating condition, so that the pure neutron channels may be identified during the analysis. As such, the singles data has been collected using the best (resolution and efficiency wise) backward and forward angle detectors, which have also been used for Doppler correction during the analysis. The detailed discussion on the off-line analysis of data is given in the following section.

4.4 Data Analysis

In the present work, in-beam prompt γ-ray spectra have been analyzed in the multi-parameter mode. After recording the list mode data, the off-line data analysis has been performed by sorting the data and subsequent projection of gating conditions on spectra using nuclear physics analysis software INGAsort [81]. The sorting of list-mode data went

through a series of data processing before the twelve energy ADCs (γ-energies recorded in HPGe detectors) have fired. The gain of all ADCs are approximately matched during the experiment, but a precise gain matching is required to add the projected spectra of all the HPGe detectors. The efficiency determination and gain matching of HPGe detectors have been done by using standard radio-active sources of known strength to cover the energy range from $\approx$ 80-1408 keV. In these experiments, the efficiency of HPGe γ-detectors have been determined by putting ^{152}Eu and ^{133}Ba γ-sources at the target position. In order to show the quality of calibration and gain matching, as a typical example, calibrated and gain matched spectra (from channel no. 286 to 859) taken by Ge7 and Ge8 detectors are shown in Fig.4.9, where different peaks of standard ^{152}Eu-source are marked.

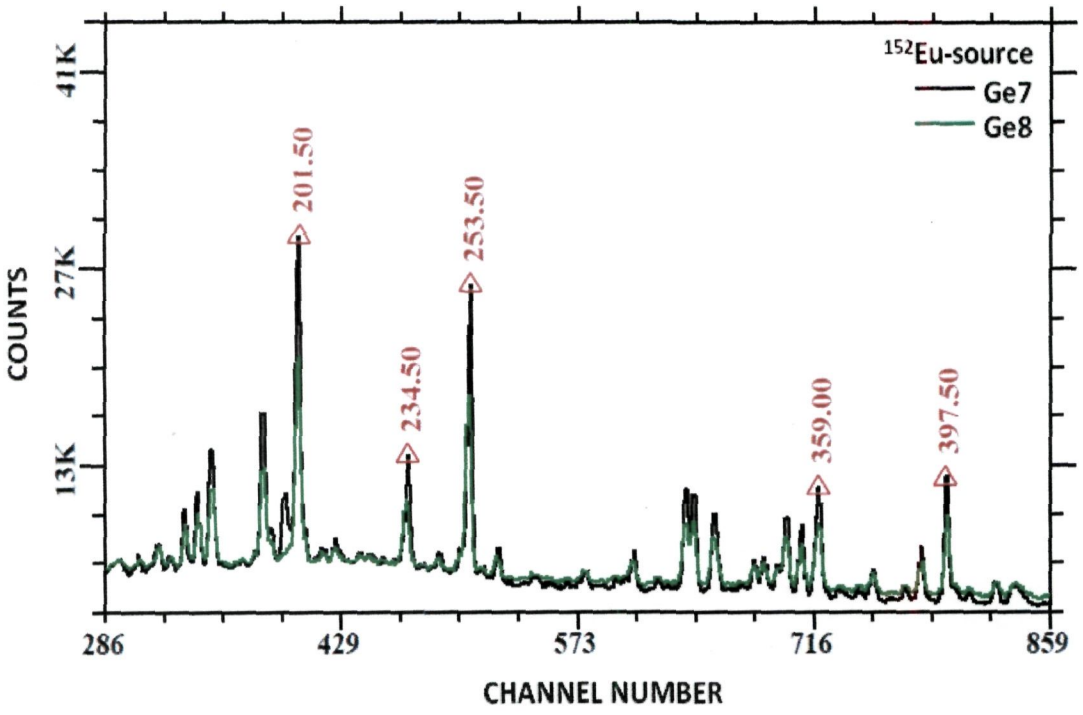

Figure 4.9: Typical partial γ-ray spectra of standard ^{152}Eu-source. Gain matching with Ge7 and Ge8 is also shown in this figure.

It may, however, be pointed out that each γ-ray may have contribution due to background, therefore, its contribution has been corrected by subtracting separately taken background spectra. After gain matching of the detectors, different gating conditions

as given in the earlier section have been projected onto energy spectra to generate the particle (Z=1,2) gated spectra. The width of different particle gates have been projected in such a way that covers the essential part of particle (Z=1,2) gates. In order to improve the data statistics, assuming the angular distribution of the observed γ-rays to be isotropic, all gated spectra for a particular gating condition have been summed up.

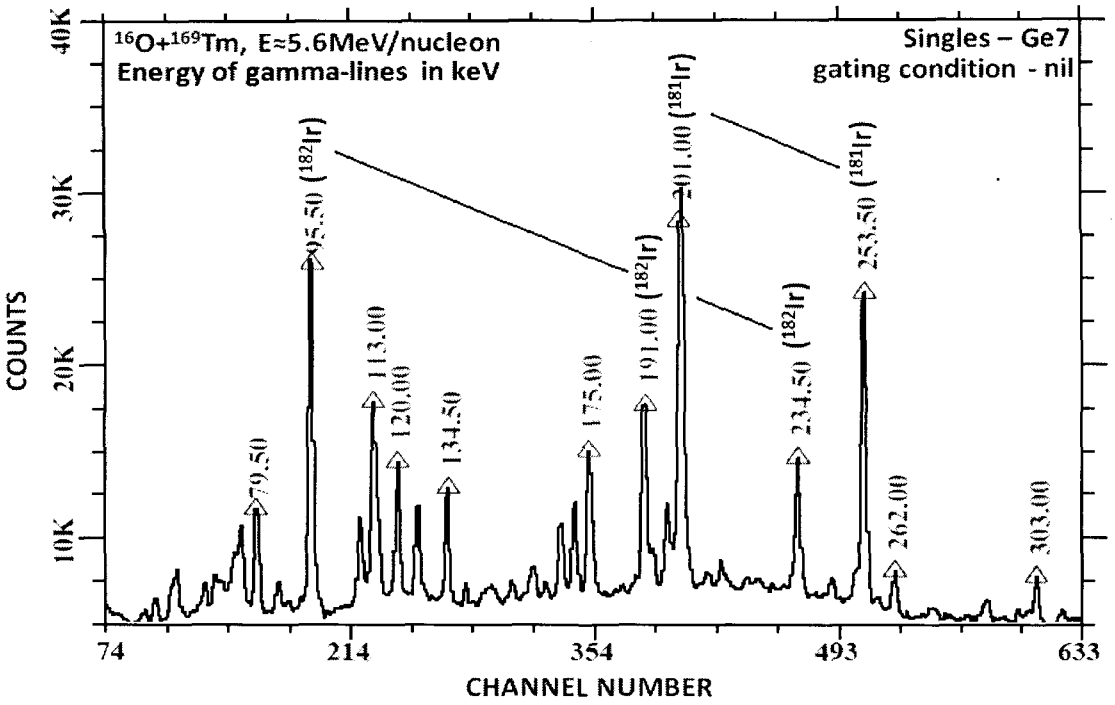

Figure 4.10: A typical partial γ-ray spectrum for ^{16}O+^{169}Tm system at ≈5.6MeV/nucleon in singles mode. Peaks has been assigned to different CF products, predominantly populated via xn-channels.

Further, in addition to the particles (Z=1,2) gated data, singles data has been collected to identify the CF products (xn-channels). Specific reaction products produced via CF and/or ICF have been identified by looking into various particle(s) and α-gated spectra. As mentioned above, the pure neutron channels (xn-channels) have been identified by looking into the singles data taken from the best Ge-detectors (resolution and efficiency wise). These channels, as a matter of confidence, have also been confirmed by the identification of their characteristic decay γ-lines from the decay spectra recorded time to time during the experiment without beam. However, CF products populated via pxn/αxn-channels have been identified from the backward (B)-particles(Z=1,2) and α-

gated spectra. In particular, for the identification of pxn-channels, backward(B)-α-gated spectra has been subtracted from the backward(B)-particles (Z=1,2)-gated spectra to achieve only proton-gated spectra. While, αxn/2αxn-channels produced via CF have been identified from the backward(B)-α-gated spectra. Further, as per the kinematical definition of ICF, the fast-α-particles (particles having velocity of the order or projectile velocity) produced in an ICF reaction are expected to flow only in forward cone ($10^\circ - 60^\circ$). As such, the ICF products produced via αxn/2αxn-channels have been identified from forward(F)-α-gated spectra. It has already been mentioned that, the CN-α component of most probable energy i.e., $E_{CN-\alpha} \approx$ 18MeV (simulated by PACE4), has been completely cut-off by putting an Al-absorber of appropriate thickness on the forward cone ($10^\circ - 60^\circ$) Charged Particle Detectors (CPDs). However, in order to, further, remove contamination of CN-α's, the backward(B)-α-gated spectra has been subtracted from forward(F)-α-gated spectra.

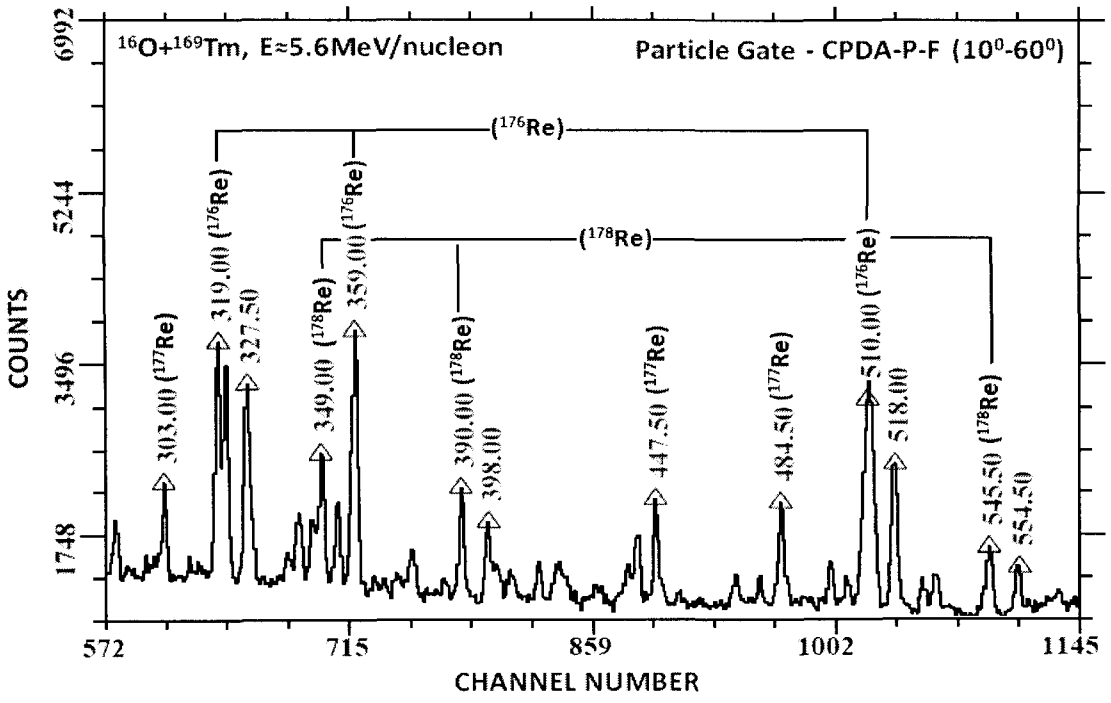

Figure 4.11: A typical partial γ-ray spectrum gated with CPDA-P-F. This spectrum has been generated for the identification of pxn-channels.

The intensity and area under the photo-peak (efficiency corrected) of the characteristic prompt γ-transitions were used to determine the relative production yield for the observed

spin. The γ-ray energies and their intensities used in the present work have been taken from RADWARE and/or NNDC [86]. A typical γ-ray spectum of $^{16}O+^{169}Tm$ system recorded in singles mode is shown in Fig.4.10, while the γ-ray spectra in coincidence with proton(s) and α-particle(s) are shown in Fig.4.11 and Fig.4.12, respectively. In order to show the quality of selection and the accuracy of calibration, γ-ray peaks have been labelled belonging to the different residual nuclei expected to be populated via CF and/or ICF channels in $^{16}O+^{169}Tm$ system at 5.6 MeV/nucleon. In order to further improve the statistics, subtracted spectra have been added up for all four forward angles CPD's. Out of these γ-ray spectra, γ-transitions belonging to the xn, αxn and 2αxn-channels have been assigned. Area under the peaks of relevant γ-transitions assigned to the different reaction products have been used to obtain the relative production yield of ER's.

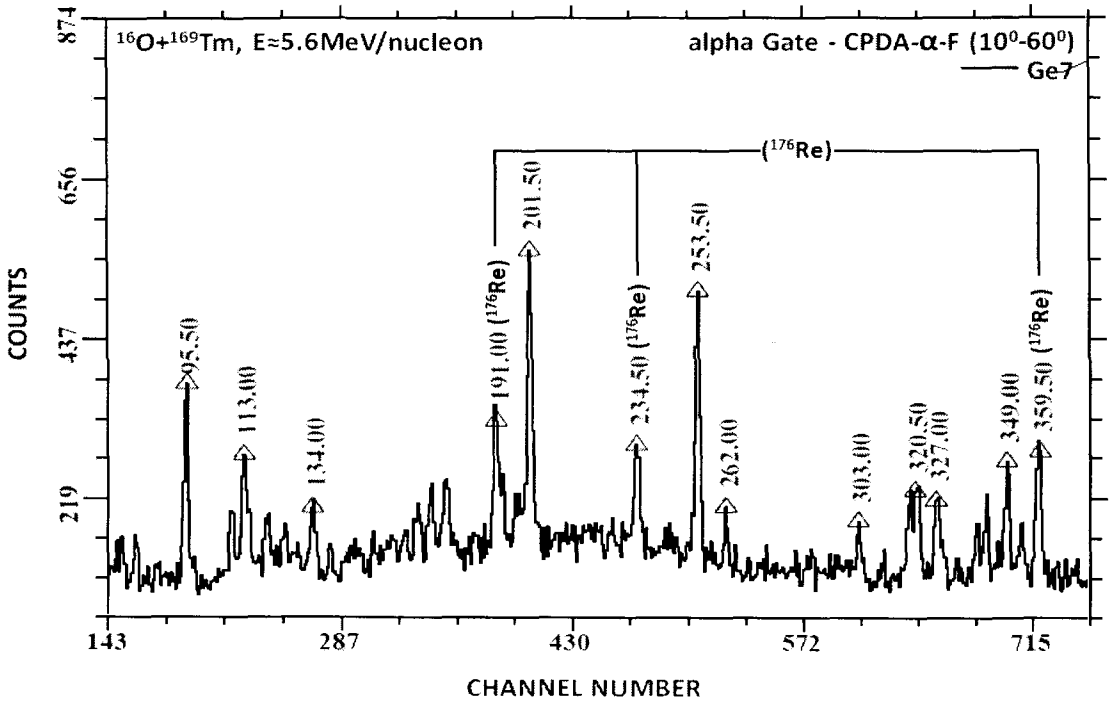

Figure 4.12: A typical partial γ-ray spectrum gated with CPDA-α-F (CPDA-α-forward). This spectrum has been obtained after subtraction of backward(B)-α-gated spectra from forward(F)-α-gated spectra for the identification of direct-α-emitting channels.

4.5 Results and interpretation: $^{16}O+^{169}Tm$ system

In the present work, different reaction modes have been identified on the basis of experimentally observed spin population in a residual nucleus prior to its de-excitation, which are expected to be distinctly different for CF and ICF reactions. In order to generate experimental spin-distributions [i.e., the yield (intensity) profile as a function of observed spin (J_{obs})] of various CF and ICF reaction products, relative production yields have been plotted as a function of experimentally observed spin (J_{obs}^{exp}) corresponding to prompt γ-transitions. For better comparison of different reaction channels (xn, αxn and 2αxn) in a panel, relative production yields have been normalized with their own highest experimentally measured values (Y_{obs}^{max}) at lowest J_{obs}^{min}. The spin-distributions of evaporation residues obtained as mentioned above have been fitted to a function of following type adopted as the simplest analytical representation of data[23];

$$Y = Y_\circ/[1 + exp(J - J_\circ)/\Delta] \tag{4.2}$$

Where; Δ is related to the width of input angular momentum ($J_\circ$) and $Y_\circ$ is the normalization constant. Here, $J_\circ$ is a sensitive parameter which provides the qualitative information about the mean driving input angular momenta associated with various reaction channels. The main reaction channels that were identified in the forward (F) cone in coincidence with fast α-particle(s) are ^{169}Tm(^{16}O,αxn)$^{181-x}$Re, ^{169}Tm(^{16}O,αpxn)$^{180-x}$W, ^{169}Tm(^{16}O,2αxn)$^{177-x}$Ta and ^{169}Tm(^{16}O,2αpxn)$^{176-x}$Hf. However, the residues which have been identified in backward cone are ^{169}Tm(^{16}O,αxn)$^{181-x}$Re and ^{169}Tm(^{16}O,pxn)$^{184-x}$Os. The normal xn-channels ^{169}Tm(^{16}O,xn)$^{185-x}$Ir(CF products) have been identified from singles spectra and confirmed from decay gamma-lines.

4.5.1 Spin-distributions: $^{16}O+^{169}Tm$ system

Experimentally measured spin-distributions for xn, αxn and 2αxn-channels are presented in Figs.4.13-4.15. Notations 'F' and 'B' represent the reaction products identified respectively from 'Forward' & 'Backward' α-gated spectra. The lines and curves through data points are the results of best fit to the data points. The errors have not been shown in these figures and are estimated to be $\leq$ 10 %. The normalized yield (Y_{nor}) at different J_{obs} for a particular reaction product has been obtained as the ratio of Y_{obs}^{max} at J_{obs}^{min} to Y_{obs} at different J_{obs} values. As such, the fractional errors are significantly reduced in the value of Y_{nor}. It has been checked that the inclusion of these reduced errors does not alter the fitting of spin-distributions, and hence the present analysis. The reaction

channels are labelled by self-explanatory notations of corresponding emission cascade, as discussed in text.

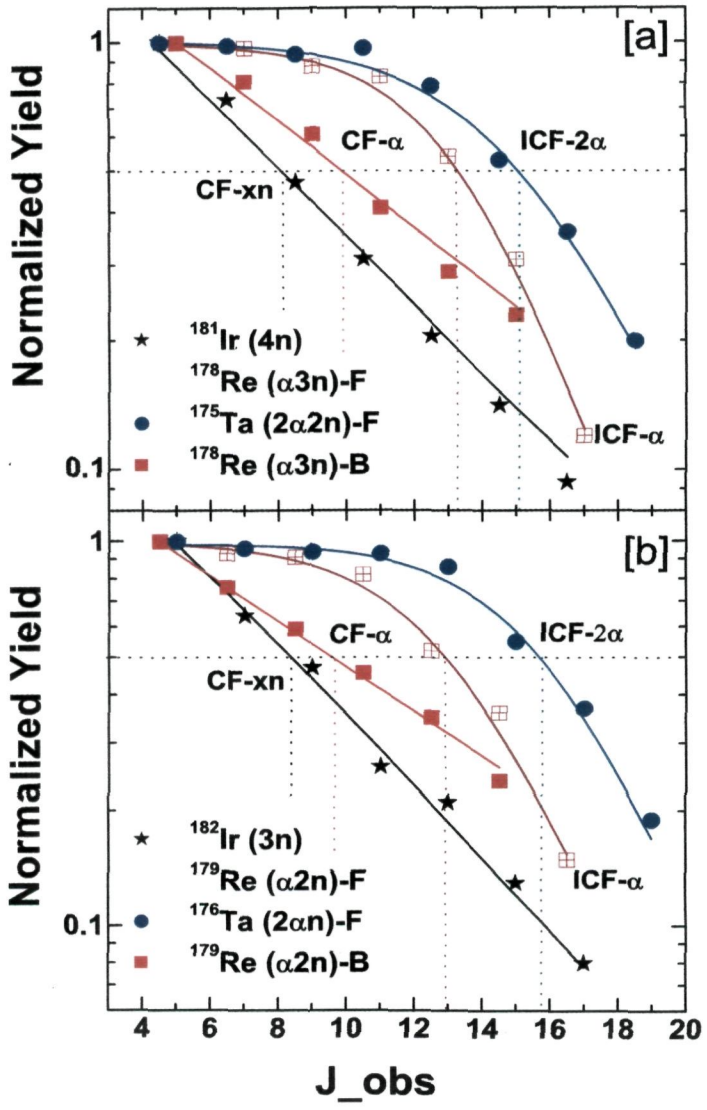

Figure 4.13: Experimentally measured spin-distributions for xn(CF) and αxn/2αxn(CF and/or ICF) channels in ^{16}O+^{169}Tm system at $\approx$ 5.6 MeV/nucleon.

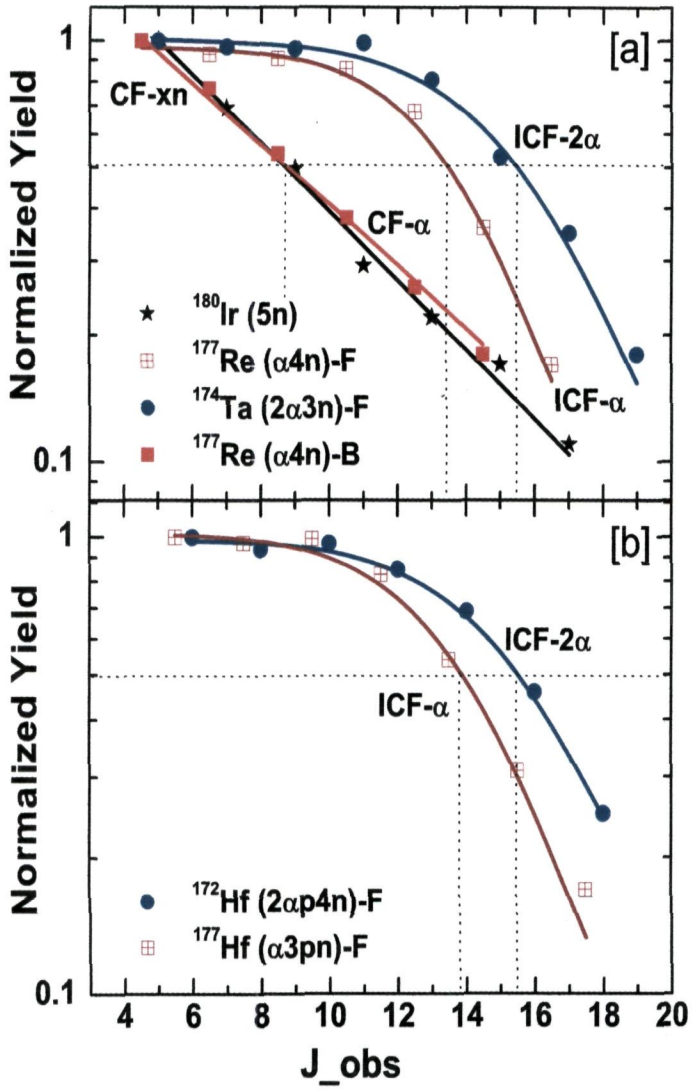

Figure 4.14: Experimentally measured spin-distributions for different residues populated via xn and αxn/2αxn-channels in ^{16}O+^{169}Tm system at $\approx$ 5.6 MeV/nucleon.

It can be observed from the Figs.4.13-4.15, that there is a striking difference in the experimentally measured spin-distributions of different reaction products expected to

be populated via CF and ICF processes, which indicates the involvement of entirely different reaction dynamics in the production of these reaction products. As shown in these figures, the intensity of xn-channels (predominantly populated via CF) falls off rather quickly with J_{obs} or the intensity is increasing steeply towards the band head, indicating the strong feeding during the deexcitation of CN. This gradual monotonic increase in the intensity towards the band head may be because of the fact that the CF process leads to a CN of definite excitation energy (E^*), and a broad spin states populations. In this case, the yrast states are expected to be fed over a broad spin range. It may, further, be pointed out from the Figs.4.13-4.15 that the spin-distributions for αxn and/or 2αxn channels identified from forward(F)-α-gated spectra (associated with ICF) are found to distinctly different as that observed for CF. In this case, the yield appears to be almost constant upto J$\approx$10$\hbar$ and J$\approx$12$\hbar$ for $\alpha/2\alpha$-emitting channels, respectively, and then decreases rapidly for higher J-values.

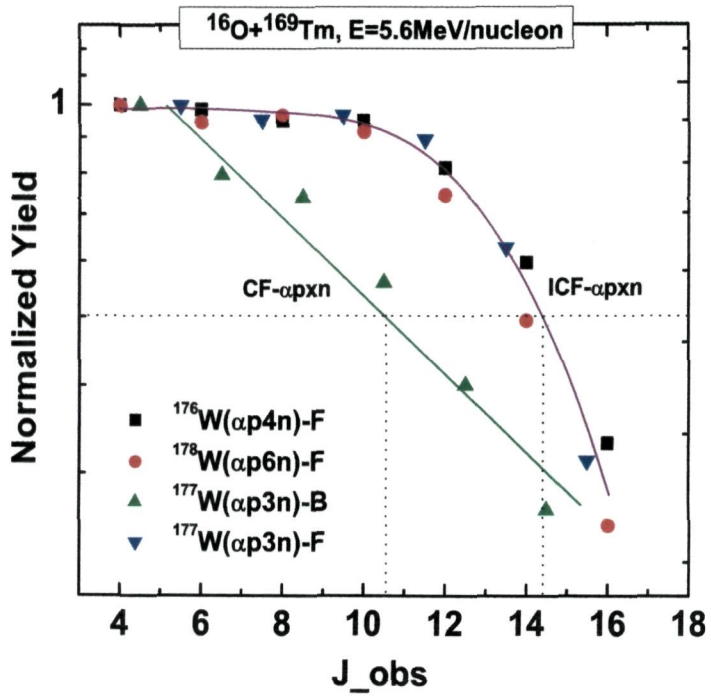

Figure 4.15: Experimentally measured spin-distributions for W-isotopes populated via αpxn-channels in ^{16}O+^{169}Tm system at $\approx$ 5.6 MeV/nucleon.

Furthermore, in order to have better insight into the spin-distributions of α-emitting channels, the spin-distributions of ^{178,179}Re-isotopes identified from backward-α-gated spectra (CF products) and forward-α-gated (ICF products) spectra have been compared in a panel in Figs.4.13(a)-(b). As given in these figures, the spin-distributions for ICF products are found to be distinctly different than that observed for CF products. It may, further, be pointed out that the yield of ^{178,179}Re-isotopes [Figs.4.13(a) and (b)] identified from the backward(B)-α-gated spectra is found to fall steeply with observed spin, indicating strong feeding as expected for CF products. While, the yields of the same residues ^{178,179}Re identified from the forward(F)-α-gated spectra (ICF products) are found to increase towards band head upto a certain value of J_{obs} and then is almost constant upto the lowest J_{obs}. The similar characteristics (spin-distributions) as that observed for ICF-channels have been observed for ^{172,177}Hf-isotopes (populated via 2αpxn and αxpn channels) identified from the forward(F)-α-gated spectra, which are shown in Fig.4.14(b). These results imply the absence of feeding to the lowest members of the 'yrast' band, or the population of low spin states are strongly hindered in direct-α-emitting channels (ICF products). Moreover, the increase in yield from highest J_{obs} to J $\approx$10-12$\hbar$, indicates significant feeding even in case of ICF for some initial spin states from the entry side. The spin-distributions for W-isotopes populated via CF and or ICF processes are given in Fig.4.15. The residue ^{177}W (αpxn) has been identified from backward(B)-α-gated spectra and the residues (^{176,177,178}W) produced via αpxn-channels have been identified from forward(F)-α-gated spectra. As can be seen from the figure, the residues, which are identified from forward(F)-α-gated spectra are showing the same trend as has been observed for ICF reaction products, however for αpxn-channel identified from backward(B)-α-gated spectra, the yield is falling exponentially with spin, as has been observed in case of CF products.

As such, it may be inferred that the trends of experimentally measured spin-distributions are likely to reflect the fact that the spin population for ICF reaction products is narrow and peaked at large ℓ-values associated with the large values of impact parameters at a given projectile energy. However, the CF products are found to be originated from the relatively low ℓ-values associated with the small values of impact parameters. The dispute on this point has been discussed by Gerschel[82]. Further, in general, the spin at half yield i.e., the mean value of input angular momenta ($J_\circ$) is found to be $\approx$ 9-10 $\hbar$ for xn-channels, while for direct-αxn and 2αxn-channels (ICF products) the value of $J_\circ$ approaches upto $\approx$ 13 $\hbar$ and $\approx$ 16 $\hbar$, respectively. Again, it is interesting to note that, the value of $J_\circ$ for α-emitting channels (^{178,179}Re isotopes) identified from backward(B)-α-gated spectra is also found to be $\approx$ 9-10 $\hbar$, which indicates involvement of significantly less input angular momenta as compared to ^{178,179}Re-isotopes populated via direct-α-emitting channels ($\approx$13-14 $\hbar$). It may, however, be pointed out (from the

deduced values of $J_\circ$) that the multiplicity of direct-α-particles increases with the driving input angular momenta. The above observation indicates the variation of available ℓ-bins due to different interaction trajectories at a given projectile energy. It may also be inferred that the lower ℓ-values do not contribute to the ICF, significantly, and the smallness of $J_\circ$ indicates the involvement of less input angular momenta in CF reactions as compared to ICF reactions.

4.5.2 Analysis with PACE4:^{16}O+^{169}Tm system

Accuracy and self-consistency of presently measured spin-distributions have been tested by comparing experimental data with the predictions of theoretical model code PACE4. Description of code PACE is already given in Chapter-2, Section-2.4.

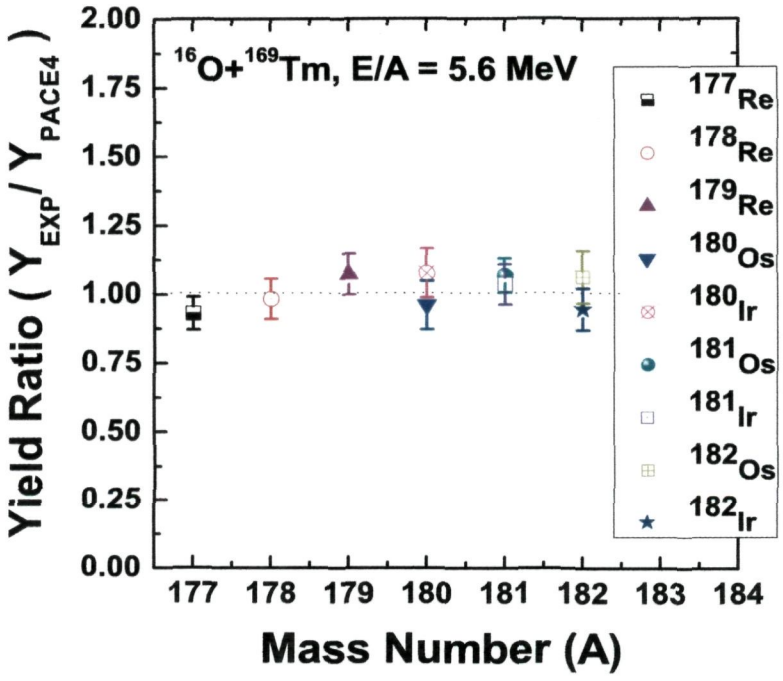

Figure 4.16: The yield ratio Y_{EXP}/Y_{PACE4} of different residues produced only via CF of ^{16}O with ^{169}Tm at projectile energy ≈5.6MeV/nucleon.

As has already been mentioned in this section, this code does not take ICF into consideration, therefore, the relative production yields of CF products populated via xn,αxn,2αxn-channels may be compared. As such, the production yields of CF products have been deduced from experimentally measured spin-distributions of CF reaction products identified from backward particle(Z=1,2) gated spectra and from singles spectra. The experimentally measured yields of CF reaction products have been extrapolated up to J=0$\hbar$, and the yield value at J=0$\hbar$ ($Y^{J=0}$) has been normalized with the total yield (sum of all fusion-evaporation channels) to deduce relative yield value of each reaction product. In the same way, the production yield of individual reaction products, calculated using theoretical model code PACE4, have been normalized with the total yield of fusion-evaporation channels. The ratio of experimentally measured and theoretically calculated relative production yields of different residues populated via CF and/or ICF in ^{16}O+^{169}Tm system at $\approx$ 5.6 MeV/nucleon have been plotted in Fig.4.16. As can be seen from Fig.4.16 that both the experimental data and theoretical predictions agree reasonably well, as the yield ratio (Y_{EXP}/Y_{PACE}) of different ER's is found to be nearly unity within the experimental uncertainties. The above agreement strengthens/gives confidence in the measured spin-distributions.

4.5.3 Feeding intensity profiles:^{16}O+^{169}Tm system

It has already been pointed out from the spin-distributions of different ERs (as shown in Figs.4.13-4.15), the intensity of 'yrast'-line transitions decreases gradually with high spin states for CF. While, in case of ICF the intensity remains almost constant up to a certain limiting spin value and decreases rapidly for transitions of higher spin states, indicating entirely different de-excitation patterns for CF and ICF from entry states to the 'yrast' line. This implies a rather smooth and broad feeding distribution for the 'yrast'-states in case of CF. However, for ICF channels this distribution must have a 'narrow window' meaning thereby a well localized angular momentum region, where a given projectile-like fragment is emitted in contrast to the large ℓ-window than that involved in the fusion reactions. As such, in order to understand the feeding intensity pattern in different reaction channels associated with CF and/or ICF, the feeding intensities of γ-population have been deduced from the experimentally measured spin-distributions of different reaction products. The feeding intensity profiles for different studied reaction channels have been plotted as a function of J_{obs} in Figs.4.17-4.19. As shown in Figs.4.17-4.19, the feeding intensity for αxn and 2αxn-channels identified from forward(F)-α-gated spectra is found to be increasing upto J $\approx$ 14 $\hbar$ and J $\approx$ 17 $\hbar$, respectively from the higher spin states (entry side), indicating that the high spin states are strongly fed even

in case of ICF channels.

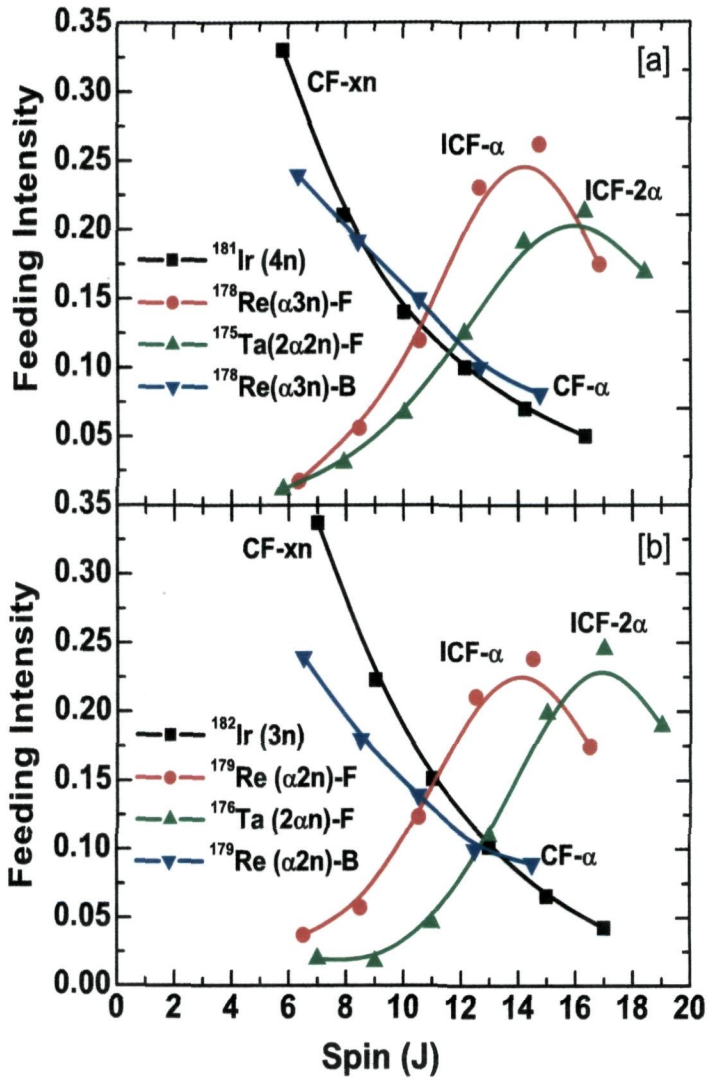

Figure 4.17: Feeding intensities in the 'yrast'-bands of different ER's expected to be produced via; xn, αxn and/or 2αxn channels in ^{16}O+^{169}Tm system at $\approx$ 5.6 MeV/nucleon.

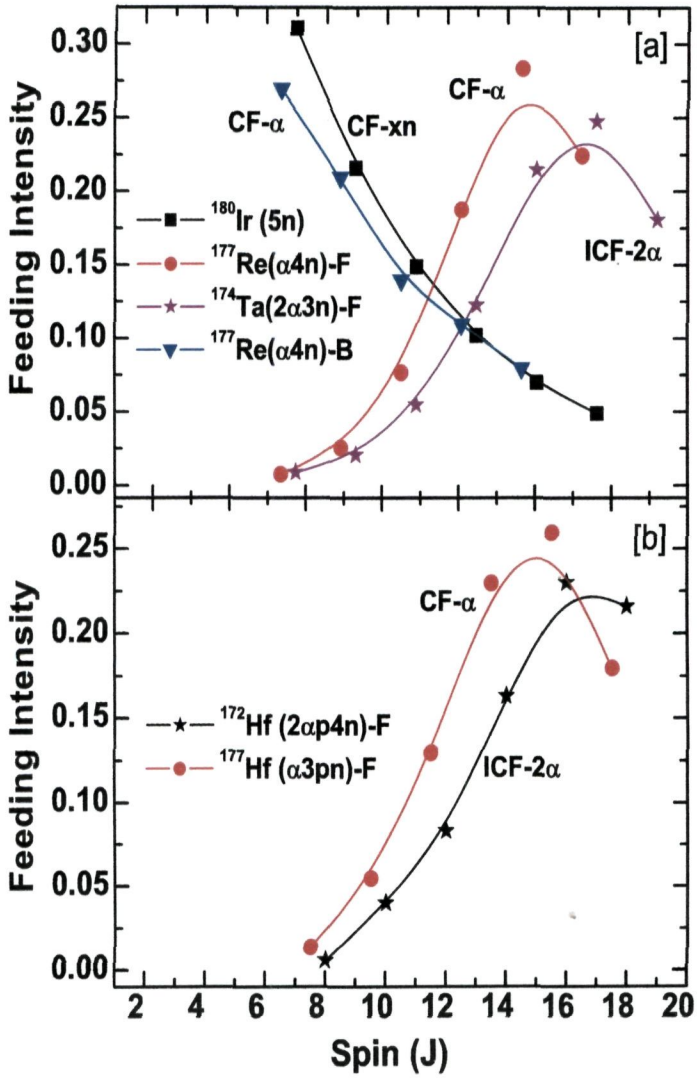

Figure 4.18: Feeding intensities in the 'yrast'-bands of different ER's expected to be produced via; xn, αxn and/or 2αxn channels in ^{16}O+^{169}Tm system at $\approx$ 5.6 MeV/nucleon.

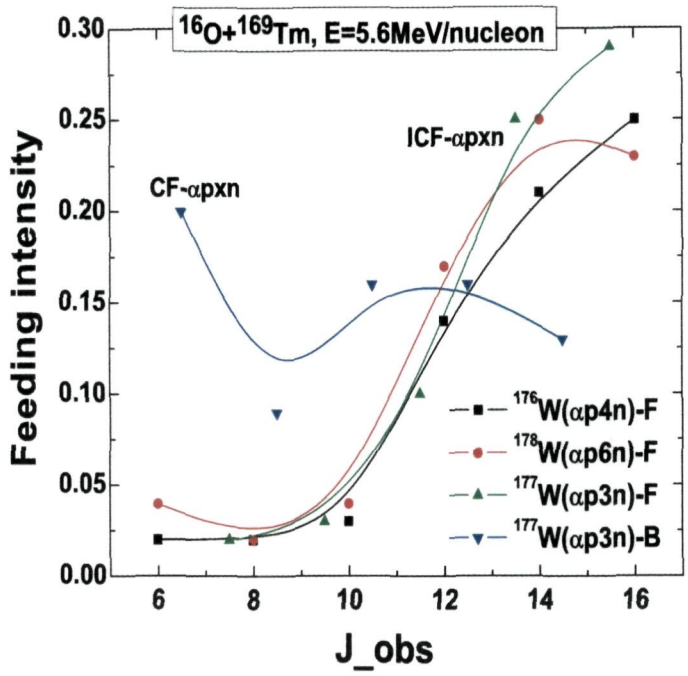

Figure 4.19: Feeding intensities in the 'yrast'-bands for W-isotopes populated via αpxn-channels indicated as CF-αpxn (predominantly CF-channel) and ICF-αpxn (ICF-channels), in $^{16}O+^{169}Tm$ system at $\approx$ 5.6 MeV/nucleon. Lines and curves are drawn to guide the eyes.

However, as J decreases further the feeding intensity also decreases. As such, it may be pointed out that as the residual nucleus de-excites, the feeding intensity decreases gradually with the available excitation energy and/or angular momentum, which indicates the absence of feeding to the lowest members of the 'yrast' band or the low spin states are less populated in αxn and 2αxn-channels identified from forward-α-gated spectra. Such feeding intensity pattern is expected to arise from narrow ℓ-window, localized near and/or above to the critical angular momentum for CF, that is associated with ICF, where a given projectile-like fragment is emitted. Furthermore, as shown in Figs.4.17-4.18, the feeding intensity is showing sharp exponential rise towards low spin states for all xn-channels (CF), indicating strong feeding. Apart from that, for better comparison

of forward and backward α-channels populated via ICF and CF, respectively, the feeding intensity profiles for backward(B)-α-channels alongwith forward(F)-α-channels have also been plotted in Figs.4.17-4.19. As can be seen from these figure, the feeding intensity of αxn-channels identified from backward(B)-α-gated spectra shows exponential rise towards lower spin states, as expected for CF channels, where the band is fed over a broad spin range. Further, the feeding intensity profiles for W-isotopes populated via αpxn-channels indicated as CF-αpxn (predominantly CF-channel) and ICF-αpxn (ICF-channels) are given in Fig.4.19. As can be seen from this figure, feeding intensity for ^{177}W (αp3n) identified from backward-α-gated spectra (CF product) is found to increase toward band head as expected in case of CF products. However, the feeding intensity for ^{176,177,178}W (αpxn) identified from forward-α-gated spectra (ICF products), in general, is found to be increasing with spin up to some extent and then found to decrease with low spin states, as has been observed in case of ICF reaction products. Moreover, it may, further, be pointed out that the feeding intensity is found to be less in the production of ^{177,178,179}Re isotopes identified from backward-α-gated γ-spectra, as compared to xn-channels. This difference may be because of the fact that the neutron emission carry almost negligible angular momentum from CN, however, emission of an α-particle from CN takes away significant amount of angular momentum and excitation energy, which may not provide broad feeding range towards the band head. As such, it can be inferred that the trends of feeding intensity profiles suggest that the α-emitting channels identified from forward-α-gated spectra particles are produced via ICF, however, those detected at backward cone are mainly from CF, which are expected to produce an isotropic α distribution in the center-of-mass.

4.5.4 Remarks on associated ℓ-values: ^{16}O+^{169}Tm system

In order to get an idea of driving input angular momenta involved in the production of various reaction channels, mean input angular momenta have been plotted as a function of reaction channels in Fig.4.20. Data presented in the Fig.4.20 have been obtained from the best fitting procedure of spin-distributions. It can be observed from this figure that the value of mean input angular momenta for xn, αxn and 2αxn-channels are $\approx 10\hbar$, $\approx 13\hbar$ and $\approx 16\hbar$, respectively. As such, an approximate but quite useful essence which emerged from these measurements about how the driving input angular momenta (ℓ) increases with the direct-α multiplicity, can be represented as follows;

- The mean input angular momenta associated with αxn-channel identified from forward-α-gated spectra (CPDA-alpha-forward) is found to be 1.3 times than that observed for xn/αxn-channel identified from backward-α-gated spectra (CPDA-alpha-backward) and/or singles spectra, and may be represented as;

$\ell_{ICF-\alpha xn} \approx 1.3\ \ell_{CF-xn/\alpha xn}$

- Similarly, the mean input angular momenta associated with 2αxn-channel identified from forward-α-gated spectra (CPDA-alpha-forward) is found to be 1.6 times than that observed for xn/αxn-channel identified from backward-α-gated spectra (CPDA-alpha-backward) and/or singles spectra, and may be represented as;

$\ell_{ICF-2\alpha xn} \approx 1.23\ \ell_{ICF-\alpha xn} \approx 1.6\ \ell_{CF-xn/\alpha xn}$

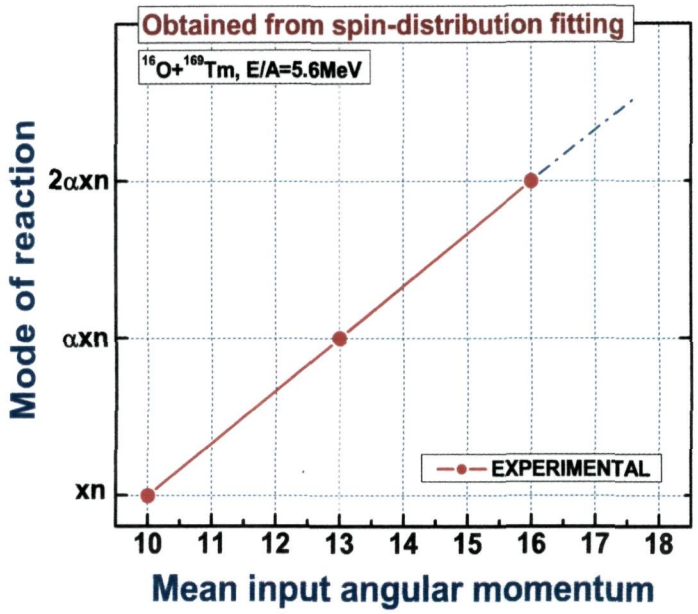

Figure 4.20: A typical plot to show the dependence of reaction mode on mean input angular momentum.

It may, further, be pointed out that the multiplicity of direct-α-particles in forward cone (ICF-α) increases with J_o, indicates the variation of ℓ-values (impact parameter dependent) even at energy as low as 5.6 MeV/nucleon. As such, on the basis of aforementioned description, it may be quite safely inferred that the CF predominantly occurs at lowest driving input angular momenta values. However, ICF occurs in the peripheral interactions (at finite values of impact parameters) at large input angular momenta, which have been found to be increasing with decreasing fused mass from projectile to target nucleus.

4.6 Results and interpretation: $^{12}C+^{169}Tm$ system

In Section-4.5 of this Chapter, it has been demonstrated that the ICF processes generally occur at large driving input angular momenta, as compared to that involved in CF processes, which is assumed to be imparted into the system due to the availability of high ℓ-values at different interaction trajectories. An approximate but quite useful information about the driving input angular momenta associated with CF and/or ICF processes have also been deduced from the experimentally measured spin-distributions. It has been observed that as the angular momenta imparted into the system increases, the fused mass from projectile to target nucleus decreases. The measurements presented in the earlier section have been performed for $^{16}O+^{169}Tm$ system at 5.6 MeV/nucleon, which provided significant understanding of ICF reaction dynamics within the framework of driving input angular momenta. It may, further, be pointed out that the energy dependence of driving input angular momenta could not be understood from the measurements presented in the earlier section. As such, keeping in view the outcome of $^{16}O+^{169}Tm$ data, as motivation, to explore the behavior of spin-distributions associated with different CF and/or ICF-channels a complementary experiment has been performed for $^{12}C+^{169}Tm$ system within the energy range $\approx$4-7 MeV/nucleon, using similar experimental technique. In this experiment, variation of input angular momenta involved in the production of CF and ICF residues have been investigated at different projectile energies. The ^{12}C has been chosen as a projectile, so that residues produced via direct-α-emitting channels in $^{16}O+^{169}Tm$ system will be similar to those produced via pure neutron(n)-emitting channels in $^{12}C+^{169}Tm$ system, and also to understand the entrance channel dependence of spin state population at the same projectile energy i.e., 5.6 MeV/nucleon. In the present work, experimental data obtained for $^{16}O+^{169}Tm$ and $^{12}C+^{169}Tm$ systems at the same projectile energy i.e., $\approx$ 5.6 MeV/nucleon have also been compared. The data reduction procedure and analysis are similar to that adopted for $^{16}O+^{169}Tm$ system in the earlier section. The results and interpretation of experimental data obtained for $^{12}C+^{169}Tm$ system at different projectile energies are given in the following subsections.

4.6.1 Spin-distributions: $^{12}C+^{169}Tm$ system

It has already been mentioned that the variation of driving input angular momenta involved in CF and/or ICF products at different projectile energies can be studied by the measurement and analysis of spin-distributions. Therefore, spin-distributions of various CF and/or ICF products in $^{12}C+^{169}Tm$ system have been obtained in the similar way as demonstrated in earlier section. It may, further, be pointed out that the spin-distributions of different ERs have been obtained using some systematics, viz; the experimentally

measured yields of a particular reaction product at different projectile energies have been plotted as a function of observed spin (J_{obs}). In order to plot full studied energy range (i.e., ≈57-90 MeV) in a panel, experimentally measured yields have been normalized with its own maximum value (Y^{max}) at minimum observed spin (J_{obs}^{min}). For better analytical representation of data and to achieve the qualitative information about mean value of driving input angular momenta involved in various reaction channels, normalized data points have been fitted with a function as given in earlier section (and in ref.[23]). The experimentally measured spin-distributions of ^{175,176,177,178}Re, ^{176,177}W, ^{174,175}Ta, and ^{172}Hf isotopes populated via CF and/or ICF are given in Figs.4.21-4.26. The Figs.4.21 and 4.22 show the spin-distributions of Re-isotopes (^{175,176,177,178}Re) produced after emission of 6n,5n,4n and 3n, respectively, from the excited composite nucleus ^{181}Re* formed via CF. Since, these reaction products have been populated via successive neutron decay (xn-channels, where; x=3,4,5 and 6) from excited composite nucleus ^{181}Re*, therefore, the identification of these reaction products have been made by looking into the singles spectra collected without employing any hard or soft gate. The identification of these reaction products have also been confirmed from the decay-γ-lines at different projectile energies by looking into the decay spectra recorded for each projectile energy after the irradiation. As can be seen from the Figs.4.21 and 4.22, the yield values at different projectile energies are found to increase towards band head, which indicates continuous population of spin states over a broad spin range. The above trend (increase in yield towards band head) of spin-distributions may be the indication of strong feeding to the low spin states, as has already been observed for CF reaction products produced in ^{16}O+^{169}Tm.

Further, the spin-distribution for ^{176,177}W-isotopes populated via emission of p4n and p3n from the excited composite nucleus ^{181}Re*, respectively, are shown in Figs.4.23(a-b). These reaction products (^{176,177}W-isotopes) have been identified from the backward(B)-proton-gated spectra, obtained by subtracting backward (B)-α-gated spectra from backward (B)-particle(Z=1,2)-gated spectra. As shown in Figs.4.23(a-b), the spin- distribution of ^{176,177}W-isotopes show the similar trend as that observed in case of Re-isotopes identified from singles spectra, indicating the involvement of same reaction process in the production of these residues. The observed trend of spin-distribution clearly indicates the broad spin- population during de-excitation, where γ-transitions of these reaction products are expected to be strongly fed over a broad spin range. Moreover, as can be observed from the spin-distributions of Re and W-isotopes (Figs.4.21-4.23), that the highest observed spin (J_{obs}^{max}) in case of ^{175}Re-isotope (as a representative case) is found to be J = 18 $\hbar$ at energies within the range ≈84-90 MeV. while, at relatively low bombarding energies i.e., ≈72-78 MeV, it is only approaching upto J_{obs}^{max} = 16 $\hbar$. Similar systematics can be seen in other Re and W-isotopes (Figs.4.21-4.23). As such, on the

basis of above observation, it can be inferred that the probability of high spin state population increases with projectile energy.

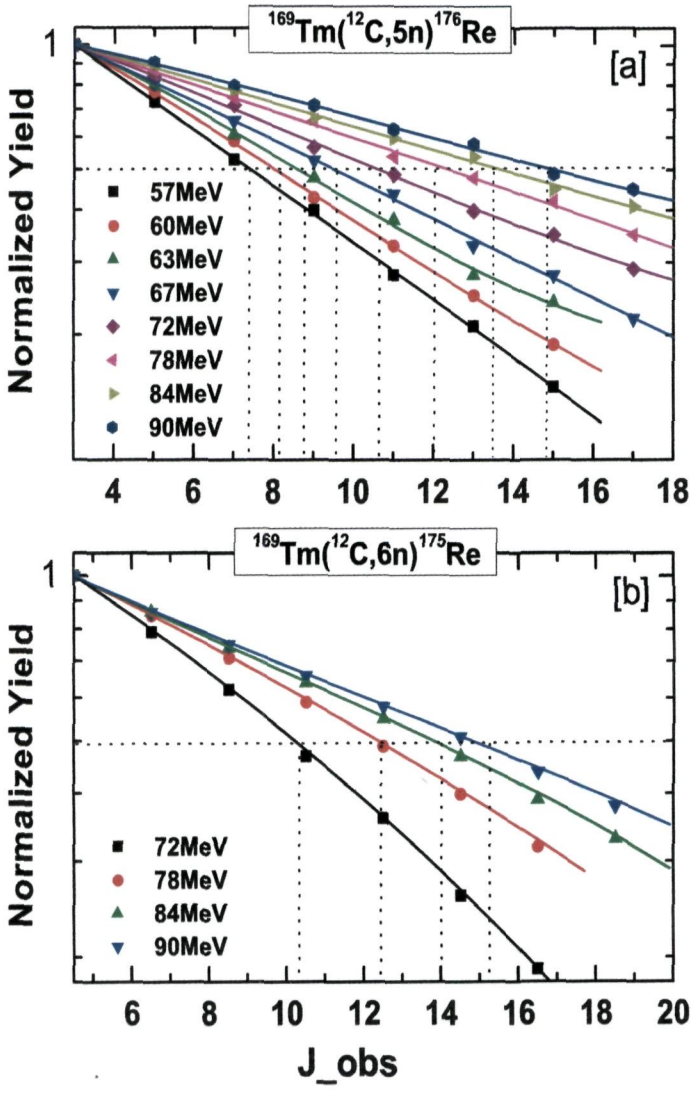

Figure 4.21: Spin-distributions for (*a*) ^{176}Re (5n), and (*b*) ^{175}Re (6n) ERs produced via CF. Lines are drawn to the best fit of data points as mentioned in text.

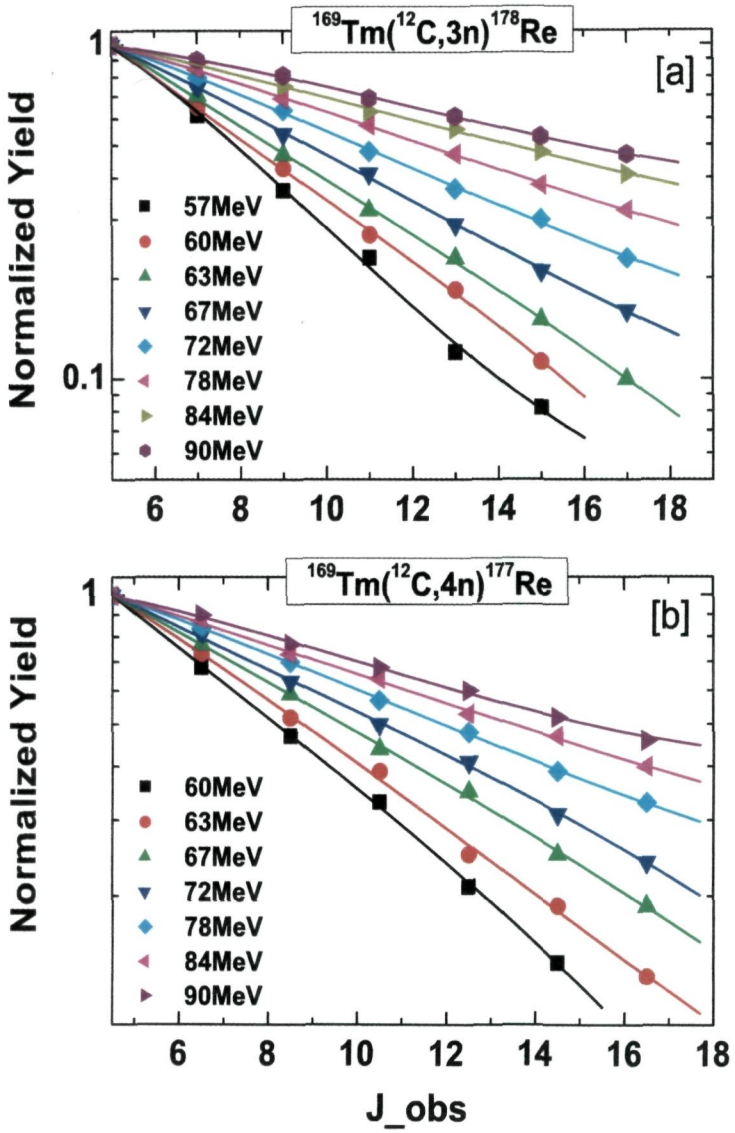

Figure 4.22: Experimentally measured spin-distributions for (*a*) ^{178}Re (3n), and (*b*) ^{177}Re (4n) ERs produced via CF in ^{12}C+^{169}Tm system at projectile energy ≈4-7MeV/nucleon.

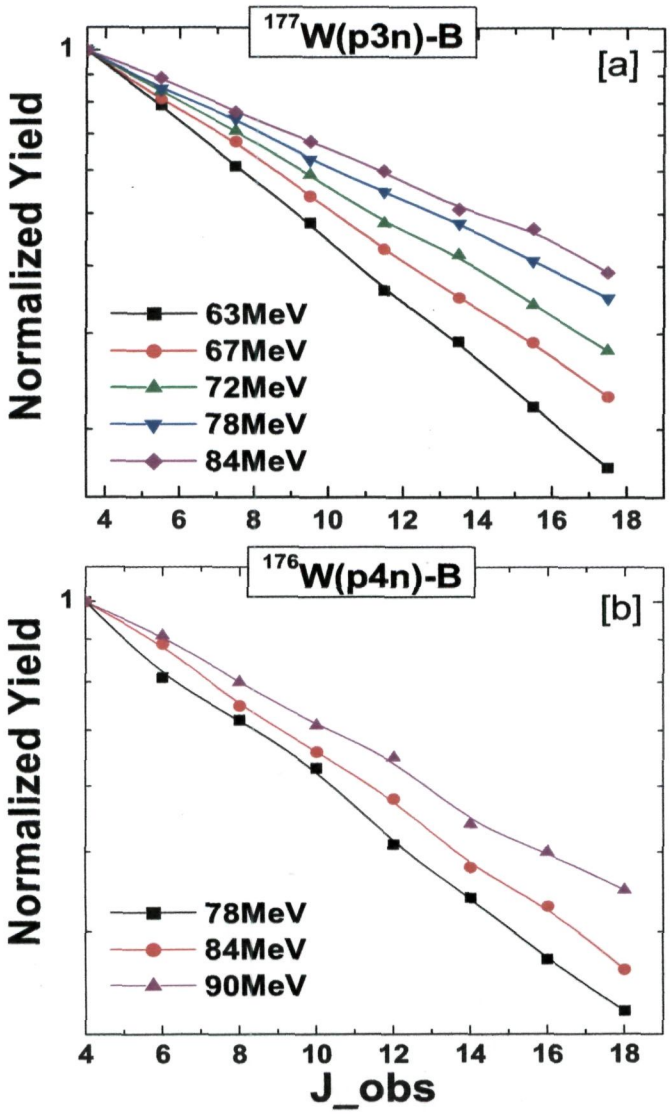

Figure 4.23: Experimentally measured spin-distributions for (*a*) ^{176}W (p4n), and (*b*) ^{177}W (p3n) ERs identified from Backward(B)-particle-gated spectra.

However, as more energy is provided to the system, the population of high spin states somewhat saturates at $\approx$ 18 $\hbar$ even at highest studied energy. The saturation in the

population of high spin states indicates the hindrance of high spin states population due to onset of other reaction modes at relatively higher projectile energies or at high input angular momenta. It can be inferred that at relatively higher projectile energies, the increased input angular momenta imparted into the system may be subdivided into other reaction channels, where less mass and charge of projectile is expected to fuse with target nucleus to provide sustainable input angular momenta.

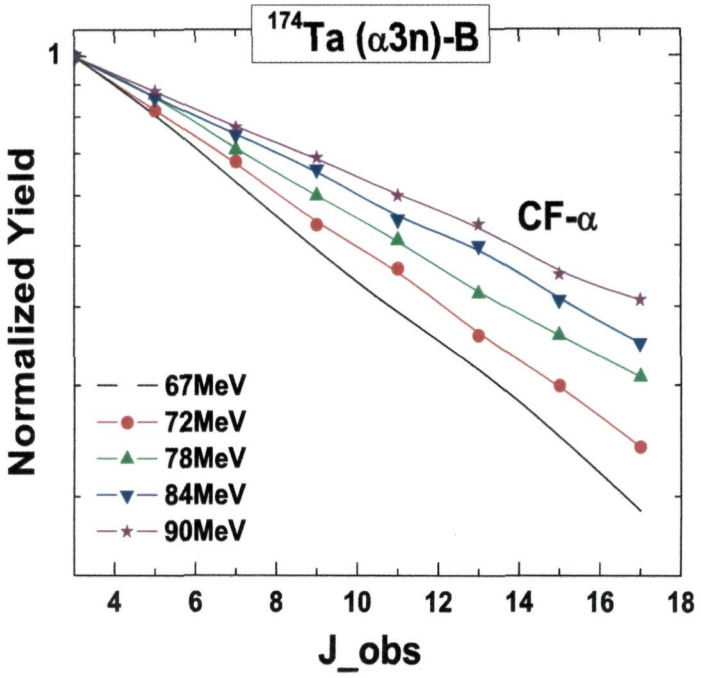

Figure 4.24: Experimentally measured spin-distributions for ^{174}Ta (α3n) identified from Backward(B)-α-gated spectra.

Furthermore, in order to compare α-emitting channels identified at backward (predominatly populated via CF) and forward (ICF products) cones, the spin- distributions of different α-emitting channels have been measured. The spin-distribution of ^{174}Ta (α3n) identified from Backward(B)-α-gated spectra is given in Fig.4.24. As can be seen from this figure, the yield is showing exponential rise towards the band head, which is similar to the non-α-emitting CF products, i.e., similar to xn-channels. As such, the

reaction product ^{174}Ta identified from backward(B)-α-gated spectra, is expected to be populated only via CF. It may, further, be pointed out on the basis of above observations (Figs.4.21-4.24), that the slope of spin-distributions is found to decrease for higher projectile energies, which indicates large probability of high spin states population. However, at lowest measured energy the large value of slope indicates less probability of high spin states population. In order to get energy dependence, and qualitative information of driving input angular momenta, the spin-distributions at different energies have been plotted in a panel (Figs.4.21-4.24). In general, the values of mean input angular momenta ($J_\circ$, obtained from the best fitting procedure of experimentally measured spin-distributions) associated with the production of Re-isotopes (Figs.4.21-4.22) are found to be $\approx$ 7,8,9,10,12,13,14 and 15 $\hbar$, respectively at energies $\approx$ 57,60,63,67,72,78,84 and 90 MeV. However, as indicated in Figs.4.23 and 4.24, the values of mean input angular momenta ($J_\circ$) are found to be almost similar in case of W-isotopes (populated via pxn-channels and identified from backward-proton-gated spectra) and ^{174}Ta (populated via αxn-channels and identified from backward-α-gated spectra) at respective projectile energies as that observed for Re-isotopes, which indicates the production of these reaction products via same reaction dynamics i.e., CF.

Apart from CF channels identified from backward(B)-α-gated and singles spectra, some ICF channels (^{174,175}Ta and ^{172}Hf) have also been identified from forward(F)-α-gated spectra and are shown in Figs.4.25-4.26. These residues are identified from forward(F)-α-gated spectra, where the prompt-γ-lines of only ICF products are expected to be recorded. As shown in Figs.4.25 and Figs.4.26, the spin-distributions for both Ta and Hf-isotopes are found to be distinctly different than that observed for fusion evaporation channels given in Figs.4.21-4.24, where a monotonic increase in the yield has been observed towards the band head. However, in case of α-emitting channels (^{174,175}Ta and ^{172}Hf) shown in Figs.4.25-4.26, the yields at different projectile energies show sharp exponential rise from entry side to a certain value of J_{obs} towards the band head. This exponential rise in the normalized yield may be the indication of continuous spin state population or may be because of the feeding from unknown and/or known yrast-line transitions. It may, further, be pointed out that the normalized yield appears to be almost constant upto a certain limiting value of J_{obs}. The limiting value where the yield is showing constant behaviour is found to increase with projectile energy. Here, the values of normalized yield are found to be constant up to J$\approx$ 8,9,10,11,12 and 13 $\hbar$ for α-emitting channels, respectively at projectile energies $\approx$ 63,67,72,78,84 and 90 MeV. This constant behaviour of normalized yield with J_{obs} may be because of the fact that the population of low spin states is strongly hindered in case of direct-α-emitting channels, as expected in case of ICF processes. It may, further, be pointed out that the highest J_{obs} in case of α-emitting channels identified from forward(F)-α-gated spectra

is found to be higher at a particular projectile energy than that observed for CF.

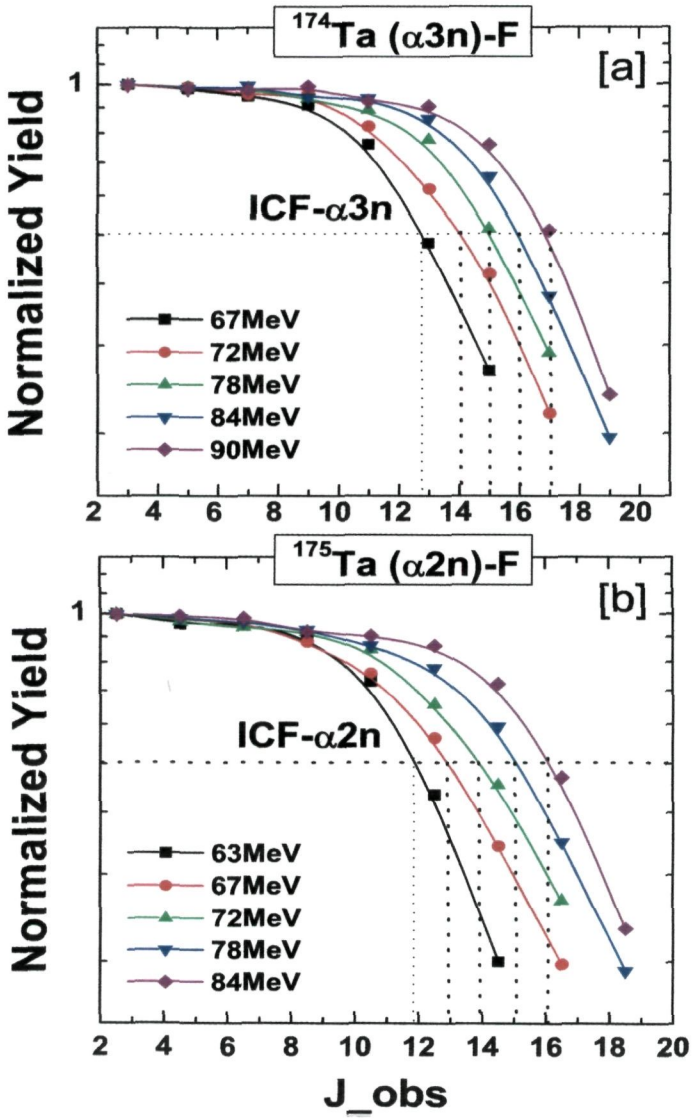

Figure 4.25: Experimentally measured spin-distributions for (a) ^{174}Ta (α3n), and (b) ^{175}Ta (α2n), ERs identified from Forward(F)-α-gated spectra.

As indicated in Figs.4.25-4.26, the highest observed spin increases with projectile energy, which shows the dependence of spin-population on projectile energy, as expected. Further, as has already been pointed out in the earlier section that the fast-α-emitting channels associated with ICF are expected to be originated from the relatively higher ℓ-values. The same can be observed from Figs.4.25-4.26, for α-emitting channels, as the value of $J_\circ$ (mean input angular momenta obtained from the best fitting procedure of experimentally measured spin-distributions) associated with the production of ^{174,175}Ta and ^{172}Hf isotopes are found to be $\approx$ 12,13,14,15,16 and 17 $\hbar$, respectively at energies $\approx$ 63,67,72,78,84 and 90 MeV. It may, however, be pointed out that the mean input angular momenta (at a particular projectile energy) obtained from the spin-distributions of direct-α-emitting channels identified from forward(F)-α-gated spectra are found to be almost 4 $\hbar$ higher than that observed for xn/pxn/αxn-channels identified from backward-α-gated spectra. The above stricking observation clearly indicates the involvement of high input angular momenta in case of direct-α-emitting channels (associated with ICF) as compared to the CF channels. In case of direct-α-emitting channels, the observation of slightly higher angular momenta imparted into the system may be due to the peripheral interactions, as expected for ICF processes.

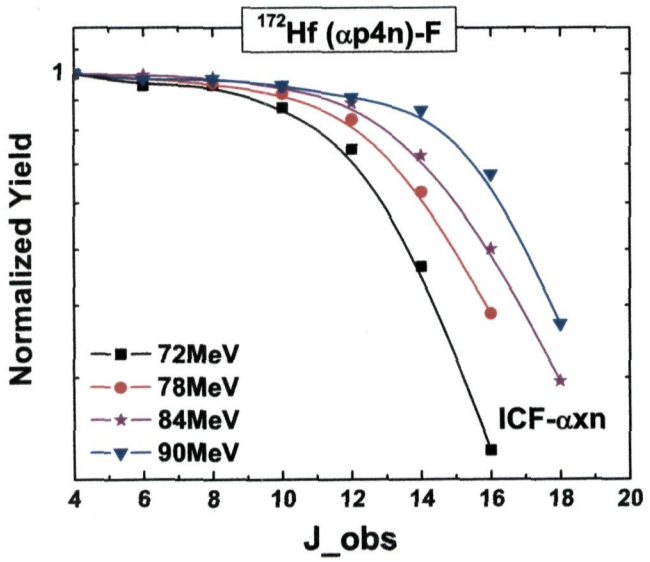

Figure 4.26: Experimentally measured spin-distributions for ^{172}Hf (αp4n), identified from Forward(F)-α-gated spectra.

4.6.2 Analysis with PACE4:^{12}C+^{169}Tm system

In order to check the accuracy of data reduction procedure and for self-consistency of presently measured spin-distributions, experimentally measured relative EFs for different CF products produced in ^{12}C+^{169}Tm system within the energy range ≈4-7MeV/nucleon have been compared with the predictions of PACE4. It may be pointed out that the code PACE4 does not take ICF into consideration, therefore, the relative production yields of CF products (xn,αxn,2αxn) can only be compared. In order to plot EFs, the production yields have been deduced from the experimentally measured spin-distributions of different reaction products identified from backward particle(Z=1,2) gated spectra and from singles spectra. The experimentally measured yields of CF reaction products have been extrapolated up to J=0$\hbar$, and the yield value at J=0$\hbar$ ($Y^{J=0}$) has been normalized with the total yield (sum of all fusion-evaporation channels) to deduce relative yield value of each reaction product.

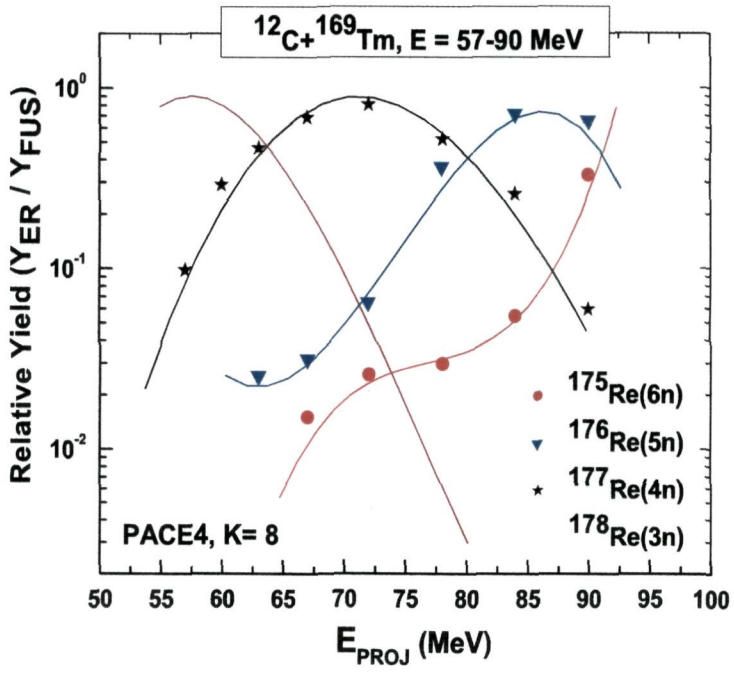

Figure 4.27: Relative EFs of different xn-channels produced via CF in ^{12}C+^{169}Tm system

The ratio of experimentally measured and theoretically calculated relative production yields of different residues populated via CF and/or ICF in $^{12}C+^{169}Tm$ system within the energy range $\approx$ 4-7 MeV/nucleon have been plotted as a function of projectile energy. The relative EFs of different xn-channels are shown in Fig.4.27, while the relative EFs of pxn/αxn-channels are plotted in Fig.4.28, where lines and/or curves indicate the polynomial fitting to the PACE4 predictions.

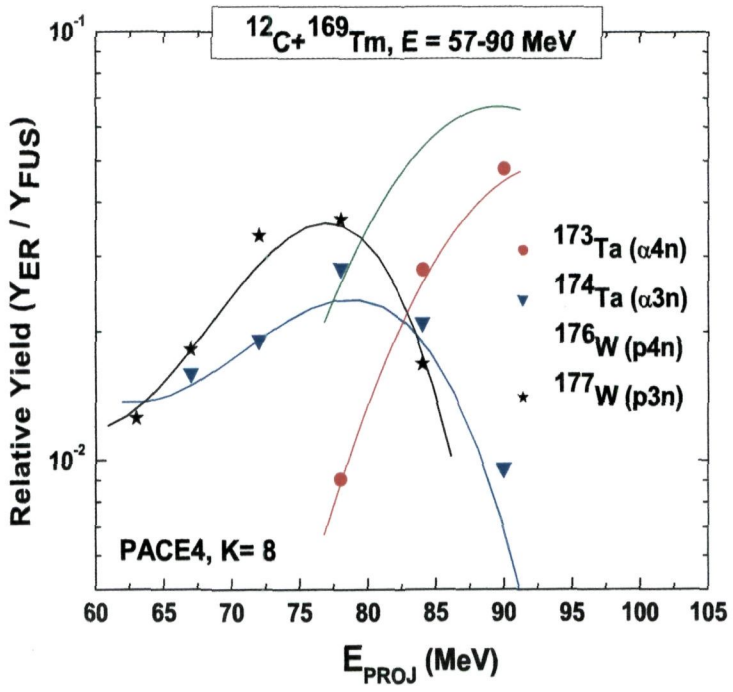

Figure 4.28: Relative EFs of different pxn/αxn-channels produced via CF in $^{12}C+^{169}Tm$ system.

As can be seen from the Figs.4.27 and 4.28 that both the experimental data and theoretical predictions agree reasonably well. It may, further, be pointed out that the most suitable set of parameters have been used in the present calculations. Different values of level density parameter, which is an important parameter in this code, have been tested. In the present work, a value of $K = 8$ is found to give a satisfactory reproduction of experimental data for CF-channels. The above agreement of theoretical EFs with the

experimental ones strengthens/gives confidence in the measured spin-distributions.

4.6.3 Feeding intensity:^{12}C+^{169}Tm system

It has been understood from the measurement of spin-distributions that the CF products are strongly fed over the broad spin range, however, population of low spin states are strongly hindered or γ-transitions are less fed in case of the reaction products formed via ICF. Further, in order to have better insight into the feeding pattern of differeent reaction products at a given projectile energy, feeding intensity profiles of different reaction products produced via CF and/or ICF in ^{12}C+^{169}Tm system at ≈4-7 MeV/nucleon have been generated from their experimentally measured spin-distributions. In order to figure out the effect of projectile energy on the strength of feeding, the feeding intensity profiles of various reaction products obtained at different projectile energies have been compared in a panel. The feeding intensity profiles have been obtained in the similar way as given in the section-4.5.2, and are plotted in Figs.4.29-4.34. Feeding intensity profiles of ^{175,176,177,178}Re-isotopes populated via xn-channels are shown in Figs.4.29 and 4.30. As can be seen from these figures, the feeding intensity for all of xn-channels, in general, increases towards the band head, as has been observed for the CF products in ^{16}O+^{169}Tm system also. It has already been pointed out that the observed trends of feeding intensity profiles indicate the significant feeding from the side bands and/or from the unidentified bands towards the band head during the de-excitation of excited composite nucleus. The observed trend of feeding intensity profiles may be because of the strong feeding over the broad spin range. It may, further, be pointed out that the observed feeding intensity profiles may also be the indication of the population of low spin states with finite intensity, which fairly support the measurements presented in earlier section for ^{16}O+^{169}Tm system at $\approx 5.6 MeV/nucleon$.

Further, the feeding intensity profiles for ^{176,177}W-isotopes populated via $p4n$ and $p3n$-channels, respectively are given in Figs.4.31. As shown in these figures, the feeding intensity increases towards the band head, in general, similar to that of Re-isotopes (CF products), which shows rather broad spin population. It may be pointed out that, though the feeding intensity increases, in general, towards the band head, however, the observed fluctuations may arise due to the variation of direct and/or side-feeding values at different energies. The above variation becomes dominant at relatively higher energies, as expected. Moreover, in order to disentangle the feeding intensity profiles of xn and αxn-channels, feeding intensity profile of ^{174}Ta formed via emission of α3n, identified from backward(B)-α-gated spectra, from excited composite nucleus ^{181}Re* is given in Fig.4.32. As can be seen from Fig.4.32 that the feeding intensity profile is showing the same characteristics as that expected for CF product. The production of

this product via CF is also supported with the fact that this reaction product (^{174}Ta) has been identified from the backward(B)-α-gated spectra.

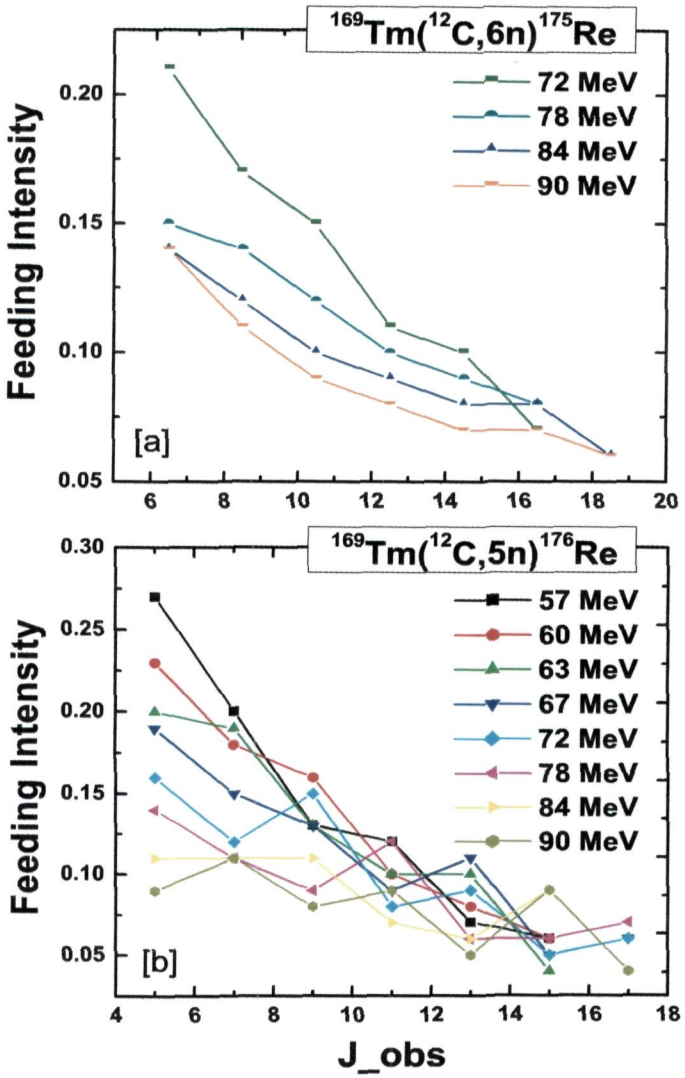

Figure 4.29: Experimentally observed feeding intensity profiles for the production of (a) ^{175}Re, and (b) ^{176}Re isotopes in ^{12}C+^{169}Tm system at energies 4-7MeV/nucleon. Lines and curves are drawn to guide the eye.

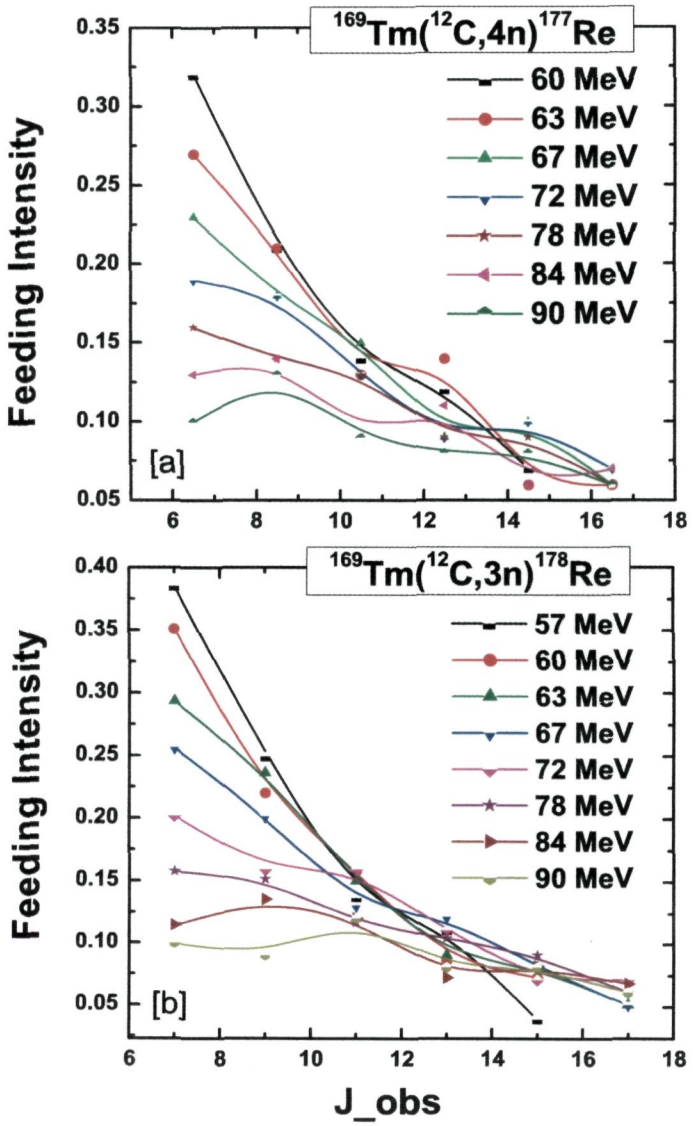

Figure 4.30: Experimentally observed feeding intensity profiles for the production of (a) ^{177}Re, and (b) ^{178}Re isotopes in ^{12}C+^{169}Tm system at energies 4-7MeV/nucleon.

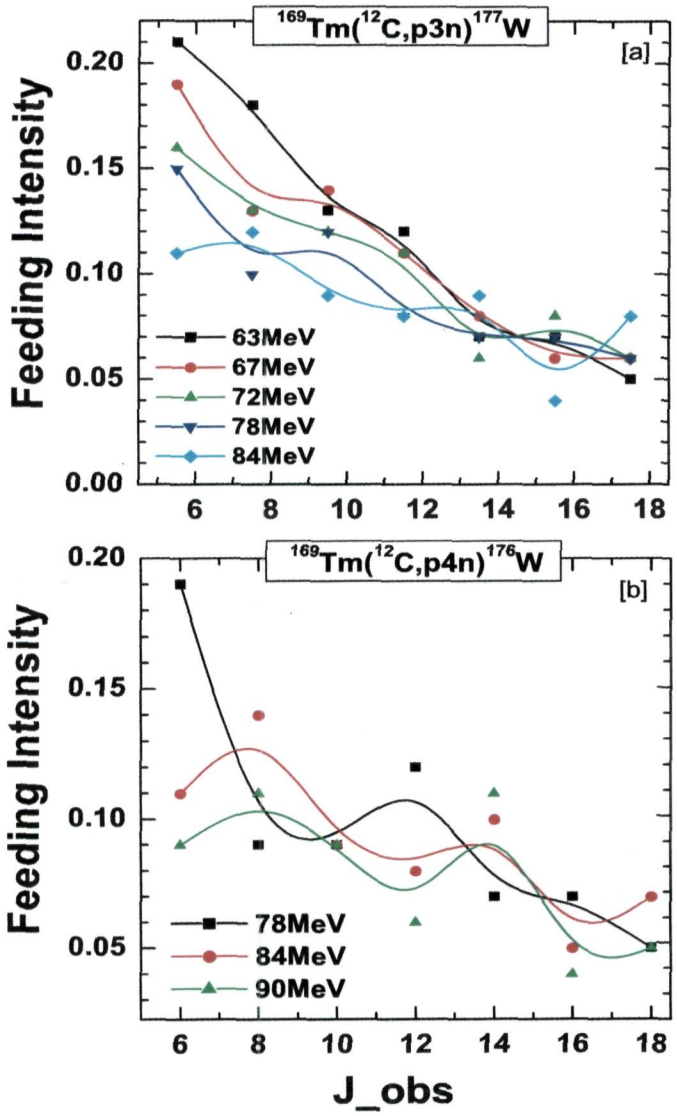

Figure 4.31: Experimentally observed feeding intensity profiles for the production of (*a*) ^{176}W (p4n), and (*b*) ^{177}W (p3n) in ^{12}C+^{169}Tm system at projectile energy ≈4-7MeV/nucleon.

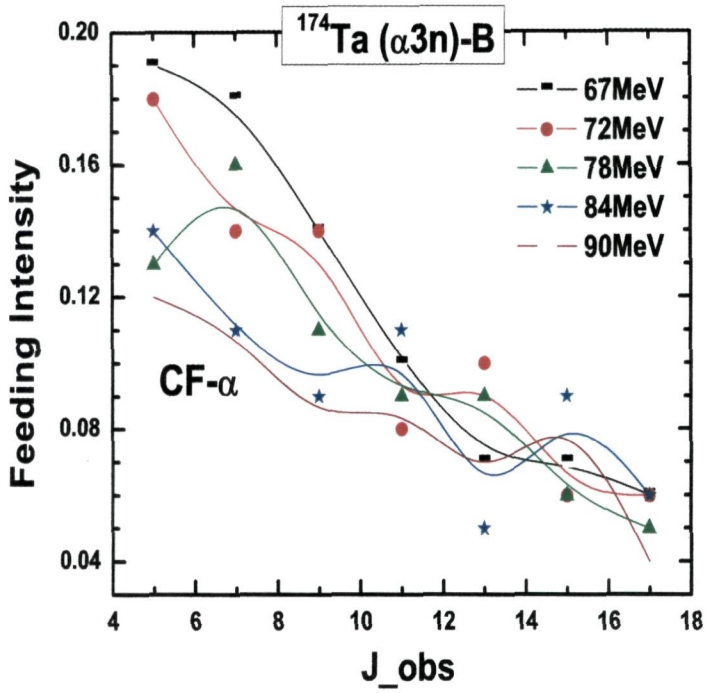

Figure 4.32: Experimentally observed feeding intensity profile for the production of ^{174}Ta (α3n), identified from backward(B)-α-gated spectra.

Further, the feeding intensity profiles for ^{174,175}Ta-isotopes populated via α3n and α2n-channels are shown in Figs.4.33(a-b), respectively. These reaction products have been identified from the Forward(F)-α-gated spectra, and hence, are named as direct-α-emitting channels. As can be seen from these figures that the feeding intensity increases from entry side towards the band head upto a limiting value, and then, in general decreases toward band head. This trend shows narrow spin population associated to ICF reactions. It may, further, be pointed out that the feeding intensity profiles for ^{172}Hf (Fig.4.34), identified from Forward(F)-α-gated spectra are also found to be qualitatively same as that observed for ^{174,175}Ta-isotopes (direct-α-emitting channels). The observed striking difference in the feeding intensity profiles, of CF and/or ICF residues, shows

involvement of entirely different reaction mechanisms in the production of these residues.

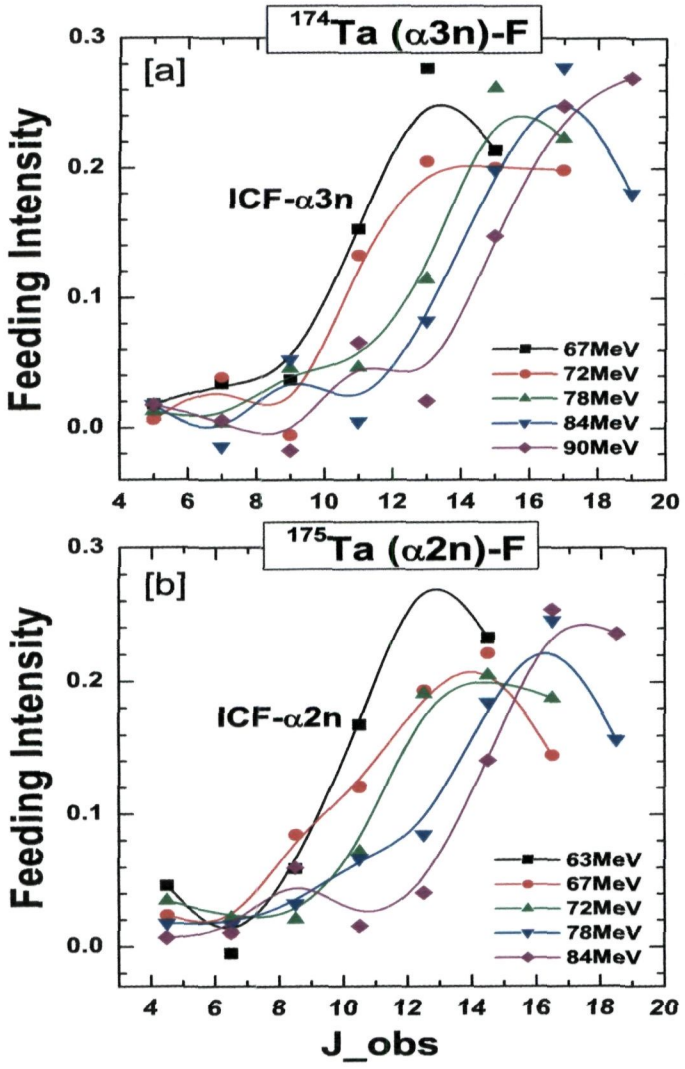

Figure 4.33: Experimentally observed feeding intensity profiles for the production of (*a*) ^{174}Ta(α3n), and (*b*) ^{175}Ta(α2n) identified from Forward(F)-α-gated spectra.

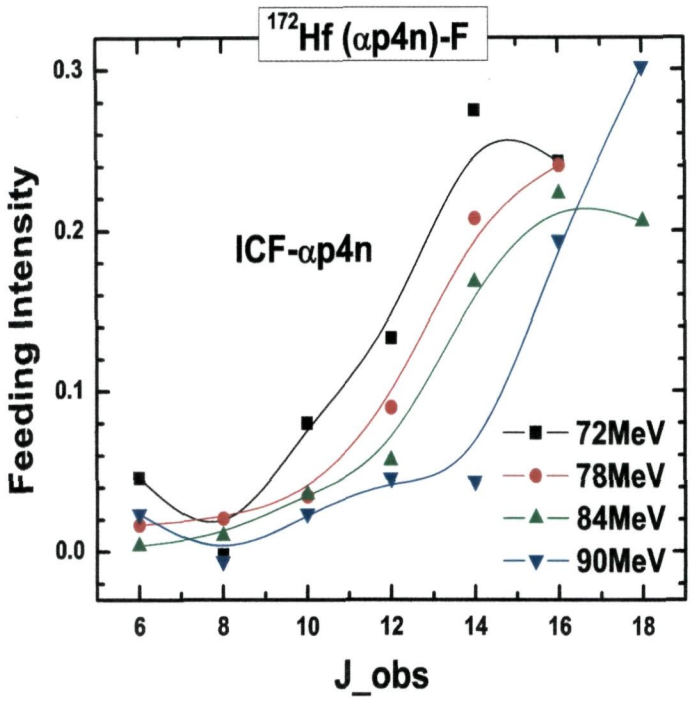

Figure 4.34: Experimentally observed feeding intensity profile of ^{172}Hf produced via αp4n, identified from Forward(F)-α-gated spectra, at various incident energies.

4.6.4 Remarks on associated ℓ-values:^{12}C+^{169}Tm system

In order to have better picture of projectile energy dependence on mean input angular momenta, the value of mean input angular momenta involved in various reaction channels have been obtained from the best fitting procedure of experimentally measured spin-distributions. Deduced values of mean input angular momenta for xn,pxn and αxn-channels produced via both CF and/or ICF have been plotted as a function of projectile energy in Fig.4.35. As shown in this figure, in general, the mean input angular momenta is found to increase almost linearly with projectile energy. In particular, the values of mean input angular momenta involved in the production of Re(xn-channels), W(pxn-channels) and Ta(αxn-channels, identified from backward(B)-α-gated spectra) isotopes are found to be $\approx$ 7 $\hbar$ at lowest projectile energy i.e., $\approx$57 MeV. However, as the

projectile energy increases, the value of mean input angular momenta approaches upto $\approx$15 $\hbar$ at $\approx$90MeV. Further, the mean input angular momenta increases linearly with projectile energy, and is found to be almost same (within $\leq$1 $\hbar$) for all CF-channels [Re(xn-channels), W(pxn-channels) and Ta(αxn-channels)] at a given projectile energy.

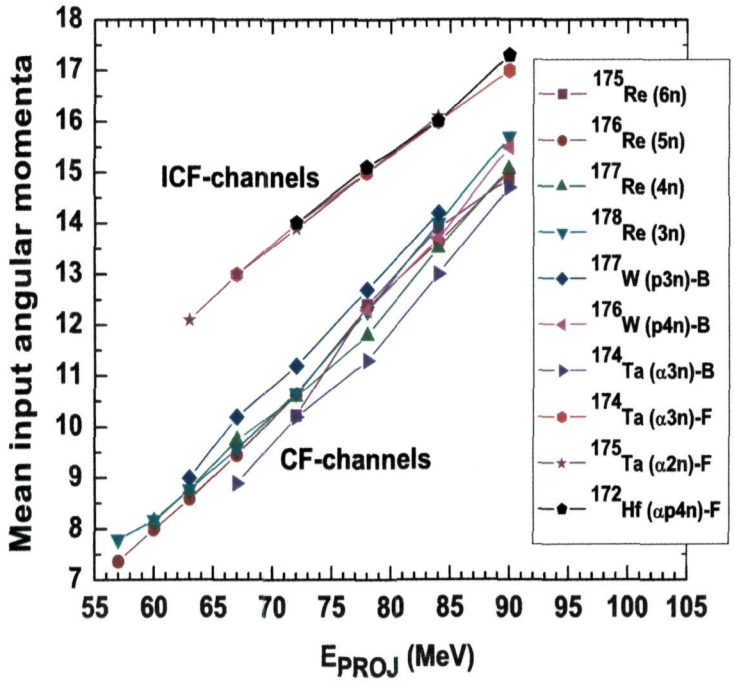

Figure 4.35: Experimentally measured mean input angular momentum associated with the production of various isotopes in ^{12}C+^{169}Tm system at energies 4-7MeV/nucleon. The nomenclature used in the plots indicate the involved reaction dynamics, where F and B represent the reaction products identified respectively from Forward and Backward α-gated spectra. The lines and curves through data points are drawn just to guide the eyes.

It may, further, be pointed out that the observation of nearly similar mean input angular momenta in case of Re-isotopes (populated via neutron emission channels) at studied energies shows that the neutron emission from excited nucleus does not depend strongly on involved angular momenta, and it seems to depend on the available excitation

energy of the composite nucleus. In order to have better comparison of mean input angular momenta involved in CF/ICF-channels, the values obtained for different α-emitting channels in forward cone (ICF products) have also been plotted in Fig.4.35. As can be seen from this figure, the values of mean input angular momenta for ICF-channels are found to be higher by 3 to 4 $\hbar$ in comparison to the CF-channels at the respective energies. This observation indicates the variation of ℓ-values with the mode of reaction, which strongly supports the systematics presented in the earlier section. As such, on the basis of aforementioned description, it may be inferred that the ICF occurs in the peripheral interactions (at finite values of impact parameter or with relatively higher ℓ-values) at a particular projectile energy.

4.7 Summary

Spin-distributions and feeding intensity profiles of various reaction products populated via CF and/or ICF in ^{16}O+^{169}Tm system at $\approx$ 5.6 MeV/nucleon, and ^{12}C+^{169}Tm system at $\approx$ 4-7 MeV/nucleon have been measured. Particle-γ-coincidences have been employed to achieve the information about involved reaction modes on the basis of their experimentally observed spin states populations during the de-excitation. For both the systems, the experimentally measured spin-distributions and feeding intensity profiles of ICF products have been found to be distinctly different than those observed for CF products, which indicate the involvement of entirely different de-excitation patterns for CF and ICF products. The driving input angular momenta associated with ICF products have been found to be relatively higher than that involved in the production of CF products, and found to increase with direct-α-multiplicity. It has also been observed that ICF products are less fed and/or the population of lower spin states are strongly hindered, while CF products indicate strong feeding over a broad spin range during the de-excitation.

=*=*=*=

Chapter 5

Conclusions and Future Perspectives

On the basis of results and analysis presented in Chapters-2,3 and 4 of this thesis, significant information about CF and ICF reactions have been obtained. In Chapter-2, to study the influence of ICF on CF, EFs of four radio-nuclides; ^{168m,167}Lu, ^{167}Yb and ^{166}Tm produced in ^{16}O+^{159}Tb system, and five radio-nuclides; ^{179,177}Re, ^{177}W, ^{178}Ta and ^{177}Hf produced in ^{16}O+^{169}Tm system have been measured in the energy range $\approx$ 75-95 MeV [59]. In order to get the indication of ICF dynamics and to deduce the ICF contribution at a particular energy, experimentally measured EFs have been compared with the predictions of theoretical model code PACE2. As demonstrated in Chapter-2, enhancement in the experimentally measured production cross-sections over the theoretical model predictions have been observed for most of the α-emission channels. It has been shown that the enhancement is not the discrepancy in the measured cross-sections, as the overall errors from all the possible sources have been found to $\leq$15 %. As such, this enhancement has been attributed to the contribution coming from ICF dynamics. In order to understand the influence of ICF on CF, the percentage fraction of incomplete fusion (F_{ICF}) has been deduced as a function of projectile energy and mass asymmetry of interacting partners. The F_{ICF} has been found to be sensitive to the projectile energy, and also to the mass symmetry of interacting partners. For ^{16}O+^{159}Tb system, the F_{ICF} is found to be $\leq$1% at $\approx$75 MeV, while, as the energy of projectile increases, it approaches to $\approx$20% of the total fusion cross-section at the highest measured energy i.e., $\approx$95 MeV. On the other hand, the F_{ICF} is found to be $\approx$10% at $\approx$75 MeV and $\approx$30% of σ_{TF} at $\approx$95 MeV for ^{16}O+^{169}Tm system. On the basis of the above findings, it may be pointed out that the F_{ICF} at almost same projectile energy is large for ^{16}O+^{169}Tm system than that observed for ^{16}O+^{159}Tb system. This striking observation indicates

the dependence of F_{ICF} on mass-asymmetry of interacting partners. As such, the F_{ICF} has been deduced as a function of mass-asymmetry of interacting partners at a constant relative velocity, where, the F_{ICF} is found to be higher for more mass-asymmetric systems. It has also been observed that the data for ICF can not be explained only on the basis of mass-asymmetry of interacting partners without taking into account the projectile structure effect. As such, it may be inferred that the projectile structure effect also plays an important role in the mass-asymmetry systematics. Further, the observation of large percentage F_{ICF} may be attributed to the prompt break-up of projectile into its α-clusters (^{16}O $\Rightarrow$ ^{12}C+^{4}He and/or ^{8}Be+^{8}Be). The probability of break-up increases with the incident projectile energy, and hence the percentage F_{ICF} has been found to increase with projectile energy. It may, however, be pointed out that the present observations are in agreement with the systematics presented by Morgenstern *et al.*[24, 25, 26]. However, the observation of large percentage F_{ICF} in case of ^{16}O-projectile as that observed for ^{12}C-projectile induced reactions may be because of the fact that the ^{16}O is assumed to be a bunch of 4α-clusters, while ^{12}C consists only of 3α-clusters. As such, in ^{16}O induced reactions the probability of successive α-emitting channels is more as compared to ^{12}C induced reactions. The above mentioned description/discussion on ICF based on the measurement and analysis of EFs strongly reveal that apart from CF, the ICF is also a process of greater importance at these energies, and hence, while predicting the total reaction cross-section, the contribution coming from ICF may also be taken into consideration. It may, however, be pointed out that while predicting percentage F_{ICF} in the frame work of mass-symmetry of interacting partners, it is also required to take projectile structure effect into consideration.

Further, in order to study the fusion incompleteness at energies ≈5-7 MeV/nucleon, forward recoil ranges (RRDs) of nine evaporation residues; ^{168m}Lu, ^{167}Lu, ^{167}Yb, ^{166}Tm, ^{179}Re, ^{177}Re, ^{177}W, ^{178}Ta and ^{177}Hf produced in $^{16}O + ^{159}Tb$ and $^{16}O + ^{169}Tm$ systems respectively, at ≈ 90 MeV and ≈ 87 MeV have been measured [60] and are presented in Chapter-3. The results presented in this chapter on the measurement and analysis of forward recoil ranges of heavy reaction products, strongly reveal significant contribution coming from partial linear momentum transfer of projectile associated with incomplete fusion. Different linear momentum transfer components attributed to the fusion of ^{16}O and/or transfer of ^{12}C and/or ^{8}Be from ^{16}O-projectile to the target nucleus have been observed. An attempt has also been made to obtain the percentage relative contributions of complete and/or incomplete fusion components, which shows ICF as a competing mode of reaction at these energies. The absolute production cross-sections of different reaction products have been obtained by integrating the cross-sections obtained from the experimentally observed recoil range distributions. The contributions of various CF components have been deduced from the experimentally measured RRDs, and then com-

pared with that calculated using theoretical model code PACE, where a fine agreement has been noticed. On the basis of above description based on RRDs analysis, it may be inferred that the residues are not only populated via CF but ICF is also found to play an important role in the production of different reaction products involving direct α-cluster emission. However, in case of ^{166}Tm, ^{177}W, ^{178}Ta and ^{177}Hf residues, the RRDs data clearly indicate that ICF is dominant at the energies of interest in the present work. Moreover, an attempt has also been made to validate the experimentally measured most probable recoil ranges (obtained from the fitting of experimental data points). The experimentally measured most probable recoil ranges have been compared with those estimated by using range energy formulations, and are found to be in good agreement. The measurements presented in Chapter-3, clearly indicate the partial fusion of projectile with target nucleus associated with ICF at these energies.

In order to have information about the involved input angular momenta in various reaction channels, spin distributions and side-feeding intensity profiles of several reaction products produced in ^{16}O+^{169}Tm and ^{12}C+^{169}Tm systems at 5.6 MeV/nucleon and $\approx$4-7MeV/nucleon have been studied, and are presented in Chapter-4. Comparison of spin distributions and side-feeding intensity profiles in the ^{12}C and ^{8}Be capture reactions have been made with those observed for fusion-evaporation reactions for both the systems. From the above comparison, it has been observed that the experimentally measured spin-distributions of direct-$\alpha/2\alpha$-emitting channels (ICF reaction products) identified from forward(F)- α-gated spectra have been found to be distinctly different than that observed for CF reaction products. Further, the population of low spin states are observed to be strongly hindered and/or less fed in case of ICF reaction products, while significant feeding has been observed over the broad spin range in case of CF products. It may, further, be pointed out that, the values of mean input angular momentum increases with direct-α-multiplicity in the forward cone, which indicates the competition from successively opened ICF channels for each ℓ-value above ℓ_{crit} for normal fusion (CF) at respective projectile energies. This confirms the fact that ICF reactions predominantly occur due to influence of centrifugal potential at higher values of impact parameters, where only CF is expected to be dominant. As such, it may not be out of place to mention that the ICF is a natural extension of the fusion processes for those interaction trajectories for which the limit of input angular momenta do not allow CF.

Further, as an extention of the present work, it is proposed to perform some experiments to measure the energy spectra of projectile-like fragments, which are supposed to be an extra degree of freedom to explain the findings of present work. The extension of the present work at relatively higher energies would be interesting, and helpful for the refinement of the present findings. Since, it has already been mentioned that there is no reliable theoretical model available for ICF process at these energies, as such, in order

to develop some model/systematics, it is also required to have a rich data set at these energies.

$=*=*=*=$

Bibliography

[1] J. J. Thomson, Phil. Mag., **44**, 293 (1897).

[2] E. Rutherford, Phil. Mag., **21**, 669 (1911).

[3] H. Becquerel, Comp. Rend., **122**, 450 (1896).

[4] E. Rutherford, Phil. Mag., **37**, 537 (1919).

[5] E. Rutherford, Phil. Mag., **37**, 581 (1919).

[6] R.-D. Herzberg, *et al.*, Nature, **442**, 896 (2006).

[7] P. E. Hodgson, *et al.*, Introductory Nuclear Physics, Chapter **23**, Clarendon Press , Oxford (1997).

[8] R.-D. Herzberg, *et al.*, Nature, **442**, 24 (2006).

[9] Yuri Oganessian, Nature, **413**, 122 (2001).

[10] N. Bohr, Nature, **137**, 344 (1936).

[11] S. N. Ghoshal, Phy. Rev. **80**, 939 (1950).

[12] M. Blann, Phys. Lett. **27**, 337 (1971).

[13] M. Blann, *et al.*, Phys. Rev. **C31**, 1285 (1985).

[14] J. Wilczynski, *et al.*, Nucl. Phys. **A373**, 109 (1982).

[15] A. C. Berriman, Nature, **413**, 144 (2001).

[16] E. Gadioli, et al, Nucl. Phys. **A641**, 271 (1998).

[17] Kauffmann and Wolfgang, Phys. Rev. **121**, 206 (1961)

[18] Manoj Kumar Sharma *et al.*, Phys. Rev. **C70**, 044606(2004), Phys. Rev. **C75**, 064608 (2007), Nucl. Phys. **A774-4**, 83 (2006).

[19] S. Chakrabarty, *et al.*, Nucl. Phys. **A678**, 355 (2000).

[20] P. Vergani, *et al.*, Phys. Rev. **C48**, 1815 (1993).

[21] D. J. Parker, *et al.*, Phys. Rev. **C44**, 1528 (1991).

[22] Unnati Gupta, *et al.*, Nuclear Physics **A811**, 77 (2008).

[23] T. Inamura, *et al.*, Phys. Lett. **B68**, 51 (1977).

[24] H. Morgenstern, *et al.*, Phys. Rev. Lett. **52**, 1104 (1984).

[25] H. Morgenstern, *et al.*, Z. Phys. **A313**, 39 (1983).

[26] H. Morgenstern, *et al.*, Phys. Lett. **B113**, 463 (1982).

[27] I. Tserruya, *et al.*, Phys. Rev. Lett. **60**, 14 (1988).

[28] C. Gerschel, Nucl. Phys. **A387**, 297 (1982).

[29] G. D. Dracoulis, *et al.*, J. Phys. G: Nucl. Part. Phys. **23**, 1191 (1997).

[30] G. J. Lane, *et al.*, Phys. Rev. **C60**, 067301 (1999).

[31] S. M. Mullins, *et al.*, Phys. Lett. **B393**, 279-284 (1997), Phys. Rev. **C61**, 044315 (2000).

[32] D. J. Hinde, *et al.*, Phys. Rev. **C39**, 2268 (1989).

[33] D. J. Hinde, *et al.*, Phys. Rev. **C45**, 1229 (1992).

[34] L. M. Pant, *et al.*, Eur. Phys. J. **A11**, 47 (2001).

[35] R. Tripathi, *et al.*, Phys. Rev. **C69**, 024613 (2004).

[36] S. Gupta, *et al.*, Phys. Rev. **C61**, 064613 (2000).

[37] H. C. Britt and A. R. Quinton, Phys. Rev. **124**, 877 (1961).

[38] J. Galin, *et al.*, Phys. Rev. **C9**, 1126 (1974).

[39] R. Weiner and Westrom, Nucl. Phys. **A386**, 282 (1977).

[40] T. Udagawa and T. Tamura, Phys. Rev. Lett. **45**, 1311 (1980).

[41] J. P. Bondrof, *et al.*, Nucl. Phys. **A333**, 285 (1980).

[42] W. Trautmann, *et al.*, Phys. Rev. Lett. **53**, 1630 (1984).

[43] T. Inamura, *et al.*, Phys. Lett. **B84**, 71 (1982).

[44] T. Inamura, *et al.*, Phys. Rev. **C32**, 1539 (1985).

[45] J. B. Natowitz, *et al.*, Z. Phys. **A325**, 467 (1986).

[46] J. P. Bondrof, *et al.*, Nucl. Phys. **A333**, 285 (1980).

[47] D. H. E. Gross and J. Wilczynski, Phys. Lett. **B67**, 1 (1977).

[48] H. Tricoire, *et al.*, Z. Phys. **A312**, 221 (1983).

[49] T. C. Awes, *et al.*, Phys. Rev. **C24**, 89 (1981).

[50] S-Wilczynska K., *et al.*, Phys. Rev. Lett.**42**, 1599 (1979).

[51] Manoj Kumar Sharma, *et al.*, J. Phys. Soc. Japan **72**, 1917 (2003).

[52] Pushpendra P. Singh, M. Phil. Dissertation, A. M. University, Aligarh, India (2005), unpublished.

[53] Sunita Gupta, *et al.*, J. Phys. Soc. Japan **71**, 2434 (2002).

[54] D. J. Parker, *et al.*, Phys. Rev. **C39**, 2256 (1989).

[55] M. F. Vineyard, *et al.*, Phys. Rev. **C45**, 1784 (1992).

[56] C. Beck, *et al.*, Phys. Rev. **C39**, 2202 (1989).

[57] C. Rubbia, *et al.*, Report CERN/AT/95-94(ET).

[58] M. M. Musthafa, *et al.*, App. Rad. Isot. **62**, 419 (2005).

[59] Pushpendra P. Singh, *et al.*, Phys. Rev. **C77**, 014607 (2008), references therein.

[60] Pushpendra P. Singh, *et al.*, Euro. Phys. J. **A34**, 29-39 (2007), references therein.

[61] Pushpendra P. Singh, *et al.*, Phys. Rev. **C78**, 017602 (2008), references therein.

[62] Pushpendra P. Singh, *et al.*, Phys. Lett. **B** (2008), **doi:10.1016 / j.physletb.2008.11.035** (in press), references therein.

[63] G. K. Mehta and A. P. Patro, Nucl. Inst. and Meth. **A268**, 334 (1988).

[64] B. P. Ajithkumar, *et al.*, Nucl. Inst. and Meth. **A343**, 327 (1994).

[65] R. C. Kotch, Activation Analysis Handbook, Academic Press, New York and London, 1960.

[66] **SRIM06**, http://www.srim.org/

[67] B. P. Ajithkumar, *et al.*, SANAI, Trombay, India 1997.

[68] E. Brown and R. B. Firestone, Table of Isotopes, Wiley, New York, 1986.

[69] Jagdish K. Tuli, Nuclear Wallet Cards, National Nuclear Data Center, Upton, New York, 2000.

[70] Pushpendra P. Singh, *et al.*, Int. J. of Mod. Phys. **E17**, 549 (2008).

[71] A. Garvon, Phys. Rev. **C21**, 230 (1980).

[72] R. Bass, Nucl. Phys. **A231**, 45 (1985).

[73] F. D. Becchetti and G. W. Greenlees, Phys. Rev. **182**, 1190 (1969).

[74] G. R. Satcher, Nucl. Phys. **70**, 177 (1965).

[75] P. M. Endt, *et al.*, At. Data Nucl. Data Tables **26**, 47 (1981).

[76] J. P. Lestone, Phys. Rev. **C53**, 2014 (1996).

[77] A. Gilbert, A. G. N. Cameron, Canand. J. Phys. **43**, 1446 (1965).

[78] M. Cavinato, *et al.*, Phys. Rev. **C52**, 2577 (1995).

[79] K. S. Babu, *et al.*, J. Phys. **G29**, 1011 (2003).

[80] P. R. S. Gomes, *et al.*, Phys. Lett. **B601**, 20 (2004).

[81] R. K. Bhowmik, *et al.*, Nucl. Phys. Symp. **V34B**, 419 (1991), Nucl. Phys. Symp. **V44B**, 422 (2001).

[82] C. Gerschel, *et al.*, Nucl. Phys. **A387**, 297 (1982).

[83] G. D. Dracoulis *et al.*, J. Phys. G: Nucl. Part. Phys. **23**, 1191 (1997).

[84] G. J. Lane, *et al.*, Phys. Rev. **C60**, 067301 (1999).

[85] S. M. Mullins, *et al.*, Phys. Lett. B **393**, 279 (1997), Phys. Rev. **C61**, 044315 (2000).

[86] **RADWARE**, Developed by David Radford, http://radware.phy.ornl.gov/agsdir1.html, and **National Nuclear Data Center (NNDC)**, http://www.nndc.bnl.gov/databases/databases.html.